# Grid-based procedures for the mechanical analysis of heterogeneous solids

( Gitterbasierte Verfahren zur mechanischen Analyse heterogener Festkörper )

DISSERTATION

zur Erlangung des akademischen Grades

Doktor-Ingenieur

an der Fakultät Bauingenieurwesen

der Bauhaus-Universität Weimar

vorgelegt von

## Stefan Häfner

geboren am 12. November 1973 in Nürnberg

Hauptberichter: Prof. Dr.-Ing. habil. Carsten Könke

Mitberichter: Prof. Dr.-Ing. Dr.-Ing. E.h. Dr. h.c. Ekkehard Ramm

Mitberichter: Prof. Dr. rer. nat. habil. Klaus Gürlebeck

Tag der Disputation: 25. Mai 2007

Institut für Strukturmechanik der Bauhaus-Universität Weimar

Weimar 2007

# Kurzfassung

Die wichtige Bedeutung moderner Simulationsverfahren in der mechanischen Analyse heterogener Festkörper wird eingangs ausführlich dargestellt. Dabei wird als Problem festgestellt, dass die erforderliche hochauflösende Analyse bereits für relativ kleine Körper an die Grenzen heutiger Rechenleistung stößt, sowohl bezüglich Speicherbedarf als auch akzeptablen Rechenaufwands. Ein weiteres Problem stellt die häufig unzureichend genaue geometrische Modellierung der Zusammensetzung heterogener Körper dar.

Die vorliegende Arbeit führt eine systematische Kombination und Anpassung von gitterbasierten Methoden ein, um dadurch eine wesentlich höhere Auflösung in der numerischen Analyse heterogener Körper zu erzielen. Gitterverfahren eignen sich ebenfalls ausgezeichnet, um effiziente und numerisch stabile Algorithmen zur flexiblen geometrischen Modellierung zu entwickeln. Ein Schlüsselaspekt stellt ein gleichmäßiges Datenmanagement für Gitter dar, welches dafür eingesetzt werden kann, um den Aufwand und die Komplexität von nahezu allen beteiligten Methoden zu reduzieren. Ein neues Finite-Elemente Programm, namens Mulgrido, wurde eigens dafür entwickelt, um das vorgeschlagene Konzept konsistent zu realisieren und zu untersuchen. Einige Nachteile, die sich klassischerweise aus Gitterdiskretisierungen ergeben, werden gezielt durch modifizierte Verfahren korrigiert.

Die gegenwärtige Arbeit gliedert sich in ein geometrisches Modell, ein mechanisches Modell und ein numerisches Modell. Das geometrische Modell beinhaltet neben Methoden der digitalen Bildverarbeitung, insbesondere sämtliche Verfahren zur künstlichen Generierung von Einschluss-Matrix Geometrien. Wesentliche Beiträge werden bezüglich variabler Form, Größenverteilung, Überschneidungsabfragen und Platzierung von Einschlüssen geleistet. Das mechanische Modell bereitet durch Grundlagen der Kontinuumsmechanik, der Homogenisierung und der Schädigungsmodellierung auf eine numerische Umsetzung vor. Als erstes Thema des numerischen Modells wird eine besondere Umsetzung von B-Spline Finiten Elementen vorgestellt. Diese Finite Elemente können generisch für eine beliebige Ordnung k der B-Splines erzeugt werden. Für homogene Körper verfügen diese somit über beliebig skalierbare Approximationseigenschaften. Mittels des Konzepts mehrphasiger Finite Elemente in Kombination mit Übergangszonen entlang von Materialgrenzen gelingt eine hochwertige Erweiterung für heterogene Körper. Durch die Formulierung auf Elementebene, kann die Speicherung der globalen Steifigkeitsmatrix und somit wesentlicher Speicherplatz eingespart werden. Dies ist möglich in Kombination mit iterativen Lösungsverfahren, die das zweite Thema des numerischen Modells darstellen. Dabei liegt der Fokus auf Mehrgitterverfahren. Diese zeichnen sich dadurch aus, dass die Anzahl der erforderlichen Operationen um ein lineares Gleichungssystem zu lösen, nur linear mit der Problemgröße ansteigt. Durch Vorkonditionierung wird für schlecht konditionierte Probleme eine ganz wesentliche Verbesserung erreicht. Als drittes Thema des numerischen Modells werden Aspekte der Schädigungssimulation diskutiert, die in engem Zusammenhang mit der Gitterdiskretisierung stehen. Die hohe Effizienz der linearen Analyse kann durch ein schädigungskontrolliertes, schrittweise lineares Iterationsschema für die Schädigungsanalyse aufrecht erhalten werden.

Abschließend wird eine Studie über das effektive Materialverhalten heterogener Körper vorgestellt. Insbesondere wird der Einfluss der Form von Einschlüssen untersucht. Mittels insgesamt weit über hunderttausend zufälliger geometrischer Anordnungen wird das effektive Materialverhalten statistisch analysiert und bewertet.

# Abstract

The importance of modern simulation methods in the mechanical analysis of heterogeneous solids is presented in detail. Thereby the problem is noted that even for small bodies the required high-resolution analysis reaches the limits of today's computational power, in terms of memory demand as well as acceptable computational effort. A further problem is that frequently the accuracy of geometrical modeling of heterogeneous bodies is inadequate.

The present work introduces a systematic combination and adaption of grid-based methods for achieving an essentially higher resolution in the numerical analysis of heterogeneous solids. Grid-based methods are as well primely suited for developing efficient and numerically stable algorithms for flexible geometrical modeling. A key aspect is the uniform data management for a grid, which can be utilized to reduce the effort and complexity of almost all concerned methods. A new finite element program, called Mulgrido, was just developed to realize this concept consistently and to test the proposed methods. Several disadvantages which generally result from grid discretizations are selectively corrected by modified methods.

The present work is structured into a geometrical model, a mechanical model and a numerical model. The geometrical model includes digital image-based modeling and in particular several methods for the theory-based generation of inclusion-matrix models. Essential contributions refer to variable shape, size distribution, separation checks and placement procedures of inclusions. The mechanical model prepares the fundamentals of continuum mechanics, homogenization and damage modeling for the following numerical methods. The first topic of the numerical model introduces to a special version of B-spline finite elements. These finite elements are entirely variable in the order k of B-splines. For homogeneous bodies this means that the approximation quality can arbitrarily be scaled. In addition, the multiphase finite element concept in combination with transition zones along material interfaces yields a valuable solution for heterogeneous bodies. As the formulation is element-based, the storage of a global stiffness matrix is superseded such that the memory demand can essentially be reduced. This is possible in combination with iterative solver methods which represent the second topic of the numerical model. Here, the focus lies on multigrid methods where the number of required operations to solve a linear equation system only increases linearly with problem size. Moreover, for badly conditioned problems quite an essential improvement is achieved by preconditioning. The third part of the numerical model discusses certain aspects of damage simulation which are closely related to the proposed grid discretization. The strong efficiency of the linear analysis can be maintained for damage simulation. This is achieved by a damage-controlled sequentially linear iteration scheme.

Finally a study on the effective material behavior of heterogeneous bodies is presented. Especially the influence of inclusion shapes is examined. By means of altogether more than one hundred thousand random geometrical arrangements, the effective material behavior is statistically analyzed and assessed.

# Vorwort

# Contents

# Nomenclature

The following lists include the most relevant variables. Exceptional, different notation of variables is defined in the context. Statistical measures are only applied within Chapter 7. Corresponding notation of variables is given by Equations 7.7 to 7.14 in Section 7.2.

**Capital letters**

| | |
|---|---|
| $A$ | area |
| $A^e$ | surface of element $e$ |
| $\boldsymbol{B}^e$ | strain-displacement matrix of element $e$ |
| $\boldsymbol{B}^J$ | strain-displacement matrix of element type $J$ |
| $\boldsymbol{B}^{j_x,j_y}$ | strain-displacement matrix of element type $(j_x, j_y)$ |
| $\boldsymbol{C}$ | material matrix |
| $\boldsymbol{C}^{\mathrm{app}}$ | apparent properties |
| $\boldsymbol{C}^e$ | material matrix of element $e$ |
| $\boldsymbol{C}^{\mathrm{eff}}$ | effective properties |
| $\boldsymbol{C}^E$ | linear elastic material matrix |
| $\mathbb{C}$ | fourth-order material tensor |
| $C_{T,D}$ | scalar constant which depends on $D$ |
| $D$ | dimension of finite element: 1, 2 or 3 |
| $\boldsymbol{D}$ | diagonal of a matrix |
| $D_{\mathrm{max}}$ | maximum size of aggregates |
| $E$ | Young's modulus |
| $E^a$ | Young's modulus of element $a$ |
| $E_i^e$ | Young's modulus in integration point $i$ of element $e$ |
| $E_W$ | External work |
| $\hat{E}$ | reduced Young's modulus according to damage |
| $F$ | Airy function |
| $\boldsymbol{F}_i$ | external point load $i$ within finite element |
| $H$ | height of rectangular domain |
| $\boldsymbol{H}^{-1}$ | preconditioning matrix |
| $\boldsymbol{J}$ | Jacobian matrix |
| $\boldsymbol{K}$ | global stiffness matrix |
| $\boldsymbol{K}_i$ | global stiffness matrix of mesh $i$ |
| $\boldsymbol{K}_{i,j}$ | submatrix $(i, j)$ of $\boldsymbol{K}$ |

| | |
|---|---|
| $\bar{K}_{i,j}$ | element in $i$-th row and $j$-th column of element stiffness matrix with Young's modulus $E = 1$. |
| $\hat{K}_{i,j}$ | element in $i$-th row and $j$-th column of effective stiffness in center node of element patch |
| $\boldsymbol{K}^e$ | element stiffness matrix of element $e$ |
| $\bar{\boldsymbol{K}}^e$ | element stiffness matrix sorted into global degrees of freedom |
| $\boldsymbol{K}_X$ | element stiffness matrix of the scaled element |
| $\boldsymbol{K}_Z$ | element stiffness matrix of the initial element |
| $\boldsymbol{L}$ | negative strictly lower triangle of a matrix |
| $\boldsymbol{M}$ | iteration matrix |
| $\boldsymbol{N}^e$ | shape functions of element $e$ |
| $\boldsymbol{N}^J$ | one-dimensional shape functions of element type $J$ |
| $\boldsymbol{N}^{j_x,j_y}$ | two-dimensional shape functions of element type $(j_x, j_y)$ |
| $P(s)$ | Legendre polynomial |
| $\boldsymbol{Q}$ | square matrix |
| $R$ | ratio of Young's modulus between inclusion and matrix (Chapter 5) *or* interaction radius of weighting function (Chapters 3 and 6) |
| $R_1, R_2$ | resulting force in $x_1$- or $x_2$-direction |
| $\boldsymbol{S}$ | splitting matrix |
| $S_i^e$ | principal stress with $S_1 > S_2 > S_3$ of $\sigma^e$ |
| $\boldsymbol{U}$ | displacement vector (or tensor) *or* negative strictly upper triangle of a matrix (only in Section 5.3) |
| $\boldsymbol{U}_D$ | prescribed displacements |
| $\boldsymbol{U}^e$ | interpolated displacements within element $e$ |
| $\boldsymbol{U}^i$ | displacements in domain $\Omega_i$ |
| $U(x)$ | one-dimensional displacement as function of $x$ |
| $V$ | volume |
| $V^e$ | volume of element $e$ |
| $W$ | width of rectangular domain |
| $X_1, X_2$ | uniform random numbers in the unit interval [0;1] |
| $\boldsymbol{X}$ | vector of coordinates |
| $\boldsymbol{Z}$ | vector of coordinates |

**Lower case letters**

| | |
|---|---|
| $b^k(x)$ | univariate B-spline of order $k$ |
| $b_j^k(x)$ | univariate B-spline of order $k$ numbered by $j$ |
| $b_{d,h}^k(x)$ | univariate B-spline scaled to segment length $h$, translated by distance $d$ |
| $b^{j_x,j_y}(x, y)$ | bivariate B-spline of element type $(j_x, j_y)$ |
| $c$ | scalar variable |
| $\bar{c}_j$ | coefficient $j$ of polynomial |
| $\bar{c}_{i,j}$ | coefficient $j$ of piecewise polynomial $\bar{p}_i(x)$ |
| $d_1, d_2, d_3$ | main dimensions of particle |
| $\boldsymbol{e}_i$ | unit vector $i$ of coordinate system |
| $\boldsymbol{e}^k$ | error of displacements after $k$-th iteration |
| $\boldsymbol{f}$ | global vector of loads |

| | |
|---|---|
| $\boldsymbol{f}_i$ | subvector $i$ of $\boldsymbol{f}$ |
| $\boldsymbol{f}_m$ | force vector of mesh $m$ |
| $\boldsymbol{f}^e$ | load vector of element $e$ |
| $\hat{f}_i$ | applied external force of $i$-th degree of freedom of element patch |
| $\bar{\boldsymbol{f}}^e$ | element load vector sorted into global degrees of freedom |
| $\boldsymbol{f}^k$ | product $\boldsymbol{K}\boldsymbol{u}^k$ |
| $f_t$ | tensile strength |
| $f(\boldsymbol{x})$ | any function of $\boldsymbol{x}$ |
| $\bar{f}(\boldsymbol{x})$ | nonlocal equivalent of $f(\boldsymbol{x})$ |
| $\Delta\boldsymbol{f}^k$ | increment of $\boldsymbol{f}^k$ after the $k$-th iteration |
| $g(x)$ | one-dimensional function of $x$ |
| $h$ | grid size and element size |
| $h_x,\ h_y$ | grid size in $x$- and $y$-direction |
| $i$ | imaginary unit $i = \sqrt{-1}$ in context of complex numbers |
| $i,\ j,\ k,\ l$ | integer variables (e.g. also indices) |
| $i_e,\ i_n$ | global numbering of elements and nodes |
| $i_{eg},\ i_{ng},\ i_{sg}$ | global numbering of elements, nodes and B-spline coefficients |
| $i_{cg}$ | local numbering of B-spline coefficients within an element |
| $i^*,\ j^*$ | additional integer variables |
| $k$ | order of B-splines (Chapter 4) |
| | *or* number of iterations (Chapter 5) |
| $k_1, k_2$ | constants |
| $\ell$ | internal length of a material |
| $\ell_c$ | characteristic length of a material |
| $l_a,\ l_b,\ l_c$ | size of element in $x$-, $y$- and $z$-direction |
| $l_x,\ l_y,\ l_z$ | size of orthogonal domain in $x$-, $y$- and $z$-direction |
| $m$ | number of meshes is $m+1$, such that $i = 0\ldots m$ counts all meshes |
| $\boldsymbol{n}$ | normal vector |
| $n$ | integer variable (e.g. upper limit of series or sum) |
| $\bar{n}$ | number of bivariate spline segments in one element |
| $n_x, n_y$ | number of integration points in $x$- and $y$-direction |
| $n_{ex}, n_{ey}, n_{ez}$ | number of elements of grid in $x$-, $y$ and $z$-direction |
| $n_{nx}, n_{ny}, n_{nz}$ | number of nodes of grid $(x, y, z)$ |
| $n_{sx}, n_{sy}, n_{sz}$ | number of spline coefficients of grid $(x, y, z)$ |
| $n_{cx}, n_{cy}, n_{cz}$ | number of spline coefficients in one element $(x, y, z)$ |
| $\boldsymbol{p}^k$ | search direction after $k$-th iteration |
| $\boldsymbol{p}^e$ | loads of element $e$ in combination with $\boldsymbol{p}_b$ and $\boldsymbol{p}_s$ |
| $\boldsymbol{p},\ \boldsymbol{p}_b$ | body loads |
| $\boldsymbol{p}_s$ | surface loads |
| $p(x)$ | one-dimensional load |
| $\bar{p}_i(x)$ | piecewise polynomial $i$ with respect to $x$ |
| $\boldsymbol{q}$ | vector |
| $r$ | positive distance between effect point and source point |
| $r_1, r_2, r_3$ | radii of ellipsoid (also superellipsoid) |
| $\boldsymbol{r}^k$ | residual forces after the $k$-th iteration |

| | |
|---|---|
| $\boldsymbol{r}_m^k$ | residual forces after the $k$-th iteration on mesh $m$ |
| $\hat{r}_i$ | residual force of $i$-th degree of freedom of element patch |
| $s$ | scalar variable |
| $s_i$ | coordinate of integration point $i$ |
| $s_t$ | size of transition zone |
| $s_{x,i}, s_{y,i}$ | distance in $x$- and $y$-direction within finite element |
| $\bar{s}(x)$ | univariate spline |
| $\boldsymbol{t}$ | surface tractions |
| $t$ | thickness of two-dimensional finite element |
| $\boldsymbol{u}$ | global vector of displacements |
| $\boldsymbol{u}_i$ | subvector $i$ of $\boldsymbol{u}$ |
| $\boldsymbol{u}_m$ | displacement vector of mesh $m$ |
| $\boldsymbol{u}^e$ | degrees of freedom of element $e$ |
| $\boldsymbol{u}^k$ | vector $\boldsymbol{u}$ after the $k$-th iteration |
| $\Delta\boldsymbol{u}^k$ | vector increment after the $k$-th iteration |
| $\Delta u_i$ | displacement increment of $i$-th degree of freedom of element patch |
| $\boldsymbol{v}$ | vector with size of global degrees of freedom |
| $\boldsymbol{v}^e$ | vector with size of local degrees of freedom of element $e$ |
| $\bar{\boldsymbol{v}}^e$ | vector $\boldsymbol{v}^e$ sorted into global degrees of freedom |
| $w_{x,i}, w_{y,i}$ | weighting factors of numerical integration in $x$- and $y$-direction numbered by $i$ |
| $\boldsymbol{x}$ | position in a global coordinate system |
| $x$ | scalar variable |
| $x_i$ | supporting point $i$ of a spline |
| $x^j$ | for convenience: $x$ to the power of $j$ |
| $x_1; x_2$ | range of aggregate sizes is $[x_1; x_2]$ |
| $y$ | scalar variable associated with a coordinate system |
| $z$ | scalar variable associated with a coordinate system |

## Greek letters

| | |
|---|---|
| $\Gamma_D$ | Dirichlet boundary (prescribed displacements) |
| $\Gamma_N$ | Neumann boundary (prescribed forces) |
| $\Gamma_{ij}$ | boundary between domain $\Omega_i$ and domain $\Omega_j$ |
| $\Omega$ | two- or three-dimensional domain |
| $\Omega_i$ | defined domain $i$ |
| $\Omega_X$ | domain of mapped element geometry |
| $\Omega_Z$ | domain of initial element geometry |
| | |
| $\alpha$ | scalar variable |
| $\alpha(\boldsymbol{x}, \boldsymbol{\xi})$ | effective weighting function which satisfies $\int_\Omega \alpha(\boldsymbol{x}, \boldsymbol{\xi}) = 1$ |
| $\alpha_0(\boldsymbol{x}, \boldsymbol{\xi})$ | an initial weighting function |
| $\beta$ | angle within triangle |
| $\delta_{ij}$ | Kronecker symbol |
| $\boldsymbol{\epsilon}$ | strain vector (or tensor) |

| | |
|---|---|
| $\boldsymbol{\epsilon}_0$ | limit elastic strain |
| $\boldsymbol{\epsilon}^0$ | constant strain |
| $\boldsymbol{\epsilon}_a$ | absolute error according to Euclidean norm |
| $\boldsymbol{\epsilon}_r$ | relative error according to Euclidean norm |
| $\boldsymbol{\epsilon}_E$ | measure for relative error of energy |
| $\boldsymbol{\zeta}$ | position in a local coordinate system, equivalent to $\boldsymbol{\xi}$ |
| $\eta$ | exponent, integer variable |
| $\kappa$ | maximum equivalent strain in the history of a material point |
| | *or* bulk modulus (only in Section 3.3.4) |
| $\lambda,\ \mu$ | Lame constants |
| $\lambda_k$ | scalar factor after $k$-th iteration |
| $\nu$ | Poisson's ratio |
| $\nu^a$ | Poisson's ratio of element $a$ |
| $\boldsymbol{\xi}$ | position in a local coordinate system |
| $\boldsymbol{\sigma}$ | stress vector (or tensor) |
| $\boldsymbol{\sigma}^E$ | stress of linear elastic (undamaged) material |
| $\boldsymbol{\sigma}^0$ | constant stress |
| $\boldsymbol{\varphi}_V$ | density function of aggregate volume |
| $\boldsymbol{\Phi}_m$ | cumulative distribution function of aggregate mass |
| $\boldsymbol{\Phi}_V$ | cumulative distribution function of aggregate volume |
| $\omega$ | relaxation factor (Chapter 5) |
| | *or* damage parameter (Chapters 3 and 6) |

## Mathematical notation

| | |
|---|---|
| $\lvert \cdot \rvert$ | absolute value of a scalar value $(\cdot)$ |
| $(\cdot)^{\mathrm{T}}$ | transposed of vector or matrix $(\cdot)$ |
| $\langle \cdot \rangle$ | average value of $(\cdot)$ from integral over domain |
| | *or* positive part which means maximum of 0 and $(\cdot)$ (only in Section 3.4.2) |
| $\frac{\partial (\cdot)}{\partial x}$ | partial derivative of $(\cdot)$ with respect to $x$ |
| $(\cdot)_{,x}$ | partial derivative of $(\cdot)$ with respect to $x$ |
| $(\cdot)_{,xx}$ | is equivalent to $((\cdot)_{,x})_{,x}$ |
| $\Delta$ | Laplace operator |
| $\mathrm{C}^k$ | $\mathrm{C}^k$-continuous denotes: $k$ derivatives are continuous |
| $\det(\cdot)$ | determinant of $(\cdot)$ |
| $\operatorname{grad}(\cdot)$ | gradient of $(\cdot)$ |
| $\mathrm{Re}$ | real part of a complex number |

# Chapter 1

# Introduction

## 1.1 Practical Importance and Application

Numerical simulation of heterogeneous solids has already been successfully performed in many kinds of scientific and engineering disciplines. Moreover it attracts increasing interest and still gains in importance. Numerical simulation is not only promising for improving existing materials but establishes additional insights, leads to novel manufacturing processes and essentially initiates new technologies while new applications arise. In the present context several terms are closely related to the entitled heterogeneous solid, such as composite material, multiphase material, microstructural material, advanced materials, engineering materials, while there are many specific terms within a hierarchic categorization of heterogeneous solids.

The chance to simulate the mechanical behavior of heterogeneous solids has only been established by the immense increase of computational power in the recent decades. In computational mechanics the analysis of materials can partially be based on the well-established analysis of structures. In fact, the adequate magnification of a heterogeneous material often reveals a concise arrangement of one or more material phases which remind of a structure. This indicates an explanation for the term microstructural materials. However, the analysis of materials requires additional theoretical considerations as well as further advanced computational methods. In comparison to structural analysis of traditional objects, the geometrical description of a heterogeneous solid or microstructure is particularly more complex. The mechanical theory needs to be revisited for an adequate adaption of modeling e.g. material interfaces. Especially volumetric modeling and analysis of heterogeneous solids require advanced numerical methods. This outline characterizes some present challenges in the research of the simulation of heterogeneous solids.

The basic idea of this research is the direct modeling of a heterogeneous solid. The material is not homogenized, but the various constituents are explicitly represented in the computational model. Therefore the mechanical behavior of the heterogeneous solid can be based on clear defined material laws of the constituents rather than creating a new phenomenological material law for each specific composite. In damage mechanics this means a consistent simulation from initial cracks on the material level (microcracks) up to macroscopic cracks and structural failure. Cause and effect in the behavior of a certain material become more direct and transparent. Therefore it is possible to analyze a wide variety of materials which could so far only investigated by physical experiments. Zohdi and Wriggers (2005) state: "Minimally, no one can argue that computations cannot now play a strong complementary role to laboratory experiments.". In fact, computational

material testing implicates several further opportunities. The proposed mechanical simulation of heterogeneous solids based on defined properties of the constituents reaches from effective elastic properties up to complex damage behavior. It is noted that such simulation techniques are also applied for other physical properties such as e.g. dynamic, thermal, hydrological or acoustic properties. However, besides only analyzing existing natural or artificial materials, numerical simulation essentially supports the design of novel, advanced materials. Selective prototyping of materials by simulation enables to develop tailored materials with specific, optimal or extremal properties. For the typical application, the simulation supports an increase of strength or crack resistance, a reduction of weight or heat expansion, as well as a combined optimization of various physical properties. Therefore virtual material testing has become and will further develop as a valuable tool for material scientists and structural engineers.

Figure 1.1 illustrates the complexity and diversity of heterogeneous solids. Also materials which are generally classified to be homogeneous, such as cement stone, metals or bone, exhibit a heterogeneous character on a magnified level and are therefore microheterogeneous. Besides, natural materials, such as bone and wood, there is a large range of engineering materials. Such composites consist of polymers, metals or ceramics, and as embedded material also carbon and glass are applied. The embedded phase is most often included to strengthen the matrix material. The variable design of the composite allows to establish various other material properties. Fibers, flakes, small particles, larger inclusions, as well as voids, denote various entities within composites. There are numerous subcategories such as long, continuous fibers or short, discontinuous fibers. The microstructural arrangement ranges from a regular order, directed orientations to completely random geometries. The application of such materials has become profitable and indispensable for aerospace, automotive, sports equipment, construction and several other fields of engineering.

In civil-engineering concrete plays a key role. In fact it is one of the most common materials for building massive structures. It is applied for bridges, tunnels, dams, repositories, foundations and high-rise buildings. The manifold use of concrete for various purposes has lead to numerous, different material types of concrete for achieving certain properties. The corresponding research still continues. Generally concrete is reinforced by steel bars, but concrete itself is already a heterogeneous material. The classic material consists of sand, natural aggregates and cement which hardens almost completely within one month by a reaction with water. There are many aspects to consider not only with regard to the final product such as effective strength, but also to its manufacturing process such as segregation and workability. Special processes such as creep and shrinkage need to be considered. Various aggregates, such as river gravel, crushed gravel, polystyrene beads, steel fibers and recycling material are applied in concrete mixtures to achieve certain properties or serve as economical filler. Textile reinforcement and glass fiber reinforced concrete are actual research topics. But also the cementitious matrix material with various additives spans a wide spectrum. Also in the research of concrete, computational material testing serves as important tool in analysis and design.

As a further microheterogeneous solid, bone tissue is considered. As it is a natural material, it is expected to be optimal (Sigmund 2002). The microstructure of trabecular bone is open-walled. The computational simulation revealed, however, that from a mechanical point of view, a close-walled microstructure would be optimal. This difference can be ex-
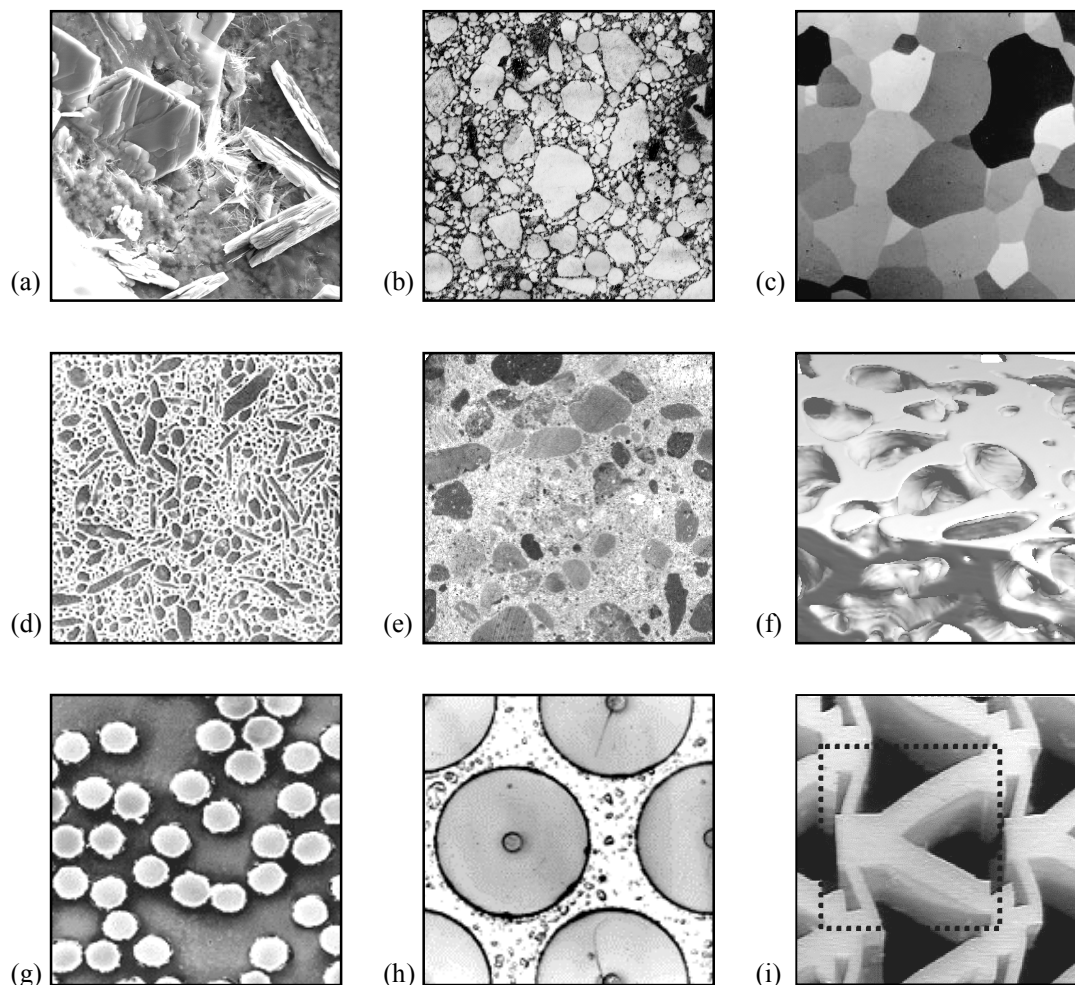
Figure 1.1: Examples of heterogeneous and microheterogeneous materials (sources of images, page 162): (a) cement stone with flat portlandite crystals, (b) mortar material with natural aggregates smaller than 2 mm, (c) crystals of a aluminum-silicon-germanium alloy, (d) ceramic material of silicon nitride with ultimate toughness, (e) concrete material with natural aggregates, (f) remodeled trabecular bone of the human femur, (g) carbon fibers in magnesium-lithium alloy, (h) boron fibers in aluminum matrix, (i) manufactured material with negative Poisson's ratio.

plained as for the flow of nutrition within the bone, conductivity needs to be established. Bone tissue not only performs as a structural element, but in multiple tasks. Computational simulation of bone tissue is promising and has become a respectable research topic.

Finally, it is pointed out to the research of Sigmund (2002) on the design of extreme materials. By topology optimization within computational simulation Sigmund (2002) has designed several new materials with outstanding properties. It is shown that several of such materials come close to the theoretical limits. As modern manufacturing processes, such as etching techniques and coextrusion, allow to create an enormous range of microstructural materials, several extremal materials have been manufactured. An example of a manufactured material with negative Poisson's ratio is shown in Fig. 1.1 (i). Moreover, Sigmund (2002) designed extremal and optimal materials with respect to thermal expansion coefficient, buckling, wave propagation and other material properties. Some of these materials have already found industrial application. It is highlighted, that the design of these extremal materials, completely originates from computational simulation.

## 1.2    Real Material, Model and Simulation

The observed character of materials often changes with different magnification. Therefore a classification of length scales or material levels is introduced in Table 1.1.

| | | | | |
|---|---|---|---|---|
| Macroscale | $10^{-2}$ m | - | $10^{+2}$ m |
| Mesoscale | $10^{-4}$ m | - | $10^{-1}$ m |
| Microscale | $10^{-6}$ m | - | $10^{-3}$ m |
| Nanoscale | $10^{-8}$ m | - | $10^{-7}$ m |

Table 1.1: Definition of length scales

The defined ranges which are assigned to the various length scales partially overlap and in fact can only be considered as approximate reference values. In fact these terms rather describe an abstraction level of a material than just a specific length. Within this context a macroscale model means that the material is homogenized. The mesoscale refers to an intermediate order of magnitude. For concrete material the mesoscale model explicitly includes the two phases aggregates and cement stone. On this level the material phases themselves are homogenized. It is possible to assign larger voids to the mesoscale model. Furthermore also a phenomenologic interface law in between the phases may be added. However, only an increased resolution of the interfacial transition zone on the microscale enables an improved insight into its microstructure and provides a reasonable cause for the special behavior of an interface. The term macro defines visibility to the naked eye and micro defines the opposite. At this microscopic level also the cement stone appears as heterogeneous material. Some further dimensions below, on the nanoscale, the material is recognized as molecules and atoms. At this resolution level the material is generally not considered being continuous. The present generation of computers and probably the next few of the future do not allow to simulate a macroscopic structure, by a nanoscale model, a microscale model and only hardly by a mesoscale model. Only some tiny relevant parts, as e.g. cracks or crack tips, of the macroscale model can be replaced by a model of higher resolution to increase the approximation quality. Such a combination is denoted as multiscale model.

This thesis only refers to models of the microscale and the mesoscale. In the following the term subscale is applied as a general reference to both. In different approaches, subscale models may differ in dimension and type of abstraction. Therefore the reader is referred to Fig. 1.2 which illustrates the proposed abstraction type as a continuous multiphase material. Figure 1.2 does not yet put the model into mechanical context such as loads and boundary conditions. It is only considered as a geometrical model which consists of a certain geometrical arrangement of various phases, denoted as material A, B, C and so on. The geometry of the model and the real heterogeneous material need to correspond adequately. Otherwise, as a real material with a modified geometry might significantly differ in its behavior, the same has to be expected from the model. But besides the importance of the geometry, there are several further things to consider which have been summarized in Fig. 1.3.

Besides the geometrical model, Fig. 1.3 further includes the mechanical model and the numerical model. It is highlighted that these models are mostly independent of each other.
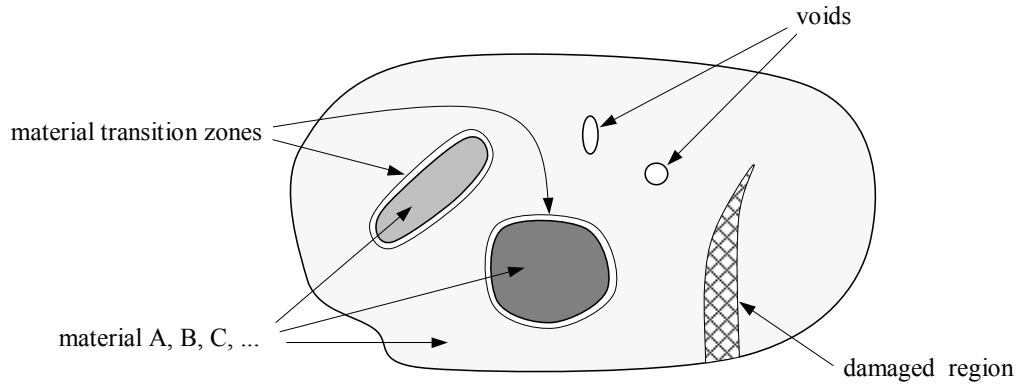
Figure 1.2: Geometrical model of multiphase material

One can apply various mechanical models to the geometry, such as continuum mechanics, discontinuum mechanics or the Cosserat continuum. Moreover, many constitutive laws for modeling damage, creep, shrinkage or the behavior of material interfaces are available. The numerical model denotes applied methods of numerical mathematics. For the discretization of the material, finite elements are common in use, but only to point out to one relevant alternative it is referred to meshless methods. Moreover, the numerical model includes methods for solving linear and nonlinear equation systems. Finally, certain dependencies and connections between geometry, mechanics and numerics will occur. But besides stating a manifold range of possible combinations, it is summarized that each of these three instances deserves considerate appreciation and understanding to achieve an accurate simulation of heterogeneous materials.

Besides, a stochastic model is mentioned in Fig. 1.3. The stochastic model is not in the focus of the present work. Scatter and disturbances in the material are omnipresent and often relevant conditions for a certain material behavior. For concrete material it
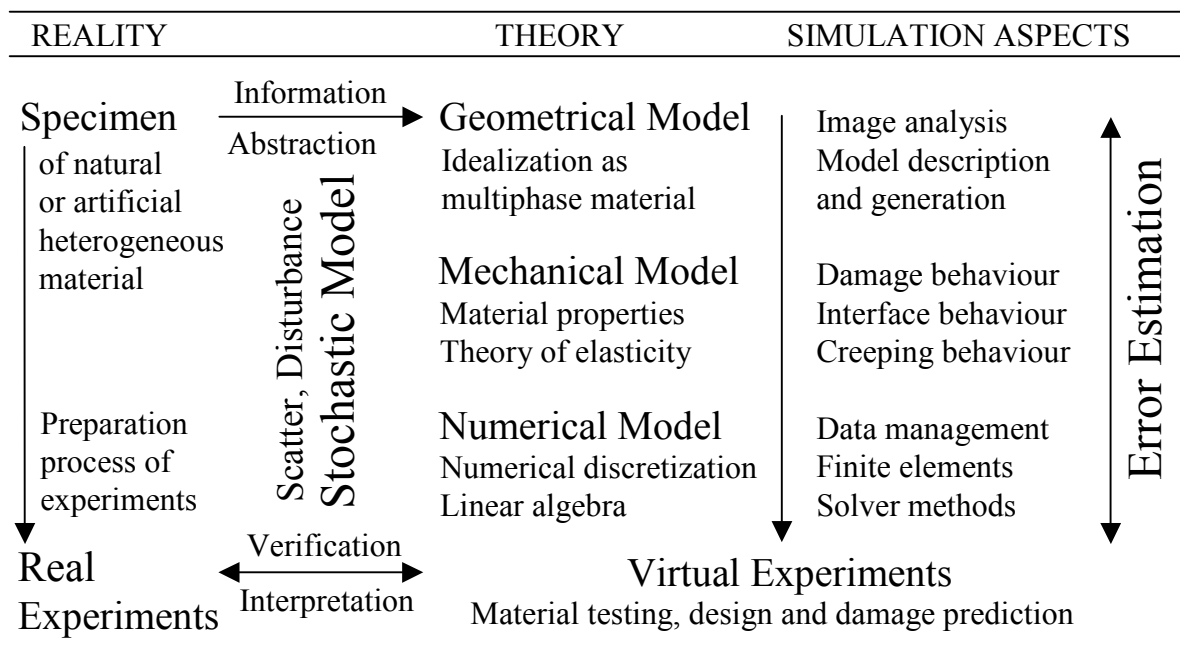


Figure 1.3: General overview of models in the simulation of heterogeneous materials

is the usual practice to perform an experiment not on one but a series of specimen, as the results might significantly scatter. Not only measured values might differ, but also failure mechanisms as for example shown by Ebert (2002). Again, one can distinguish between randomness of geometrical arrangement or mechanical properties with regard to the proposed multiphase model.

Furthermore an error estimation is included in Fig. 1.3. It would be the ideal case that the total error between the behavior of the real material and that of the computational model could be approximated from theoretical consideration only. Accurate error estimators are available for numerical methods. However, the error of geometry and especially of mechanical parameters can not completely be derived from theory, but remains directly associated to the real material. With respect to Fig. 1.3, it is noted that, beyond the fundamental theory, an accurate simulation requires numerous computational methods and algorithms. Finally, the computational simulation, denoted as virtual experiments, needs to be compared to real experiments. However, once the simulation model has been verified, it can replace certain real experiments. Moreover, virtual experiments can be performed to design and optimize heterogeneous solids which represents an important gain for numerous applications, as outlined in Section 1.1.

## 1.3    Statement of Problem

The present work discusses geometrical, mechanical and numerical modeling aspects of multiphase material as introduced in Section 1.2. The present work started from the mechanical analysis of concrete on the mesoscale in 2003. Several corresponding models of the literature showed an obvious lack in the geometrical representation of the concrete material, while these works often focused on mechanical aspects. The motivation for Häfner, Eckardt and Könke (2003) was to achieve an accurate geometrical mesoscale model of concrete. A result is shown in Fig. 1.4 (left). It is a three-dimensional model with a few spherical inclusions which are cut along the edges of the cube. While the theory of concrete mixes has thoroughly been considered, it is clear that the shapes of aggregates in concrete are not spheres.
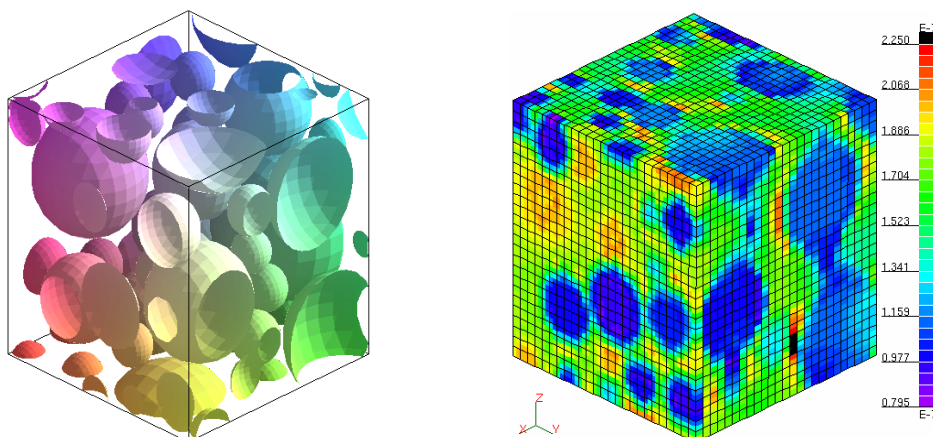


Figure 1.4: Mesoscale geometry of concrete model (left) and strain $\epsilon_{xx}$ of finite element solution for uniaxial load in x-direction (right) from Häfner, Eckardt and Könke (2003).

In the context of the **geometrical model** the following major questions arose:

Q1    How can a more realistic geometrical representation of inclusion-matrix materials be created? How can a model with arbitrary inclusion shapes be generated? How can other materials with a different micro- or mesostructure be modeled?

On the right hand side Fig. 1.4 shows a finite element solution according to the defined mesoscale geometry on the left. In this analysis multiphase finite elements have been applied. The geometry of inclusions is mapped onto the integration points of finite elements, while a regular grid of finite elements is applied. This method avoids complex three-dimensional meshing and is completely flexible for the application of any material. However, at that time the shown model of about 50000 degrees of freedom was near to the maximum possible model size which could comfortably be handled on a desktop computer within the finite element program SLang. It is highlighted that meanwhile considerably more efficient solver packages have been implemented into SLang as documented in (Schrader 2004a, 2004b; Most and Eckardt 2004). However, besides there are other relevant restrictions of model size. With larger models the post-processing and graphical output slow significantly down. The major limitation is defined by the required memory which is significantly predetermined by the storage of the global stiffness matrix.

In the context of the **numerical model** the following major questions arose:

Q2    If the resolution of the finite element model is restricted in this way, especially by the memory demand, is there any way to increase model size to simulate a more complex heterogeneous material, e.g. with a much larger number of inclusions?

Q3    An increase of model size leads to disproportional increase of computation times for solving the linear equation system. What kind of solver method is appropriate for very large problems?

Q4    The approximation quality of the applied finite elements with linear shape functions is known to be relatively poor. What kind of finite elements are best to apply for this problem?

A possible answer to the questions Q1 to Q4 is covered by the present grid-based approach. However, this concept also lead to several, additional challenges, such as e.g.

•    an improvement of the defective stress solution at material interfaces due to grid discretization and

•    an improvement of the applied multigrid method which remains efficient for high ratios of Young's modulus within the heterogeneous solid,

which are also discussed in the present work. Such aspects will be highlighted in the corresponding chapters.

The foregoing aspects referred to the linear analysis of heterogeneous specimen. Therefore the linear elastic theory already represents the required mechanical model. But especially with regard to the damage behavior the simulation of heterogeneous materials becomes most relevant.

In the context of the **mechanical model** the following additional question arose in close relationship to the **numerical model**:

Q5    How can damage effectively be modeled by the proposed grid-based approach? It needs to be considered that there might be a relevant mesh bias due to grid-discretization. It needs further to be considered that the achieved efficiency for the linear analysis is kept as high as possible for the nonlinear analysis.


## 1.4    Outline of Thesis

Several objectives of this thesis have already indirectly been declared by the question Q1 to Q5 in Section 1.3. In the following the proposed grid-based solution strategy is depicted in more detail. In analogy to the questions Q1 to Q5 the developed answers A1 to A5 are outlined:

A1    Grid discretization can be considered as a pixel or voxel model. Any geometries can be mapped onto the orthogonal grid. A proper theoretical background of inclusion-matrix models is prepared. It includes formulas for various inclusion shapes. Digital-image based modeling represents an important option to achieve a realistic geometrical representation of heterogeneous solids in general.

A2    The regular topology of elements enables to formulate the problem by equilibrium equations on the element level. In combination with iterative solver techniques the storage of a global stiffness matrix is superseded. Therefore the memory demand essentially decreases or the possible model size increases. Besides, the effort and memory demand of several other procedures can be reduced in adaption to the grid.

A3    The grid discretization is ideal for the efficient use of the multigrid method. The computational effort of the multigrid method only increases linear with number of degrees of freedom. While there are faster solvers for small problems, there is no solver known where the effort scales better than linear. Therefore the gain of the multigrid method increases the larger the problem becomes.

A4    A B-spline finite element formulation is developed which is completely variable in the order $k$ of B-splines. For homogeneous models the approximation quality of these elements can arbitrarily be scaled. For modeling heterogeneous solids the multiphase concept and transition zones along material interfaces are introduced. The local equilibrium condition according to A2 is maintained for these finite elements.

A5    An isotropic material law is applied for simulating the damage behavior. A nonlocal model reduces mesh bias. Due to the high resolution of the material, complex crack patterns or damage processes can be simulated on the subscale level. According to a damage-controlled, sequentially linear iteration scheme, this method is efficient and remains numerically stable along the softening branch.

For best classification of the proposed approach some restrictions are added. With focus on the analysis of materials it is sufficient to consider orthogonal bodies in contrast to the analysis of structures. The methods are designed for a general multiphase material

as introduced in Section 1.2. Several procedures will be exemplified for concrete. The work mainly focuses on geometrical and numerical modeling. The concerning procedures are variable in application to other materials. As the specific constitutive behavior of a certain material is not considered, the present work is assigned to the general class of heterogeneous solids. The applied mechanical damage law is only regarded as a prototype for a principal extension to simulate nonlinear effects.

The present grid-based strategy is dedicated to an efficient mechanical analysis of heterogeneous materials on the micro- or mesoscale by a continuum model. It is the **major objective** to work out possible advantages and to reduce several disadvantages of the grid-based simulation approach by a systematic combination and enhancement of various methods. The present approach is proposed as an alternative to standard finite element procedures in the mechanical analysis of heterogeneous materials. Some relevant parts of this approach have recently been published (Häfner, Eckardt, Luther and Könke 2006; Häfner, Kessel and Könke 2006; Häfner and Könke 2006a; Häfner and Könke 2006b).

For the proposed, particular approach of this thesis, a grid-based finite element program has been developed. It is labeled Mulgrido. This name represents a fancy modification of the word multigrid. Most of the described methods in this thesis have been implemented into Mulgrido which is also the testing environment of the provided numerical examples. However, this work does not discuss the program itself, but is restricted to the corresponding relevant theory. For more information about Mulgrido, it is referred to (Häfner 2005).

The thesis is organized as follows. Chapter 2 presents the geometrical model (item A1). Chapter 3 covers the mechanical model and prepares for the numerical model. It includes the governing equations of continuum mechanics, some theory of homogenization and relevant aspects of damage modeling (item A5). The Chapters 4, 5 and 6 refer to the numerical model. The numerical model includes B-Spline finite elements (Chap. 4, items A4 and A2), fast iterative solver methods with focus on the multigrid method (Chap. 5, items A2 and A3) and numerical aspects of damage simulation (Chap. 6, item A5). A study on the effective material behavior of heterogeneous solids is provided in Chapter 7. More than altogether one hundred thousand random geometrical arrangements are tested with respect to various aspects, such as e.g. effect from shape of inclusions. The scattering answers are evaluated statistically. Chapter 8 discusses particular aspects from the present work, summarizes major contributions and presents the final conclusions.

# Chapter 2

# Geometrical Model

## 2.1 General Overview

The subscale geometry according to which the material phases are arranged within the heterogeneous solid essentially influences the effective material behavior. Therefore, besides the physical properties of the individual material phases, the subscale geometry plays a significant role for an accurate simulation of a heterogeneous solid. The direct, relevant reference for creating an accurate geometrical model is the real material itself. Various methods are applied to detect and store geometrical material data such as digital photos, computer tomography or laser scan methods. After some processing of the obtained data, it can be employed for computational simulation. However, this procedure requires the existence of and the access to the real material. Provided both conditions are valid, this procedure is relatively expensive while the result might not be representative for possible variations of the material.

As an alternative solution, indirect geometrical modeling based on theoretical information of the material is proposed. For precisely manufactured materials of regular geometry, such as honeycomb material or material with negative Poisson's ratio (Section 1.1), an adequate plan of the geometry exists. However, there are several random materials for which such a clear specification is not available. One can distinguish between plane random arrangement, which is useful for composites with long, uniaxial oriented fibers, and spatially random arrangement as for many inclusion-matrix composites, as for example various types of concrete, semi-crystalline polymers with rubber particles (Van Dommelen et al. 2002) and other advanced engineering materials (Michaud 1993). In these cases knowledge about the constituents and the manufacturing process provides theoretical information for generating adequate geometrical models. It is principally possible to simulate processes such as crystal growth of alloys or growth of bone tissue. However, often simplified algorithms are used to reconstruct an observed typical material structure without physical background.

This work discusses aspects of direct and indirect modeling. According to its importance in the present scope of civil-engineering, the selected material of focus is concrete, while several methods can be transfered to model other random materials, especially inclusion-matrix materials. The geometry of concrete on the mesoscale is mainly characterized by particle shapes, particle size distribution, the total volume of particles and their arrangement.
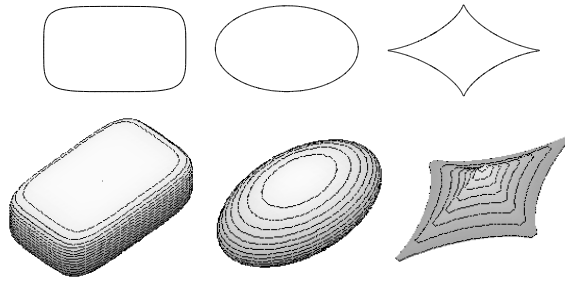
Figure 2.1: Shapes of modified ellipsoid function: n=5, 2 and 0.7
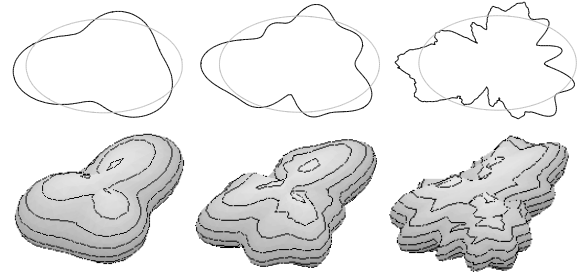
Figure 2.2: Additional sine functions added to ellipsoid

## 2.2   Particle Shapes

Particle shapes influence the stress distribution within the composite. Round shapes cause rather smooth stress distributions. Angular shapes lead to stress concentrations. A corresponding initiation of cracks can be relevant for accumulating damage and finally macroscopic failure. In asphalt material an effect of the particle shape on tensile strength and shear resistance is observed (Al-Rousan et al. 2006). Zaitsev and Wittmann (1981) compare crack patterns in two-dimensional random structures of normal concrete with polygonal inclusions and idealized lightweight concrete with circular inclusions. The approach of circular aggregates is frequently applied, as for example in (Bažant et al. 1990; Van Mier et al. 2002; Van Mier and van Vliet 2003). To consider the effects resulting from the nature of aggregates, rounded particle shapes according to a morphological law of gravel are used in mesoscale models in (Wittmann et al. 1993). A detailed description of two-dimensional random aggregate structures with crushed as well as with round particles is presented in (Wang et al. 1999). Therein crushed particles are generated as randomly shaped polygons with a prescribed elongation ratio and furthermore round particles are formed with shapes according to the morphological law of Beddow and Meloy (1980). The first three-dimensional geometrical models applied spherical inclusions which were extended to ellipsoids with different sizes and roundness (Guidoum and Navi 1993; Leite et al. 2004). For advanced studies on inclusion-matrix models it is favorable to use various particle shapes which can be controlled by only a few parameters. Therefore the superellipsoid is proposed, which is also applied by Zohdi (2001).

$$\left|\frac{x}{r_1}\right|^n + \left|\frac{y}{r_2}\right|^n + \left|\frac{z}{r_3}\right|^n = 1 \tag{2.1}$$

For $z = 0$ Eq. 2.1 reduces to the superellipse (Gardner 1993). Equation 2.1 includes one parameter in the variable exponent $n$, with $n > 0$, to vary the shape between round and angular as shown in Fig. 2.1. Therefore this variant is well suited to study the effect of particle shape upon the mechanical behavior and is applied in the present work. Additional sine functions such as $f_i$ (Eq. 2.2) with an even number of sine-phases $p_i$, amplitude $a_i$ and phase shift $e_i$ are applicable to modify the particle shape (Häfner et al. 2003).

$$f_i = a_i \cdot \sin\left(\arctan\left(\frac{y}{x}\right) \cdot p_i + e_i\right) \tag{2.2}$$

Therefore based on a few parameters some more or less controlled irregularity and roughness can be included as illustrated in Fig. 2.2. An analog extension of $f_i$ to the $z$-coordinate
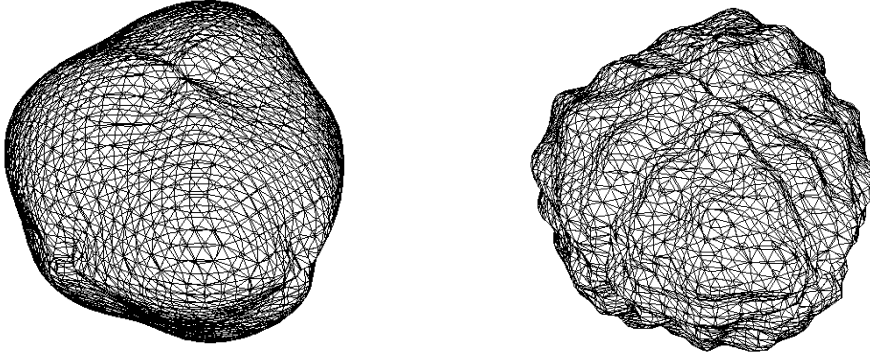
Figure 2.3: Particles shapes generated by adding sinus functions on ellipsoid

lead to the particle shapes of Fig. 2.3. A similar two-dimensional formulation is labeled as a *roughened circle* in (Beddow and Meloy 1980). A recent approach to achieve a wide variety of two-dimensional shapes is called superformula as introduced by Gielis (2003).

$$\left( \left| \frac{1}{a} \cos \left( \frac{m}{4} \phi \right) \right|^{n_2} + \left| \frac{1}{b} \sin \left( \frac{m}{4} \phi \right) \right|^{n_3} \right)^{\frac{1}{n_1}} = \frac{1}{r} \tag{2.3}$$

The variables $r$ and $\phi$ refer to a polar coordinate system. The primary parameters to control the shape are $m$, $n_1$, $n_2$ and $n_3$. Examples of the superformula are provided in Section 2.7.

Garboczi (2002) detects the shape of real aggregates in concrete using X-ray tomography and approximates the shape by spherical harmonics. These continuum surface models lead to accurate representations of complex shapes by a low number of parameters, while the memory demand is drastically reduced compared to the original full voxel representation of the particle. A profound study on modeling of polar shapes, based on e.g. a sample of surface boundary points, by double fourier series as well as spherical harmonics is provided by Li (2002). However, besides generating various, complex particle shapes for computational simulation, there is the need to quantify or classify the shape (of real particles and model particles), such that a general, meaningful relationship between characteristic of particle shape and its effect on the mechanical behavior can be formulated.

A typical measure of particle shape is sphericity $p_s$ which refers to the three main dimensions of the particle $d_1 \geq d_2 \geq d_3$. In (Al-Rousan et al. 2006; Mora and Kwan 2000) sphericity is defined by

$$p_s = \sqrt[3]{\frac{d_2 d_3}{d_1^2}} \tag{2.4}$$

Further shape measures are flatness or flakiness $p_f = d_2/d_3$ and elongation $p_e = d_1/d_2$ as well as a flat and elongated ratio $p_c = d_1/d_3$ (Al-Rousan et al. 2006). The basic definition that most measures are based on a ratio of two particle dimensions is confirmed in (Stark, Liebezeit and Müller 2005). However, for these, but especially for other shape factors various attributes and definitions are presented in (Kwan et al. 1999). Further references are (Beddow and Meloy 1980; Kwan et al. 1999; Mora and Kwan 2000; Jamkar and Rao 2004; Al-Rousan et al. 2006). It is only summarized that additional important measures refer to roughness, angularity and texture of particles. Shape measures can refer to two-dimensional projections or to the real three-dimensional shape. For example angularity

can be categorized according to graphical drafts, as e.g. assembled in (Koensler 1989), or by fourier analysis as proposed in (Beddow and Meloy 1980; Al-Rousan et al. 2006). In fourier analysis the relevant frequencies increase from global form to angularity to texture of particle. However, it is noted that the applied measure also depends on the available data. For concrete material, in practice the ratio of disproportionate aggregates can be determined according to specific sieve analysis, thickness and length gages or automatic image analysis (Brzezicki and Kasperkiewicz 1999). Undoubtfully, the recent detection and description of three-dimensional particle shapes (Garboczi 2002) is most accurate and therefore promising for a detailed categorization. At present and with regard to the present context, the available alternative is bringing the observed mechanical behavior directly into relationship with the parameters of the applied functions, Eqs. 2.1 to 2.3, or the application of clear measures such as Eq. 2.4.

## 2.3 Particle Size Distribution

For the generation of aggregates in a concrete specimen the particle size distribution is an essential aspect in combination with maximum aggregate size and total volume of aggregates, generally between 60% and 90% (Shakhmenko and Birsh 1998). In practice the aggregate grading of concrete is mostly designed after the Fuller curve. It stems from optimal packing of spheres and generally leads to high density and strength, while it also provides low segregation and good workability. Consequently the Fuller curve is frequently applied to geometrical mesoscale modeling of concrete (Schlangen and van Mier 1992; Schlangen 1993; Wittmann et al. 1993; Van Mier et al. 2002). Variable predefined grading curves are considered in (Wang et al. 1999; Leite et al. 2004). A thorough and extensive study about particle size distributions and an analysis of the wall effect in finite bodies with respect to spatial distribution of aggregate sizes is presented in (Zheng 2000). As a particle size distribution function naturally corresponds to a three-dimensional geometry, it is not directly applicable for two-dimensional models. Based on the Fuller curve Walraven (1980) provides a formula for the particle sizes in an intersection plane of a theoretical three-dimensional model, which is adopted in (Schlangen and van Mier 1992; Van Mier et al. 2002). As an alternative way slice cut-outs can be created from a generated three-dimensional specimen to obtain two-dimensional geometries (Leite et al. 2004; Eckardt et al. 2004). In the following the inverse cumulative distribution function of particle number with respect to particle size is derived from grading curves of mass. The procedure adapts to various grading curves and provides a short, convenient formula to generate consistent particle sizes for three- and two-dimensional models.

The size distribution of aggregates in concrete is described by a cumulative distribution function of mass $\Phi_m(x)$ with respect to the particle size $x$. Assuming a constant mass density $\varrho$ of the aggregates, the cumulative distribution function of particle volume $\Phi_V(x)$ is given by

$$\Phi_V(x) = \Phi_m(x) \qquad (\varrho = const.) \tag{2.5}$$

and the associated density function $\varphi_V(x)$ is

$$\varphi_V(x) = \frac{\mathrm{d}\Phi_V(x)}{\mathrm{d}x} \tag{2.6}$$
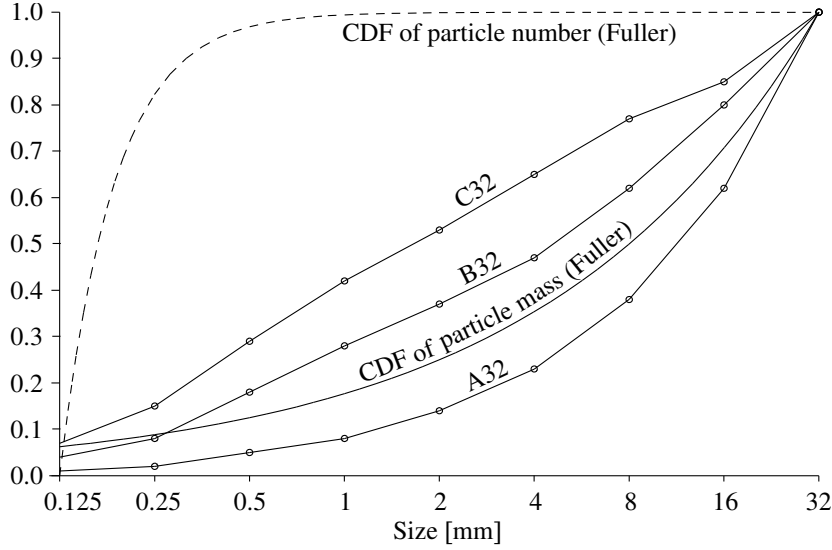
Figure 2.4: Cumulative distribution functions (CDF) of particle sizes of German standard DIN 1054: ideal range between A32 and B32, upper limit C32 and the Fuller curve

In the differential interval of $[x, x + dx]$ the increment of particle number $\widetilde{\varphi}_N(x)$ follows the condition

$$\widetilde{\varphi}_N(x) = \frac{\varphi_V(x)}{V(x)} \tag{2.7}$$

whereby $V(x)$ is the volume of a particle with reference length $x$ (e.g. in case of a sphere $x$ defines the diameter), which is assumed to define the sieve passing of a particle. The number of particles within the range $[x_1; x_2]$ of a reference volume equal to "1" is calculated by

$$N[x_1; x_2] = \int_{x_1}^{x_2} \widetilde{\varphi}_N(z) \mathrm{d}z \tag{2.8}$$

The cumulative distribution function of particle number within the range $[x_1; x_2]$ is defined as

$$\Phi_N(x) = \frac{N[x_1; x]}{N[x_1; x_2]} \tag{2.9}$$

The inverse formulation of Eq. (2.9) with respect to $x$ can be used to generate consistent particles sizes within the range of $[x_1; x_2]$ according to the provided cumulative distribution function of mass $\Phi_m(x)$.

The analysis from Eqs. (2.5)-(2.9) is exemplified for the following cumulative distribution function of volume

$$\Phi_V(x) = k_1 x^\alpha \tag{2.10}$$

This function covers the Fuller curve (Fig. 2.4) for $\alpha = 0.5$ and $k_1 = D_{\max}^{-\alpha}$ where $D_{\max}$ denotes the maximum particle size $x$ of the considered sieve curve. The corresponding density function is

$$\varphi_V(x) = \alpha k_1 x^{(\alpha-1)} \tag{2.11}$$

As the volume is a cubic function $V(x) = k_2 x^3$ (whereby $k_2$ is independent of $x$ and e.g. in case of a sphere $k_2 = \frac{\pi}{6}$), this leads to

$$\widetilde{\varphi}_N(x) = \alpha k_1 k_2^{-1} x^{(\alpha-4)} \tag{2.12}$$

As a result the following cumulative distribution function of particle number is established

$$\Phi_N(x) = \frac{x^{(\alpha-3)} - x_1^{(\alpha-3)}}{x_2^{(\alpha-3)} - x_1^{(\alpha-3)}} \tag{2.13}$$

The Fuller curve as cumulative distribution function of particle number is shown in Fig. 2.4. Then, the following inverse cumulative distribution function enables consistent generation of particle sizes, where $X_1$ denotes a uniform random number in the interval $[0; 1]$.

$$x = \left( X_1 \left( x_2^{(\alpha-3)} - x_1^{(\alpha-3)} \right) + x_1^{(\alpha-3)} \right)^{\frac{1}{(\alpha-3)}} \tag{2.14}$$

The lognormal distribution of particle volume corresponds to a linear graph in the lognormal diagram of Fig. 2.4 and is described by

$$\Phi_V(x) = m \cdot \log_2(x) + n \tag{2.15}$$

and

$$\varphi_V(x) = \frac{m}{\ln 2} x^{-1} \tag{2.16}$$

which leads to Eqs. (2.13) and (2.14) with $\alpha = 0$.

For consistent generation of various particle shapes, it is assumed that a sphere can be replaced by an irregular shape of the same volume. The prior equations only describe the three-dimensional case. Neglecting wall effects, the probability to cut a sphere of diameter $x$ in a volume of depth $z$ equals to $\frac{x}{z}$. Therefore the particle increment defined in Eq. (2.7) can be adapted to that of a two-dimensional section.

$$\widetilde{\varphi}_N^*(x) = \frac{\varphi_V(x)}{V(x)} \cdot \frac{x}{z} \tag{2.17}$$

The depth $z$ cancels in the evaluation of the cumulative distribution function of particle number. Additionally, in case a certain sphere is cut, its effective diameter of a random section is reduced by the factor $\sqrt{1 - X_2^2}$. The uniform random numbers $X_1$ and $X_2$ in the interval $[0; 1]$ are not correlated. These natural assumptions lead to the following inverse function which is directly applicable to generating particle sizes of a two-dimensional section

$$x = \left( X_1 \left( x_2^{(\alpha-2)} - x_1^{(\alpha-2)} \right) + x_1^{(\alpha-2)} \right)^{\frac{1}{(\alpha-2)}} \sqrt{1 - X_2^2} \tag{2.18}$$

While the particle size distribution of a section differs to that of the volume, expected area ratio and volume ratio correspond. The derived functions can either be used to generate particle sizes of individual mineral size classes or the complete range in case of the Fuller curve. To exemplify the analysis, the number of particles in a $(100 \text{ mm})^3$-concrete cube designed according to the Fuller curve (assuming 70% aggregate volume fraction) are provided in Table 2.1 where Eq. (2.8) leads to

$$N[x_1; x_2] = \frac{\alpha}{\alpha - 3} k_1 k_2^{-1} \left( x_1^{\alpha-3} - x_2^{\alpha-3} \right) V_{\text{agg.}} \tag{2.19}$$

with the following parameters $\alpha = 0.5$, $D_{\max} = 32$ mm, $k_1 = D_{\max}^{-\alpha}$, $k_2 = \frac{\pi}{6}$ and $V_{\text{agg.}} = 700000 \text{ mm}^3$. A corresponding number of particles has been generated by the derived
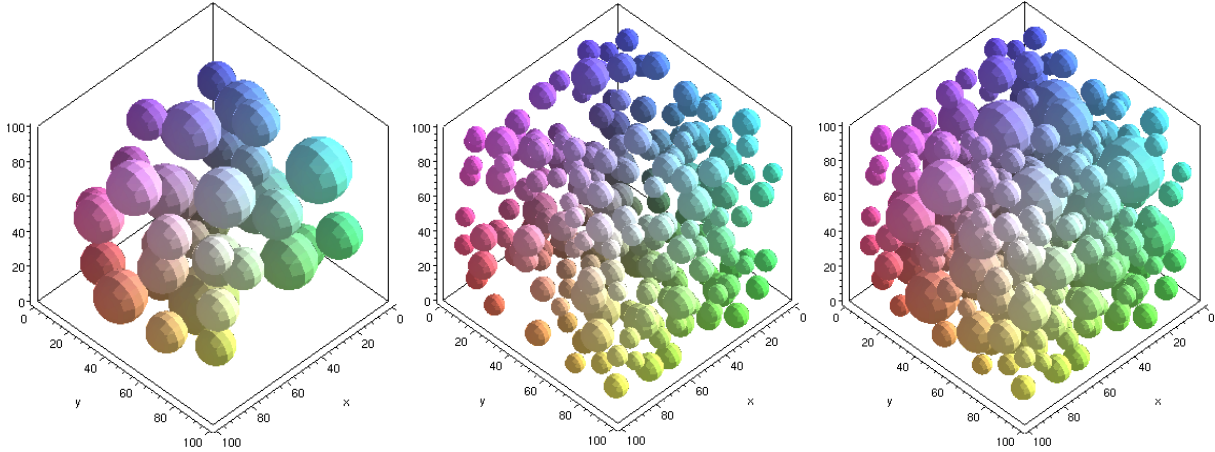
Figure 2.5: Particle configurations in accordance to Table 2.1: 38 particles of fraction 16-32mm, 215 particles of fraction 8-16mm and the combination of 253 particles.

inverse function for the intervals $[x_1 = 8; x_2 = 16]$ and $[x_1 = 16; x_2 = 32]$. The resulting volume fractions agree within the statistical deviation. The relationship in number and volume between larger and smaller aggregates is illustrated in Fig. 2.5.

From one to the next lower mineral size class the related particle number in Table 2.1 increases by the factor $5.66 \approx 1/2^{\alpha-3}$ while mass fraction reduces by the factor $0.71 \approx 1/2^{\alpha}$. This recursive character of particle sizes provides an indication to research on fractal properties of concrete (Carpinteri et al. 2004).

| $x_1$[mm] | $x_2$ [mm] | Mass [%] | Number |
|---|---|---|---|
| 16.0 | 32.0 | 29.3 | 38 |
| 8.0 | 16.0 | 20.8 | 215 |
| 4.0 | 8.0 | 14.6 | 1216 |
| 2.0 | 4.0 | 10.4 | 6879 |
| 1.0 | 2.0 | 7.3 | 38910 |
| 0.5 | 1.0 | 5.2 | 220114 |
| 0.25 | 0.5 | 3.7 | 1245151 |
| 0.125 | 0.25 | 2.6 | 7043638 |

Table 2.1: An example of corresponding particle mass and number according to the Fuller curve

## 2.4   Separation Check of Two Particles

A separation check of two particles denotes a basic procedure of generating random materials with inclusions in a matrix. In contrast to pores, solid inclusions can obviously not overlap. The problem is trivial to solve for spheres. If the center distance of two spheres is larger than the sum of their radii, the two spheres do not overlap and otherwise they do. For other, variable particle shapes as described in Section 2.2, this problem becomes essentially more complicated.

### 2.4.1 Coarse Detection Methods

As a simple and fast method to detect whether two particles possibly overlap, larger spheres which completely include each particle can be generated and the separation check be performed for these spheres instead. This coarse detection method requires a valid approximation about the maximum dimension of a particle. With a similar idea, orthogonal bounding boxes for each particle can be generated which is illustrated in Fig. 2.6 (left). If these bounding boxes are separated, it is clear that the included particles are separated, too. It is intuitive that the definition of tight bounding boxes is favorable. Converse conditions, namely interior boxes, can possibly assure overlapping of close particles. However, the foregoing conditions are not sufficient to decide about the overlapping of two particles in any case. In the critical cases when the coarse detection method fails to provide a unique answer, namely when bounding boxes do overlap and interior boxes do not overlap, an additional more accurate and also more costly separation check needs to be performed.

### 2.4.2 Separation Check of Two Ellipsoids

Ellipsoids represent an exception within non-spherical particle shapes for which an analytical separation check is available. Nevertheless, due to variable spatial rotation and location of two ellipsoids, a corresponding separation check is quite involving. In the following a recent approach (Wang et al. 2001) is outlined, which is applied by Eckardt in (Häfner, Eckardt, Luther and Könke 2006). An ellipsoid is defined by Eq. (2.20), where $\mathbf{X} = (x, y, z, 1)^T$ are the homogeneous coordinates.

$$\mathbf{X}^T \mathbf{A} \mathbf{X} = 0 \tag{2.20}$$

The 4x4 matrix $\mathbf{A}$ includes the complete information of the three ellipsoid diameters, of the position and of the rotation angles of the ellipsoid. The characteristic polynomial of two ellipsoids is defined by

$$f(\lambda) = \det(\lambda \mathbf{A_1} + \mathbf{A_2}) \tag{2.21}$$

The separation status of the two ellipsoids is determined by the number of positive roots of the characteristic equation $f(\lambda) = 0$. If the characteristic equation has two distinct positive roots, then the ellipsoids do not overlap and otherwise they do. The exact roots of Eq. 2.21 are not required. The number of positive distinct roots can effectively be determined by Sturm sequences (Dickson 1914). The advantage of this solution is its accuracy and efficiency.

### 2.4.3 Separation Check of Two Arbitrary Shapes

The discussion of variable particle shapes according to Section 2.2 raised the need to include separation checks for variable shapes. However, because an analytical solution, as for ellipsoids, is not available, the corresponding strategy rather refers to a computational algorithm than a mathematical formulation. If the coarse detection method of Section 2.4.1 does not lead to a unique conclusion about the separation of two particles, then the overlapping region of two bounding boxes is the critical region which needs to be examined additionally. Figure 2.6 (center) shows a regular grid of points within the overlapping
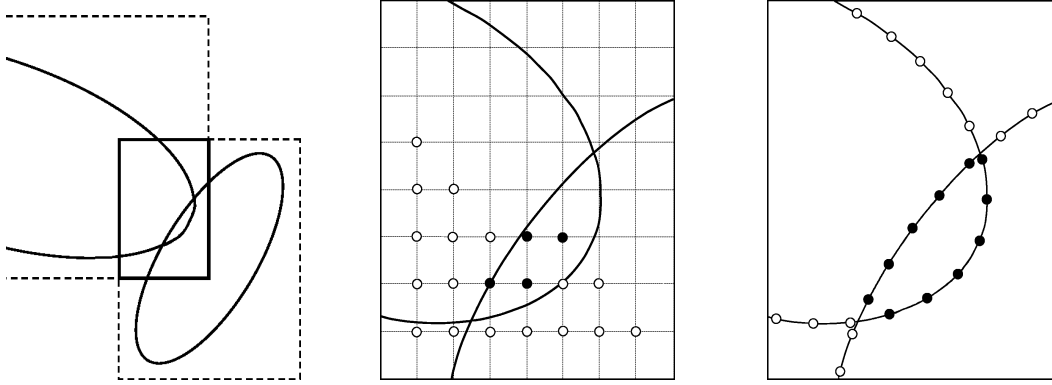
Figure 2.6: Overlapping bounding boxes (left). Separation check on grid (center) and on surfaces (right) within overlapping bounding boxes.

region. One point after another is tested, if it is within both inclusions until such a point is found or all points have been tested. This method can be applied to any particle shape, but it is relative expensive, especially with regard to the three-dimensional case. A modified, alternative method is illustrated in Fig. 2.6 (right). Less of such selective checks are required, if predetermined points on the surface of a particle are considered. But on the other hand the detection of these surface points, e.g. by a directional bisection method, requires additional effort. An advantage especially occurs if a particle needs to be tested several times before a valid position is found. With both methods principally any required accuracy for the separation of variable particle shapes can be achieved. A detailed study of these methods is documented in (Theuer 2003).

### 2.4.4   Speed–Up by Division into Sub-Domains

Up to the $n$-th particle to place, at least $(n^2 - n)/2$-times two boundary boxes have to be compared. As this denotes a quadratic function of $n$, the efficiency of the algorithm essentially reduces with increasing number of particles. A decomposition of the total domain into sub-domains represents a possible remedy to this problem. For the placement of a new particle, only particles which are part of the corresponding sub-domain need to be considered for separation check. This method is demonstrated by Eckardt in (Häfner, Eckardt, Luther and Könke 2006) and it is shown that the computational effort is particularly decreased for a model with a very large number of inclusions. The optimal size of a sub-domain refers to the size of a particle. With varying particle sizes during one placement process, the size of the sub-domain might ideally also be adaptive. It can be summarized that the following hierarchy of methods has been developed: sub-domain method, coarse detection method as described in Section 2.4.1 and accurate separation check according to Section 2.4.2 or 2.4.3 .

### 2.4.5   Separation Check on Domain Grid

With respect to the present grid-based approach, a separation check directly on the global domain grid is proposed. This method covers any random concave or convex shaped particles in two or three dimensions. There is only the condition that for each particle

---

**Algorithm 1** Grid-based boundary tracing and placement of particles on domain grid

---

 1: **repeat**
 2:       create one random particle according to given statistics
 3:       determine and save pixels of particle boundary: follow the boundary and draw pixels into a virtual domain until the first boundary pixel is found again.
 4:       determine and save particle area: fill particle and count its pixels.
 5: **until** defined particle volume ratio is reached
 6: sort particles by area (pixels).
 7: prepare domain: initialize domain grid to '0'. set domain boundary pixels to a non-zero number.
 8: **loop** {through all particles, starting from the largest}
 9:       **repeat**
10:             pick random particle position in domain grid
11:       **until** all boundary pixels of this particle are still '0' in the domain
12:       set boundary pixels of particle in the domain
13:       fill particle in the domain by a non-zero number
14: **end loop**

---

a coordinate of its interior is known. Then all neighboring coordinates of the particle interior on the grid can be determined. For the two-dimensional problem the domain grid can be regarded as a pixel image. An object can be placed into the domain, if the corresponding pixels at the considered position are not yet occupied by another object. The procedure for the two-dimensional model is summarized by Algorithm 1. In the first part, lines 1-5, a pixel representation of each particle is generated. As the particle size in this specific algorithm will be decreasing during particle placement, it is sufficient to detect and store the boundary pixels of each particle. After lines 1-5 the original and maybe expensive analytical formulation of each particle will not be revisited. By a simple comparison of pixel values in the last part, lines 8-14, this method is very fast, even for complex particle shapes. This method can be extended to model other objects, just by generating a corresponding pixel representation. An extension to three-dimensional voxel models is almost straightforward. The defined grid model can directly be applied to the mechanical analysis using the finite element method. In this regard the accuracy of the geometrical model is directly adjusted to the subsequent numerical analysis. Therefore in any case the generation of the geometrical model will not be critical with respect to computation time in comparison to the following mechanical analysis. For damage analysis using finite elements, it is useful to require at least one pixel gap between the particles, which can simply be controlled by this method. In summary this method is flexible for any object shape, its accuracy can arbitrarily be adjusted and therefore it is the applied method of the present work.

## 2.5   Placement Procedures

Different methods have been developed to generate a realistic particle arrangement. Numerous publications (Bažant et al. 1990; Schlangen and van Mier 1992; Schlangen 1993; Van Mier and van Vliet 2003) describe an arrangement procedure which is labeled as the take-and-place-method in (Wang et al. 1999). It is based on a set of particles which are sequentially placed into the matrix starting by the largest one and using checks to obviate overlapping. In most procedures a new particle is removed if overlapping occurs and it is tested to place it again at any other position. Alternatively Leite et al. (2004) propose a stochastic-heuristic algorithm in order to obtain a more realistic concrete structure. If the last placed particle overlaps with any previously placed particle a new position is found by rotation and translation along heuristically determined directions. In addition to the take-and-place-method, Van Mier and van Vliet (2003) describe other algorithms for arrangement of particles, e.g. the random particle drop method.

The present approach of generating geometrical inclusion-matrix models follows the take-and-place-method. To the largest extent it is already outlined by the foregoing paragraph and within Algorithm 1. After generating grading curve consistent particles, the particles are sorted by size and one after another placed into the domain, starting with the largest particle. The generation of the position coordinates for each particle bases on a uniform distribution over the whole domain. If the current position of a particle is not valid, then any other random position according to the uniform distribution is determined. Nevertheless, this placement procedure results in a natural wall effect (Van Mier and van Vliet 2003). This means that while approaching the boundary of the domain the concentration of smaller particles increases, while the concentration of larger particles will be larger in the center region. This explains why the wall effect can only partially be avoided by a cut-out of an oversized domain as proposed in (Prado and van Mier 2003). A complete elimination of the wall effect is possible by a periodic domain, also denoted as periodic unit cell. The left model boundary is considered as a continuation of the right boundary, and analog the bottom, the continuation of the top.

For achieving very dense particle arrangements an additional compaction algorithm is introduced in (Häfner, Eckardt and Könke 2003). The basic idea stems from the imagination of shaking the domain. Based on a globally adapting step size all particles are at once tested for an incremental movement either to the right, to the left, up or down, always given a random, particle individual direction variance of up to 45 degrees. Compaction is then achieved by a higher repetition of the sequence towards the preferred direction (e.g. down). For each sequence the particles are sorted by coordinates for a higher mobility towards the next direction. The global movement stepsize is increased if more than a certain percentage (e.g. 80%) of particles were able to move, or decreased if these were less than a certain limit (e.g. 20%). It is considered as advantageous that this algorithm forces to pack the particles tighter, without necessarily pushing them towards contact. Unequal distributions can be compensated by applying sequences of random directions. This algorithm is heuristic. It shows a considerable compaction result in the test example which is illustrated in Fig. 2.7.
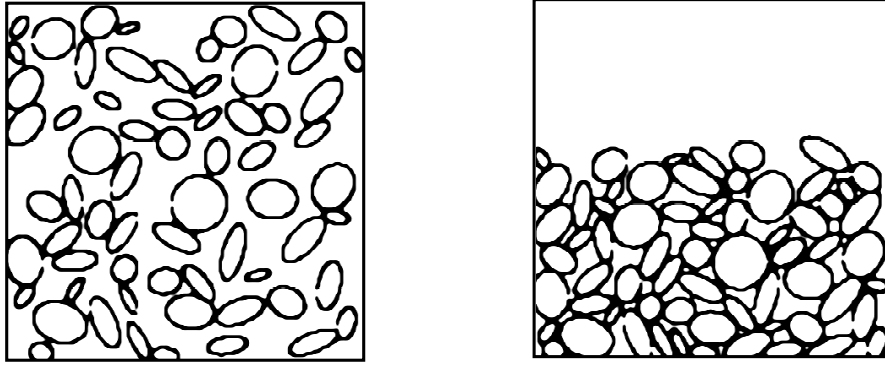
Figure 2.7: Particles before and after 60 iterations of compaction

# 2.6 Digital Image-Based Modeling

Digital image-based modeling can smoothly be integrated into the proposed grid-based approach. However, the term digital image may associate that the data has been derived from a real existing object. This is not necessarily appropriate for the present approach and therefore grid-based modeling is preferred as the more general term. In fact, there are numerous examples of digital image-based modeling in the mechanical analysis of heterogeneous solids where a real object is used as direct source of the model data. A broad overview on this research related to mesomechanical finite element modeling is provided in (Mishnaevsky and Schmauder 2001), among others, the application of digital-image based modeling for bone tissue, alloys and metal matrix composites is mentioned. In this context image-based modeling may refer to two-dimensional pixel models, but also to the three-dimensional equivalent, voxel models. For concrete material Garboczi (2002) exemplifies X-ray tomography to create a high-resolution inclusion-matrix model of a cube with $270^3 \approx 1.97 \cdot 10^7$ voxels. A similar concrete model is generated by Nagai et al. (2000) by a destructive procedure, piecewise scraping of a physical specimen and standard scanning of each section. Then, the voxel model is assembled by a stack of two-dimensional images. Moreover, the application of digital-image based modeling within the field of computational mechanics is documented for geomaterials (Yue et al. 2003), engineering alloys and glass ceramic matrix composites (Shan and Gokhale 2004), and metal matrix composites with particles or fibers (Steinkopff et al. 1995). Advanced mesh refinement with respect to finite element analysis is presented for voxel-based models of textile composites in (Kim and Swan 2003).

An extraordinary procedure is presented by Shan and Gokhale (2004), which proposes to assemble many microstructural images by montage and apply digital image compression with selective access to relevant details for achieving multiscale analysis. Moreover, it is aimed for a characterization of the composite, such that parameters of a generation method can be adapted to create a model with similar properties as for the microstructural image, which describes a relevant goal of this research. For some materials a numerical identification of the various phases is straightforward to achieve by standard image software such that little or no emphasis is put on digital image processing. However, for concrete or geomaterials the identification of the various phases requires several procedures and even then might not be quite clear and unique. For concrete material Nagai et al. (2000) outlines the applied basic procedure which includes an interesting distance
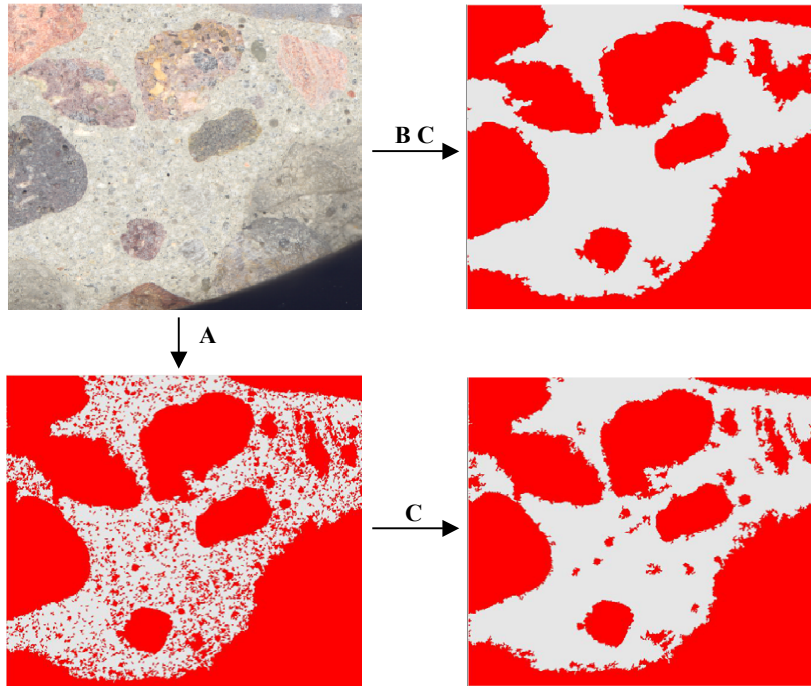
Figure 2.8: Original image of concrete section and images after processing: **A** application of color threshold value, **B** application of color gradient search and **C** filtering of noise or small objects

transformation for noise reduction. With respect to geomaterials Yue et al. (2003) describe various methods of digital image processing, such as image contrast enhancement, image noise removal, neighborhood averaging, low pass filtering, edge detection and several more. However, the methods also include manual processing as well as trial-and-error. It is remarkable that, there, after transforming the digital image into a model of phase edges, finally an aligned meshing of material phases is performed.

In cooperation with the present author, a study of Backoff (2003) is concerned with the identification of aggregates in concrete material based on digital images. Figure 2.8 (top, left) shows a typical original image. It is obvious that the aggregates can not be assigned to one specific color range. Even worse, certain colors occur in both, cement stone and aggregates. In this study some interesting concepts are developed to tackle this difficult problem. It includes the typical application of a color threshold value which splits the color range into two parts. However, only in the ideal case one part exclusively includes either inclusions or matrix material. The threshold value is defined by the user in manual adaption to the achieved result. In a more sophisticated procedure the user defines a box of pixels within the matrix material. Then, all colors which lie within a small user-defined tolerance to any of these predefined pixels will be assigned to the matrix material. In contrast to one threshold value many adequate color ranges are generated by this method. Furthermore it is assumed, that the matrix material is one continuous region around the aggregates. Then, starting from one pixel of the matrix, further pixels will also be assigned to the matrix if the gradient to at least one neighbor pixel is below a user-defined tolerance. For some cases the latter method leads to an improved identification of aggregates. Finally a noise filter is applied to eliminate small objects or particles which only cover a few pixels and can therefore not accurately be detected. Some results are presented in Fig. 2.8. In summary, reasonable identification of aggregates has been established by this study

which might also include some novel aspects. Nevertheless, an additional adaption to documented methods of digital image-based processing, as e.g. described in (Yue et al. 2003), would be valuable for further enhancement of the present approach.

## 2.7 Examples

In the following some examples of geometrical models are presented to provide an overview on the present possibilities of the proposed grid-based approach. Figure 2.9 shows the first example. It represents a two-dimensional inclusion-matrix model of a concrete section with the dimensions 100 mm × 100 mm. The shapes of the aggregate are various superellipses according to Eq. 2.1. The particle sizes in the range of 0.1 mm to 32 mm have been generated to meet the Fuller curve by the inverse function of the two-dimensional problem, as given by Eq. 2.18. The high aggregate contents of 85.8 % was achieved by the take-and-place method described in Section 2.5 without additional compaction. Fast separation checks as outlined by Algorithm 1 in Section 2.4.5 lead to a total generation time of 25.26 seconds on one present standard processor (2.8 GHz). 45549 inclusions are placed on a matrix of $4096 \times 4096 = 1.6710^7$ elements. There is at least one element of matrix material between any two aggregates. The minimum inclusion size corresponds to approximately four elements in one dimension. The minimum image size with one bit per pixel without compression only corresponds to 2 MB. Thus in the 24 bit standard of the bitmap format the image size is 48 MB. The total memory demand of Mulgrido to solve the corresponding finite element problem is about 4 GB which will further be discussed in Section 5.11.1. Therefore this problem is one of the largest which can be processed by the present approach on standard computers with adequate memory extension. It is summarized that the achieved complexity of this model is respectable in comparison to several other models of the present literature. While this model represents a maximum of size, smaller models are introduced for best visibility of the relevant effect in the following.
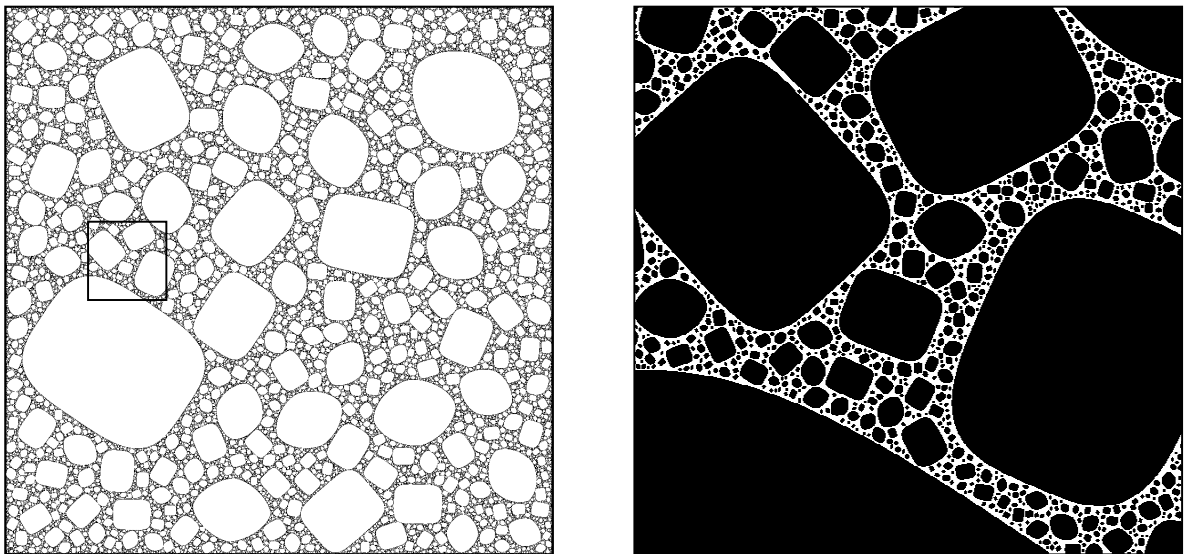


Figure 2.9: 45549 inclusions with sizes from 0.1 to 32 mm graded after the Fuller curve on a $4096 \times 4096$ element matrix occupy 85.8 % of the area. Element size is 0.024 mm. Generation time was 25,26 seconds. Full model (color inverted) is shown on the left and the marked box is magnified on the right.
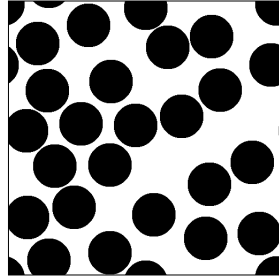
Figure 2.10: Example of periodic unit cell of fiber composite. Fiber orientation is orthogonal to section.

A typical example of a periodic unit cell in the context of fiber materials is shown in Fig. 2.10. Various statistical measures can be applied to control if a periodic unit cell adequately represents the geometrical characteristics of a larger section (Sejnoha et al. 2001). In this context the periodic unit cell is also denoted as representative volume element. It is generated to replace the real microstructure by a smaller model, while it is intended to keep the involving loss of quality low. However, such a model reduction will not be considered in detail within the present work. This example is rather included to present the generation of a periodic material structure in general. An example for a periodic concrete section is shown in Fig. 2.11. For a direct comparison Figure 2.12 illustrates a model of similar parameters, but with typical wall effect as described in Section 2.5. Only a few additional steps are required to trim Algorithm 1 for the generation of a periodic structure. Whenever the actual coordinate within any process would leave the domain by a certain distance, it re-enters the domain by this distance at the opposite side. This works for the separation check as well as for the filling process of the particle. However, as in each step some additional operations are required to control if the coordinate is within the domain, the computation time slightly increases. For generating models with wall-effect such a control is not required as all boundary pixels are initially marked as end
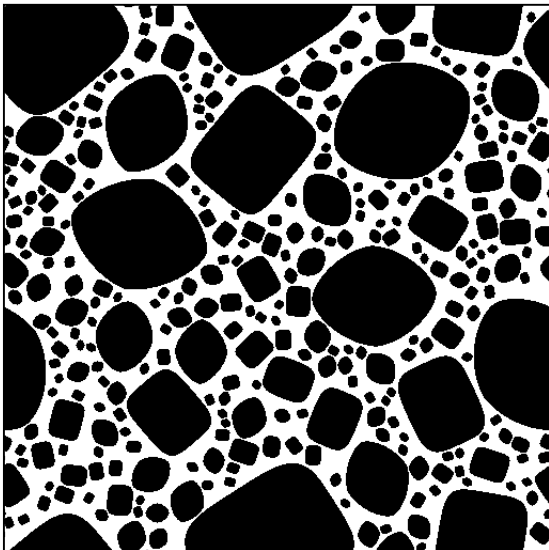


Figure 2.11: Periodic geometry. 309 inclusions, 66.9 % volume ratio, generation time 0.87 seconds, 5191 separation checks.
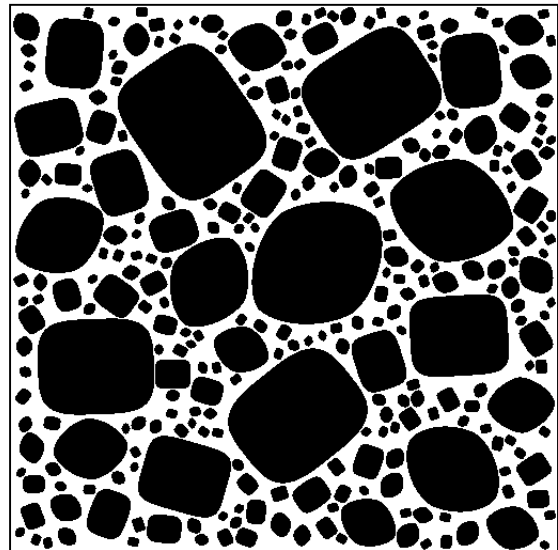


Figure 2.12: Non-periodic geometry. 291 inclusions, 65,2 % volume ratio, generation time 0.55 seconds, 5683 separation checks.
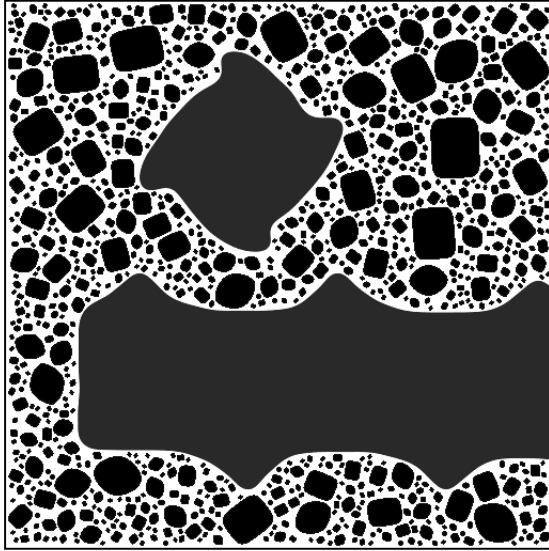
Figure 2.13: Two objects and 979 inclusions, volume ratio of inclusions 35 %, 512 × 512 elements 20193 separation checks took 0.35 seconds
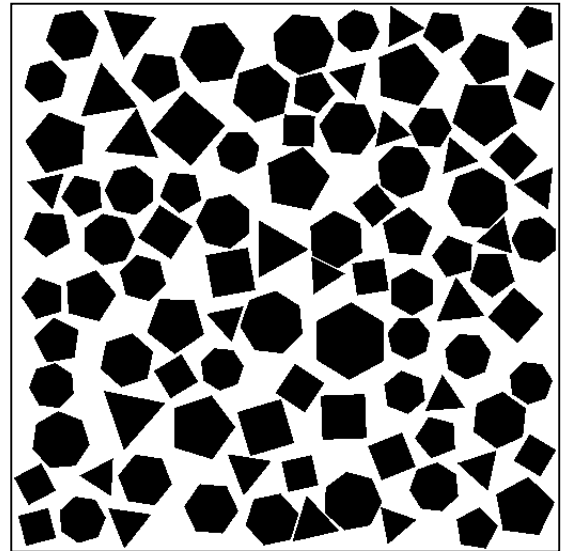
Figure 2.14: Quasi-polygonial shapes according to superformula. 98 inclusions, volume ratio 50 %, 512 × 512 elements

of domain. The periodic model is advantageous for homogenization while the model with wall effect rather corresponds to the section of an equally sized specimen.

Figure 2.13 illustrates the possibility to include arbitrary image data. Here, two objects which are stored in the bitmap format have been loaded into the Mulgrido program. The user can select the option that in addition to any present model, particles can be generated and be placed within a defined color or range of colors. Therewith this arrangement was generated where the particles closely surround, but do not intersect, the predefined objects. Here also the wall-effect occurs. This method clearly also includes the possibility to load any other available image data and regard it as final geometrical model. For each color a new material can be defined. Relevant image processing can be performed by external applications e.g. as described in Section 2.6.

Figure 2.14 includes various shapes according to the superformula as given by Eq. 2.3. In fact, the superformula establishes various interesting shapes which motivated Gielis (2003) for its application to remodel various species. In the present model only quasi-polygonal shapes based on the superformula are included. The shapes are not exact polygons, but represent very close approximations. The applied parameters are summarized in Table 2.2, as they have been approximated by the present author. The parameters $a$ and $b$ in Eq. 2.3 are set to $a = b = 1$. A variation of the supershapes in size can be achieved by

|            | m   | n1   | n2=n3 |
|------------|-----|------|-------|
| Triangle   | 3.0 | 0.54 | 0.92  |
| Quadrangle | 4.0 | 1.00 | 1.00  |
| Pentagon   | 5.0 | 1.61 | 1.02  |
| Hexagon    | 6.0 | 2.26 | 1.07  |
| Heptagon   | 7.0 | 3.00 | 1.11  |

Table 2.2: Parameter combinations of the superformula for the generation of quasi-polygons
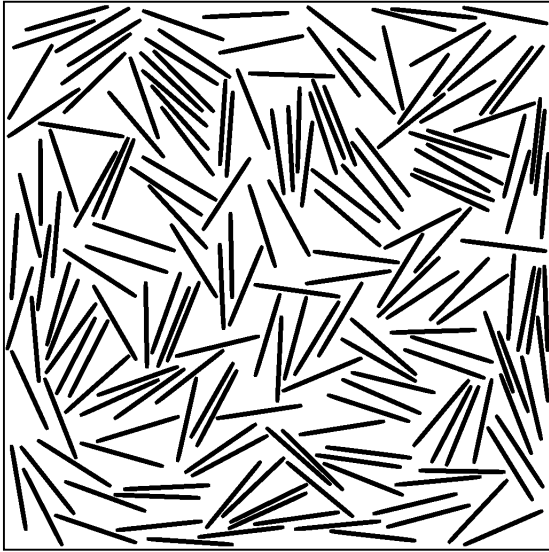
Figure 2.15: 185 fibrous inclusions occupy 25 % in the model of 1024 × 1024 elements.
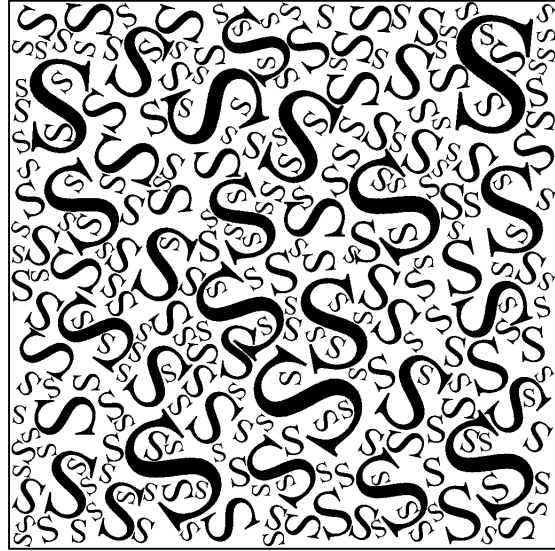
Figure 2.16: 256 objects, volume ratio 30 %, 11644 separation checks took 1.13 seconds.

a transformation of the base coordinate system. A superellipse according to Eq. 2.1 with large length-to-height ratio lead to the geometrical arrangement of Fig. 2.15. It represents a contrast to the foregoing compact shapes and might refer to an idealization of a fibrous composite.

Figure 2.16 illustrates a further option of the present approach. Instead of only importing digital image-based data as a complete model, as for the generation of Fig. 2.13, such data can also define a particle shape. For achieving a high complexity of the model the letter S with serifs has been selected. The original letter is represented by a 512 × 512 pixel image in the bitmap format. Instead of testing if a coordinate lies within an analytical shape, the corresponding coordinate of the pixel object is determined and tested. The original Algorithm 1 detects the boundary pixels of an object and fills the object subsequently. If the algorithm is modified such that any pixel in the defined size is tested and stored, additional filling is not required. Then the object can also be hollow or consist of several parts. It is clear that it is straightforward to mix various objects. A corresponding object library represents a further possible option. It is summarized that this method further increases the flexibility of including complex objects into the geometrical generation process.

In the following some three-dimensional models are presented. Generally most methods for pixel models are straightforward to extend for voxel models. However, the detection of a particle boundary and subsequent filling is especially more complex. For simplicity a modified algorithm which includes each possible coordinate of a particle, as discussed in the last paragraph, has been implemented for the three-dimensional model. With respect to this and some other details the current implementation still allows for several possible enhancements. Nevertheless, the achieved efficiency is still satisfactory. The examples of Figs. 2.17 to 2.20 include $128^3$ voxels each. The total memory demand to solve such a finite element problem is 776 MB in the present implementation. Therefore it can well be processed on a standard computer. Figure 2.17 shows a model of spheres with similar parameters as the model of Fig. 2.5 (right). It is noted that the model of Fig. 2.17 with $128^3$ finite elements is considerably larger than that in the statement of problem (Section 1.3)
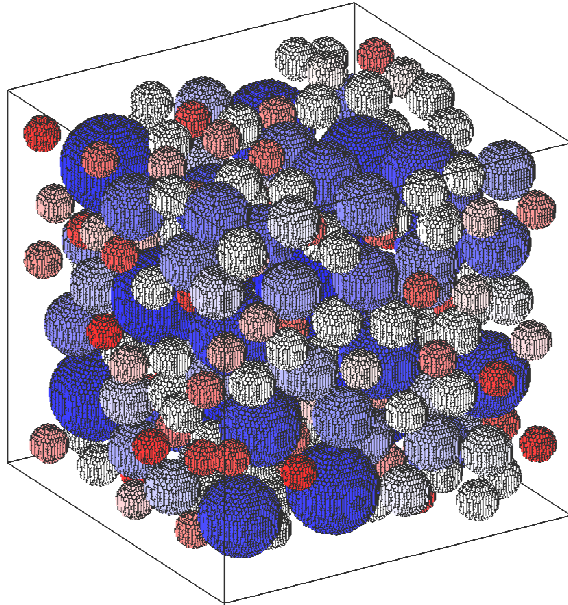
Figure 2.17: 262 spherical inclusions projected onto a $128^3$ voxel model. Volume ratio is 30 %. 16754 placement trials. Total time 8.42 seconds.
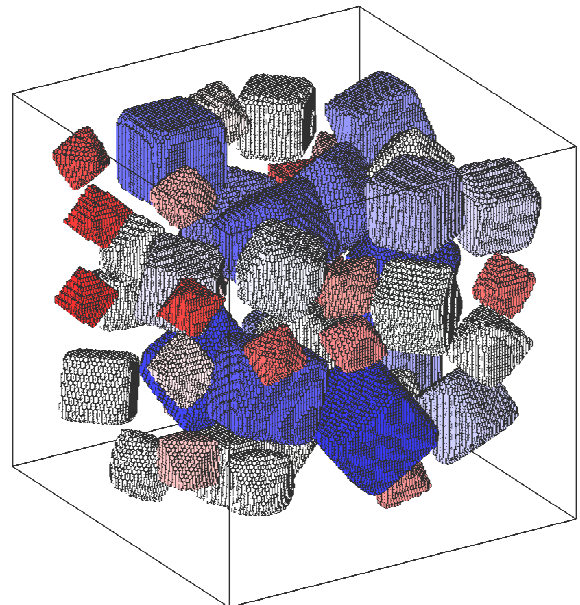


Figure 2.18: Example with inclusions shapes according to the superellipsoid. 51 inclusions occupy 20 % of the volume.
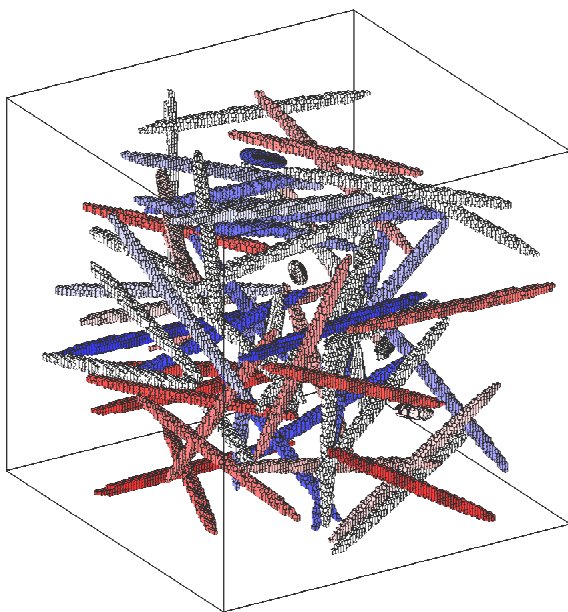


Figure 2.19: 69 fibrous inclusions occupy 2 % of the volume.
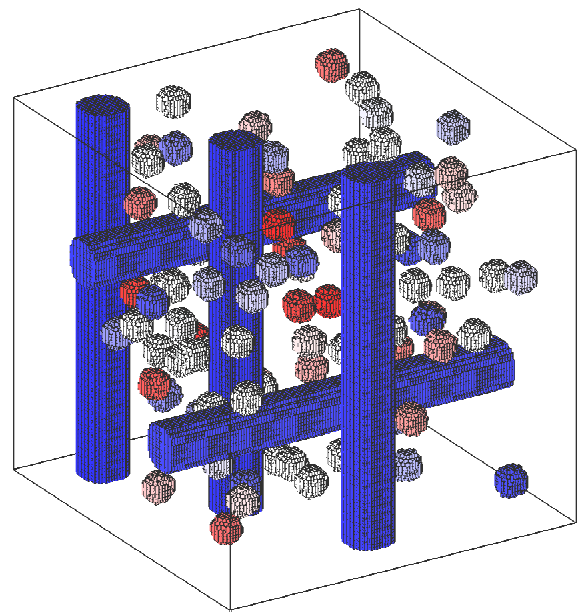


Figure 2.20: Five bars surrounded by 94 small inclusions which occupy 2.5 % of the volume.

with $25^3$ finite elements (Fig. 1.4, right). Figure 2.18 illustrates various shapes according to the superellipsoid (Eq. 2.1). A possible three-dimensional random arrangement of fibers in a cube is shown in Fig. 2.19. The option to include other objects into the geometrical model is demonstrated in Fig. 2.20. It is clear that for the graphical visualization of the three-dimensional model, the matrix material is set to a mode of invisibility. Finally, it is noted that automatically for each example the memory of the corresponding finite element problem is allocated, where one pixel or voxel corresponds to one finite element. Otherwise if only the geometrical model would be of interest essentially larger models could be
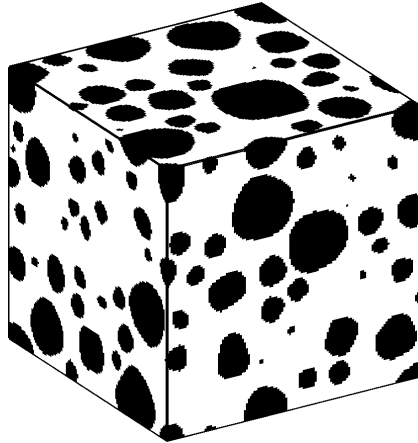
Figure 2.21: Example of three-dimensional periodic unit cell

created. Finally, in analogy to Fig. 2.11, a three-dimensional example of a periodic unit cell is shown in Fig. 2.21.

## 2.8    Conclusions

Grid-based methods are applied for two- and three-dimensional geometrical models. It is shown that such pixel and voxel models bear a high potential to create adequate models of heterogeneous solids. It is highlighted that it is not required to generate a complete analytical formulation of the heterogeneous body. In fact, any algorithm only needs to read or change the state of a discrete number of pixels or voxels. Therefore any change of the geometry is based on a clear and stable operation. Grid-based modeling is closely related to digital image-based modeling. Digital images represent a relevant aspect for the practical application to existing heterogeneous solids. Advanced methods which have been achieved for digital-image based modeling support the present approach. However, the major present contribution of the geometrical model refers to theory-based modeling of heterogeneous solids with focus on inclusion-matrix models. Besides, often applied inclusion shapes such as spheres and ellipsoids, arbitrary regular and irregular shapes are discussed. Special attention is paid to superellipsoids and the superformula which has recently been discovered in the field of botany. These formulas establish a rich variation of shapes by the modification of only a few parameters. Adequate distributions of particle sizes are essential for concrete material. Based on the common mass distribution function of particle sizes, convenient formulas for the generation of particle sizes are developed for three- and two-dimensional modeling. These formulas are flexible such that they can be adapted to various distribution functions. The observed size distribution for the generated particles will naturally converge to the expected distribution function with increasing number of particles. For the placement of particles, a separation check of two particles is required to avoid overlapping. An analytical separation check is generally not available if the inclusions are not spheres or ellipsoids. Various numerical separation checks are presented for arbitrary shapes of inclusions. An efficient solution is developed for grid meshes. There, for the placement of a new particle, it is not required to perform a separation check with all previously placed particles, but it is only tested if the relevant area of the domain

is still empty. Moreover, own results of digital-image based analysis are presented. It is shown that arbitrary, complex objects, which may originate from digital images, can be included into the geometrical model in diverse ways. Various examples demonstrate the high flexibility and efficiency of the present approach.

# Chapter 3

# Mechanical Model

## 3.1  Introduction

In contrast to the geometrical model and the numerical model which originate from mathematics, the mechanical model is rooted in physics. Therefore the mechanical model represents the essential core to describe and simulate the behavior of solids subjected to forces and deformation. A mechanical theory of solids includes a formulation of kinematics, constitutive relationship, state of equilibrium and boundary conditions. The constitutive relationship varies for different materials. In general such constitutive relationships are developed based on macroscopic responses of a certain material in physical experiments. In the present context such a constitutive relationship, or material law, for a heterogeneous material is denoted as phenomenologic, if it relates to strains of a homogeneous body. In fact, then the actual stress-strain relationships within the heterogeneous material are not discovered. For any change of the material structure, the specimen size, the specimen geometry, the experimental setup or the loading state, the phenomenological material law, which has been derived from the prior experiment, might not be adequate for the next one. Based on many experiments complex phenomenological laws and theories have been developed which cover several different loading states. Besides, phenomenological material laws often include some parameters which are adapted for agreement to the experiments. However, the physical meaning and determination of these parameters is often not clear.

The present approach is characterized by a direct modeling of heterogeneous solids as a geometrical assembly of multiple phases. This can be considered as a geometrical-mechanical approach. The prior phenomenological material laws are replaced by a combination of geometrical model and mechanical model. Only this combination of geometrical model and mechanical model provides the chance for the simulation of heterogeneous solids based on correct stress-strain relationships within the material. Once the constitutive relationships of the material phases have been established, numerous different heterogeneous solids containing these material phases can accurately be simulated. Therefore this method allows for many new possibilities, as introduced in Chapter 1.

The present chapter prepares the relevant mechanical background of the proposed methods to compute the mechanical behavior of heterogeneous solids. It includes the fundamental equations of continuum mechanics. Moreover, it prepares some formulations from mixing theory which is also labeled as homogenization or mean field theory. This covers the linear elastic part and links the mesoscale model and macroscale model in terms of effective elastic properties. Nevertheless, it is the general intention of this research to develop a transparent and accurate simulation model for nonlinear material behavior.

For example such a relevant material behavior originates from damage. The considered isotropic damage law for tension is exemplary and does by no means represent the current state-of-the-art. However, due to the high resolution of the subscale models complex damage mechanisms can be simulated. It represents one step away from phenomenologic macroscopic models which lack of transparency and flexibility, towards direct modeling of damage with respect to different material phases. However, the damage model is only considered as principal extension of the grid-based approach, as already outlined in the Sections 1.3 and 1.4.

## 3.2 Continuum Mechanics of Solids

### 3.2.1 Three-Dimensional Continuum

An elastic three-dimensional body in a Cartesian coordinate system with base vectors $\boldsymbol{e}_i$, with $i = 1, 2, 3$, is considered. In the view of continuum mechanics the body is continuous as well as all corresponding vector fields, such as displacements $\boldsymbol{U} = U_i \, \boldsymbol{e}_i$, strains $\boldsymbol{\epsilon} = \epsilon_{ij} \, \boldsymbol{e}_i \otimes \boldsymbol{e}_j$ and stresses $\boldsymbol{\sigma} = \sigma_{ij} \, \boldsymbol{e}_i \otimes \boldsymbol{e}_j$. For the linearized theory it is unique to introduce only one coordinate system. In an initial, undeformed state a material point of the body is located at position $\boldsymbol{X} = X_i \, \boldsymbol{e}_i$. All field variables refer to this initial configuration and thus can be considered as a function of $\boldsymbol{X}$: $\boldsymbol{U} = \boldsymbol{U}(\boldsymbol{X})$, $\boldsymbol{\epsilon} = \boldsymbol{\epsilon}(\boldsymbol{X})$ and $\boldsymbol{\sigma} = \boldsymbol{\sigma}(\boldsymbol{X})$. Due to the following symmetry[1] of strain coordinates $\epsilon_{ij} = \epsilon_{ji}$ and stress coordinates $\sigma_{ij} = \sigma_{ji}$, the elastic problem includes 15 unknown variables in the coordinates of $\boldsymbol{U}$, $\boldsymbol{\epsilon}$ and $\boldsymbol{\sigma}$; respectively $3 + 6 + 6 = 15$. As a formal solution to determine these unknown state variables a system of 15 equations is introduced, while as well predefined displacements and tractions on the surface of the body need to be satisfied. This describes the elliptic boundary value problem of linear elasticity. Six kinematic equations

$$\boldsymbol{\epsilon} = \frac{1}{2} \left( \operatorname{grad} \boldsymbol{U} + (\operatorname{grad} \boldsymbol{U})^{\mathrm{T}} \right) , \qquad \epsilon_{ij} = \frac{1}{2} \left( U_{i,j} + U_{j,i} \right) \tag{3.1}$$

define the relationship of strains $\boldsymbol{\epsilon}$ and displacements $\boldsymbol{U}$. Six constitutive equations

$$\boldsymbol{\sigma} = \mathbb{C} \, \boldsymbol{\epsilon} , \qquad \sigma_{ij} = C_{ijkl} \, \epsilon_{kl} \tag{3.2}$$

couple stresses $\boldsymbol{\sigma}$ and strains $\boldsymbol{\epsilon}$ where in the case of the generalized Hooke's law for homogeneous, isotropic material the material tensor $C_{ijkl}$ is defined as

$$C_{ijkl} = \lambda \, \delta_{ij} \, \delta_{kl} + \mu \, \left( \delta_{ik} \, \delta_{jl} + \delta_{il} \, \delta_{jk} \right) \tag{3.3}$$

It is noted that the Einstein summation convention defines summation over repeated indices. The Kronecker delta $\delta_{ij}$ is equal to 1 for $i = j$ and equal to 0 for $i \neq j$. The material specific variables $\mu$ and $\lambda$ are the Lamé constants. The Lamé constants can be substituted by Young's Modulus $E$ and Poisson's ratio $\nu$. The corresponding conversions are

$$\mu = \frac{E}{2(1+\nu)} , \quad \lambda = \frac{\nu E}{(1+\nu)(1-2\nu)} , \quad E = \frac{\mu \, (2\mu + 3\lambda)}{\mu + \lambda}, \quad \nu = \frac{\lambda}{2 \, (\mu + \lambda)} \tag{3.4}$$

---

[1]For this symmetry the general absence of body moments is presumed.

Equilibrium is described by the following three equations

$$\int_V p_i dV + \int_A \sigma_{ji} n_j dA = 0 \tag{3.5}$$

which mean that, in total, body forces $p_i \boldsymbol{e}_i$ and surface tractions $\sigma_{ji} n_j \boldsymbol{e}_i$ of any considered volume $V$, which is bounded by the surface area $A$, vanish. By the divergence theorem this equation is transformed into the following well-known fundamental strong form of equilibrium

$$\text{div } \boldsymbol{\sigma} + \boldsymbol{p} = \boldsymbol{0} \ , \qquad \sigma_{ji,j} + p_i = 0 \tag{3.6}$$

The analytical solution requires a state of equilibrium at any point on the surface and within the volume of the considered body. The body is fixed to avoid rigid body motion. It is loaded by body loads $\boldsymbol{p} = p_i \, \boldsymbol{e}_i$ and surface tractions $\boldsymbol{t} = t_i \, \boldsymbol{e}_i$. The surface tractions at the boundary of the body correspond to the adjacent stresses $t_i \, \boldsymbol{e}_i = \sigma_{ji} n_j \boldsymbol{e}_i$ where $n_j$ are the components of the outward oriented normal unit vector $\boldsymbol{n} = n_j \, e_j$. It is a boundary value problem with prescribed displacements $\boldsymbol{U}_D$ on $\Gamma_D$ and prescribed surface tractions $\boldsymbol{t}$ on $\Gamma_N$

$$
\begin{aligned}
\boldsymbol{U} &= \boldsymbol{U}_D & \text{on } \Gamma_D \tag{3.7} \\
\boldsymbol{\sigma} \, \boldsymbol{n} &= \boldsymbol{t} & \text{on } \Gamma_N \tag{3.8}
\end{aligned}
$$

The solution is unique, if rigid body modes are excluded and under some further assumptions, which generally apply to engineering models (e.g. Young's modulus is positive).

### 3.2.2   Reduction to Two- and One-Dimensional Continuum

Under certain conditions and presumptions a three-dimensional elasticity problem can be reduced to a two-dimensional problem. For example, labels of such special states are plane stress, plane strain or axisymmetric. In this thesis only the plane stress state is considered. For plane stress parallel to the $X_1 X_2$-plane, the stress components $\sigma_{13}$, $\sigma_{23}$ and $\sigma_{33}$ are equal to zero. The other stress components are constant with respect to $X_3$. The kinematics equation and the equilibrium equation can directly be reduced to two-dimensional by reducing the range of the indices $i$ and $j$ to 2. The constitutive relationship in the plane stress state is

$$\sigma_{11} = \frac{E}{(1-\nu^2)} \left( \epsilon_{11} + \nu \epsilon_{22} \right) \ , \quad \sigma_{22} = \frac{E}{(1-\nu^2)} \left( \nu \epsilon_{11} + \epsilon_{22} \right) \ , \quad \sigma_{12} = \frac{E}{2(1+\nu)} \gamma_{12} \tag{3.9}$$

with $\gamma_{12} = 2\epsilon_{12}$ according to Eq. 3.1. A reduction to one dimension as to the uniaxial stress problem corresponds to the typical model of a bar. All stress components except $\sigma_{11}$ are equal to zero. In this case the kinematics equation, constitutive equation and equilibrium equation are

$$\epsilon_{11} = U_{1,1} \ , \qquad \sigma_{11} = E\epsilon_{11} \ , \qquad \sigma_{11,1} + p_1 = 0 \tag{3.10}$$

## 3.3 Homogenization

### 3.3.1 General Objectives

Homogenization is performed to determine the effective properties of heterogeneous materials. In heterogeneous materials the material properties can differ from point to point. This characteristic can result from an assembly of different materials. Therefore the corresponding fundamentals are also denoted as *mixing theory*. As generally volume averages are the basis to treat such physical phenomena, a further synonym is *mean field theory*. Homogenization aims at the approximation of one unique constitutive relationship between strains and stresses of any arbitrary material. If the linearized theory can be assumed, the determined constitutive relationship describes the effective linear elastic properties of the heterogeneous material. The achieved result can only be accurate, if the observed material sample is sufficiently representative for this material. Then, the effective properties describe the macroscopic material behavior from sole knowledge of an arrangement of different components on a subscale. This scale transfer achieved by homogenization is denoted as upscaling. The opposite is downscaling, which means that e.g. parameters of a subscale model are approximated from macroscopic responses. Principally up- and downscaling is possible between any two scales and not necessarily needs to include the macroscale. Such procedures are relevant for exploring, understanding and evaluating the complex material behavior of heterogeneous materials which is observed at various scales. The gained knowledge is important for accurate simulation of heterogeneous materials as well as for many practical applications of engineering.

### 3.3.2 Three-Dimensional Continuum

The absence of body moments supposed, the condition $\sigma_{ij} = \sigma_{ji}$ holds, and with $\epsilon_{ij} = \epsilon_{ji}$ the general constitutive relationship of Eq. 3.2 can be rewritten in the following matrix form.

$$
\begin{bmatrix} \sigma_{11} \\ \sigma_{22} \\ \sigma_{33} \\ \sigma_{12} \\ \sigma_{23} \\ \sigma_{13} \end{bmatrix} = \begin{bmatrix} C_{1111} & C_{1122} & C_{1133} & C_{1112} & C_{1123} & C_{1113} \\ C_{2211} & C_{2222} & C_{2233} & C_{2212} & C_{2223} & C_{2213} \\ C_{3311} & C_{3322} & C_{3333} & C_{3312} & C_{3323} & C_{3313} \\ C_{1211} & C_{1222} & C_{1233} & C_{1212} & C_{1223} & C_{1213} \\ C_{2311} & C_{2322} & C_{2333} & C_{2312} & C_{2323} & C_{2313} \\ C_{1311} & C_{1322} & C_{1333} & C_{1312} & C_{1323} & C_{1313} \end{bmatrix} \begin{bmatrix} \epsilon_{11} \\ \epsilon_{22} \\ \epsilon_{33} \\ 2\epsilon_{12} \\ 2\epsilon_{23} \\ 2\epsilon_{13} \end{bmatrix} \tag{3.11}
$$

If no information about further material symmetry is provided, this means that there are 36 material parameters $C_{ijkl}$ to determine. From the conditions that $\sigma_{ij} = \sigma_{ji}$ and $\epsilon_{ij} = \epsilon_{ji}$ follows that the matrix $\boldsymbol{C}$ (Eq. 3.11) is symmetric and thus the number of possibly different parameters reduces to 21. For heterogeneous materials the constitutive relationship refers to averages over the domain $\Omega$, but may not be valid for any arbitrary material point. Thus for homogenization, the notation of variables in the the constitutive relationship, $\boldsymbol{\sigma} = \boldsymbol{C}\boldsymbol{\epsilon}$ (Eq. 3.11), is redefined while two different cases are distinguished.

$$
\langle \boldsymbol{\sigma} \rangle_\Omega = \boldsymbol{C}^{\text{eff}} \langle \boldsymbol{\epsilon} \rangle_\Omega \quad \text{in case 1 (effective properties)} \tag{3.12}
$$

$$
\langle \boldsymbol{\sigma} \rangle_\Omega = \boldsymbol{C}^{\text{app}} \langle \boldsymbol{\epsilon} \rangle_\Omega \quad \text{in case 2 (apparent properties)} \tag{3.13}
$$

The variables $\langle\boldsymbol{\sigma}\rangle_\Omega$ and $\langle\boldsymbol{\epsilon}\rangle_\Omega$ refer to the averaged stresses and strains, respectively, in the domain $\Omega$ of the observed heterogeneous material sample. The effective properties of the heterogeneous material are denoted by $\boldsymbol{C}^{\text{eff}}$. The corresponding case 1 refers to an ideal theoretical arrangement. The observed material sample is exactly statistically homogeneous, it ideally represents this material and there is no disturbing effect from sample size and boundary conditions. This generally requires an infinite domain. Otherwise, if these strict assumptions do not apply, then only apparent properties $\boldsymbol{C}^{\text{app}}$, according to case 2, can be determined by any simulation method. The distinction of two cases is useful, as by applying various boundary conditions, various apparent properties $\boldsymbol{C}^{\text{app}}$ can be determined, which establish accurate bounds of the effective properties $\boldsymbol{C}^{\text{eff}}$.

For homogeneous boundary conditions (Aboudi 1991), the following equations apply for average stresses and strains, respectively.

$$\langle\sigma_{ij}\rangle_\Omega = \frac{1}{V}\int_\Omega \sigma_{ij}\mathrm{dV} \tag{3.14}$$

$$\langle\epsilon_{ij}\rangle_\Omega = \frac{1}{V}\int_\Omega \epsilon_{ij}\mathrm{dV} \tag{3.15}$$

There are two types of homogeneous boundary conditions (Aboudi 1991). One type are pure displacement boundary conditions imposed on the boundary $\Gamma$.

$$U_i(\Gamma) = \epsilon^0_{ij}X_j \tag{3.16}$$

The variable $\epsilon^0_{ij}$ denotes constant strains which would occur in a homogeneous body according to this boundary condition. Equation 3.16 describes *kinematic uniform boundary conditions* (KUBC). The other type are pure traction boundary conditions imposed on the boundary $\Gamma$.

$$t_i(\Gamma) = \sigma^0_{ij}n_j \tag{3.17}$$

The variable $\sigma^0_{ij}$ means any constant stresses and $n_j$ are the coordinates of the unit outward normal vector to $\Gamma$. Equation 3.17 describes *static uniform boundary conditions* (SUBC) (Amieur, Hazanov and Huet 1993).

For any load cases according to homogeneous boundary conditions, the Eqs. 3.14 and 3.15 establish the averages $\langle\sigma_{ij}\rangle_\Omega$ and $\langle\epsilon_{ij}\rangle_\Omega$ from determined fluctuating fields $\sigma_{ij}$ and $\epsilon_{ij}$ within the heterogeneous body. Thus, in analogy to Eq. 3.11 the relationship of Eq. 3.13, $\langle\sigma_{ij}\rangle_\Omega = C^{\text{app}}_{ijkl}\langle\epsilon_{ij}\rangle_\Omega$, can be exploited to solve for the unknowns $C^{\text{app}}_{ijkl}$. As one load case provides six equations, altogether six load cases are required to determine 36 unknowns. It is clear that these load cases need to be linear independent. Zohdi and Wriggers (2005) propose the following combination of load cases. According to Eq. 3.16 all strains $\epsilon^0_{ij}$ are set to $\epsilon^0_{ij} = 0$ for all $i, j = 1\ldots3$ except for the following strain(s) in the load cases (1) to (6),

$$(1)\qquad\qquad \epsilon^0_{11} = c_\epsilon \tag{3.18}$$

$$(2)\qquad\qquad \epsilon^0_{22} = c_\epsilon \tag{3.19}$$

$$(3)\qquad\qquad \epsilon^0_{33} = c_\epsilon \tag{3.20}$$

$$(4)\qquad\qquad \epsilon^0_{12} = \epsilon^0_{21} = c_\epsilon \tag{3.21}$$

$$(5)\qquad\qquad \epsilon^0_{23} = \epsilon^0_{32} = c_\epsilon \tag{3.22}$$

$$(6)\qquad\qquad \epsilon^0_{13} = \epsilon^0_{31} = c_\epsilon \tag{3.23}$$

where $c_\epsilon$ denotes any constant value. Alternatively, an analog scheme of load cases can be constructed, for traction boundary conditions according to Eq. 3.17, for $\sigma_{ij}^0$ with $c_\sigma$.

For the valid assumption of an orthotrophic material there are three orthogonal planes of symmetry and the number of independent material parameters reduces to nine (Sejnoha et al. 2001). In transversally isotropic material, there is one plane of symmetry and a perpendicular axis of symmetry which leads to five independent material parameters. Isotropic material is defined by three axis of rotational symmetry. Then only two independent material parameters exist, which can either be expressed by the Lame constants or Young's modulus and Poisson's ratio (Eq. 3.4). Then one load case is sufficient to determine these two material parameters. Anyway, principally for any material which includes a plane or axis of symmetry also the full scheme according to Eqs. 3.18 to 3.23 can be applied. However, it is reasonable to use an adequate reduced scheme for the remaining independent material parameters.

An essential principle of homogenization is Hill's energy condition (Hill 1963)

$$\langle \sigma_{ij} \epsilon_{ij} \rangle_\Omega = \langle \sigma_{ij} \rangle_\Omega \langle \epsilon_{ij} \rangle_\Omega \tag{3.24}$$

which is proven to be valid for homogeneous boundary conditions, which are defined by Eqs. 3.16 and 3.17. Thus, it is possible to express the strain energy within the heterogeneous material of the domain $\Omega$ as a quadratic form in terms of $\langle \boldsymbol{\sigma} \rangle_\Omega$ or in terms of $\langle \boldsymbol{\epsilon} \rangle_\Omega$. As already introduced in connection with Eqs. 3.13 and 3.12, the average stresses $\langle \boldsymbol{\sigma} \rangle_\Omega$ and strains $\langle \boldsymbol{\epsilon} \rangle_\Omega$ depend on the boundary conditions. The apparent properties according to homogeneous displacement boundary conditions are denoted as $\boldsymbol{C}_\epsilon^{\mathrm{app}}$ (Eq. 3.16) and those according to homogeneous traction boundary conditions as $\boldsymbol{C}_\sigma^{\mathrm{app}}$ (Eq. 3.17) . From classical energy minimum theorems it can be derived that the apparent properties according to the defined two homogeneous load cases represent the following bounds on the effective properties (Amieur, Hazanov and Huet 1993).

$$\boldsymbol{C}_\sigma^{\mathrm{app}} \ < \ \boldsymbol{C}^{\mathrm{eff}} \ < \ \boldsymbol{C}_\epsilon^{\mathrm{app}} \tag{3.25}$$

The inequalities of matrices in Eq. 3.25 do not refer to all individual entries of the matrices (Eqs. 3.11 - 3.13), but in terms of quadratic forms (Hazanov and Amieur 1995). Then, the following inequality $\boldsymbol{C} > \boldsymbol{D}$ means that

$$\boldsymbol{\epsilon}^{\mathrm{T}} \boldsymbol{C} \boldsymbol{\epsilon} \ > \ \boldsymbol{\epsilon}^{\mathrm{T}} \boldsymbol{D} \boldsymbol{\epsilon} \tag{3.26}$$

where $\boldsymbol{\epsilon}$ is any arbitrary, but non-zero vector and therewith

$$\boldsymbol{\epsilon}^{\mathrm{T}} (\boldsymbol{C} - \boldsymbol{D}) \boldsymbol{\epsilon} \ > \ 0 \tag{3.27}$$

Equation 3.27 is valid if the matrix $(\boldsymbol{C} - \boldsymbol{D})$ is positive definite which is satisfied if all eigenvalues of $(\boldsymbol{C} - \boldsymbol{D})$ are positive.

These bounds will improve with increasing size of the specimen. The presented homogenization approach is applicable for general three-dimensional materials, if numerical methods are available to solve for the field variables $\sigma_{ij}$ and $\epsilon_{ij}$ within the heterogeneous material according to the specified load case.
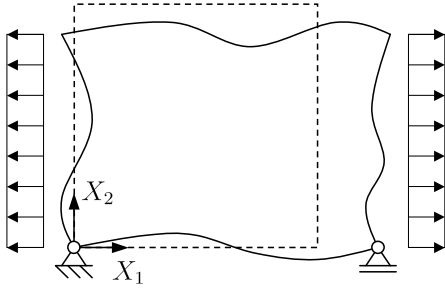
Figure 3.1: Example of homogeneous traction boundary conditions (SUBC)
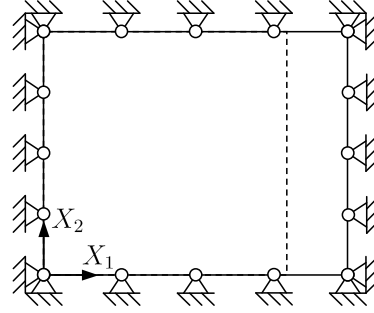


Figure 3.2: Example of homogeneous displacement boundary conditions (KUBC)
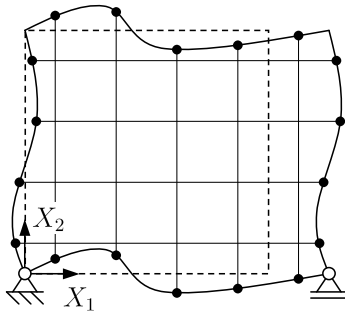


Figure 3.3: Example of periodic boundary conditions
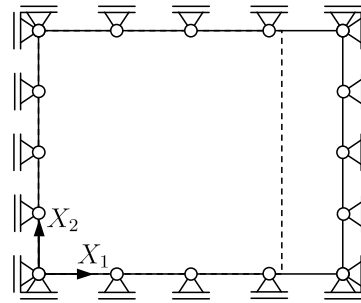


Figure 3.4: Example of mixed boundary conditions (MBC)

### 3.3.3  Two-Dimensional Continuum

The theory of the foregoing section also includes the two-dimensional case of e.g. plane stress or plane strain. However, a more illustrative introduction to the homogenization of two-dimensional, heterogeneous material samples follows. Various types of boundary conditions are shown in Figs. 3.1 to 3.4. The dashed line corresponds to the undeformed state of the heterogeneous material sample. Figure 3.1 illustrates a possible deformed state of the material sample according to an example of homogeneous traction boundary conditions as defined by Eq. 3.17 with

$$\sigma_{11}^0 = c_\sigma \text{ and } \sigma_{12}^0 = \sigma_{21}^0 = \sigma_{22}^0 = 0 \tag{3.28}$$

There are point supports to avoid rigid body motion of the body. As the body is in equilibrium by the tractions only, there will be no supporting forces and the boundary conditions can be considered homogeneous with respect to traction. Homogeneous displacement boundary conditions are shown in Fig. 3.2. With respect to Eq. 3.16 the strains are

$$\epsilon_{11}^0 = c_\epsilon \text{ and } \epsilon_{12}^0 = \epsilon_{21}^0 = \epsilon_{22}^0 = 0 \tag{3.29}$$

The variables $c_\sigma$ and $c_\epsilon$ define a constant value. Periodic boundary conditions refer to the assumption of a periodic material structure. Periodic boundary conditions can also be applied to the three-dimensional continuum. Similar to Eq. 3.16, the general formulation is

$$\Delta U_i(\Gamma) = \epsilon_{ij}^0 \, \Delta X_j \tag{3.30}$$

Again $\epsilon_{ij}^0$ defines constant strains. However, these strains do not prescribe the absolute displacements $U(\Gamma)$, but the difference of displacements $\Delta U_i(\Gamma)$ on the boundary $\Gamma$. Such prescribed relative displacements between opposite boundaries are illustrated in Fig. 3.3. By this condition the solution of this problem is already unique. Then, the deformed periodic unit cell can continuously be extended in any direction by the same periodic unit cell of the same deformation state. Moreover, across the boundary $\Gamma$ also the stresses automatically adapt themselves to continuity. It is noted that Hill's condition (Eq. 3.24) is also valid for periodic boundary conditions (Zohdi and Wriggers 2005). The obtained, apparent material properties $\boldsymbol{C}_p^{\mathrm{app}}$ due to periodic boundary conditions are bounded by

$$\boldsymbol{C}_\sigma^{\mathrm{app}} < \boldsymbol{C}_p^{\mathrm{app}} < \boldsymbol{C}_\epsilon^{\mathrm{app}} \tag{3.31}$$

and possibly provide a direct, close approximation of the effective properties $\boldsymbol{C}^{\mathrm{eff}}$. However, $\boldsymbol{C}_p^{\mathrm{app}}$ neither represents a lower nor an upper bound of $\boldsymbol{C}^{\mathrm{eff}}$. The deformed body of Fig. 3.3 is consistent with the periodic boundary conditions according to Eq. 3.30 with $\boldsymbol{\epsilon}^0$ as defined in Eq. 3.29. Figure 3.4 shows an example of mixed boundary conditions. This means that the boundary conditions are partially tractions and partially prescribed displacements. If both parts are uniform then this is denoted as uniform mixed boundary conditions. In laboratory experiments often only mixed boundary conditions can effectively be applied to the specimen. For several classical testing conditions (Amieur, Hazanov and Huet 1993; Hazanov 1998) the corresponding mixed boundary conditions also satisfy Hill's condition (Eq. 3.24). The apparent material properties $\boldsymbol{C}_m^{\mathrm{app}}$ obtained from mixed boundary conditions are bounded by

$$\boldsymbol{C}_\sigma^{\mathrm{app}} < \boldsymbol{C}_m^{\mathrm{app}} < \boldsymbol{C}_\epsilon^{\mathrm{app}} \tag{3.32}$$

similar as stated by Eq. 3.31 for periodic boundary conditions.

### Homogenization for Specific Mixed Boundary Conditions

Figure 3.5 sketches the tractions $t$ and resulting forces $R$ of a heterogeneous and a homogeneous body, both of width W and height H, for the mixed boundary conditions

$$\left.\begin{array}{ll} U_1(X_1) & = \epsilon_{11}^0 X_1 \\ t_2(X_1) & = 0 \end{array}\right\} \text{ for } X_1 \in \{0; W\} \ , \qquad \left.\begin{array}{ll} U_2(X_2) & = 0 \\ t_1(X_2) & = 0 \end{array}\right\} \text{ for } X_2 \in \{0; H\} \tag{3.33}$$

where $\epsilon_{11}^0$ defines a constant value. The resulting force is the integral of traction, e.g.

$$R_{1+} = \int_0^H t_{1+} \, dX_2 \tag{3.34}$$

The absence of body loads supposed, the sign subscript of $R$ is superseded. In the following it is assumed that the resulting forces of the two models $a$ and $b$ in Fig. 3.5 are equal

$$R_1^a = R_1^b \ , \quad R_2^a = R_2^b \tag{3.35}$$

and that the effective material behavior of model $a$ is isotropic. Then, model $a$ is replaced by the homogeneous, isotropic model $b$, where

$$\sigma_{11}^b = \frac{R_1}{H} \ , \quad \sigma_{22}^b = \frac{R_2}{W} \ , \quad \sigma_{12}^b = 0 \tag{3.36}$$
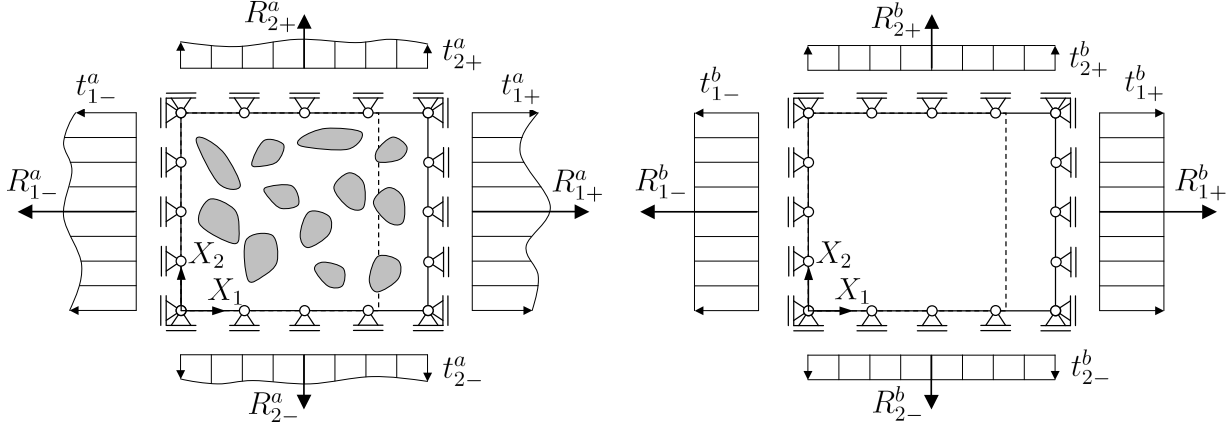
Figure 3.5: Model $a$ on the left is a heterogeneous body and model $b$ on the right is a homogeneous body. To both models identical mixed boundary conditions according to Eq. 3.33 are applied.

The present load case and the plane stress condition (Eq. 3.9) yield

$$\sigma_{11}^b = \frac{E}{1 - \nu^2}\, \epsilon_{11}^0 \,, \quad \sigma_{22}^b = \frac{E}{1 - \nu^2}\, \nu\, \epsilon_{11}^0 \tag{3.37}$$

from which follows that with Eq. 3.36 the elastic properties are

$$E = \frac{R_1}{H\, \epsilon_{11}^0}\left(1 - \left(\frac{R_2 H}{R_1 W}\right)^2\right), \quad \nu = \frac{R_2 H}{R_1 W} \tag{3.38}$$

As the external work of both models is equal, $\frac{1}{2}R_1^a \epsilon_{11}^0 W = \frac{1}{2}R_1^b \epsilon_{11}^0 W$, it follows that also the internal energy corresponds, $\frac{1}{2}\int_\Omega \sigma_{ij}^a \epsilon_{ij}^a dA = \frac{1}{2}\int_\Omega \sigma_{ij}^b \epsilon_{ij}^b dA$. Therefore it is valid to determine the apparent properties (according to these mixed boundary conditions) of the heterogeneous body by Eq. 3.38. In this alternative method only the resulting forces $R_1^a$ and $R_2^a$ need to be evaluated, instead of computing averages of strains and averages of stresses for the complete domain.

### 3.3.4   Classical Bounds on Effective Properties

First bounds of effective elastic properties were formulated by Voigt (1889) and by Reuss (1929). With respect to Young's modulus in an idealized one-dimensional medium of two phases the Voigt bound $E_{\text{Voigt}}$ is derived as

$$E_{\text{Voigt}} = c_1 E_1 + c_2 E_2 \tag{3.39}$$

where $E_1$ and $E_2$ are the Young's moduli of the two phases. The variables $c_1$ and $c_2$ denote the total volume ratios of these phases where $c_1 + c_2 = 1$. The Reuss bound is defined as

$$\frac{1}{E_{\text{Reuss}}} = \frac{c_1}{E_1} + \frac{c_2}{E_2} \tag{3.40}$$

The Voigt bound bases on the assumption of constant strain within the composite and the Reuss bound on that of constant stress. In the three-dimensional continuum, both states

violate compatibility of either tractions or displacements between the phases. Nevertheless, these complementary measures represent important bounds. The effective Young's modulus $E^{\text{eff}}$ of statistically isotropic heterogeneous material is bounded by

$$E_{\text{Reuss}} \; < \; E^{\text{eff}} \; < \; E_{\text{Voigt}} \tag{3.41}$$

The tightest possible bounds for heterogeneous materials of two phases with effective isotropic material behavior (Zohdi and Wriggers 2005) were developed by Hashin and Shtrikman (1963). They provide the following upper and lower bounds in terms of shear modulus $\mu$ (Eq. 3.4) and bulk modulus $\kappa = \frac{E}{3(1-2\nu)}$

$$\kappa_1 + \cfrac{c_2}{\cfrac{1}{\kappa_2 - \kappa_1} + \cfrac{3c_1}{3\kappa_1 + 4\mu_1}} \; < \; \kappa^{\text{eff}} \; < \; \kappa_2 + \cfrac{c_1}{\cfrac{1}{\kappa_1 - \kappa_2} + \cfrac{3c_2}{3\kappa_2 + 4\mu_2}} \tag{3.42}$$

$$\mu_1 + \cfrac{c_2}{\cfrac{1}{\mu_2 - \mu_1} + \cfrac{6c_1(\kappa_1 + 2\mu_1)}{5\mu_1(3\kappa_1 + 4\mu_1)}} \; < \; \mu^{\text{eff}} \; < \; \mu_2 + \cfrac{c_1}{\cfrac{1}{\mu_1 - \mu_2} + \cfrac{6c_2(\kappa_2 + 2\mu_2)}{5\mu_2(3\kappa_2 + 4\mu_2)}} \tag{3.43}$$

for $\kappa_2 > \kappa_1$ and $\mu_2 > \mu_1$. The Hashin-Shtrikman bounds are derived under the assumption that the body is infinite and the effective material behavior is isotropic. Hence, for finite bodies the Hashin-Shtrikman bounds are only exactly valid asymptotically with increasing sample size.

Hill's energy condition (Eq. 3.24) represents an important principle in the derivation of homogenization theories. Besides, several approaches start by a splitting of the field variables into an average mean and a fluctuating part (Zohdi and Wriggers 2005), such as e.g. for the strains $\boldsymbol{\epsilon} = \langle \boldsymbol{\epsilon} + \rangle_\Omega + \tilde{\boldsymbol{\epsilon}}$. Some approaches base on the Eshelby solution (Eshelby 1957). It describes the linear elastic mechanical solution of one ellipsoid in an infinite domain under uniform external loading. This obviously includes the case of a sphere in an infinite domain, but the Eshelby solution is also available for other inclusion shapes. One classical approach for the estimation of effective linear elastic properties of composites is the dilute approximation. It bases on the solution of one sphere within a matrix material and supposes that there is no interaction between inclusions in the domain (Aboudi 1991). Therefore this method is only adequate if the volume ratio of inclusions in the matrix material is very low. The self-consistent scheme does not put the inclusion into the matrix material, but as an improvement to the dilute approximation, into an effective medium with unknown properties. There exist several additional enhancements of this method and further analytical homogenization approaches. For corresponding formulations and related references it is referred to (Aboudi 1991; Zohdi and Wriggers 2005; Sejnoha et al. 2001; Nemat-Nasser and Hori 1999). While classical analytical approaches still present valuable bounds, approximations and reference values, today, computational micromechanics provides the chance for achieving essentially, improved homogenization results.

# 3.4   Damage Model

## 3.4.1   General Classification

In the regard of the present thesis damage modeling is considered as principal extension of the grid-based approach from linear elastic mechanical analysis to modeling nonlinear effects. For this general purpose a simple isotropic damage law is introduced by the following Section 3.4.2. There exist several important nonlinear effects in the material behavior of solids, such as damage, plasticity, creep and shrinkage. However, according to the major objectives stated in Sections 1.3 and 1.4, an adequate introduction to any of these nonlinear effects would distract from the focus of the present work. Therefore only some selected references are provided for the present topic of modeling damage.

An introduction to numerous material models is given in (Jirásek 1999; Desai 2001). Various damage models of concrete are discussed in (Bažant and Planas 1998). The isotropic damage model for tension of Section 3.4.2 is treated in detail in (Jirásek and Patzák 2002). It represents one simple example of a continuum damage model. Continuum damage models can be adapted in many different ways to simulate damage for tension, for compression, as well as a combination of both (Mazars 1986). Various aspects of damage, also for example anisotropy, are treated in (Lemaitre and Chaboche 1990). For concrete it is indicated to combine damage with plasticity for compression (Pölling 2000). Another important category of damage models are crack models which are based on fracture mechanics (Hertzberg 1986). Such cracks can either be smeared over the area of finite elements or explicitly modeled as a discrete crack, on which is commented in (De Borst et al. 2004). A discrete model for damage processes of cohesive frictional materials is presented in (D'Addetta, Kun and Ramm 2002; D'Addetta 2004). The discrete model is based on an assembly of particles which are linked by beams or interfaces in combination with a contact formulation. Moreover, it is pointed out that microplane models represent an effective and flexible solution for modeling complex material behavior (Leukart 2005; Leukart and Ramm 2006). There, based on a set of planes with different orientation, also anisotropic material behavior can be described in a natural way. Relevant damage effects result from the special behavior of material interfaces. In concrete an interfacial transition zone (ITZ) of about 20 to 50 $\mu$m (Van Mier et al. 2002) thickness between aggregate and matrix is considered. The influence of the aggregate type and of the mortar on the constitutive behavior of the ITZ is analyzed in (Caliskan 2003).

## 3.4.2   Isotropic Damage Model for Tension

For the application of an isotropic material law in the mesoscale model it is presumed that the finite element resolution of the heterogeneous solid on the mesoscale is very high. Then even crack patterns can be reproduced by isotropic damage of small subregions. Therefore the overall behavior of the considered specimen can become essentially anisotropic. On the macroscale, modeling of such a material behavior would require a more complex material law. The considered model only includes damage in tension and does not include plasticity. This means that for complete unloading of the specimen the displacements return to zero. For concrete this presumption is not quite realistic. However, it is a prototype to examine the proposed grid-based concept.

In the isotropic material model, damage is described by the scalar damage parameter $\omega$. If the material is not damaged then $\omega = 0$. The damage parameter $\omega$ can continuously increase up to 1, and $\omega = 1$ means that the material is completely damaged. The damage parameter $\omega$ couples the linear elastic stress $\boldsymbol{\sigma}^E$ and the effective stress $\boldsymbol{\sigma}$.

$$\boldsymbol{\sigma} = (1 - \omega)\,\boldsymbol{\sigma}^E \tag{3.44}$$

There are several different measures of equivalent strain (Jirásek 1999). As one main criterion, the equivalent strain shall lead to a realistic response in uniaxial tension. Here, the following definition is selected.

$$\widetilde{\epsilon} = \frac{1}{E}\sqrt{\sum_{i=1}^{3}\langle S_i^E\rangle^2} \tag{3.45}$$

where $E$ is the Young's modulus and $\boldsymbol{S}^E$ denotes the principal stresses of $\boldsymbol{\sigma}^E$. The brackets $\langle S_i^E\rangle$ mean the positive part of $S_i^E$ or symbolically $\langle S_i^E\rangle = \max(0, S_i^E)$. Equation 3.45 refers to the three-dimensional case. For the plane stress problem, it can be reduced to

$$\widetilde{\epsilon} = \frac{1}{E}\sqrt{\langle S_1^E\rangle^2 + \langle S_2^E\rangle^2} \tag{3.46}$$

with the descriptive derivation of $S_1$ and $S_2$ from the Mohr circle as

$$S_{1,2} = \frac{\sigma_{xx} + \sigma_{yy}}{2} \pm \sqrt{\left(\frac{\sigma_{xx} - \sigma_{yy}}{2}\right)^2 + \sigma_{xy}^2} \tag{3.47}$$

The maximum equivalent strain in the history of a material point is stored in $\kappa$. The damage parameter $\omega$ is defined by

$$\omega = \begin{cases} 0 & if \quad \kappa \leq \epsilon_0 \\ 1 - \dfrac{\epsilon_0}{\kappa}\exp\left(-\dfrac{\kappa - \epsilon_0}{\epsilon_f - \epsilon_0}\right) & if \quad \kappa > \epsilon_0 \end{cases} \tag{3.48}$$

where $\epsilon_0$ is the limit elastic strain under uniaxial tension which is related to the tensile strength $f_t$ by

$$\epsilon_0 = \frac{f_t}{E} \tag{3.49}$$

The parameter $\epsilon_f$ controls the ductility of the material in terms of the exponential softening branch (Fig. 3.6). In contrast, a linear softening branch tends to exhibit a defective snap-back and therefore is not proposed (Jirásek 1999). The linear elastic material matrix $\boldsymbol{C}^E$ establishes the relationship between stress vector $\boldsymbol{\sigma}^E$ and strain vector vector $\boldsymbol{\epsilon}$.

$$\boldsymbol{\sigma}^E = \boldsymbol{C}^E\boldsymbol{\epsilon} \tag{3.50}$$

With the equality $\boldsymbol{C}(E, \nu) = E\boldsymbol{C}(1, \nu)$ where $\nu$ is the Poisson's ratio, Eq. 3.44 corresponds to $\boldsymbol{\sigma} = E\,(1 - \omega)\,C(1, \nu)\boldsymbol{\epsilon}$ which allows to define a degraded Young's modulus $\hat{E}$ as

$$\hat{E} = E\,(1 - \omega) \tag{3.51}$$

The equivalent strain and damage parameter are stored as an additional layer on the finite element grid (Section 6.2). A corresponding data field is also created for the degraded Young's modulus. Then the data field of $E$ relates to the initial linear elastic stiffness and $\hat{E}$ to the secant stiffness of the damaged material. It is noted that this is simply possible as the Poisson's ratio is not modified by this material model.
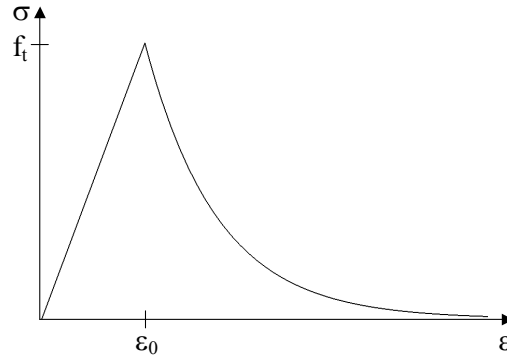
Figure 3.6: Stress-strain diagram of damage model with exponential softening

### 3.4.3 Motivation of Nonlocal Formulation

A nonlocal formulation in this context means that a value of a field variable at any point will be influenced by the value of another, neighboring point, and reverse. This is established by weighted averaging over source points of a predefined local domain around the considered material point, denoted as effect point. Such a nonlocal averaging can refer to various quantities. There are the following reasons from different perspectives to introduce nonlocal formulations in the considered numerical damage analysis:

a.1 By a local formulation of the damage model only, the damaged region could be infinitely small. Then the energy which is dissipated during the damage process would be equal to zero. The resulting ideally brittle behavior of the material would be pathologic. From a mathematical point of view this defect results from a loss of ellipticity in the governing differential equations (Jirásek 1999). Therefore a localization limiter has to be introduced.

a.2 The physical experiment also indicates a nonlocal model. For example in the damage process of materials the development of crack bands or damage regions is observed. This effect is assigned to an internal length of the material.

a.3 A discrete numerical model will generally converge to the analytical solution and therefore the reasons for a nonlocal formulation of (a.1) also apply to finite element modeling. Without localization limiter, a defective sensitivity to the size of finite elements would be observed. Besides there are comfortable side-effects of nonlocal formulations in finite element modeling. Nonlocal averaging can be applied to recover strains or stresses, which is useful especially for the proposed grid discretization.

The items (a.1) to (a.3) refer to the defect of strain localization from a rather mathematical, physical and numerical point of view. There are several solutions to this problem. In regularization techniques the material law is adapted such that the fracture energy is invariant to the size of finite elements, e.g. (Rots and Invernizzi 2003). Another important category are nonlocal formulations which are reviewed in (Bažant and Jirásek 2002).
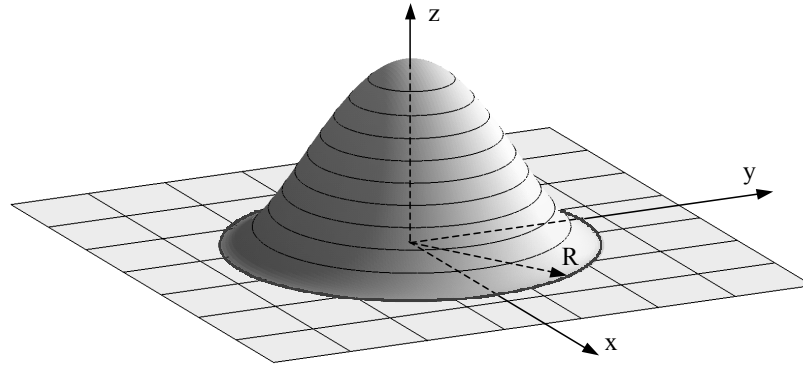
Figure 3.7: Graph of bell-shaped function over two-dimensional domain with interaction radius $R$

### 3.4.4 Nonlocal Formulation by a Weighting Function

The nonlocal formulation by a weighting function $\alpha$ is applied to an arbitrary function $f$. The weighted average is denoted by $\bar{f}$.

$$\bar{f}(\boldsymbol{x}) = \int_\Omega \alpha(\boldsymbol{x}, \boldsymbol{\xi}) f(\boldsymbol{\xi}) \, \mathrm{d}\boldsymbol{\xi} \tag{3.52}$$

The integral includes source points at coordinate $\boldsymbol{\xi}$ in the relevant domain $\Omega$ around the effect point $\boldsymbol{x}$. The effective weighting function $\alpha(\boldsymbol{x} - \boldsymbol{\xi})$ satisfies

$$\int_\Omega \alpha(\boldsymbol{x} - \boldsymbol{\xi}) = 1 \tag{3.53}$$

which is achieved by scaling of an initial weighting function $\alpha_0(\boldsymbol{x} - \boldsymbol{\xi})$ by

$$\alpha(\boldsymbol{x}, \boldsymbol{\xi}) = \frac{\alpha_0(\boldsymbol{x} - \boldsymbol{\xi})}{\displaystyle\int_\Omega \alpha_0(\boldsymbol{x} - \boldsymbol{\zeta}) \, \mathrm{d}\boldsymbol{\zeta}} \tag{3.54}$$

Equation 3.53 establishes that the nonlocal average $\bar{f}(\boldsymbol{x})$ and the function $f(\boldsymbol{x})$ are identical if the function $f(\boldsymbol{x})$ is constant. A favored weighting function in the context of nonlocal damages models is the bell-shaped function. A two-dimensional representation of the bell-shaped function is shown in Fig. 3.7. With the general definition that $r$ is the positive distance between the effect point and the source point $r = \|\boldsymbol{x} - \boldsymbol{\xi}\|$, it follows that the subsequent formulation of the bell-shaped function is valid for one, two or three dimensions.

$$\alpha_0(r) = \begin{cases} \left(1 - \dfrac{r^2}{R^2}\right)^2 & \text{if } 0 \leq r \leq R \\ 0 & \text{if } R \leq r \end{cases} \tag{3.55}$$

In order to compare various weighting functions an internal length $\ell$ is introduced which is defined by the radius of inertia of the weighting function.

$$\ell = \sqrt{\frac{\displaystyle\int_0^\infty r^2 \alpha_0(r) \mathrm{d}r}{\displaystyle\int_0^\infty \alpha_0(r) \mathrm{d}r}} \tag{3.56}$$

Another common weighting function is the Gauss distribution function which already includes the internal length $\ell$ by definition.

$$\alpha_0(r) = \exp\left(-\frac{r^2}{2\ell^2}\right) \tag{3.57}$$

A further relevant measure is the characteristic length $\ell_c$ which is defined by

$$\ell_c = \frac{\displaystyle\int_{-\infty}^{\infty} \alpha_0(r)\mathrm{d}r}{\alpha_0(r=0)} = \frac{1}{\alpha(r=0)} \tag{3.58}$$

For the damage analysis of heterogeneous materials the internal length $\ell$ and the characteristic length $\ell_c$ have a certain interpretation in regard to the (heterogeneous) character of the material. The ratio of $\ell_c/\ell$ depends on the type of weighting function. It will be fixed, but generally different from 1 (Jirásek 1999). As final remark to this section of defining nonlocal weighting in general, it is pointed out that B-splines, beyond the application as finite element shape functions (Häfner, Kessel and Könke 2006), in assignment to a polar coordinate system would also define adequate weighting functions.

## 3.5   Conclusions

This chapter establishes the relevant theory of continuum mechanics with respect to the scope of the present thesis. The governing equations of Section 3.2 represent the basis for the displacement-based finite element formulation in Section 4.2. As the geometrically nonlinear theory is not applied in this work, its formulation is not introduced[2]. Rigid bond of material phases is discussed for two-dimensional domains in connection with multiphase finite elements in Section 4.6. Homogenization according to Section 3.3 is relevant for the study on effective material behavior of Chapter 7. The damage model of Section 3.4 serves as a principal extension to nonlinear analysis and will be applied in Chapter 6 to analyze certain numerical aspects with respect to the present grid-based approach.

---

[2]In general the linear theory is adequate for the mechanical analysis of brittle and compact bodies with realistic strength criteria. Then the limit state rather results from limited physical strength instead of instability. It shall only be noted that due to extreme localization, relevant geometrically nonlinear effects could possibly occur on the material level.

# Chapter 4

# Numerical Model: Multiphase B-Spline Finite Elements

## 4.1  Introduction

### 4.1.1  Basic Ideas of Multiphase B-Spline Finite Elements

Advanced finite elements are proposed for the mechanical analysis of heterogeneous materials. The approximation quality of these finite elements can be controlled by a variable order of B-spline shape functions. An element-based formulation is developed such that the finite element problem can iteratively be solved without storing a global stiffness matrix. This means a relevant reduction of memory demand. The heterogeneous material is modeled by projection onto a uniform, orthogonal grid of elements. Conventional grid-based finite element models show severe oscillating defects in the stress solutions at material interfaces. This problem is tackled by the extension to multiphase finite elements. This concept enables to define a heterogeneous material distribution within the finite element. This is possible by a variable number of integration points to each of which individual material properties can be assigned. Based on an interpolation of material properties at nodes and further smooth interpolation within the finite elements, a continuous material function is established. With both, continuous B-spline shape function and continuous material function, also the stress solution will be continuous in the domain. It is shown that the inaccuracy implied by the continuous material field is by far less defective than the prior oscillating behavior of stresses. One- and two-dimensional examples are presented.

### 4.1.2  Overview of Alternative Finite Element Methods

For modeling of heterogeneous solids several different discretization types are recognized in (Häfner, Eckardt, Luther and Könke 2006). The following selected types are based on continuum mechanics: aligned meshes of phase boundaries by finite elements, unaligned projection on conventional solid finite elements, projection on multiphase finite elements and the extended finite element method. Other discretization types are discrete models such as the projection on truss elements or beam elements and models of discrete particles which are connected by beam elements.

Aligned meshing precisely defines the inclusion surfaces as e.g. shown in (Huet 1993; Wittmann et al. 1993; Guidoum and Navi 1993; Wang et al. 1999; Kwan et al. 1999; Eckardt et al. 2004). However, standard algorithms might fail to mesh complex geometries,

especially with respect to three-dimensional models. In (Guidoum and Navi 1993) element subdivision of a regular mesh is proposed. Aligned meshing supports bond modeling of aggregates in a matrix. The bond zone, labeled as interfacial transition zone (ITZ), shows an important influence in the mechanical analysis of composites. Often the ITZ represents the weakest phase. Then the initiation of the first micro-cracks occurs in the ITZ. Several research groups have recognized the importance of this zone and consider this additional component by special interface elements e.g. Goodman type elements (Kwan, Wang and Chan 1999).

The projection method on conventional finite elements is demonstrated by Nagai et al. (2000) who apply a regular grid of cubical finite elements which directly correspond to voxel data of image analysis. The two-dimensional analogy is shown in (Häfner and Könke 2004). Paz et al. (2003) discretize a model of concrete by a uniform mesh of tetrahedrons. In the projection method each finite element is assigned to one certain phase according to the underlying mesoscale geometry. It is a major drawback of the projection method that the aggregate surfaces are not accurately represented. An improved variant is the projection on multiphase elements where each individual integration point of a finite element is assigned to a certain phase. The present approach applies this concept of multiphase finite elements. The extended finite element method represents an advanced method to model a material interface within a finite element (Sukumar et al. 2000). Modeling failure of material interfaces by the extended finite element method and level sets is presented in (Hettich and Ramm 2006).

Various research groups demonstrate the discretization by projection on one-dimensional elements, so-called lattice-type models. Regular triangular lattices of beam elements are applied in (Schlangen and van Mier 1992; Schlangen 1993; Van Mier et al. 2002; Van Mier and van Vliet 2003). There the material behavior is described by a brittle fracture law, namely tension cut-off, with different strength values of each phase. In a similar way Leite et al. (2004) apply a uniform mesh of truss or frame elements in two or three dimensions, respectively. Leite et al. (2004) use a material model with softening branches in tension and compression. In several lattice models the ITZ is explicitly considered and assigned as material type to elements which intersect both aggregate and matrix. Due to computational effort the element length tends to be considerably larger than the thickness of ITZ which ranges from 20 to 50 $\mu$m (Van Mier et al. 2002). In general the consistency of these methods to the mechanical theory is not quite obvious. Nevertheless, these methods lead to good results in the fracture simulation of concrete on the mesoscale. Discrete models, as described in (D'Addetta, Kun and Ramm 2002; D'Addetta 2004), are considered as further discretization type. Various materials, for example geomaterials and concrete, can be modeled by a discrete granular particle assembly. Therefore the solid is divided into particles by Voronoi tesselation. This means that the particles are formed as randomly shaped convex polygons. The centers of particles are connected by beam elements. An enhancement of particle models by interface elements is proposed in (D'Addetta and Ramm 2006) for an accurate simulation of debonding processes.

### 4.1.3 B-Spline Finite Elements and Multiphase Finite Elements

The present approach introduces a combination of B-spline finite elements with the multiphase finite element concept. In the following the major references for the development of this approach are introduced. The mathematical theory of B-spline finite elements is prepared in (Höllig 2003). It includes so-called web-splines (weighted extended B-splines) for modeling of curved domains. The corresponding method is applied to various physical applications such as in the computation of a stationary temperature distribution, the velocity of an incompressible flow and the deformation of linear elastic bodies. However, while the domains are variable in shape they are principally homogeneous. The present approach only considers rectangular domains, but it is designed to model heterogeneous material inside the domain. A possible application of this approach is the mechanical analysis of heterogeneous materials on the mesoscale where the macroscopic shape of the analyzed body is not of importance.

Multiphase finite elements are presented in (Steinkopff, Sautter and Wulf 1995; Zohdi 2001). Besides several other advanced finite elements methods (Mishnaevsky and Schmauder 2001), multiphase finite elements provide an interesting alternative to model heterogeneous materials. Arbitrary geometries of the heterogeneous material can be mapped on the integration points of e.g. a uniform orthogonal mesh of finite elements. Generally this method is expected to be less accurate than aligned meshing. However, this method only requires pointwise information of the material. Therefore it is convenient for modeling very complex heterogeneous solids even by three-dimensional models. This method is demonstrated in (Häfner, Eckardt and Könke 2003).

The present method integrates the multiphase finite element concept into B-spline finite elements of variable order $k$ while several advantages of grid-based modeling can principally be maintained. As a result, the combination of high performance and improved accuracy lead to a new quality in grid-based modeling of heterogeneous solids.

### 4.1.4 Outline and Key Aspects of Present Approach

Section 3.2 summarizes the boundary value problem of linear elasticity and introduces to the applied notation. By means of the principle of virtual displacements, the classical displacement-based finite element formulation is provided in Section 4.2. Relevant aspects with regard to B-spline finite elements are included. Section 4.3 introduces to univariate splines and B-splines. As a key aspect specific modified B-splines according to (Schwetlick and Kretzschmar 1991) are introduced which will allow for a comfortable definition of displacement boundary conditions. A transparent introduction to one-dimensional B-spline finite elements is provided in Section 4.4. As an important aspect, the B-splines are split to form individual finite elements which are assigned to one grid cell as presented in (Kessel 2004). The analysis is exemplified for two problems of a homogeneous bar. These examples are comprehensible by hand calculation and provide clear access to this method.

In Section 4.5 two-dimensional B-spline finite elements of variable order $k$ are introduced. It includes the Gauss-Legendre numerical integration for polynomials of variable order as given in (Duschek 1961), the formulation of the global stiffness problem, the definition of boundary conditions and an adaption to iterative solving methods without storage of

a global stiffness matrix. Corresponding implementation issues are discussed in (Kessel 2005). A two-dimensional homogeneous test problem with higher-order polynomial loading establishes a verification of the implemented method. The convergence rates of relative error in energy are analyzed with respect to order $k$ of elements ($p$-version) and size of elements ($h$-version) in comparison to classical error estimates provided in (Zienkiewicz and Taylor 1997).

Section 4.6 introduces to the proposed multiphase finite element concept to model heterogeneous materials. The mechanical theory of a material discontinuity is outlined. In the idea of this approach the original mechanical problem is transformed into a substitute problem with continuous material function. While the B-spline finite elements showed severe local defects for the original problem, they are well applicable to the substitute problem. The accuracy of the substitute problem can be scaled by one parameter $s_t$ and in the theoretical limit state $s_t \longrightarrow 0$ the substitute problem converges to the original problem. After a corresponding introduction to multiphase finite elements, a simple bar example highlights the effect of transforming the mechanical problem. Two further examples deal with a circular inclusion in a matrix. A plain grid discretization of the circle and an exact mapping of the transformed problem are presented and analyzed with respect to the defect in the stress solution. Another example of only one material transition establishes a thorough analysis of the multiphase B-spline finite element method with regard to type of transition function of the substitute problem, order of elements and size of elements. Similar to the homogeneous problem an error analysis in terms of stresses and energy follows. Finally also an effective overall error is estimated. This allows to identify optimal parameter combinations of the presented method and supplies evidence of its potential.

## 4.2  Finite Elements for Mechanical Analysis

### 4.2.1  Principle of Virtual Displacements

Based on the stated boundary value problem of elasticity the principle of virtual displacements can be derived, as for example shown in (Bathe 1996). Assuming a body in equilibrium the principle of virtual displacements states that for any virtual displacements $\delta \boldsymbol{U}$, which are conform to the displacement boundary conditions, the total internal virtual work (l.h.s.) is equal to the total external virtual work (r.h.s.).

$$\int_{\Omega} \delta \boldsymbol{\epsilon}^{\mathrm{T}} \boldsymbol{\sigma} dV = \int_{\Omega} \delta \boldsymbol{U}^{\mathrm{T}} \boldsymbol{p}_b \, dV + \int_{\Gamma_N} \delta \boldsymbol{U}^{\mathrm{T}} \boldsymbol{p}_s \, dA \qquad (4.1)$$

The virtual displacements $\delta \boldsymbol{U}$ must be continuous and vanish at the surface of prescribed displacements $\Gamma_D$. The virtual strains $\delta \boldsymbol{\epsilon}$ are directly related to the virtual displacements $\delta \boldsymbol{U}$ according to Eq. 3.1. The external virtual work is induced by body loads $\boldsymbol{p}_b$ and surface loads $\boldsymbol{p}_s$. The principle of virtual displacements is the basis of the displacement-based finite element formulation.

## 4.2.2 Displacement-Based Finite Elements

A linear elastic, continuous body is considered according to the stated three-, two- or one-dimensional boundary value problem of elasticity (Section 3.2). For finite element approximation the continuum is divided into a finite number of parts, which will be labeled as finite elements. These elements are interconnected at nodes. Therefore the continuous problem is transformed into a discrete problem with a finite number of degrees of freedom. The interpretation of degrees of freedom as nodal values is only valid for classical finite elements, but not for B-spline finite elements (except for B-splines of order $k{=}1$). However, the property remains that a degree of freedom is a factor which is assigned to a shape function such that the principal interpolation rule remains.

The degrees of freedom are stored in a global vector $\boldsymbol{u}$ in a predefined order. To each element a local order of degrees of freedom is assigned. For each element $e$ an individual matrix of shape functions $\boldsymbol{N}^e$ defines the displacement interpolation field $\boldsymbol{U}^e$ within the volume $V^e$ of this element as a function of degrees of freedom $\boldsymbol{u}^e$ of this element

$$\boldsymbol{U}^e = \boldsymbol{N}^e \boldsymbol{u}^e \,, \qquad U_i^e = N_{ij}^e u_j^e \tag{4.2}$$

where $i$ counts from 1 to the dimension of the stated boundary value problem (1,2 or 3) and $j$ counts through all local degrees of freedom of element $e$. The displacement field as a continuous function within the element $e$ enables to apply the kinematics (Eq. 3.1) and leads to

$$\boldsymbol{\epsilon}^e = \boldsymbol{B}^e \boldsymbol{u}^e \,, \qquad \epsilon_k^e = B_{kj}^e u_j^e \tag{4.3}$$

where $\boldsymbol{B}^e$ defines the strain-displacement matrix and $k$ refers to the number of strain components of vector $\boldsymbol{\epsilon}^e$. The material matrix $\boldsymbol{C}$ establishes a unique relationship between stresses $\boldsymbol{\sigma}^e$ and strains $\boldsymbol{\epsilon}^e$

$$\boldsymbol{\sigma}^e = \boldsymbol{C}^e \boldsymbol{\epsilon}^e \,, \qquad \sigma_k^e = C_{kl}^e \epsilon_l^e \tag{4.4}$$

with both variables $k$ and $l$ in the range of 1 to 6 for the three-dimensional case. Then, the finite element definitions (Eqs. 4.2-4.4) of discretized state variables adopted by the principle of virtual displacements (Eq. 4.1) for one element $e$ yield[1]

$$\int_{V^e} \delta \boldsymbol{u}^{e\mathrm{T}} \boldsymbol{B}^{e\mathrm{T}} \boldsymbol{C}^e \boldsymbol{B}^e \, \boldsymbol{u}^e dV = \int_{V^e} \delta \boldsymbol{u}^{e\mathrm{T}} \boldsymbol{N}^{e\mathrm{T}} \boldsymbol{p}_b^e \, dV + \int_{A^e} \delta \boldsymbol{u}^{e\mathrm{T}} \boldsymbol{N}^{e\mathrm{T}} \boldsymbol{p}_s^e \, dA \tag{4.5}$$

As the entries of the vectors $\boldsymbol{u}^e$ and $\delta \boldsymbol{u}^e$ are not functions in $V^e$ or $A^e$, but constants, these vectors can both be extracted from the integral, which further allows for a complete elimination of $\delta \boldsymbol{u}^e$. This results in the following fundamental relationship

$$\boldsymbol{K}^e \boldsymbol{u}^e = \boldsymbol{f}^e \tag{4.6}$$

for one element, where $\boldsymbol{K}^e$ is the element stiffness matrix with

$$\boldsymbol{K}^e = \int_{V^e} \boldsymbol{B}^{e\mathrm{T}} \boldsymbol{C}^e \boldsymbol{B}^e \, dV \tag{4.7}$$

and $\boldsymbol{f}^e$ is the vector of nodal forces

$$\boldsymbol{f}^e = \int_{V^e} \boldsymbol{N}^{e\mathrm{T}} \boldsymbol{p}_b^e dV + \int_{A^e} \boldsymbol{N}^{e\mathrm{T}} \boldsymbol{p}_s^e dA \tag{4.8}$$

---

[1]For two matrices $\boldsymbol{A}$ and $\boldsymbol{B}$ the equality $(\boldsymbol{A}\boldsymbol{B})^{\mathrm{T}} = \boldsymbol{B}^{\mathrm{T}}\boldsymbol{A}^{\mathrm{T}}$ is recalled.

under the implied presumption that the functions of body loads $\boldsymbol{p}_b^e$ and surface loads $\boldsymbol{p}_s^e$ are given in the same local coordinate system as the interpolation matrix $\boldsymbol{N}^e$. In Eq. 4.6 the unknown variables are the degrees of freedom of the displacement vector $\boldsymbol{u}^e$ as defined beforehand. Globally the principle of virtual displacements yields the global equation system

$$\boldsymbol{K}\boldsymbol{u} = \boldsymbol{f} \tag{4.9}$$

where the global stiffness matrix corresponds to the sum of element stiffness matrices $\bar{\boldsymbol{K}}_e$ after rearrangement according to the global degrees of freedom

$$\boldsymbol{K} = \sum_{e=1}^{n^e} \bar{\boldsymbol{K}}^e , \qquad K_{ij} = \sum_{e=1}^{n^e} \bar{K}_{ij}^e \tag{4.10}$$

and the global force vector corresponds to the sum of reordered element force vectors $\bar{\boldsymbol{f}}^e$.

$$\boldsymbol{f} = \sum_{e=1}^{n^e} \bar{\boldsymbol{f}}^e , \qquad f_i = \sum_{e=1}^{n^e} \bar{f}_i^e \tag{4.11}$$

However, the element stiffness matrix $\boldsymbol{K}^e$ as in Eq. 4.6 is singular and therefore the solution of the displacement vector $\boldsymbol{u}^e$ is not unique. Displacement boundary conditions need to be integrated into the finite element scheme. Considering all global degrees of freedom of a finite element model, then here the index 1 corresponds to degrees of freedom with a prescribed force and the index 2 corresponds to those of a prescribed displacement.

$$\begin{bmatrix} \boldsymbol{K}_{1,1} & \boldsymbol{K}_{1,2} \\ \boldsymbol{K}_{2,1} & \boldsymbol{K}_{2,2} \end{bmatrix} \begin{bmatrix} \boldsymbol{u}_1 \\ \boldsymbol{u}_2 \end{bmatrix} = \begin{bmatrix} \boldsymbol{f}_1 \\ \boldsymbol{f}_2 \end{bmatrix} \tag{4.12}$$

The initially unknowns of this system are $\boldsymbol{u}_1$ and $\boldsymbol{f}_2$. As the right hand side of the following equation is known, it is possible to compute $\boldsymbol{u}_1$

$$\boldsymbol{K}_{1,1}\,\boldsymbol{u}_1 = \boldsymbol{f}_1 - \boldsymbol{K}_{1,2}\,\boldsymbol{u}_2 \tag{4.13}$$

independent of $\boldsymbol{f}_2$. For further interest the resulting force vector $\boldsymbol{f}_2$ at fixed degrees of freedom yields

$$\boldsymbol{f}_2 = \boldsymbol{K}_{2,1}\,\boldsymbol{u}_1 + \boldsymbol{K}_{2,2}\,\boldsymbol{u}_2 \tag{4.14}$$

## 4.3    Description of B-Splines

### 4.3.1    Fundamentals of Univariate Splines

Univariate means that the spline is one-dimensional or a function of one variable, here $x$. For the definition of a univariate spline $\bar{s}$ in the interval $[x_0, x_n]$ a sequence of supporting points $x_i$ is introduced with the condition that

$$x_i < x_{i+1} \qquad \text{for} \quad i = 0, \ldots, n-1. \tag{4.15}$$

A spline function $\bar{s}$ of order $k$ is composed of piecewise polynomials $\bar{p}_i$ for $i = 0, \ldots, (n-1)$ where each polynomial $\bar{p}_i$ is at maximum of order $k$. The piecewise polynomials $\bar{p}_i$ have limited support in the interval $[x_0, x_n]$ and are defined as

$$\bar{p}_i(x) = \begin{cases} \sum_{j=0}^{k} \bar{c}_{i,j} \, x^j & \text{for } x \in [x_i; x_{i+1}) \\ 0 & \text{for } x \notin [x_i; x_{i+1}) \end{cases} \tag{4.16}$$

with $k \geq 1$. The coefficients $\bar{c}_{i,j}$ are scalar values which define the piecewise polynomial $\bar{p}_i$. In addition to the given function the last piecewise polynomial $\bar{p}_{n-1}$ also includes the upper boundary value $x_n$ to close the spline interval $[x_0, x_n]$. Therewith the spline $\bar{s}$ is defined as

$$\bar{s}(x) = \sum_{i=0}^{n-1} \bar{p}_i(x) \qquad \text{for} \quad x \in [x_0, x_n] \tag{4.17}$$

The coordinates $x_i$ for $i = 1, \ldots, (n-1)$ where the polynomials join are labeled as breaking points. In the complete interval $[x_0, x_n]$ the spline $\bar{s}$ has $(k-r)$ continuous derivatives. This property is declared as $C^{k-r}$-continuity. While each piecewise polynomial $\bar{p}_i$ is naturally $C^k$-continuous in the interval $[x_i, x_{i+1}[$, the continuity of the spline is only reduced at the breaking points by a predefined order $r \geq 1$. Otherwise, if $r = 0$ at all breaking points the spline would be one polynomial over the whole interval.

The prior definitions provide some basic fundamentals of splines. However, it is noted that the provided information is not sufficient for a practical application as e.g. in the approximation of an unknown function only by a given sequence $x_0 \ldots x_n$ of supporting points. For splines of higher order ($k \geq 2$) there are more polynomial coefficients to determine than conditions are given by the definitions above. For example, for splines of order $k = 2$, one additional condition needs to be specified, such as the minimization of the second order derivative, an additional value of the function or its derivative, while various choices lead to various approximation quality. This problem continues with increasing order $k$. An extensive mathematical theory treats many special properties and methods related to various forms of splines. The subsequent introduction is restricted to B-splines (basis splines), which as a sub-category of splines, also satisfy the given fundamentals.

## 4.3.2   B-Splines as a Functional Basis of Splines

In comparison to Eq. 4.17 any $C^{k-1}$ continuous spline of order $k$ can also be defined as linear combination of $n + k$ linear independent B-splines $b_j^k$

$$\bar{s}(x) = \sum_{j=-k}^{n-1} c_j b_j^k(x) \qquad \text{for} \quad x \in [x_0, x_n] \tag{4.18}$$

The coefficients $c_j$ are the corresponding scalar values. It can simply be shown that there exist exactly $n + k$ linear independent B-splines in the interval $[x_0, x_n]$. For the definition of each segment of a spline or piecewise polynomial $(k+1)$ coefficients have to be defined. On the whole interval this results in $n(k + 1) = nk + n$ coefficients. Presuming $C^{k-1}$ continuity, at each of $(n - 1)$ breaking points $k$ continuity conditions have to be satisfied which leads to $(n - 1)k = nk - k$ conditions. Therewith $(nk + n) - (nk - k) = n + k$ parameters can be determined to define a certain spline.

B-splines of order $k$ form a spline basis which always satisfies the intrinsic spline conditions while the choice of $(n + k)$ parameters $c_j$ allows to define any $\mathrm{C}^{k-1}$ continuous spline. A B-spline has only support on $k + 1$ neighboring intervals such that

$$b_j(x) = 0 \qquad \text{for} \quad x \notin [x_j, x_{j+k+1}] \tag{4.19}$$

Therewith Eq. 4.18 can be rewritten as

$$\bar{s}(x) = \sum_{j=i-k}^{i} c_j b_j^k(x) \qquad \text{for} \quad x \in [x_i, x_{i+1}] \ \text{ and } \ i = 0 \dots n - 1 \tag{4.20}$$

which means that in the interval $[x_i, x_{i+1}]$ there will be $(k + 1)$ B-splines defined. Equation 4.20 yields that the considered spline interval $[x_0, x_n]$ also includes B-Splines of the intervals $[x_{-k}, x_1]$ and $[x_{n-1}, x_{n+k}]$.

### 4.3.3   B-Spline Formulations

The uniform B-spline $b^k$ of order $k$ is defined by the recursion

$$b^k(x) = \int_{x-1}^{x} b^{k-1}(t)\mathrm{d}t \tag{4.21}$$

starting from the characteristic function $b^0$ of the unit interval $[0;1]$

$$b^0(x) = \begin{cases} 1 & \text{for } x \in [0; 1) \\ 0 & \text{for } x \notin [0; 1) \end{cases} \tag{4.22}$$

Alternatively, for computational reasons Eq. 4.21 can be brought into the following form, labeled as Recurrence Relation (De Boor 1978; Höllig 2003)

$$b^k(x) = \frac{x}{k}b^{k-1}(x) + \frac{k + 1 - x}{k}b^{k-1}(x - 1) \tag{4.23}$$

The application of the recursion of Eq. 4.21 to the constant B-Spline (Eq. 4.22) yields the uniform, linear B-spline

$$b^1(x) = \begin{cases} x & \text{for } x \in [0; 1) \\ -x + 2 & \text{for } x \in [1; 2) \\ 0 & \text{otherwise} \end{cases} \tag{4.24}$$

which is also known as hat-function within the context of finite elements. The same principle then leads to the uniform quadratic B-spline

$$b^2(x) = \begin{cases} \frac{1}{2}x^2 & \text{for } x \in [0; 1) \\ -x^2 + 3x - \frac{3}{2} & \text{for } x \in [1; 2) \\ \frac{1}{2}x^2 - 3x + \frac{9}{2} & \text{for } x \in [2; 3) \\ 0 & \text{otherwise} \end{cases} \tag{4.25}$$
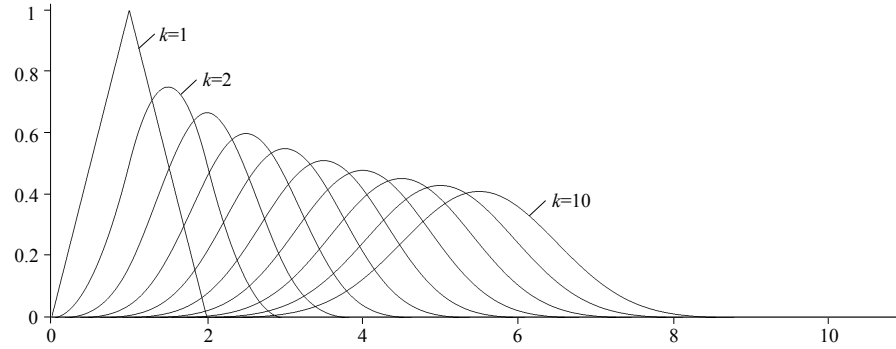
Figure 4.1: Uniform B-splines of order $k = 1 \ldots 10$

and the uniform cubic B-spline.

$$b^3(x) = \begin{cases} \frac{1}{6}x^3 & \text{for } x \in [0;1) \\ -\frac{1}{2}x^3 + 2x^2 - 2x + \frac{2}{3} & \text{for } x \in [1;2) \\ \frac{1}{2}x^3 - 4x^2 + 10x - \frac{22}{3} & \text{for } x \in [2;3) \\ -\frac{1}{6}x^3 + 2x^2 - 8x + \frac{32}{3} & \text{for } x \in [3;4) \\ 0 & \text{otherwise} \end{cases} \qquad (4.26)$$

The first ten B-splines of order $k = 1 \ldots 10$ are shown in Fig. 4.1. The uniform B-Spline of order $k$ is of the length $k + 1$. The uniform B-Spline is scaled to a segment length $h$ and translated by a distance $d$ by the following expression.

$$b_{d,h}^k(x) = b^k(x/h - d) \qquad (4.27)$$

Considering an infinite sequence of similar B-splines at a neighboring distance $d = h$, the sum of these B-splines will be equal to 1 at any coordinate (partition of unity). It also follows that in each interval $[x_i, x_{i+1}]$, with $x_{i+1} = x_i + h$, similar B-spline segments will be represented. For the following formulation of B-spline finite elements it will be useful and sufficient only to consider these $(k + 1)$ B-Spline functions in an interval $[0, h]$.

### 4.3.4   Modified B-Splines Towards Endpoints

For the following finite element approach it is advantageous to modify the B-splines such that the endpoints of the spline will either be equal to 0 or to 1. Then it will be straightforward to apply displacement boundary conditions. Therefore a special recurrence relation, as presented in (Schwetlick and Kretzschmar 1991), will be adapted. It starts by the following definition of B-splines of order $k = 1$.

$$b_j^1(x) = \begin{cases} \frac{x - x_j}{x_{j+1} - x_j} & \text{for } x \in [x_j; x_{j+1}) \\ \frac{x_{j+2} - x}{x_{j+2} - x_{j+1}} & \text{for } x \in [x_{j+1}; x_{j+2}) \\ 0 & \text{otherwise} \end{cases} \qquad (4.28)$$

Multiple knots will be introduced at the coordinates of the endpoints in the considered interval $[x_0; x_n]$.

$$x_{-k} = x_{-k+1} = \ldots = x_{-1} = x_0 \quad , \quad x_n = x_{n+1} = \ldots = x_{n+k-1} = x_{n+k} \qquad (4.29)$$

The modified B-Splines of order $k > 1$ can recursively developed by

$$b_j^k = \omega_j^{k-1}(x)b_j^{k-1}(x) + [1 - \omega_{j+1}^{k-1}(x)]b_{j+1}^{k-1}(x) \tag{4.30}$$

with

$$\omega_j^{k-1}(x) = \begin{cases} \frac{x-x_j}{x_{j+k}-x_j} & \text{if} \quad x_{j+k} > x_j \\ 0 & \text{if} \quad x_{j+k} = x_j \end{cases} \tag{4.31}$$

for $j = -k, \ldots, n-1$. This recursive formula is designed to develop (modified) B-splines in the interval $[x_0; x_n]$. For implementation issues it is referred to (Kessel 2005). Modified B-splines segments occur in $(k-1)$ intervals (of length $h$) towards the endpoints. This means that in $(2k-1)$ intervals, one regular B-spline segment will be created in the center. A larger number of intervals leads to several regular B-spline segments in the center. A smaller interval causes to create modified B-splines only. For the case of $k = 2$, three segments are required to include exactly one regular B-spline. Figure 4.2 shows such modified and regular B-splines of order $k = 2$ in the interval $[x_0, x_4]$. The various occurring B-spline types in one interval according to Fig. 4.2 are highlighted in detached form in Fig. 4.3.

## 4.4   One-Dimensional B-Spline Finite Elements

As descriptive demonstration of B-spline finite elements the one-dimensional case is included. The corresponding formulation is explicitly given for quadratic B-spline finite elements. This section prepares some basic principles for the following more abstract and symbolic description of two-dimensional B-spline finite elements in Section 4.5.

### 4.4.1   Local Interpolation Scheme

As a special characteristic about the following formulation of B-spline finite elements, the B-splines are split into segments to create element stiffness matrices for each interval separately. Nevertheless, continuity of the displacement solution will be recovered by a specific assembly of the global stiffness matrix. The interpolation of the displacements (Eq. 4.2) is defined by $\boldsymbol{N}^J$ where $J$ is a placeholder for the different element types $I$, $II$ or $III$ according to Fig. 4.3 by

$$U(x) = \boldsymbol{N}^J \boldsymbol{u} \tag{4.32}$$

with the following degrees of freedom

$$\boldsymbol{u} = \begin{bmatrix} u_a & u_b & u_c \end{bmatrix}^{\mathrm{T}} \tag{4.33}$$

and the interpolation functions, or shape functions, $\boldsymbol{N}^J$

$$\begin{aligned}
\boldsymbol{N}^I &= \begin{bmatrix} \frac{x^2}{h^2} - \frac{2x}{h} + 1 &, & -\frac{3x^2}{2h^2} + \frac{2x}{h} &, & \frac{x^2}{2h^2} \end{bmatrix} \\
\boldsymbol{N}^{II} &= \begin{bmatrix} \frac{x^2}{2h^2} - \frac{x}{h} + \frac{1}{2} &, & -\frac{x^2}{h^2} + \frac{x}{h} + \frac{1}{2} &, & \frac{x^2}{2h^2} \end{bmatrix} \\
\boldsymbol{N}^{III} &= \begin{bmatrix} \frac{x^2}{2h^2} - \frac{x}{h} + \frac{1}{2} &, & -\frac{3x^2}{2h^2} + \frac{x}{h} + \frac{1}{2} &, & \frac{x^2}{h^2} \end{bmatrix}
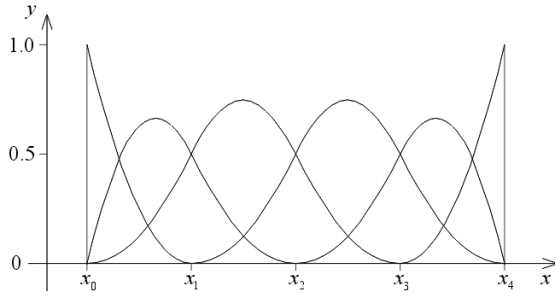\end{aligned} \tag{4.34}$$

Figure 4.2: Partition of unity by 6 B-splines ($k$=2) which are modified in the end segments $(x_0, x_1)$ and $(x_3, x_4)$ .
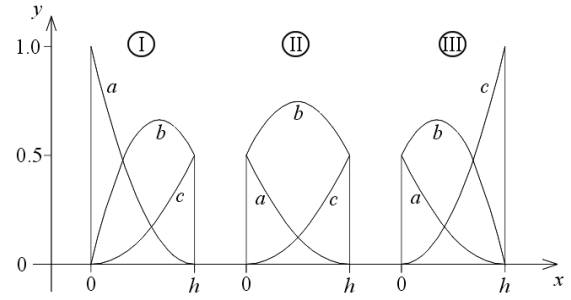
Figure 4.3: B-splines ($k$=2) split into finite elements (I,II,III) with three shape functions (a,b,c) each.

### 4.4.2  Element Stiffness Matrices

Within each element of type $J$ the strain $\epsilon(x)$ is calculated by

$$\epsilon(x) = \frac{dU(x)}{dx} = \frac{d}{dx} \mathbf{N}^J \mathbf{u} = \mathbf{B}^J \mathbf{u} \tag{4.35}$$

where $\mathbf{B}^J$ are the strain-displacement matrices (Eq. 4.3). Based on the recurrence relation there are special rules to get the derivative of a spline function. However, for the current formulation and purpose, the usual derivation as known for polynomials is also convenient and leads to

$$
\begin{aligned}
\mathbf{B}^I &= \left[ \begin{array}{ccc} \frac{2x}{h^2} - \frac{2}{h} &, & -\frac{3x}{h^2} + \frac{2}{h} &, & \frac{x}{h^2} \end{array} \right] \\
\mathbf{B}^{II} &= \left[ \begin{array}{ccc} \frac{x}{h^2} - \frac{1}{h} &, & -\frac{2x^2}{h^2} + \frac{1}{h} &, & \frac{x}{h^2} \end{array} \right] \\
\mathbf{B}^{III} &= \left[ \begin{array}{ccc} \frac{x}{h^2} - \frac{1}{h} &, & -\frac{3x}{h^2} + \frac{1}{h} &, & \frac{2x}{h^2} \end{array} \right]
\end{aligned}
\tag{4.36}
$$

For building the element stiffness matrices the material matrix $\mathbf{C}$ is required. Here, in the one-dimensional case it is a scalar matrix $\mathbf{C} = [E]$ of Young's modulus $E$. The stress $\sigma$ (Eq. 4.4) is calculated by

$$\sigma(x) = \mathbf{C} \mathbf{B}^J \mathbf{u} \tag{4.37}$$

For the segment basis length $h$ and section area $A$ the integral (Eq. 4.7)

$$\mathbf{K} = A \int_0^h \mathbf{B}^{\mathrm{T}} \mathbf{C} \mathbf{B} \, dx \tag{4.38}$$

leads to the following element stiffness matrices of type $J = I$, $II$ and $III$.

$$
\mathbf{K}^I = \frac{EA}{h} \begin{bmatrix} \frac{4}{3} & -1 & -\frac{1}{3} \\ -1 & 1 & 0 \\ -\frac{1}{3} & 0 & \frac{1}{3} \end{bmatrix} \quad
\mathbf{K}^{II} = \frac{EA}{h} \begin{bmatrix} \frac{1}{3} & -\frac{1}{6} & -\frac{1}{6} \\ -\frac{1}{6} & \frac{1}{3} & -\frac{1}{6} \\ -\frac{1}{6} & -\frac{1}{6} & \frac{1}{3} \end{bmatrix} \quad
\mathbf{K}^{III} = \frac{EA}{h} \begin{bmatrix} \frac{1}{3} & 0 & -\frac{1}{3} \\ 0 & 1 & -1 \\ -\frac{1}{3} & -1 & \frac{4}{3} \end{bmatrix} \tag{4.39}
$$

### 4.4.3  Notes on Global Stiffness Matrix

For a bar example the left boundary of the bar is modeled by element type I and the right boundary by element type III. All elements in between are of type II. It is important

to note, that all shape functions of the B-Spline are not directly associated with nodal values or nodes. It is rather useful to regard a shape function as part of an element only. To establish the continuity of the displacement solution as required, it has to be ensured that the shape function segments of one B-Spline will be associated with the same global degree of freedom. In three neighboring elements (as in Fig. 4.3) the segment (c) of the left element, the segment (b) of the middle element and the segment (a) of the right element correspond to one and the same B-Spline shape function and need therefore to be associated to the same global degree of freedom.

### 4.4.4 Example: Homogeneous B-Spline Bar Elements of Order $k{=}2$

The following example provides a clear and transparent access to the presented method of B-spline finite elements. It can be included into any introductory course on finite elements. Moreover, this example highlights some characteristics of B-spline finite elements and therefore prepares for further developments of these elements.

The stiffness matrix $\boldsymbol{K}$ of four B-Spline finite elements without consideration of displacement boundary conditions is composed of $\boldsymbol{K}^{I}$, $\boldsymbol{K}^{II}$ and $\boldsymbol{K}^{III}$ as

$$
\boldsymbol{K} = \frac{EA}{h}
\begin{bmatrix}
\frac{4}{3} & -1 & -\frac{1}{3} & 0 & 0 & 0 \\
-1 & 1+\frac{1}{3} & -\frac{1}{6} & -\frac{1}{6} & 0 & 0 \\
-\frac{1}{3} & -\frac{1}{6} & \frac{1}{3}+\frac{1}{3}+\frac{1}{3} & -\frac{1}{6}-\frac{1}{6} & -\frac{1}{6} & 0 \\
0 & -\frac{1}{6} & -\frac{1}{6}-\frac{1}{6} & \frac{1}{3}+\frac{1}{3}+\frac{1}{3} & -\frac{1}{6} & -\frac{1}{3} \\
0 & 0 & -\frac{1}{6} & -\frac{1}{6} & \frac{1}{3}+1 & -1 \\
0 & 0 & 0 & -\frac{1}{3} & -1 & \frac{4}{3}
\end{bmatrix}
\tag{4.40}
$$

For best transparency of the method an academic example of simple system parameters without dimension is chosen. Length of the beam according to Fig. 4.4(a) is 4. Young's modulus $E$ and area of section $A$ are both set to 1, such that the factor $\frac{EA}{h} = 1$. The displacement boundary condition of the left end leads to elimination of first line and column of the matrix (Eq. 4.40) and therefore to

$$
\boldsymbol{K} =
\begin{bmatrix}
\frac{4}{3} & -\frac{1}{6} & -\frac{1}{6} & 0 & 0 \\
-\frac{1}{6} & 1 & -\frac{1}{3} & -\frac{1}{6} & 0 \\
-\frac{1}{6} & -\frac{1}{3} & 1 & -\frac{1}{6} & -\frac{1}{3} \\
0 & -\frac{1}{6} & -\frac{1}{6} & \frac{4}{3} & -1 \\
0 & 0 & -\frac{1}{3} & -1 & \frac{4}{3}
\end{bmatrix}
\quad
\boldsymbol{u} =
\begin{bmatrix}
0.5 \\ 1.5 \\ 2.5 \\ 3.5 \\ 4.0
\end{bmatrix}
\quad
\boldsymbol{f} =
\begin{bmatrix}
0 \\ 0 \\ 0 \\ 0 \\ 1
\end{bmatrix}
\tag{4.41}
$$

For system of Fig. 4.4(a) with the load $F = 1$ the load vector $\boldsymbol{f}$ is straightforward to construct. The solution of the equations system $\boldsymbol{Ku} = \boldsymbol{f}$ leads to $\boldsymbol{u}$ as provided above (Eq. 4.41). The composition of the linear displacement field by the B-spline shape functions according to this example is shown in Fig. 4.5.
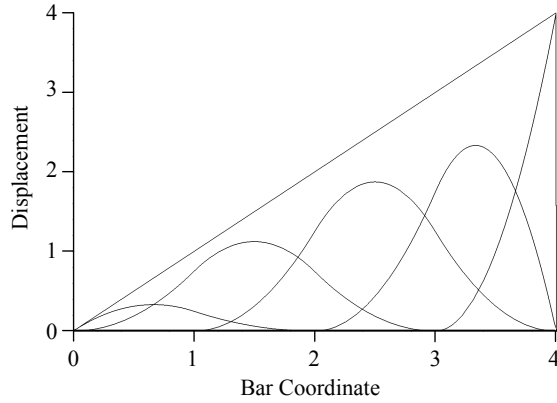
Figure 4.4: Static systems of a bar problem: (a) a bar loaded by $F$ and (b) bar with constant line load $p$.



Figure 4.5: B-Spline shape functions and displacement solution according to system in Fig. 4.4(a).
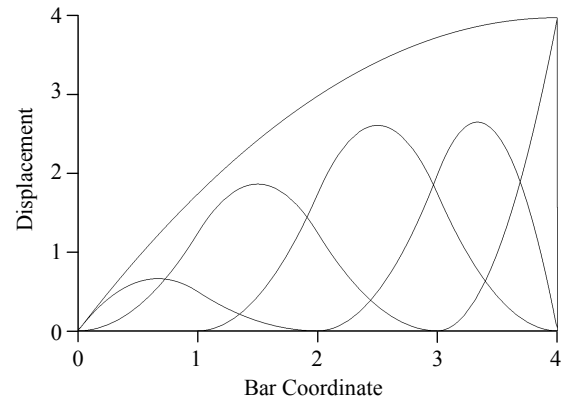
Figure 4.6: B-Spline shape functions and displacement solution according to system in Fig. 4.4(b).

A further example with the same structural parameters and stiffness matrix with constant line load $p$ as shown in Fig. 4.4(b) follows. The effective load associated to the segments of one element is the result of the integral (Eq. 4.8)

$$\boldsymbol{f} = \int_{x=0}^{h} \boldsymbol{N}^{\mathrm{T}} p(x) \mathrm{dx} \tag{4.42}$$

For a constant load of $p = 0.5$, the load function can be extracted from the integral, such that only the following integrals are relevant.

$$
\begin{aligned}
\int_{x=0}^{h} \boldsymbol{N}^{I} \ \mathrm{dx} &= \left[ \begin{array}{ccc} \frac{h}{3} & , & \frac{h}{2} & , & \frac{h}{6} \end{array} \right] \\
\int_{x=0}^{h} \boldsymbol{N}^{II} \ \mathrm{dx} &= \left[ \begin{array}{ccc} \frac{h}{6} & , & \frac{2h}{3} & , & \frac{h}{6} \end{array} \right] \\
\int_{x=0}^{h} \boldsymbol{N}^{III} \ \mathrm{dx} &= \left[ \begin{array}{ccc} \frac{h}{6} & , & \frac{h}{2} & , & \frac{h}{3} \end{array} \right]
\end{aligned}
\tag{4.43}
$$

Again, segments which belong to the same global degree of freedom are associated, such that the following load vector $\boldsymbol{f}$ and solution $\boldsymbol{u}$ to this problem is obtained.

$$\boldsymbol{f} = \left[ \begin{array}{ccccc} \frac{1}{3} & \frac{1}{2} & \frac{1}{2} & \frac{1}{3} & \frac{1}{6} \end{array} \right]^{\mathrm{T}}, \qquad \boldsymbol{u} = \left[ \begin{array}{ccccc} 1.0 & 2.5 & 3.5 & 4.0 & 4.0 \end{array} \right]^{\mathrm{T}} \tag{4.44}$$

As further explanation the first entry of $\boldsymbol{f}$ sums up from a segment b of type I and a segment a of type II, which is $\frac{1}{2} + \frac{1}{6} = \frac{2}{3}$ and multiplied by $p = 0.5$ results in $0.5\frac{2}{3} = \frac{1}{3}$. The displacement solution is graphed in Fig. 4.6. It corresponds to the exact analytical solution (Eq. 3.10), $EAU_{,xx} + p = 0$ with $U(x = 0) = 0$ and $\sigma(x = 4) = 0$, therewith $U = -\frac{1}{4}x^2 + 2x$.

## 4.5   Two-Dimensional B-Spline Finite Elements

### 4.5.1   Local Interpolation Scheme

The following method is formulated for orthogonal, two-dimensional meshes with uniform grid space $h_x$ and $h_y$ in $x$- and $y$-direction respectively. Initially, uniform, univariate B-splines of order $k$ are generated. The required minimum size of the domain corresponds to $(2k-1)$ grid intervals in both directions (Section 4.3.4). Subsequently, the uniform B-splines are scaled according to grid spaces $h_x$ and $h_y$ (Eq. 4.27). Bivariate B-splines result from the tensor product (Höllig 2003).

$$b^{j_x,j_y}(x,y) = b^{j_x}(x)\, b^{j_y}(y) \tag{4.45}$$

The superscripts $j_x$ and $j_y$ signify that various element types are used, such as in the one-dimensional case (Section 4.4.1). With respect to computational implementation it is not reasonable to explicitly build the bivariate B-splines in symbolic form, when it is sufficient to calculate discrete values of $b^{j_x,j_y}(x,y)$. Then, it is more efficient with respect to memory storage and number of operations to evaluate the factors $b^{j_x}(x)$ and $b^{j_y}(y)$, and apply these discrete values to Eq. 4.45 to obtain $b^{j_x,j_y}(x,y)$. Bivariate B-splines as shape functions of two-dimensional finite elements are shown in Fig. 4.7.
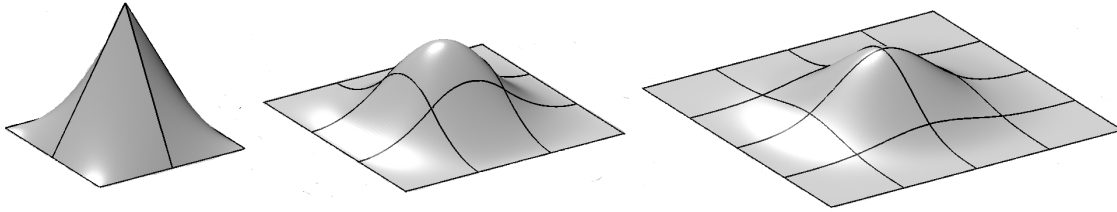


Figure 4.7: Bivariate B-spline finite element shape functions: $k$=1, $k$=2 and $k$=3 (from left to right).

### 4.5.2   Element Stiffness Matrices

Similar to the one-dimensional case and as stated by the kinematics, derivatives of the shape functions $b^{j_x,j_y}(x,y)$ need to be computed. To obtain these partial derivatives at discrete coordinates it is convenient to reuse the principle of Eq. 4.45 in the following form.

$$\frac{\partial b^{j_x,j_y}(x,y)}{\partial x} = \frac{\partial (b^{j_x}(x)\, b^{j_y}(y))}{\partial x} = \frac{\partial b^{j_x}(x)}{\partial x}\, b^{j_y}(y) \tag{4.46}$$

$$\frac{\partial b^{j_x,j_y}(x,y)}{\partial y} = \frac{\partial (b^{j_x}(x)\, b^{j_y}(y))}{\partial y} = b^{j_x}(x)\, \frac{\partial b^{j_y}(y)}{\partial y} \tag{4.47}$$

The interpolation matrices are created for individual elements which correspond to one grid patch. Analog to Eq. 4.32 this is

$$\boldsymbol{U} = \boldsymbol{N}^{j_x,j_y}\boldsymbol{u} \tag{4.48}$$

for the two-dimensional case with

$$U = \begin{bmatrix} U_x \\ U_y \end{bmatrix} \tag{4.49}$$

$$N^{j_x,j_y} = \begin{bmatrix} N_1 & \cdots & N_{\bar{n}} & & \mathbf{0} & \\ & \mathbf{0} & & N_1 & \cdots & N_{\bar{n}} \end{bmatrix}^{j_x,j_y} \tag{4.50}$$

$$u = \begin{bmatrix} u_{x,1} & \cdots & u_{x,\bar{n}} & u_{y,1} & \cdots & u_{y,\bar{n}} \end{bmatrix}^{\mathrm{T}} \tag{4.51}$$

Here, the index $\bar{n}$ denotes the number of bivariate spline segments in one element which corresponds to $\bar{n} = (k+1)^2$ or if the order of B-splines is different in $x$- and $y$-direction $\bar{n} = (k_x + 1)(k_y + 1)$. The superscripts $j_x$ and $j_y$ define the element type in $x$- and $y$-direction, respectively. The strain-displacement relationship is

$$\epsilon = B^{j_x,j_y} u \tag{4.52}$$

with the same degrees of freedom $u$ (Eq. 4.51) and

$$\epsilon = \begin{bmatrix} \epsilon_{xx} & \epsilon_{yy} & 2\epsilon_{xy} \end{bmatrix}^{\mathrm{T}} \tag{4.53}$$

$$B^{j_x,j_y} = \begin{bmatrix} \frac{\partial N_1}{\partial x} & \cdots & \frac{\partial N_{\bar{n}}}{\partial x} & & \mathbf{0} & \\ & \mathbf{0} & & \frac{\partial N_1}{\partial y} & \cdots & \frac{\partial N_{\bar{n}}}{\partial y} \\ \frac{\partial N_1}{\partial y} & \cdots & \frac{\partial N_{\bar{n}}}{\partial y} & \frac{\partial N_1}{\partial x} & \cdots & \frac{\partial N_{\bar{n}}}{\partial x} \end{bmatrix}^{j_x,j_y} \tag{4.54}$$

Recalling the constitutive law of plane stress (Eq. 3.9) yields the material matrix $C$ as

$$C = \frac{E}{1-\nu^2} \begin{bmatrix} 1 & \nu & 0 \\ \nu & 1 & 0 \\ 0 & 0 & \frac{1-\nu}{2} \end{bmatrix} \tag{4.55}$$

The stiffness matrices are evaluated by numerical integration

$$K^{j_x,j_y} = t \frac{h_x}{2} \frac{h_y}{2} \sum_{i=1}^{n_x} \sum_{j=1}^{n_y} w_{x,i} \, w_{y,j} \left( B^{j_x,j_y \, \mathrm{T}} C B^{j_x,j_y} \right) \tag{4.56}$$

where $t$ is the depth of the two-dimensional system. It is practical to substitute $C(E,\nu) = EC(1,\nu)$ and to build the element stiffness matrices for Young's modulus $E = 1$. Then the stiffness matrix can be adapted to any Young's modulus by a simple scalar factor. The variables $w_{x,i}$ and $w_{y,j}$ denote the weighting factors of the numerical integration scheme as described in the following Section 4.5.3.

## 4.5.3   Gauss-Legendre Numerical Integration of Variable Order

For a limited number of integration points the coordinates and weights of the Gauss-Legendre numerical integration can be taken from tables as given in e.g. (Bathe 1996). However, for a variable order $k$ of B-spline finite elements it is required to implement

the general scheme for a variable number of integration points. For a one-dimensional function $g(s)$ in the interval $[-1,1]$ the fundamental equation is

$$\int_{-1}^{1} g(s)\, ds \approx \sum_{i=1}^{n} w_i\, g(s_i) \tag{4.57}$$

where $w_i$ are the weights and $s_i$ are the coordinates of the integration points. An integration of $g(x)$ in the interval $[x_a, x_b]$ can be replaced by an integration of $g(s)$ in the interval $[-1,1]$

$$\int_{x_a}^{x_b} g(x)\, dx = \int_{-1}^{1} g(s)\, \det J\, ds \tag{4.58}$$

with the transformation of coordinates

$$x = \frac{1}{2}\left((x_b - x_a)\, s + x_a + x_b\right) \tag{4.59}$$

and the determinant of the Jacobian matrix

$$\det J = \frac{dx}{ds} = \frac{x_b - x_a}{2} \tag{4.60}$$

From Eqs. 4.57 to 4.60 it follows that a function $g(x)$ in an interval $[0, h]$ is numerically integrated as follows

$$\int_{0}^{h} g(x)\, dx \approx \frac{h}{2} \sum_{i=1}^{n} w_i\, g\left(\frac{h}{2}\,(1 + s_i)\right) \tag{4.61}$$

The coordinates of the integration points $s_i$ correspond to the zero points of the Legendre polynomials in the interval $[-1; 1]$. The Legendre polynomials can be generated by the following recursion as documented in (Duschek 1961)

$$P_{n+1}(s) = \frac{2n+1}{n+1} s P_n(s) - \frac{n}{n+1} P_{n-1}(s) \tag{4.62}$$

where the Legendre Polynomials $P_0(s) = 1$ and $P_1(s) = s$ are used as start values. There is no closed-form solution to obtain the $n$ zero points of $P_n(s)$, but the following lower and upper estimates of $s_i$ are available.

$$-\cos\left(\frac{n-0.5}{i+0.5}\pi\right) < s_i < -\cos\left(\frac{n}{i+0.5}\pi\right) \qquad \text{for} \quad i = 1, \ldots, n \tag{4.63}$$

There is always exactly one coordinate $s_i$ in the intervals of Eq. 4.63. For the search of this zero point within a closed interval the bisection method is applied. As an alternative the more efficient, but apparently less stable Newton method shall be mentioned.

The weights $w_i$ of the integration points $s_i$ are determined by

$$w_i = \frac{2}{n P_{n-1}(s_i) \dfrac{dP_n(s_i)}{ds}} \tag{4.64}$$

The integration points are symmetric to the origin and the corresponding weighting factors are equal. Therefore the numerical effort can be reduced to one symmetric half. Clearly, for a odd number of integration points, one is located at the origin.

An application of the one-dimensional integration formula (Eq. 4.61) to the $x-$ and $y$-coordinate successively, transforms the symbolic integral for evaluating the element stiffness matrix (Eq. 4.7) into its numerical counterpart as given in Eq. 4.56. For B-spline shape functions of order $k$ the integrands in Eq. 4.56 will at maximum be a polynomial of order $2k$ with respect to either $x$ or $y$. For the one-dimensional case $n$ integration points exactly integrate a polynomial of at most order $(2n - 1)$ such that in one dimension $n = k + 1$ integration points would be required. In two dimensions this corresponds to an (unequally spaced) grid of $n \times n$ integration points.

## 4.5.4 Global Formulation of B-Spline Finite Element Problem

A uniform, orthogonal, two-dimensional mesh of B-spline finite elements of variable order $k$ is considered. The mesh includes $n_{ex} \times n_{ey}$ elements and $n_{nx} \times n_{ny}$ nodes. The global degrees of freedom are split[2] into $x$-and $y$-direction and the following numbering system refers to one direction only. Then, without activating displacement boundary conditions, there are $n_{sx} \times n_{sy}$ B-spline coefficients[3] assigned to the global mesh. The local degrees of freedom in one element correspond to $n_{cx} \times n_{cy}$ B-spline coefficients. For these definitions the following equalities hold

$$n_{nx} = n_{ex} + 1\,, \qquad\qquad n_{ny} = n_{ey} + 1\,, \qquad\qquad (4.65)$$

$$n_{sx} = n_{ex} + k\,, \qquad\qquad n_{sy} = n_{ey} + k\,, \qquad\qquad (4.66)$$

$$n_{cx} = k + 1\,, \qquad\qquad n_{cy} = k + 1\,, \qquad\qquad (4.67)$$

The numbering of elements $i_{eg}$, nodes $i_{ng}$, global B-spline coefficients $i_{sg}$ and local B-spline coefficients $i_{cg}$ of an element can be defined as

$$i_{eg}(i,j) = i + jn_{ex} \qquad \text{with} \qquad i = 0 \ldots n_{ex} - 1, \qquad j = 0 \ldots n_{ey} - 1, \qquad (4.68)$$

$$i_{ng}(i,j) = i + jn_{nx} \qquad \text{with} \qquad i = 0 \ldots n_{nx} - 1, \qquad j = 0 \ldots n_{ny} - 1, \qquad (4.69)$$

$$i_{sg}(i,j) = i + jn_{sx} \qquad \text{with} \qquad i = 0 \ldots n_{sx} - 1, \qquad j = 0 \ldots n_{sy} - 1, \qquad (4.70)$$

$$i_{cg}(i,j) = i + jn_{cx} \qquad \text{with} \qquad i = 0 \ldots n_{cx} - 1, \qquad j = 0 \ldots n_{cy} - 1, \qquad (4.71)$$

where the universal variables $i$ and $j$ count the various entities in positive $x$- and $y$-direction, respectively. In adaption to the implementation the count variables start by 0. At the corners of element $(i, j)$ there are the nodes $(i, j)$, $(i+1, j)$, $(i+1, j+1)$ and $(i, j+1)$. Accordingly the local B-spline shape coefficients in element $(i, j)$ refer to the global B-spline coefficients $(i \ldots i + k, \ j \ldots j + k)$. Therefore, the assignment of local B-spline coefficients $(i^*, j^*)$ of an element $(i, j)$ into the global vector of B-spline coefficients $i_{sg}$ is defined as

$$i_{sg}(i, j, i^*, j^*) = (i + i^*) + (j + j^*)n_{sx} \qquad\qquad (4.72)$$

$$\text{with } i = 0 \ldots n_{ex} - 1\,, \ j = 0 \ldots n_{ey} - 1\,, \ i^* = 0 \ldots k\,, \ j^* = 0 \ldots k$$

---

[2]Similar as in the local degrees of freedom of Eq. 4.51

[3]In this context *B-spline coefficient* is used as illustrative synonym to *degree of freedom*.

As for a one-dimensional example where e.g. $j = 0$ and $j^* = 0$ with $k = 2$ this means that segment $i^* = 2$ of element $i = 0$, segment $i^* = 1$ of element $i = 1$ and segment $i^* = 0$ of element $i = 2$ are segments of one and the same B-spline $i_{sg} = 2$ (compare this to Section 4.4.3 and Fig. 4.3).

After the computation of all different element stiffness matrices, the assignment from local to global degrees of freedom as given by Eq. 4.72 provides a clear order to build the full singular global stiffness matrix. After that certain degrees of freedom need to be eliminated according to boundary conditions (Section 4.5.5).

However, one of the basic ideas of the present work is not to store a global stiffness matrix. This possibility is supported by the uniformity of B-spline shape functions and the resulting low number of varying element stiffness matrices. A corresponding scheme of an iterative solver method is outlined in Section 4.5.6. Nevertheless the defined order of entities and the global ordering according to Eq. 4.72 is maintained.

### 4.5.5   Boundary Conditions

With common finite elements boundary conditions are often treated in terms of nodal forces or nodal displacements only. In fact the underlying theory principally corresponds to that required for B-Spline finite elements. However, the characteristic of B-spline finite elements of order $k \geq 2$ that the values at nodes do not have a direct counterpart in the vector of unknowns require some more considerate treatment.

The required formulation to apply forces to the finite element system is already provided by Eq. 4.8. Analog to the element displacement vector Eq. 4.51 the element vector of forces is

$$\boldsymbol{f} = \left[ \begin{array}{ccc|ccc} f_{x,1} & \cdots & f_{x,\bar{n}} & f_{y,1} & \cdots & f_{y,\bar{n}} \end{array} \right]^{\mathrm{T}} \tag{4.73}$$

For the two-dimensional plane stress problem the vectors of body loads $\boldsymbol{p}_b$ and surface loads $\boldsymbol{p}_s$ are reduced by the dimension of depth and they are only functions of $x$ and $y$.

$$\boldsymbol{p}_b = \left[ \begin{array}{c} p_{bx} \\ p_{by} \end{array} \right] \qquad \text{and} \qquad \boldsymbol{p}_s = \left[ \begin{array}{c} p_{sx} \\ p_{sy} \end{array} \right] \tag{4.74}$$

The integrals of Eq. 4.8 are evaluated numerically as described in Section 4.5.3. The element forces can be assembled into the global vector of forces according to Section 4.5.4. The present implementation supports line forces along the edges of rectangular domains. With the modified B-splines towards the boundaries the definition of these loads principally corresponds to the one-dimensional case while still $x$- and $y$-direction need to distinguished.

Any polynomial load function $p_i(\xi)$ can be applied by defining a list of load terms $c_{i,j}\xi^j$, similar to Eq. 4.16, the result of which will be summed up. The variable $\xi$ is representative for a local, one-dimensional coordinate system of the considered edge.

Therefore it is obvious that also displacement conditions on corner points can directly be defined. With the definition of Eq. 4.70 the corresponding degrees of freedom of the four corners are

$$i_{sg}(0,0), \quad i_{sg}(n_{sx}-1,0), \quad i_{sg}(0,n_{sy}-1), \quad i_{sg}(n_{sx}-1,n_{sy}-1), \tag{4.75}$$

As further possibility only displacement conditions along the edges of the domain are considered in the following. A constant displacement along an edge which equals to 0 is straightforward to define as the degree of freedom of shape functions which are unequal to 0 at this edge needs to be set to 0. This is only possible through the introduction of the mentioned modified B-splines. The relevant degrees of freedom along the four edges are

$$i_{sg}(i,0)\,, \quad i_{sg}(n_{sx}-1,j)\,, \quad i_{sg}(i,n_{sy}-1)\,, \quad i_{sg}(0,j)\,, \tag{4.76}$$

with the range of $i$ and $j$ as in Eq. 4.70. Otherwise any polynomial displacement functions can be defined or approximated along the edges. This problem corresponds to the one-dimensional case. An equation system needs to be solved, where $n+k$ values of the predefined displacement function need to be evaluated to determine $n+k$ B-spline coefficients according to the definitions in Section 4.3.2. The $n+k$ function values are evaluated at equidistant coordinates along the edge in our approach. Other choices in the approximation of the displacement function are possible as described in Section 4.3.1. It is noted that also in this Section the applied numerical order referred to the full singular equation system as given in Eq. 4.12 such that the additional steps of Eq. 4.13 and Eq. 4.14 are required to solve for the unknowns.

## 4.5.6 Notes on Solving of B-Spline Finite Element Problem

As exemplified for one-dimensional B-spline finite elements (Section 4.4) a global stiffness matrix (e.g. Eq. 4.41) and therefore a linear equation system can be created which can be solved by any direct or iterative solver method. A global numbering system for two-dimensional B-splines finite element models is introduced in Section 4.5.4. It can either serve to build a global stiffness matrix or to solve the problem iteratively by local, element-based operations. The second option is proposed in the present work. Corresponding iterative solver methods are treated in Chapter 5. Some relevant notes with respect to B-spline finite elements are provided in the following. Any data which is required from the global stiffness matrix, as e.g. any specific entry or row, can be reconstructed on basis of the element stiffness matrices. As an essential key this is efficient by a fast access to a low number of different element stiffness matrices. Without the storage of a global stiffness matrix, the memory demand essentially reduces. In summary only a few number of vectors need to be stored, as itemized for bilinear finite elements in Section 5.11.1. The present implementation includes such a matrix-free application of the conjugate gradient method (Section 5.3.7) for two-dimensional B-spline finite elements of variable order $k$. Apart from some usual vector operations the conjugate gradient method only requires to compute the global matrix-vector product which can be performed by element-based operations (Section 5.9.1). For problems with many degrees of freedom ($> 1.0 \cdot 10^5$) the multigrid method (Section 5.4) represents a much more efficient solver method. However, the present implementation does not include the multigrid method for B-spline finite elements. It shall only be mentioned that Höllig et al. (2002) presented the multigrid method for web-splines (weighted extended B-splines). As an alternative option, it could be considered to implement B-splines finite elements into an existing multigrid environment with bilinear finite elements. Therefore Section 5.10.4 briefly discusses a transfer operator between a mesh of B-splines finite elements and a mesh of bilinear finite elements.

### 4.5.7   Example: Homogeneous Two-Dimensional Problem

In this example, the approximation quality of B-spline finite elements is evaluated with respect to variable order of B-splines (p-version) and variable size of elements (h-version). Therefore a sufficiently complex example had to be selected. The analytical solution is known such that the error analysis is accurate. The analytical solution of this example is

$$F = \mathrm{Re}\left((x + iy)^\eta\right) \tag{4.77}$$

where $F$ is the Airy function (Meleshko 2003), $i$ is the imaginary unit $i^2 = -1$ and Re means the real part of a complex number. Any valid solution to Airy's function $F$ follows the condition $\Delta\Delta F = 0$. The stresses are defined as

$$\sigma_{xx} = F_{,yy} \ , \qquad \sigma_{yy} = F_{,xx} \ , \qquad \sigma_{xy} = -F_{,xy} \tag{4.78}$$

These stresses are applied as boundary conditions in terms of load $p_x$ and $p_y$ to the system shown in Fig. 4.8. The load functions shown in Fig. 4.8 qualitatively correspond to Eq. 4.77 with $\eta = 5$ which is $F_{\eta=5} = x^5 + 10x^3y^2 + 5xy^4$. For $\eta = 5$ the analytical stress solution is

$$\sigma_{xx} = -20x^3 + 60xy^2 \ , \qquad \sigma_{yy} = 20x^3 - 60xy^2 \ , \qquad \sigma_{xy} = 60x^2y - 20y^3 \tag{4.79}$$

For the boundaries where either $x = 0$, $y = 0$, $x = 1$ or $y = 1$ it is straightforward to define the tractions $p_x$ and $p_y$ from these stresses. The inner potential energy $\Pi_i$ of the system is defined as

$$\Pi_i = \frac{1}{2} \int_{x=0}^{1} \int_{y=0}^{1} \boldsymbol{\sigma}^{\mathrm{T}} \boldsymbol{\epsilon} \, \mathrm{dx} \, \mathrm{dy} \tag{4.80}$$

For $\eta = 5$ the inner potential is $\Pi_i(\eta = 5) = 329\frac{1}{7}$. The inner potential of the finite element solution will be less, or equal in case it corresponds to the analytical solution.
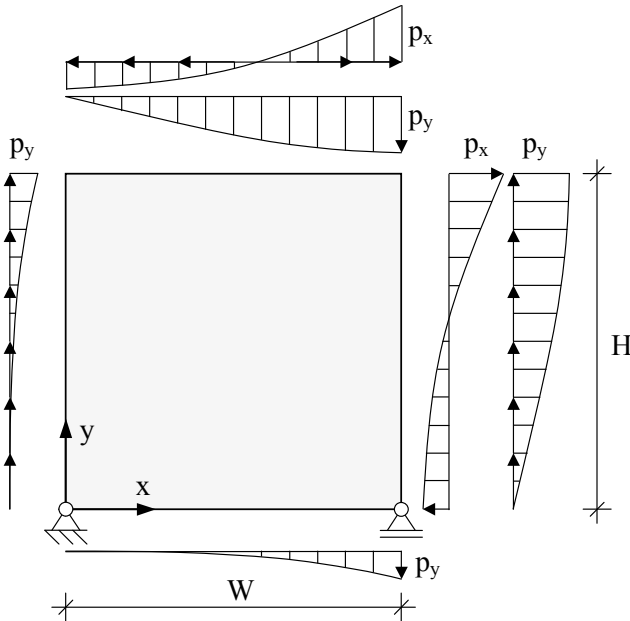


Figure 4.8: Homogeneous system with W=1 and H=1 under higher-order polynomial loads $p_x$ and $p_y$ along its boundaries.
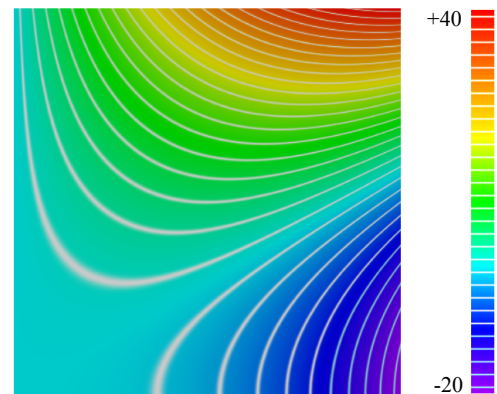
Figure 4.9: B-spline finite element solution of stress $\sigma_{xx}$ to problem of Fig. 4.8 for $k = 4$.
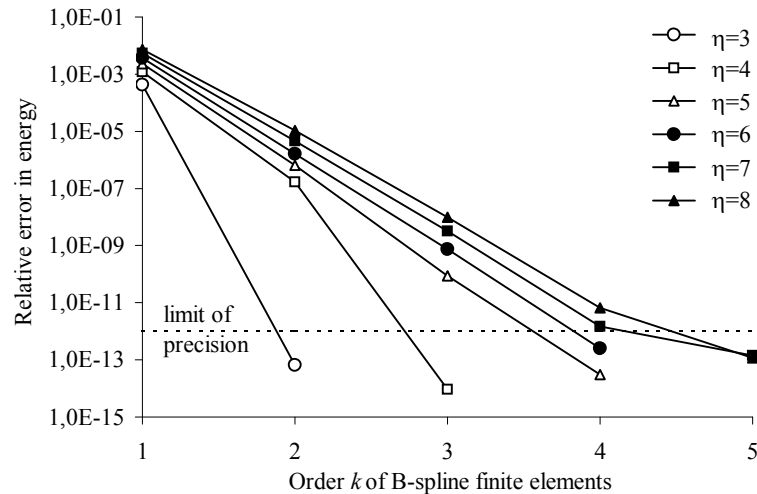
Figure 4.10: Convergence of error with respect to polynomial order $k$ for element size $h = \frac{8}{128}$
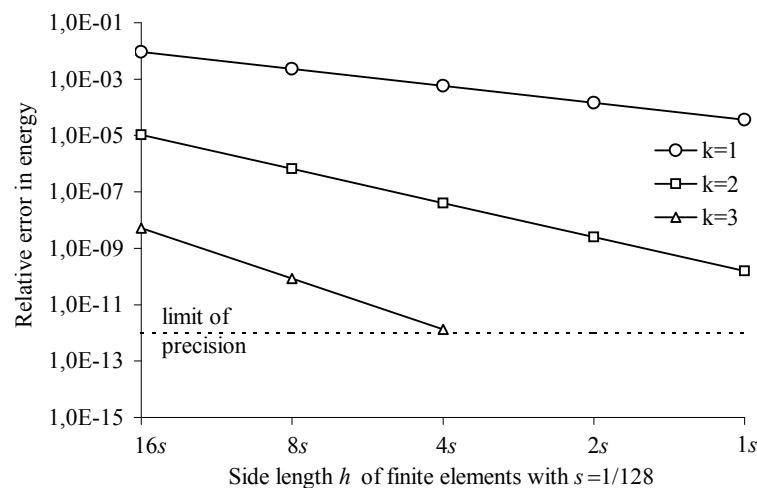


Figure 4.11: Convergence of error with respect to element size $h$ for the example $\eta = 5$

The relative error of the inner potential of the finite element solution to the analytical solution is a reference value for the accuracy of the finite elements. In Figs. 4.10 and 4.11 this error is labeled as relative error in energy. These diagrams show the convergence of this error with respect to order of B-splines $k$ (Fig. 4.10) and element size $h$ (Fig. 4.11).

It follows from these diagrams that it is much more efficient to decrease the error by an increase of polynomial order $k$ than by an increase of element number (or equivalent decrease of element size). It is a well known fact that the p-version is better for homogeneous problems than the h-version. This example shows that implementation of the proposed B-splines finite elements and the routine of defined higher-order polynomial load function is accurate. A limit of tolerance due to limited computational precision is carefully assigned to the dimension $10^{-12}$ of relative error in energy. Values below practically correspond to the exact solution. As for example for $\eta = 5$ the stress functions are at maximum of polynomial order 3, then the corresponding displacement function is at maximum of order 4. Therefore B-spline finite elements of the order $k = 4$ shall lead to the exact solution which is shown to be true in Fig. 4.10 (within the tolerance of precision). Figure 4.9 illustrates the corresponding solution of stress $\sigma_{xx}$.

According to (Zienkiewicz and Taylor 1997) some error convergence rate estimators are briefly outlined. Assuming that the exact displacement solution can be approximated by Taylor series, the displacement solution of the finite elements only include terms up to the order $k$. Then, the error only includes terms of the order $k + 1$ or higher. Therefore this error is estimated to converge by the order $O(h^{k+1})$. The strains are the first derivatives of the displacements such that the error in strains is assigned to one order below $O(h^k)$. Accordingly, an estimate of the convergence rate of the inner potential $\Pi_i$ (Eq. 4.80) leads to the order $O(h^{2k})$. For the example in Fig. 4.11, the convergence rate estimator is $O(h^2)$ for $k = 1$, $O(h^4)$ for $k = 2$ and $O(h^6)$ for $k = 3$, which fits quite well to the achieved results as illustrated in Table 4.1. Therefore without proof the results indicate that the convergence rate estimator is also applicable to B-spline finite elements of variable order $k$.

| | Error(2h) / Error(h) | | | | |
|---|---|---|---|---|---|
| | a priori | $h = 8s$ | $h = 4s$ | $h = 2s$ | $h = 1s$ |
| $k = 1$ | 4 | 3.9904 | 3.9973 | 3.9992 | 3.9998 |
| $k = 2$ | 16 | 16.043 | 16.012 | 16.003 | 16.003 |
| $k = 3$ | 64 | 60.710 | 63.577 | - | - |

Table 4.1: Convergence rates with respect to the results presented in Fig. 4.11.

# 4.6 Multiphase Finite Element Concept for Heterogeneous Solids

## 4.6.1 Mechanical Problem with Material Discontinuity and Substitute Problem with Continuous Material Function

The multiphase finite element concept is introduced for the mechanical analysis of heterogeneous solids. Before evaluating the corresponding finite element formulation, it is useful to show the main characteristics of the fundamental mechanical theory with respect to heterogeneous materials. Furthermore the original mechanical problem of heterogeneous material will be substituted by a transformed problem which will also converge to the exact solution while it initially appears less effective. However, it will be shown that this transformation cures a severe defect of the multiphase finite element solution, while the induced error by the substitute problem is comparatively low.

As a principle example of a heterogeneous material, in Fig. 4.12 an inclusion ($\Omega_1$) in a matrix material ($\Omega_2$) is shown. Without the inclusion, the illustrated problem corresponds to the boundary value problem of linear elasticity as stated in Section 3.2. Additional compatibility conditions can be formulated for the rigid bonded interface between $\Omega_1$ and $\Omega_2$ which is denoted as $\Gamma_{12}$. Rigid bond is expressed by $\boldsymbol{U}^1 = \boldsymbol{U}^2$ on $\Gamma_{12}$ where the superscript $i$ refers to the domain $\Omega_i$. In terms of stresses and strains, the compatibility conditions are

$$\sigma_{nn}^1 = \sigma_{nn}^2, \qquad \sigma_{nt}^1 = \sigma_{nt}^2, \qquad \epsilon_{tt}^1 = \epsilon_{tt}^2, \qquad \text{on } \Gamma_{12} \tag{4.81}$$
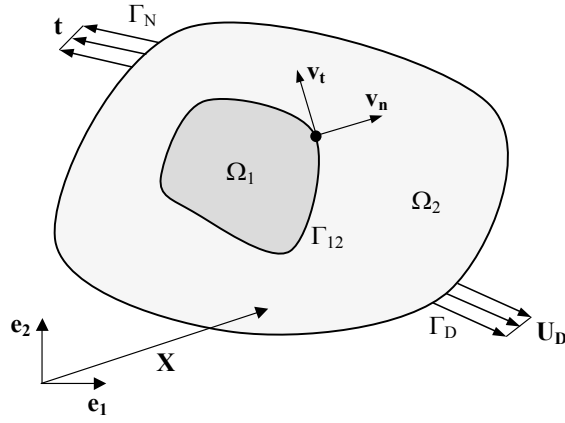
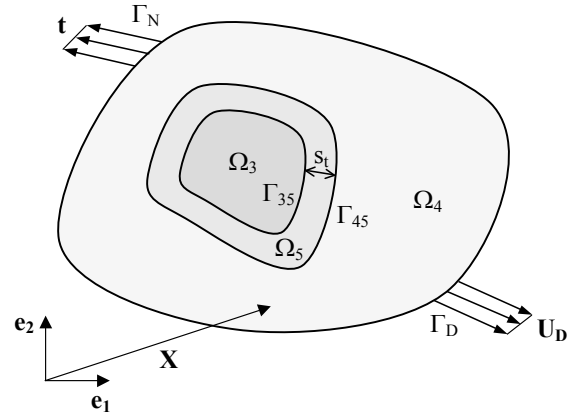Figure 4.12: Original problem with discontinuity of material

Figure 4.13: Substitute problem with continuous material

where the indices $n$ and $t$ correspond to the normal and tangential directions of the interface, $\boldsymbol{v}_n$ and $\boldsymbol{v}_t$ on $\Gamma_{12}$, as sketched in Fig. 4.12. Invoking the constitutive relationship of plane stress (Section 3.2.2) leads to

$$\epsilon_{nn}^i = \frac{1 - \nu_i^2}{E_i}\sigma_{nn} - \nu_i\epsilon_{tt} \tag{4.82}$$

$$\sigma_{tt}^i = \nu_i\sigma_{nn} + E_i\epsilon_{tt} \tag{4.83}$$

$$\epsilon_{nt}^i = \frac{1 + \nu_i}{E_i}\sigma_{nt} \tag{4.84}$$

which highlights that (in combination with Eq. 4.81) apart from some possible exceptions for different materials ($E_1 \neq E_2$ and/or $\nu_1 \neq \nu_2$), the following inequalities may occur

$$\epsilon_{nn}^1 \neq \epsilon_{nn}^2 , \qquad \epsilon_{nt}^1 \neq \epsilon_{nt}^2 , \qquad \sigma_{tt}^1 \neq \sigma_{tt}^2 , \qquad \text{on } \Gamma_{12} \tag{4.85}$$

For the subsequent approach it is especially important to note that some strains will not be continuous at a material discontinuity. However, the B-spline basis of the introduced finite elements for a polynomial order of $k \geq 2$ is always continuous in its derivatives and therefore only enables continuous strain fields. This discrepancy of continuity or discontinuity as described would lead to a severe defect if the B-Spline finite element method is applied to the original problem (Fig. 4.12).

Instead, a transformed problem is introduced (Fig. 4.13). The discontinuous material field is approximated by a smooth, continuous material field. The following conditions are introduced.

$$\Omega_3 \subset \Omega_1 , \qquad \Omega_4 \subset \Omega_2 , \tag{4.86}$$

with

$$E_3 = E_1 , \qquad E_4 = E_2 , \qquad \nu_3 = \nu_1 , \qquad \nu_4 = \nu_2 , \tag{4.87}$$

The material in $\Omega_5$ is defined such that

$$E_5(\boldsymbol{X}) = E_3 \quad \text{and} \quad \nu_5(\boldsymbol{X}) = \nu_3 \qquad \text{on } \Gamma_{35} \tag{4.88}$$

$$E_5(\boldsymbol{X}) = E_4 \quad \text{and} \quad \nu_5(\boldsymbol{X}) = \nu_4 \qquad \text{on } \Gamma_{45} \tag{4.89}$$

The defined material transition in $\Omega_5$, as well as its boundaries $\Gamma_{35}$ and $\Gamma_{45}$, is assumed to be sufficiently smooth. The material transition in $\Omega_5$ is monotonic in a section perpendicular to $\Gamma_{35}$ or $\Gamma_{45}$. Then, with the definition that

$$s_t \longrightarrow 0 \tag{4.90}$$

which corresponds to

$$\Omega_3 \longrightarrow \Omega_1 \, , \qquad \Omega_4 \longrightarrow \Omega_2 \, , \tag{4.91}$$

a continuous substitute problem is generated which will converge to the original problem and therefore to the exact solution. However, for finite values of $s_t$, the width of the transition zone $\Omega_5$ (Fig. 4.13), all strains and stresses will be continuous in the substitute problem. The B-spline finite elements can well be applied to the substitute problem, as B-spline finite elements are effective in the approximation of smooth solutions.

## 4.6.2   Description of Multiphase Finite Elements

Finite element meshes which are aligned to phase boundaries are the conventional way to analyze heterogeneous materials. But aligned mesh generation can become very complex, especially with regard to irregular shapes and three-dimensional models. Alternatively, an unaligned projection on a grid of conventional finite elements is demonstrated in (Häfner, Eckardt, Luther and Könke 2006). It is possible to refine the discretization of the mesoscale geometry by multiphase finite elements (Steinkopff, Sautter and Wulf 1995; Zohdi 2001; Zohdi and Wriggers 2005) without increasing the number of elements or degrees of freedom.

In the preparation of an element stiffness matrix for each integration point $i$ the integrands $\bar{\boldsymbol{K}}_i^e$ will initially be prepared and stored for a Young's modulus $E = 1$ in matrix $\boldsymbol{C}$ (Eq. 4.56). Based on these parts $\bar{\boldsymbol{K}}_i^e$ the assembly of specific element stiffness matrices $e$ with different Young's modulus in each integration point $(E_1^e \ldots E_n^e)$ is very fast established by

$$\boldsymbol{K}^e(E_1^e \ldots E_n^e) = \sum_{i=1}^{n} E_i^e \, \bar{\boldsymbol{K}}_i^e \tag{4.92}$$

where in comparison to Eq. 4.56 the two sums have been reduced to one sum over $i = 1 \ldots n$ with $n = n_x n_y$. For finite elements of homogeneous material the order of the integrand only depends on the order of B-splines $k$ (Eq. 4.56). With both, the shape functions and material function, being polynomials, a higher number of integration points can be determined such that the integration will be exact (Section 4.5.3). Otherwise, if an element crosses an interface a higher number of integration points generally increases the integration accuracy. Fig. 4.14 illustrates the idea of an adapted, different number of integration points according to the material defined within the finite element.

It is pointed out that the evaluation of $\boldsymbol{K}^e$ as in Eq. 4.92 will increase the effort of the conjugate gradient method by means of the global matrix-vector product (Sections 4.5.6 and 5.9.1), but only for heterogeneous elements. The number of degrees of freedom does not increase.

By the combination of the multiphase concept and B-spline elements, the geometrical resolution and the approximation quality of each finite element can be controlled based
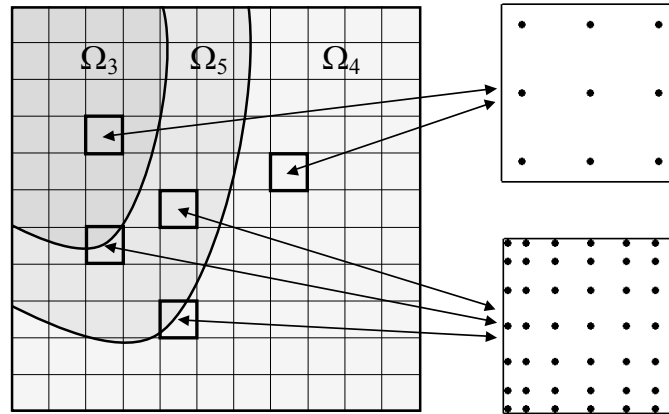
Figure 4.14: Adapted number of integration points in multiphase finite elements.

on an efficient local formulation. It is pointed out that only in combination with smoothing of the material function as defined by the substitute problem (Section 4.6.1) smooth stress solutions can be achieved. Otherwise, also with classical finite elements the multiphase concept leads to defective jumps in tractions along an material interface. Subsequently, some examples are introduced to test the proposed method in the Sections 4.6.3 to 4.6.6 and a final discussion of the overall error is found in Section 4.6.7.

## 4.6.3 Example: One-Dimensional Multiphase B-Spline Finite Elements

A one-dimensional example of a bar with material discontinuity is presented. The system corresponds to that of Fig. 4.15. The load function is $p(x) = \frac{1}{40}x - 0.5\frac{\text{kN}}{\text{cm}}$ and $F = 10\text{kN}$.
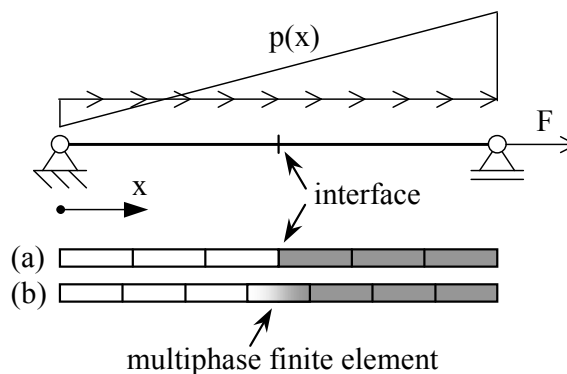


Figure 4.15: Bar system with material discontinuity and finite element discretizations

The length of the bar is 100 cm. The area of the section is constant 5 cm$^2$. A material discontinuity is located at the center of the bar at $x = 50$ cm. The Young's modulus of the left half ($0 \leq x < 50$ cm) is $E_1 = 3000\frac{\text{kN}}{\text{cm}^2}$ and that of the right half ($50 < x \leq 100$ cm) is $E_2 = 6000\frac{\text{kN}}{\text{cm}^2}$. The problem is analyzed by B-spline finite elements of order $k = 2$ in two variants. In the first example the bar is modeled by six B-spline finite elements. Three elements left of the material discontinuity obtain the parameter $E_1$ and three elements of the right the parameter $E_2$ (Fig. 4.15(a)). In the second example the bar is modeled by seven finite elements (Fig. 4.15(b)). The three left most and right most B-spline finite
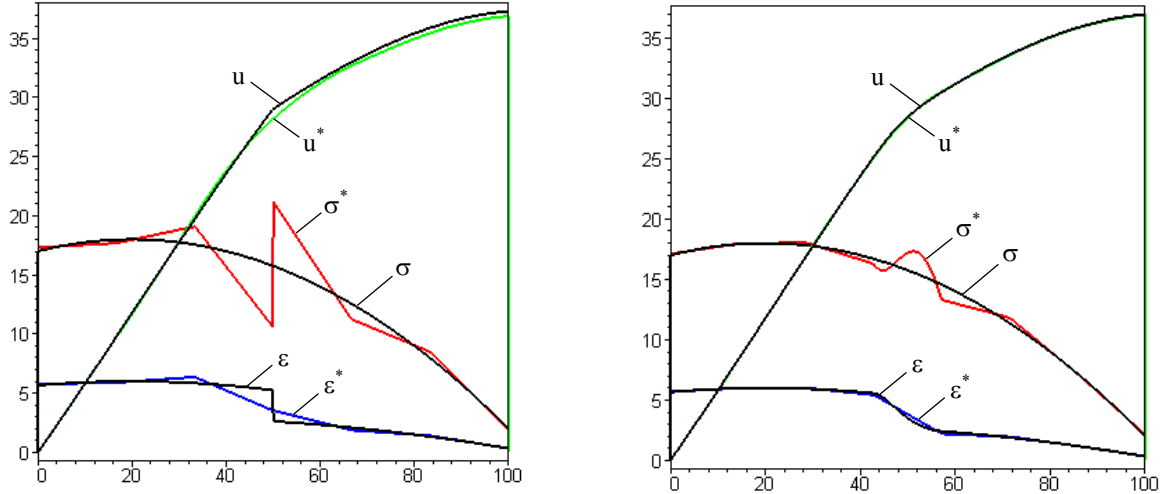
Figure 4.16: Analytical solutions and finite element solutions, marked by $^*$, for B-spline finite elements (left) and multiphase B-spline finite elements (right) for a loaded one-dimensional tension bar with material discontinuity (left) and linear material transition within one finite element (right) in terms of displacement $u$ (magnified by factor 100), strain $\epsilon$ (magnified by factor 1000) and stress $\sigma$.

elements are assigned to the parameters $E_1$ and $E_2$, respectively. In the center there is a multiphase B-spline finite element based on a linear material transition function from $E_1$ to $E_2$. The results of this example are shown in Fig. 4.16. In the variant of the multiphase element, it is visible that the stress solution is continuous and less deviating from the exact solution. Here, the exact solutions correspond to the original problem (Fig. 4.16, left) and to the transformed problem (Fig. 4.16, right).

### 4.6.4  Example: Elastic Circular Inclusion in a Matrix Based on Plain Grid Discretization

According to the provided theory on multiphase finite elements, an example of an elastic circular inclusion is introduced (Fig. 4.17). The inclusion and the matrix material are isotropic. The Young's modulus of the matrix is $E_{\mathrm{matrix}} = 100000$ and of the inclusion is $E_{\mathrm{inclusion}} = 200000$. The Poisson's ratio of both materials is $\nu_{\mathrm{matrix}} = \nu_{\mathrm{inclusion}} = 0.2$. The images of various grid discretizations of the spherical inclusions are shown in Fig. 4.18. The continuous material field, in terms of Young's modulus, is achieved by simple averaging of nodal values as illustrated in Figs. 4.19 and 4.20.

This example provides a basic study of the proposed method with respect to the mechanical analysis of materials with several inclusions as e.g. in concrete or other comparable heterogeneous solids. The example is well suitable as the analytical solution for a circular inclusion in an infinite plate is available. It is documented in (Kachanov, Shafiro and Tsukrov 2003). The defined ratio $16:1$ of plate dimension ($W, H$, in Fig. 4.17) to the diameter of the inclusion ($D$ in Fig. 4.17) is assumed to be an acceptable approximation to which the analytical solution fits. It is therefore regarded as reference solution to this example. Here, it shall only be noted that in the analytical solution the stress state within the inclusion is constant, e.g. for this example the stresses are $\sigma_{xx} = \frac{825}{68} \approx 12.132$ and $\sigma_{yy} = \frac{25}{68} \approx 0.3676$. The analytical solution of stress $\sigma_{xx}$ is shown in Fig. 4.22. The finite element solution of Model 2 with usual bilinear finite elements or, equivalent, B-spline
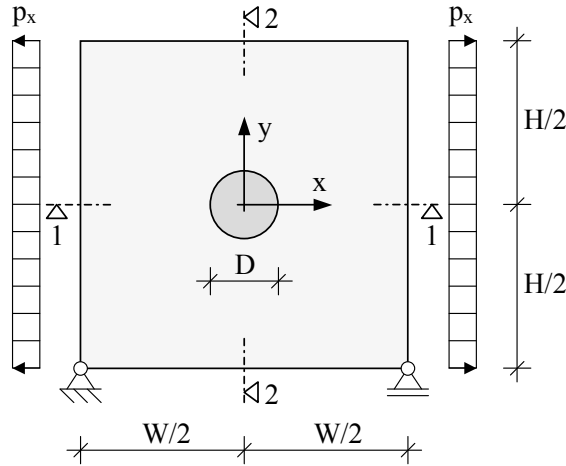
Figure 4.17: Two-dimensional solid with circular inclusion under uniaxial stress $p_x{=}10$ ($W{=}H{=}128$, $D{=}8$).
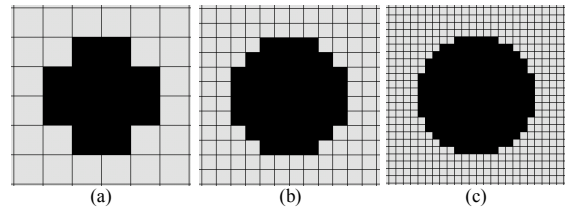


Figure 4.18: Pixel models labeled as (a) Model 1, (b) Model 2 and (c) Model 3.
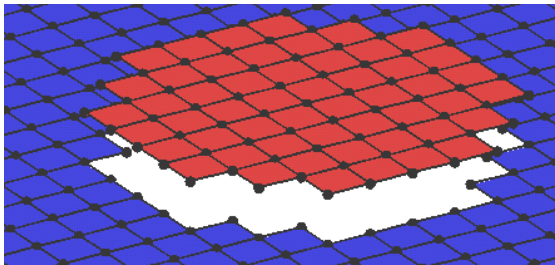


Figure 4.19: Isometric view on Young's modulus of two-dim. solid with grid discretization of circular inclusion
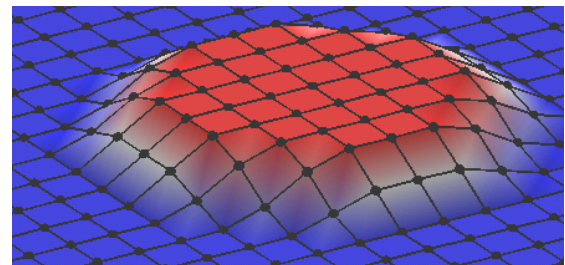


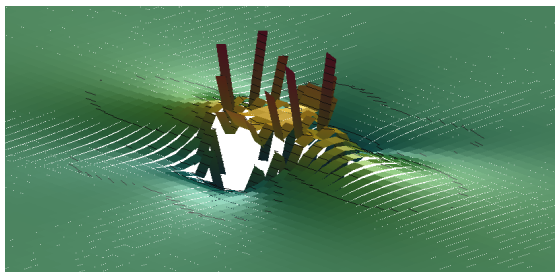Figure 4.20: Continuous Young's modulus by averaging of nodal values shown in Fig. 4.19



Figure 4.21: Stress $\sigma_{xx}$ of model in Fig. 4.19 by classical bilinear finite elements
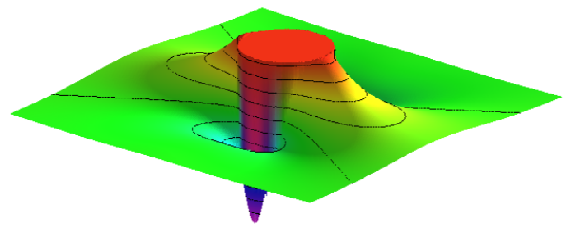


Figure 4.22: Analytical solution of stress $\sigma_{xx}$ for system of circular inclusion (Fig. 4.17)

finite elements of order $k = 1$ is shown in Fig. 4.21. In its comparison to the analytical solution it is visible by the naked eye that this finite element solution is severely defective along the grid-based material interface approximation. The same effect is observed for B-spline finite elements of order $k = 2$ (Fig. 4.23). However, the application of multiphase B-spline finite elements of order $k = 2$ in combination with the transformed model of Fig. 4.20 leads to an essentially improved solution. As expected the solution of stress is continuous according to the theory of the substitute problem (Section 4.6.1).

For a qualitative comparison of the discretization by multiphase B-spline finite elements of order $k = 2$ to the analytical solution with respect to variable resolution (Model 1 to 3) two sections are selected as illustrated in Fig. 4.17, labeled as sections 1-1 and 2-2.
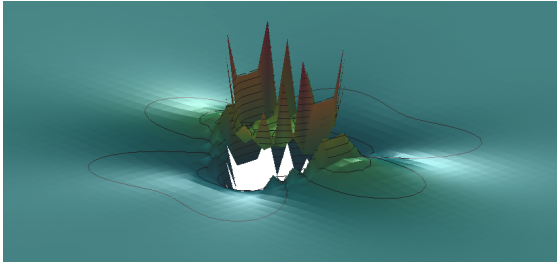
Figure 4.23: Stress $\sigma_{xx}$ of model in Fig. 4.19 by B-spline finite elements of order $k=2$
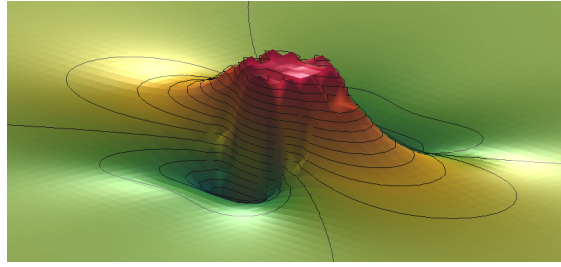


Figure 4.24: Stress $\sigma_{xx}$ of model in Fig. 4.20 by multiphase B-spline finite elements of order $k=2$

All Figs. 4.25 to 4.28 show that principally the correct dimension in the stresses is matched[4]. From Model 1 to Model 3 a slight improvement in accuracy can be seen in stress $\sigma_{xx}$ of Fig. 4.25. The evaluation of stress $\sigma_{xx}$ of Fig. 4.26 is less clear. On one hand there is an improvement in accuracy with respect to the minimum and on the other hand inaccuracies develop at the edges of the center plane. Fig. 4.27 shows that with increasing resolution the peaks in stress $\sigma_{yy}$ are approximated better. However, the development of stress $\sigma_{yy}$ in Fig. 4.28 with increasing resolution of the model is more difficult to interpret. There are parts of improved and worse approximation.

---

[4] In Figs. 4.25 to 4.28 only stress values at the corners of the elements are computed connected by linear functions.
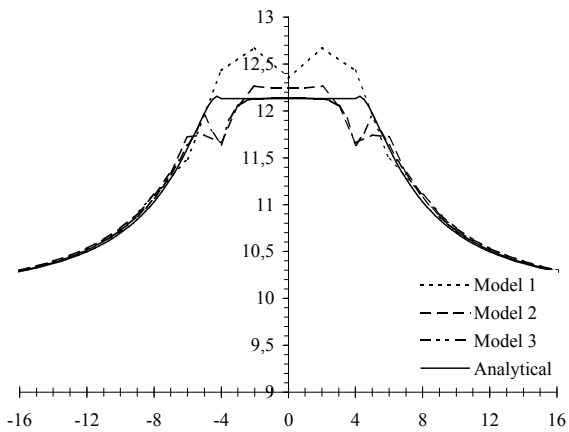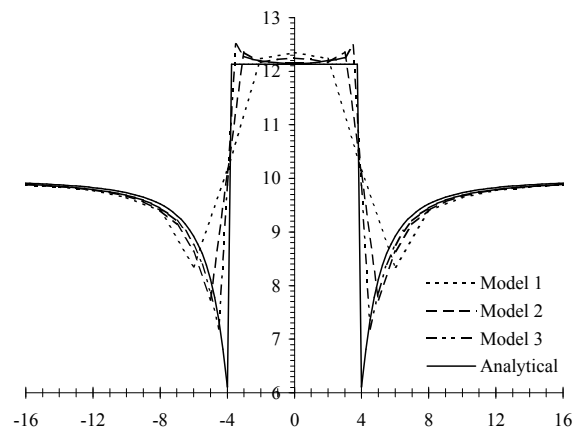


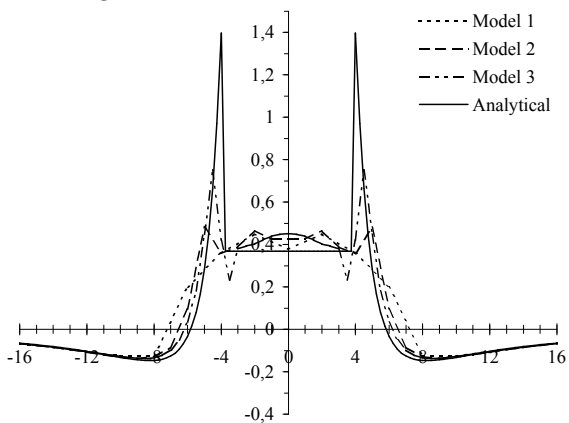Figure 4.25: Stress $\sigma_{xx}$ of section 1-1



Figure 4.26: Stress $\sigma_{xx}$ of section 2-2



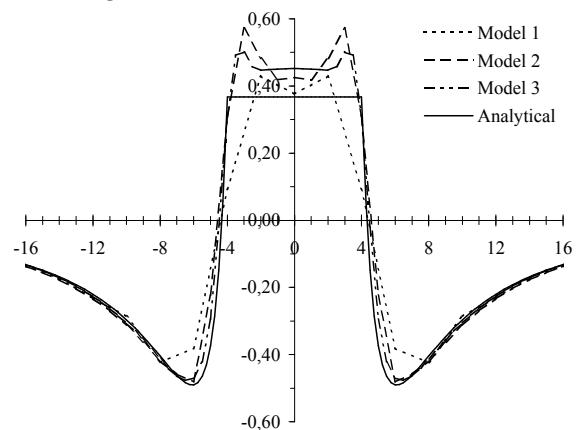Figure 4.27: Stress $\sigma_{yy}$ of section 1-1



Figure 4.28: Stress $\sigma_{yy}$ of section 2-2

Nevertheless, the major conclusion of this example is that the multiphase finite elements in combination with the transformed problem lead to reasonable results. This is quite a significant improvement with respect to the former grid discretization where the stresses are severely defective. This example demonstrates that the basic idea works in principle. But the achieved results did not lead to a clear conclusion how these models can further be improved. Therefore this aspect will be examined in the following examples.

## 4.6.5 Example: Elastic Circular Inclusion in a Matrix Based on Mapping of Geometry

This example is mostly identical to the prior example. The only, but essential difference is the effective description of the circle on the finite element mesh. In the foregoing example, first a plain grid discretization was generated where one finite element either belongs to the inclusion or to the matrix (Fig. 4.19). Then the material model was smoothed by averaging of nodal values (Fig. 4.20). The isolines which correspond to Model 2 (Fig. 4.20) are shown in Fig. 4.29(a). As an improved option the circular inclusion and a circular transition function (compare to $\Omega_5$ in Fig. 4.13) are mapped onto the centers of the elements, first. Then, the material properties of the nodes are computed as the averages of the neighboring element centers. This leads to a quite improved topology of material properties (Fig. 4.29(b)). It is interesting to note that this indirect method apparently leads to a more accurate geometrical representation than the direct mapping on the nodes with subsequent bilinear averaging within the finite elements (without illustration).

However, it is clear that some geometrical error is induced by any of these procedures which needs to be distinguished from the inherent approximation quality of multiphase B-spline finite elements. Therefore in this example the circle and the transition function are exactly mapped onto the integration points of the finite elements. This is only possible if an analytical description of the inclusion is available such as in this case of a circle. However, for other inclusion shapes such analytical functions are available as well (Section 2.2). The number of integration points is increased by 2 with respect to one dimension to cover the heterogeneous material within the finite element.



(a)                                                            (b)
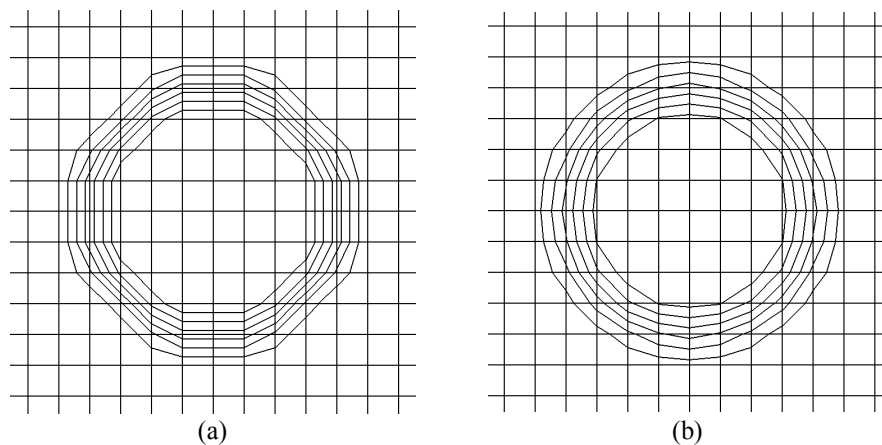
Figure 4.29: Isolines of material transition function of (a) model in Fig.4.20, (b) based on mapping of material function on element centers with subsequent interpolation at nodes.
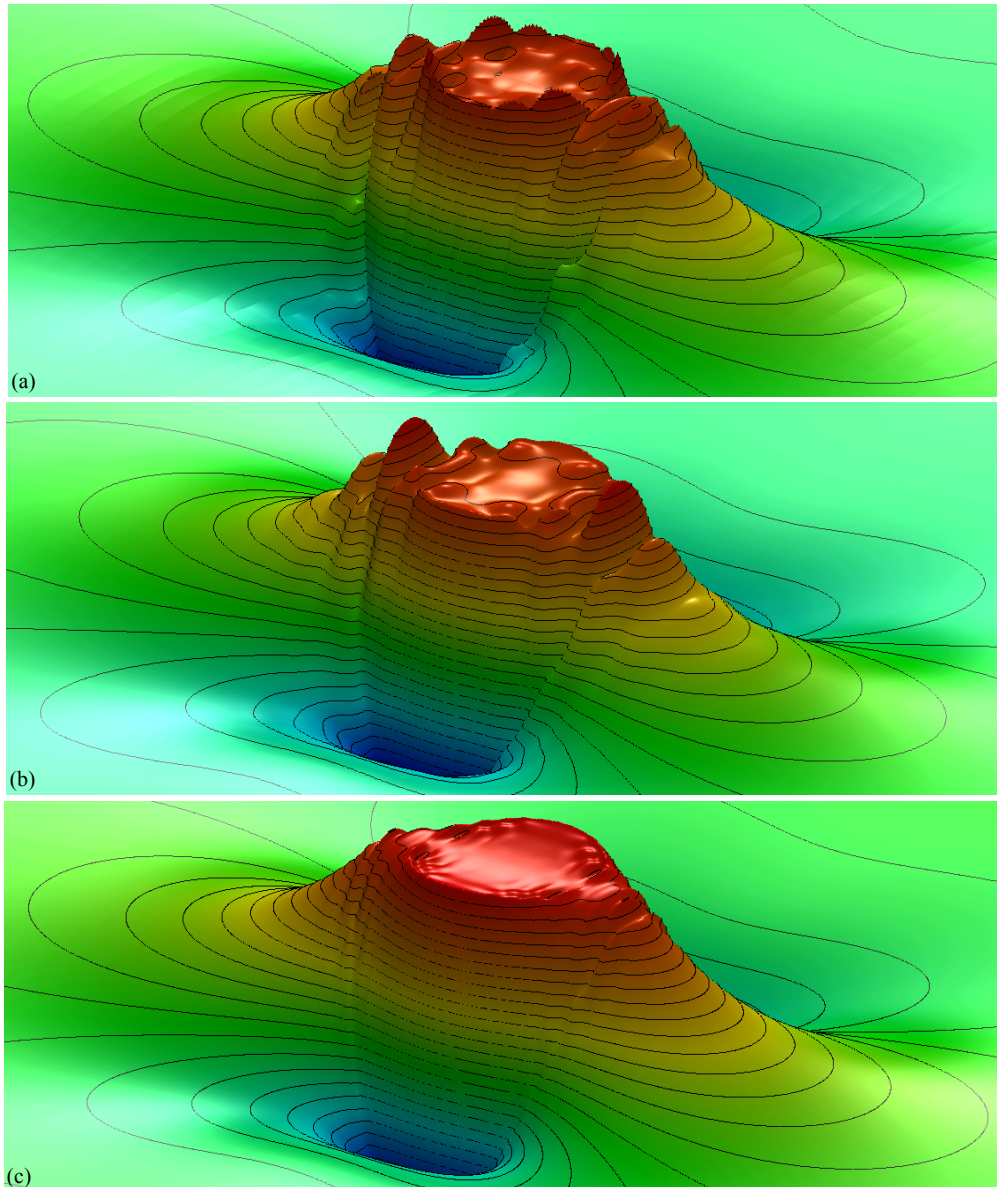
Figure 4.30: Stress solution $\sigma_{xx}$ of multiphase B-spline finite elements of order (a) $k = 2$, (b) $k = 3$ and (c) $k = 3$, finer mesh.

The basic aspect of this example is to analyze if an increase of element number (h-method) or element order $k$ (p-method) leads to improved results and shows clear convergence. Fig. 4.30(a) shows the solution of stress $\sigma_{xx}$ for multiphase B-splines of order $k = 2$. In Fig. 4.30(b) the order of the elements is $k = 3$. With a $C^2$-continuous material transition function and $C^2$-continuous B-spline finite elements this stress solution is not only $C^0$-, but $C^1$-continuous (in contrast to Fig. 4.30(a)). It appears smoother, but some defective oscillations are obvious. Halving the mesh size leads to the result of Fig. 4.30(c).

Qualitatively, this result is essentially improved. The increase of order $k$ had less visible effect. Therefore it is supposed that the h-version is more effective than the p-version for the heterogeneous case (in contrast to the homogeneous case, Section 4.5.7). From this example, it is evident that multiphase B-spline finite elements represent a promising alternative in modeling heterogeneous solids based on orthogonal grids. The required
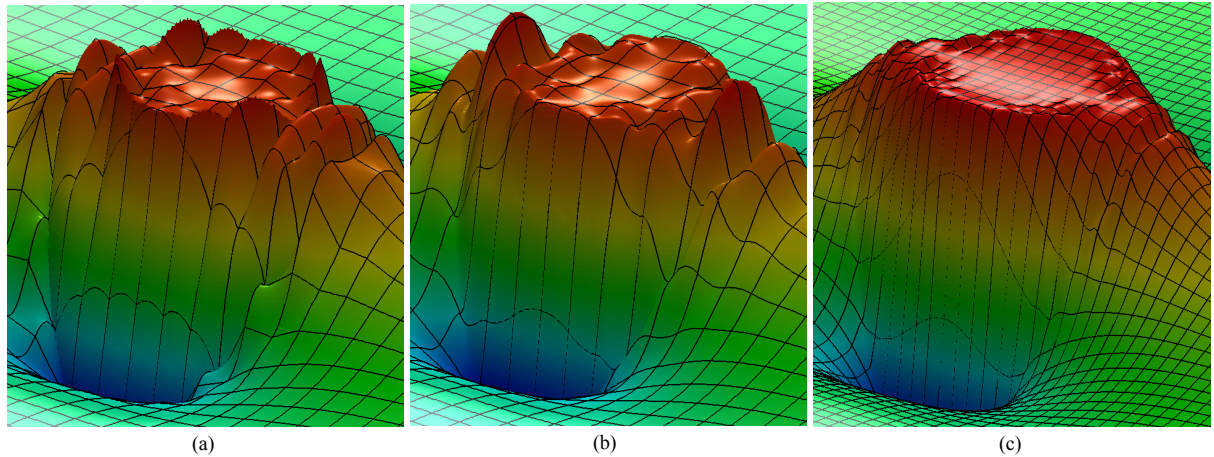
Figure 4.31: Stress $\sigma_{xx}$ as in Fig. 4.30, but magnified and with element grid (a to c correspond).

number of elements is also reasonable. The element resolution of Fig. 4.30 is shown in Fig. 4.31. For an effective use and better knowledge of this method further studies are performed in the following.

### 4.6.6 Example: Uniaxial Stress Case of One Material Transition

The focus of this example is the exact analysis of the defect in the stress solution for one material transition according to Fig. 4.32. It is a one-dimensional example but was computed by the two-dimensional implementation. The Poisson's ratio is set to zero for both materials. The parameter study includes a variation of material transition functions as is shown in Fig. 4.33. The linear function only generates a $C^0$-continuous transition. The continuity which results from the cubic function is $C^1$ and that of the quintic function is $C^2$. The material functions will be directly mapped onto the integration points of the finite elements. Furthermore a variation of element number and variation of element order $k$ is
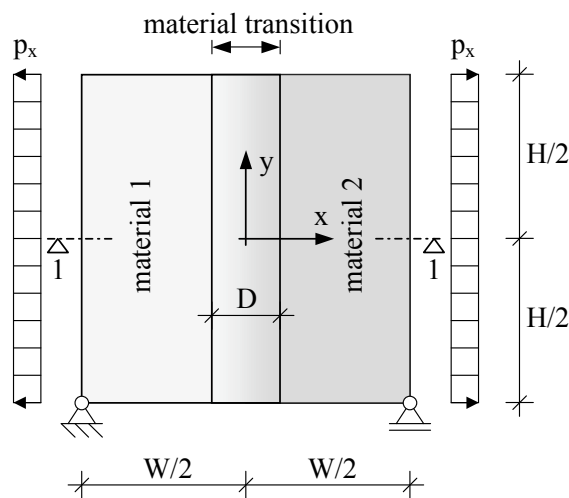


Figure 4.32: Two-dimensional solid with one material transition zone, $p_x = 1\frac{\text{N}}{\text{mm}^2}$, $W{=}H{=}128$mm, $D{=}16$mm.
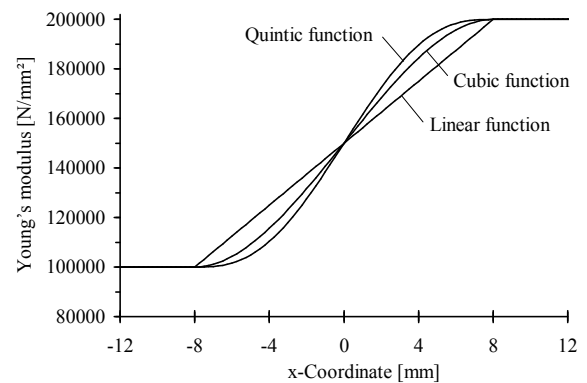


Figure 4.33: Various material transition functions for the system of Fig. 4.32

Figure 4.34: Stress $\sigma_{xx}$ in finite elements of Section 1-1 for $C^0$-continuous linear transition of Young's modulus and varying order $k$ of B-Spline finite elements.



Figure 4.35: Stress $\sigma_{xx}$ in finite elements of Section 1-1 for $C^1$-continuous cubic transition of Young's modulus and varying order $k$ of B-Spline finite elements.

examined. The finite element results will be analyzed in terms of error in stress and error in energy in comparison to the exact analytical solution.

The exact solution to this problem is $\sigma_{xx} = 1\frac{\text{N}}{\text{mm}^2}$ in the whole domain. Figs. 4.34 to 4.36 show the multiphase B-spline finite element solutions for a linear transition, a cubic transition and a quintic transition, respectively. Here, element size is constant $h = 4\text{mm}$. The varying parameter is the order $k$ of applied B-spline shape functions. Figure 4.34 shows a comparatively good solution for $k = 2$ and a change for the worse for $k = 3$. This can be explained as B-splines of order $k = 3$ are $C^2$-continuous while due to the linear transition function the exact solution to this problem in terms of displacement is only $C^1$-continuous. This leads to the significant peaks in the solution at the coordinates $x = -8$ and $x = 8$. Further increase of B-spline order $k$ does not cure this defect. Figure 4.35 shows a better solution in stress for $k = 3$ than for $k = 2$. The foregoing effect only occurs for $k = 4$, but is less severe. Again, a further increase of order $k$ does not lead to convergence.

Figure 4.36 is included to find out if a further increase of continuity in the material transition function would essentially increase the possible approximation quality with respect to an increase of $k$. In fact, then a relative good solution is achieved for $k = 5$, but
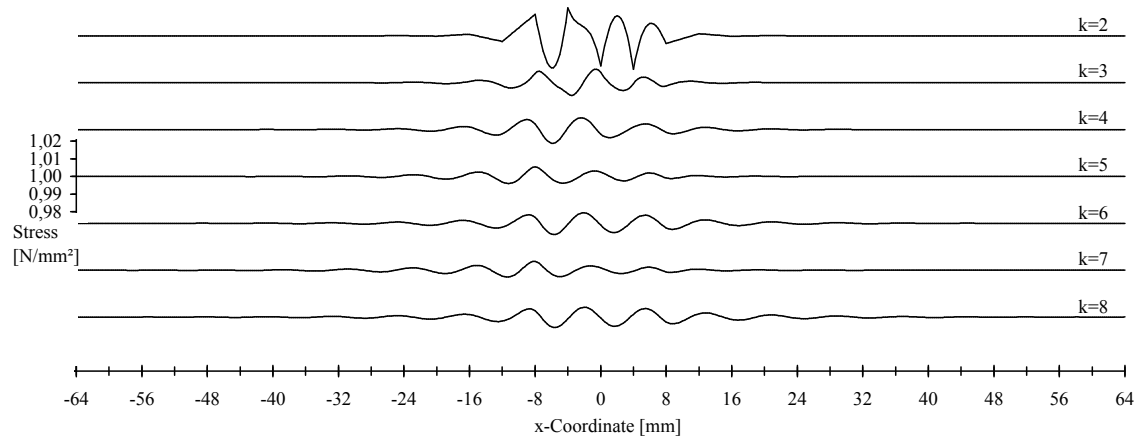
Figure 4.36: Stress $\sigma_{xx}$ in finite elements of Section 1-1 for $C^2$-continuous quintic transition of Young's modulus and varying order $k$ of B-Spline finite elements.

the effect does not appear to be relevant. Concluding, for best approximation of material transitions, multiphase B-spline finite elements of order $k = 2$ or $k = 3$ are proposed, as no further improvement can be expected for an increase of $k$ (while the p-version was much more effective for homogeneous problems).

The Figs. 4.37 to 4.39 deal with the h-version, namely a change of element number measured in terms of element size $h$. Figure 4.37 shows the combination of a linear transition function and B-splines shape functions of order $k = 2$. The stress $\sigma_{xx}$ converges very effectively with decreasing mesh size. Same effect is observed for the linear transition function
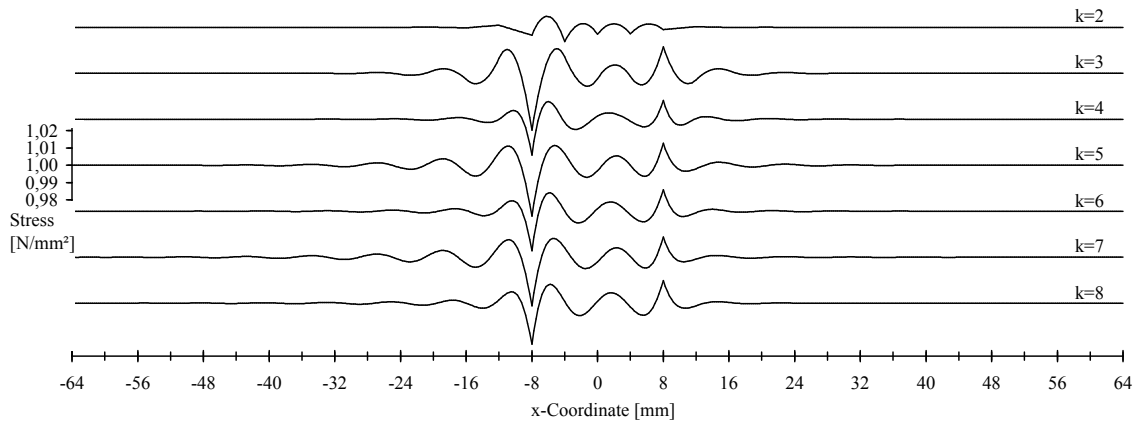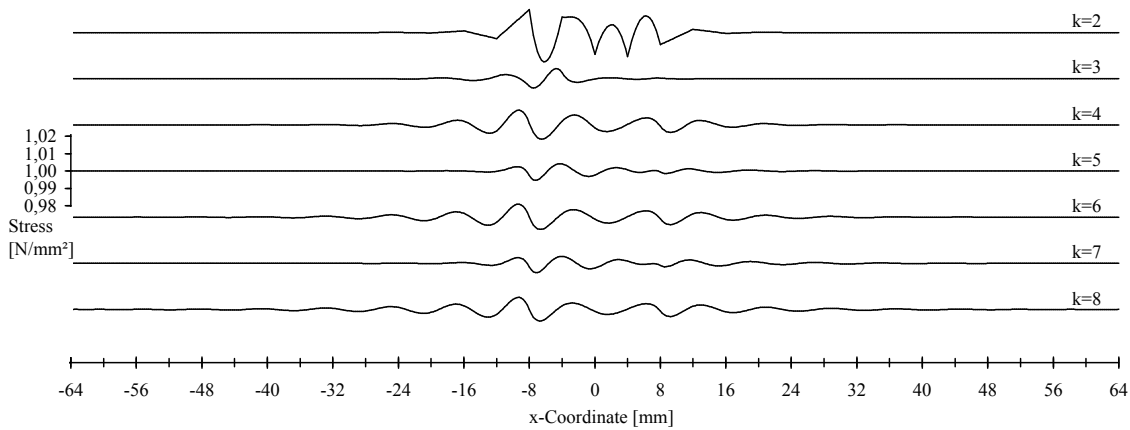


Figure 4.37: Stress $\sigma_{xx}$ in finite elements of Section 1-1 for $C^0$-continuous linear transition of Young's modulus, order $k=2$ and varying size $h$ of B-Spline finite elements.



Figure 4.38: Stress $\sigma_{xx}$ in finite elements of Section 1-1 for $C^0$-continuous linear transition of Young's modulus, order $k=3$ and varying size $h$ of B-Spline finite elements.
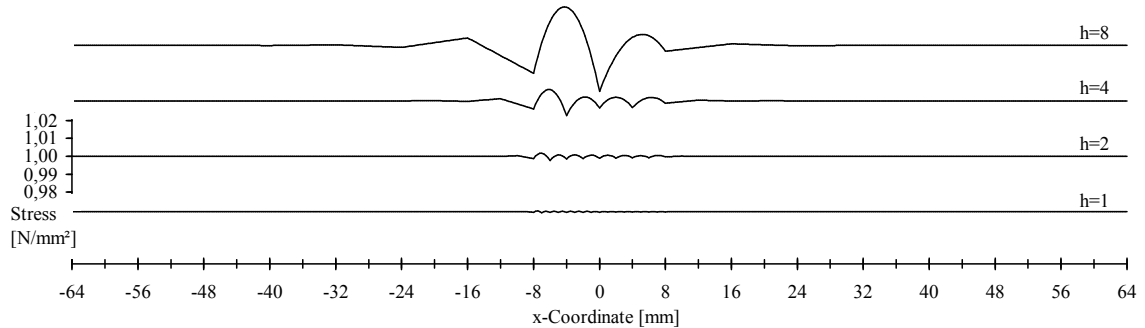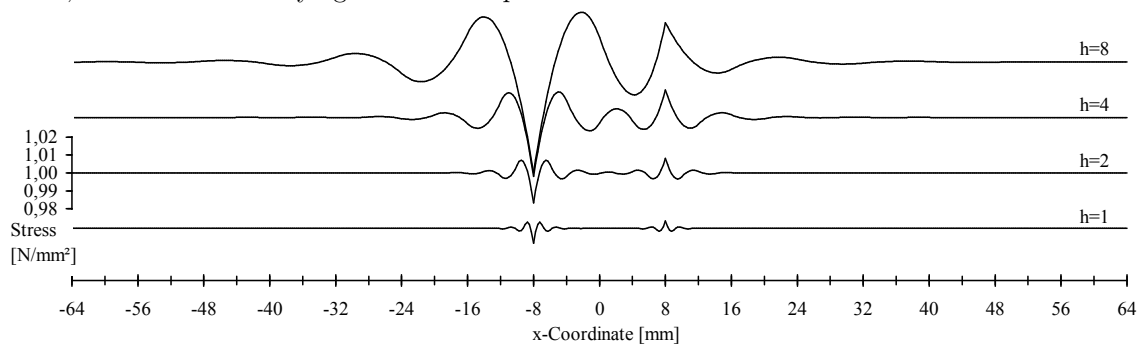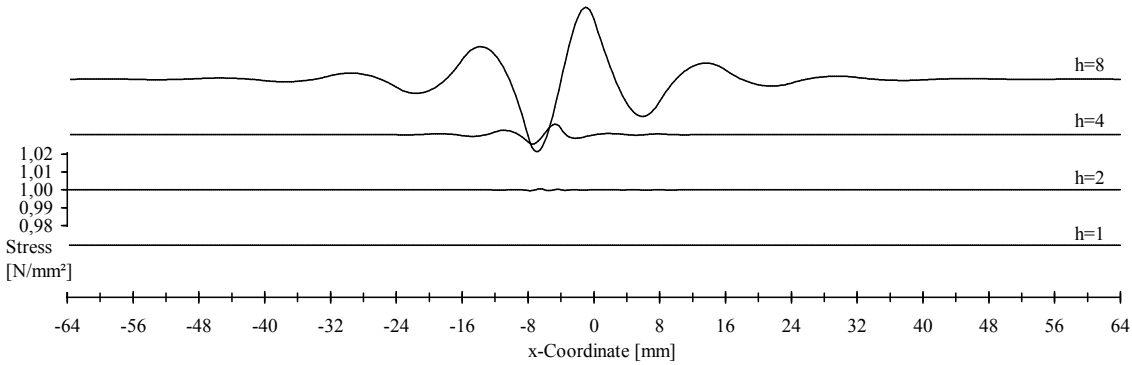
Figure 4.39: Stress $\sigma_{xx}$ in finite elements of Section 1-1 for $C^1$-continuous cubic transition of Young's modulus, order $k=3$ and varying size $h$ of B-Spline finite elements.

and $k = 3$ in Fig. 4.38. Even the discussed defect at $x = -8$ and $x = 8$ decreases, which would not have been clear without this study, but it appears to converge less effectively.

As a further study the combination of cubic transition and $k = 3$ is shown in Fig. 4.39. Without the defect the problem converges even faster then for a linear transition and $k = 2$ with respect to decreasing mesh size $h$.

As the major conclusion, it is quite obvious that the h-version is much more effective in modeling heterogeneous materials than the p-version. Best results are achieved for simple linear transitions in combination with B-spline functions of order $k = 2$. This supports the statement that a grid-based model with simple bilinear mapping functions is reasonable and a higher-order mapping function will not necessarily lead to essentially improved answers. Only exception is a cubic transition function in combination with B-splines of order $k = 3$. But then it is expected, that in fact the cubic transition function needs to be exactly mapped which is not easy to assure for arbitrary geometries of grid-based models. As a further conclusion it is noted that the dimension of error in all examples is within the acceptable tolerance of a few percent error in stress or essentially below. Again, therefore the method is well suited for modeling heterogeneous problems.

In all cases multiphase B-spline finite elements of order $k = 1$ (bilinear) lead to significantly worse results which is only summarized in the following final summaries of error in stress and energy in form of Figs. 4.40 to 4.43. Fig. 4.40 summarizes the maximum error of stress in the p-version and Fig. 4.41 that in the h-version. Similar trends in the error of energy are observed for the p-version and h-version in Figs. 4.42 and 4.43, respectively. It is quite interesting to evaluate the convergence rates of error energy from Fig. 4.43 as assembled in Table 4.2 and compare them to those of the homogeneous problem.

| Error(2h) / Error(h) | | | |
|---|---|---|---|
| | $h = 4s$ | $h = 2s$ | $h = 1s$ |
| Linear Transition, $k = 2$ | 18.041 | 19.016 | 18.575 |
| Linear Transition, $k = 3$ | 6.2506 | 7.8595 | 7.9919 |
| Cubic Transition, $k = 2$ | 10.332 | 20.836 | 20.213 |
| Cubic Transition, $k = 3$ | 107.54 | 175.00 | - |

Table 4.2: Convergence rates of error energy as in Fig. 4.43 and assignment of first row to Fig. 4.37, second row to Fig. 4.38, third row without illustration and fourth row to Fig. 4.39
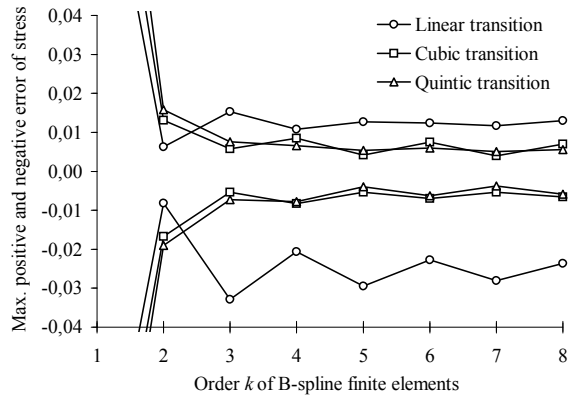
Figure 4.40: Maximum error of stress in p-version
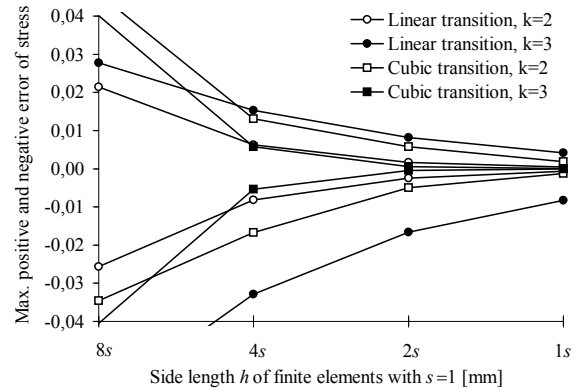


Figure 4.41: Maximum error of stress in h-version
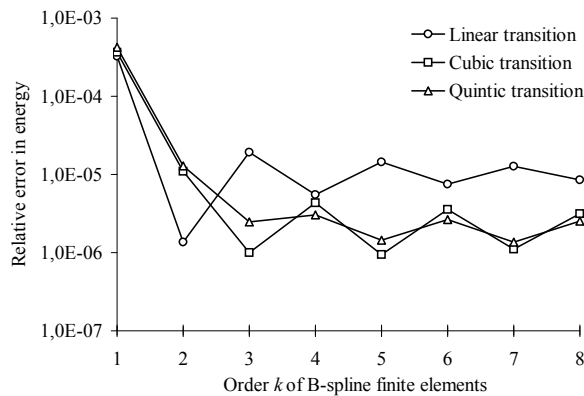


Figure 4.42: Energy error in p-version
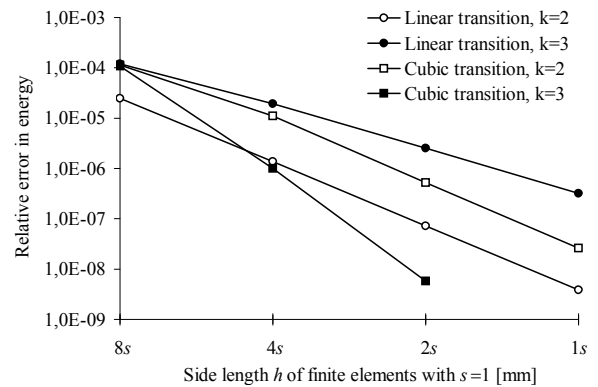


Figure 4.43: Energy error in h-version

## 4.6.7   Overall Error Estimation

Several examples showed that the presented multiphase B-spline finite elements can be applied to the mechanical analysis of heterogeneous materials and in the h-version lead to good convergence of stress and system energy. These elements were especially designed to reduce severely defective stresses along interfaces of grid-based models. However, therefore a substitute problem was introduced (Section 4.6.1), which already includes an error in advance. For an accurate assessment of the proposed method, the overall error is considered. This also allows to identify effectively optimal parameter combinations. The following sources of error are considered:

**Geometrical error** The geometrical error refers to any difference between the heterogeneous material geometry of the original problem and that of the finite element problem. Such a difference can have several reasons such as e.g. imprecise geometrical data of the material, the representation by a grid model or the introduction of a substitute problem (Section 4.6.1).

**Discretization error** The discretization error denotes the classical approximation error which results of the finite functional space of the finite elements. This error evaluates the adequacy of shape functions in the approximation of the exact solution of the posed problem. It is important to note that the discretization error refers to the posed problem, which might differ from the intended problem, e.g. by the geometrical error.

**Numerical error** The term numerical error summarizes several possible error sources. These errors can result from the limited computational precision or from user-defined tolerances such as in the iterative solution process of the linear equation system. In any case it needs to be assured that the numerical error is essentially below the geometrical error and the discretization error.

In (Häfner and Könke 2004) the common basis of error in energy appeared to be most reasonable to compare different sources of error. However, in this context the effect on the stress solution is of relevant interest. In the following the overall error, or effective error, includes the geometrical error and the discretization error. The numerical error is negligible.

The overall error is estimated with regard to the example of one material transition of Section 4.6.6. The linear material transition is considered in combination with multiphase B-spline finite elements of order $k = 2$. The size of the material transitions zone $s_t$ ($D$ in Fig. 4.32) is variable. Only some assumptions allow for a comparison of geometrical and discretization error. The geometrical error only depends on $s_t$ of the substitute problem. The geometry is exactly mapped onto the elements which are based on a sufficient number of integration points. If $s_t = 0$ the geometry corresponds to the original problem (compare to Section 4.6.3).

In example of Section 4.6.6 the analytical stress solution of the substitute problem corresponds to that of the original problem. However, the effective stiffness is changed due to the material transition zone. This can be expressed in error of potential energy. A relative error of the stress is assigned to the square root of relative error of energy. This is an assumption which presumes that the error of stress due to the geometrical error is equally distributed over the domain. The discretization error causes local defects in the stress solution. It follows that an equally distributed error and a maximum local error are of different character. However, Figs. 4.44 and 4.45 illustrate the relationship of these errors where the effective error is the sum of geometrical error and discretization error.
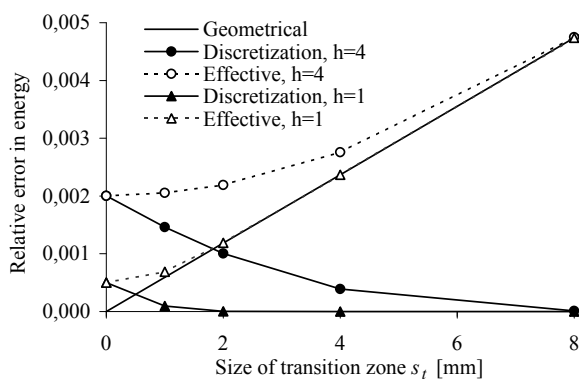


Figure 4.44: Effective error of energy
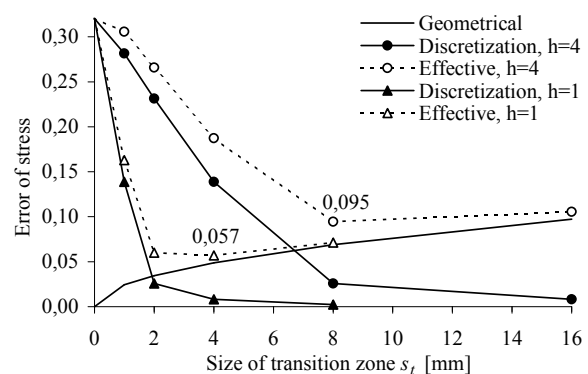


Figure 4.45: Effective maximum error of stress

With respect to the relative error of energy the introduction of a material transition zone ($s_t > 0$) is always disadvantageous. However, the dimension of the relative geometrical error of 0.5% at $s_t = 8$ in Fig. 4.44 is comparatively low and tolerable. The errors in stress according to Fig. 4.45 are essentially decreased by introduction of the material transition zone in contrast to the original problem ($s_t = 0$). For size $h = 4$ of elements the lowest

effective error is achieved for $s_t = 8$, for $h = 1$ it is $s_t = 4$. Also in the effective error of stress the proposed method converges with decreasing mesh size $h$ but less fast as the pure discretization error. However, this is a successful result of the introduced substitute problem. It is highlighted that the number of degrees of freedom connected to a specific mesh size $h$ ($h = 1$ or $h = 4$) in Fig. 4.45 remains unchanged.

## 4.7   Conclusions

The present chapter provides transparent access to B-spline finite elements by simple one-dimensional examples which are comprehensible by hand calculation. Two-dimensional B-spline finite elements are developed which are of variable order $k$. In a complex homogeneous problem these elements achieve exemplary convergence rates. They are highly accurate, as tested up to the order $k = 5$. Even with respect to the variable order $k$, only a few element stiffness matrices are required to create and solve the global finite element problem on a uniform grid. By the use of iterative solvers a global stiffness matrix needs not to be stored such that the memory demand can be reduced to a minimum of essentially required vectors. Moreover, the presented element-based modeling on uniform grids is ideally suited for an effective use of the multigrid method.

The multiphase finite element concept extends the B-spline finite elements of variable order $k$ to their application in the mechanical analysis of heterogeneous solids. Several advantages of grid-based modeling are maintained such that the extension to three-dimensional modeling of heterogeneous solids remains straightforward. The geometrical description of different phases within the material is independent of the finite element mesh. Surfaces of the phases need not to be defined as usually required in aligned meshing. The geometry can originate from pixel models or exact mapping of material functions within the finite elements. As an essential key, an original problem with material discontinuities is replaced by a substitute problem with continuous material approximations. The errors of stress and energy are analyzed with respect to B-spline order $k$, element size $h$, as well as type of material transition function and size $s_t$ of material transition zone. Therefore best parameter combinations of this method can be identified.

In contrast to homogeneous materials where an increase of B-spline order $k$ is optimal (p-version), for heterogeneous materials convergence is almost only achieved by refining the mesh (h-version). Apart from the considerate use of cubic B-spline finite elements for heterogeneous materials, bilinear material transition functions in combination with quadratic B-spline finite elements appear optimal and robust. An ideal size of the material transition zone is approximately assigned to the size of two to four elements ($2h$ to $4h$). Finally, the effective error, as sum of discretization error and geometrical error, from the substitute problem is estimated. Also for the effective error the substitute problem leads to a successful trade-off. While the effective energy error only slightly increases, severe errors in the stress solution effectively decrease by an essential magnitude. Although the effective error of stress converges less fast than the pure discretization error within the substitute problem, the presented method establishes a substantial improvement for grid-based modeling. Therefore multiphase B-spline finite elements are proposed as novel alternative in the mechanical analysis of heterogeneous solids.

# Chapter 5

# Numerical Model:
# Iterative Solver Methods

## 5.1   Introduction

The possibility to increase the model size by resolution in comparison to standard procedures would be valuable. As one major problem the possible resolution of finite element models is generally restricted due to (a) computation times and even more critical (b) memory demand. Direct solver methods require the storage of a global stiffness matrix and the corresponding memory demand limits the problem size. Iterative solvers can be based on a local element-based formulation while orthogonal grids consist of geometrical identical elements. The element-based formulation is short and transparent, and therefore efficient in implementation. A variation of the material properties in elements or integration points is possible. The multigrid method is a fast iterative solver method, where ideally the computational effort only increases linear with problem size. This is an optimal property which is almost achieved in the present implementation. In fact, no method is known which scales better than linear. Therefore the multigrid method gains in importance the larger the problem becomes. But for heterogeneous models with very large ratios of Young's moduli the multigrid method considerably slows down by a constant factor. Such large ratios occur in certain heterogeneous solids, as well as in the damage analysis of solids. An important remedy is found in the multigrid preconditioned conjugate gradient method. Various multigrid cycles are tested and results from three-dimensional analysis are presented.

## 5.2   Problem Statement and Notation

In the static case the finite element method leads to the linear equation system

$$\boldsymbol{K}\,\boldsymbol{u} = \boldsymbol{f} \tag{5.1}$$

where $\boldsymbol{K}$ denotes the stiffness matrix, $\boldsymbol{f}$ is the vector of prescribed forces and $\boldsymbol{u}$ is the solution, the displacement vector which is initially unknown. The corresponding theory of the finite element formulation is given in Section 4.2.  In the following discussion of iterative solver methods it is assumed that the problem is of the form as in Eq. 5.1 and the vector $\boldsymbol{u}$ corresponds to the displacements of the effective degrees of freedom. In the scalar

variable $u_i^k$ the superscript $k$ denotes the $k$-th iteration and the subscript $i$ indicates the $i$-th element of the vector. The increment of displacements $\Delta \boldsymbol{u}^k$ after the $k$-th iteration is

$$\Delta \boldsymbol{u}^k = \boldsymbol{u}^{k+1} - \boldsymbol{u}^k \tag{5.2}$$

and with

$$\boldsymbol{f}^k = \boldsymbol{K} \boldsymbol{u}^k \tag{5.3}$$

the increment of forces $\Delta \boldsymbol{f}^k$ is

$$\Delta \boldsymbol{f}^k = \boldsymbol{f}^{k+1} - \boldsymbol{f}^k \tag{5.4}$$

The error $\boldsymbol{e}^k$ is defined as the difference between the iterative displacement approximation $\boldsymbol{u}^k$ after the k-th iteration and the solution vector $\boldsymbol{u}$.

$$\boldsymbol{e}^k = \boldsymbol{u}^k - \boldsymbol{u} \tag{5.5}$$

The residual $\boldsymbol{r}^k$ is the difference of the prescribed force vector $\boldsymbol{f}$ and the effective right hand side $\boldsymbol{f}^k$ after the k-th iteration

$$\boldsymbol{r}^k = \boldsymbol{f} - \boldsymbol{f}^k \tag{5.6}$$

Hence, from Eqs. 5.1, 5.4, 5.5 5.6 it can be derived that

$$-\boldsymbol{K}\,\boldsymbol{e}^k = \boldsymbol{r}^k \tag{5.7}$$

## 5.3 Basic Iterative Solver Methods

### 5.3.1 Stationary Iterative Methods

As identifying characteristic, stationary iterative methods can be expressed in the simple form

$$\boldsymbol{u}^{k+1} = \boldsymbol{Q}\,\boldsymbol{u}^k + \boldsymbol{q} \tag{5.8}$$

where $\boldsymbol{Q}$ and $\boldsymbol{q}$ are placeholders for a matrix and a vector, respectively, both independent of iteration step $k$. Among others, stationary iterative methods, such as e.g. the Gauss-Seidel method, may act as smoothers within the later proposed multigrid method. A brief introduction to these methods is provided in the following. Further mathematical background of these iterative methods is treated in e.g. (Barrett et al. 1994; Hackbusch 1991; Young 1991).

The considered problem is a linear equation system of the form $\boldsymbol{K}\,\boldsymbol{u} = \boldsymbol{f}$ (Eq. 5.1). Then it is trivial to introduce any regular matrix $\boldsymbol{S}$, called the splitting matrix, as follows

$$\boldsymbol{K} = \boldsymbol{S} + (\boldsymbol{K} - \boldsymbol{S}) \tag{5.9}$$

The linear equation system can be rewritten as

$$\boldsymbol{S}\boldsymbol{u} = (\boldsymbol{S} - \boldsymbol{K})\,\boldsymbol{u} + \boldsymbol{f} \tag{5.10}$$

and the iterative scheme of the splitting method is defined as

$$\boldsymbol{u}^{k+1} = \boldsymbol{S}^{-1}\left((\boldsymbol{S} - \boldsymbol{K})\,\boldsymbol{u}^k + \boldsymbol{f}\right) \tag{5.11}$$

For further analysis of this method it is useful to introduce the iteration matrix $\boldsymbol{M}$ as

$$\boldsymbol{M} = \boldsymbol{S}^{-1}\left(\boldsymbol{S} - \boldsymbol{K}\right) \tag{5.12}$$

In consideration of Eq. 5.12 the method of Eq. 5.11 corresponds to the scheme of the stationary iterative method (Eq. 5.8) with $\boldsymbol{Q} = \boldsymbol{M}$ and $\boldsymbol{q} = \boldsymbol{S}^{-1}\boldsymbol{f}$. From the iteration scheme of Eq. 5.8, the definition of the error in Eq. 5.5 and the equality $\boldsymbol{u} = \boldsymbol{Q}\boldsymbol{u} + \boldsymbol{q}$, it follows that

$$\boldsymbol{e}^{k+1} = \boldsymbol{M}\boldsymbol{e}^{k} \tag{5.13}$$

The spectral radius $\rho$ of a matrix is its largest absolute eigenvalue. The stationary iterative method converges if and only if the spectral radius $\rho$ of the iteration matrix $\boldsymbol{M}$ satisfies the condition

$$\rho(\boldsymbol{M}) < 1 \tag{5.14}$$

Then it converges for any initial start vector $\boldsymbol{u}^{0}$ and any right hand side $\boldsymbol{f}$.

### 5.3.2   Jacobi Method

In case of the Jacobi method the diagonal $\boldsymbol{D}$ of the system matrix $\boldsymbol{K}$ is chosen as splitting matrix $\boldsymbol{S}_J = \boldsymbol{D}$. Then, analogous to Eq. 5.9 the decomposition reads as

$$\boldsymbol{K} = \boldsymbol{D} + \left(\boldsymbol{K} - \boldsymbol{D}\right) \quad \text{or} \quad \boldsymbol{K} = \boldsymbol{D} + \left(-\boldsymbol{L} - \boldsymbol{U}\right) \tag{5.15}$$

where $\left(-\boldsymbol{U}\right)$ denotes the strictly upper triangle and $\left(-\boldsymbol{L}\right)$ denotes the strictly lower triangle of the system matrix $\boldsymbol{K}$. Thus, in accordance to Eq. 5.11 the matrix form of the Jacobi method is defined by

$$\boldsymbol{u}^{k+1} = \boldsymbol{D}^{-1}\left(\left(\boldsymbol{L} + \boldsymbol{U}\right)\boldsymbol{u}^{k} + \boldsymbol{f}\right) \tag{5.16}$$

Correspondingly, the index form of the Jacobi method results as

$$u_i^{k+1} = \frac{1}{K_{ii}}\left(f_i - \sum_{j=1,\,j\neq i}^{n} K_{ij}u_j^{k}\right) \tag{5.17}$$

### 5.3.3   Gauss–Seidel Method

In case of the Gauss–Seidel method the splitting matrix is chosen as $\boldsymbol{S}_{GS} = \left(\boldsymbol{D} - \boldsymbol{L}\right)$. Then, analogous to Eq. 5.9 the decomposition reads as

$$\boldsymbol{K} = \left(\boldsymbol{D} - \boldsymbol{L}\right) + \left(\boldsymbol{K} - \left(\boldsymbol{D} - \boldsymbol{L}\right)\right) \quad \text{or} \quad \boldsymbol{K} = \left(\boldsymbol{D} - \boldsymbol{L}\right) + \left(-\boldsymbol{U}\right) \tag{5.18}$$

Thus, in accordance to the splitting method of Eq. 5.11 the Gauss–Seidel method is

$$\boldsymbol{u}^{k+1} = \left(\boldsymbol{D} - \boldsymbol{L}\right)^{-1}\left(\boldsymbol{U}\boldsymbol{u}^{k} + \boldsymbol{f}\right) \tag{5.19}$$

Some further algebraic transformations of this equation are required for the derivation of the index form of the Gauss–Seidel method, such as

$$\boldsymbol{D}\boldsymbol{u}^{k+1} - \boldsymbol{L}\boldsymbol{u}^{k+1} = \boldsymbol{U}\boldsymbol{u}^{k} + \boldsymbol{f} \tag{5.20}$$

and

$$\boldsymbol{u}^{k+1} = \boldsymbol{D}^{-1} \left( \boldsymbol{L} u^{k+1} + \boldsymbol{U} u^k + \boldsymbol{f} \right) \tag{5.21}$$

where the index form is evident.

$$u_i^{k+1} = \frac{1}{K_{ii}} \left( f_i - \sum_{j=1}^{i-1} K_{ij} u_j^{k+1} - \sum_{j=i+1}^{n} K_{ij} u_j^k \right) \tag{5.22}$$

## 5.3.4   Comparison of Jacobi- and Gauss–Seidel Method

In the computation of the $i$-th element $u_i^{k+1}$ in the $(k+1)$–iteration, the Gauss–Seidel method already includes all available iterates $u_j^{k+1}$ with $j = 1 \ldots (i-1)$, while the Jacobi method only uses the $u_j^k$ with $j = 1 \ldots N$ of the $(k)$–iteration. This is the only, but momentous difference in the algorithms of these two methods. In other words, while the Jacobi method adds all increments *simultaneously* only after cycling through all degrees of freedom, the Gauss–Seidel method adds all increments *successively* as soon available. As an advantage of the Gauss-Seidel method, one vector is sufficient to update its vector elements $i$ successively in contrast to the Jacobi method where an additional vector is required. However, in practical problems this difference of memory demand is rather not relevant. As the operations for the iteration of different vector elements do not coincide in the Jacobi method, it is not dependent on the nodal ordering and parallelization is straightforward possible. In the Gauss-Seidel method the nodal ordering influences the convergence behavior. For regular grids specific nodal orderings are summarized in (Hackbusch 1985), such as the red–black, lexicographical, zebra-line or four-color ordering. Advanced algorithms are required for successful parallelization of the Gauss-Seidel method or uncontrolled splitting of the process leads to the so-called *chaotic* Gauss-Seidel method. The convergence of both these stationary iterative methods is dependent on the spectral radius of the corresponding iteration matrix $\boldsymbol{M}$ as stated in Eq. 5.14. In general, if both methods converge, the convergence of the Gauss-Seidel method is better as each operation reverts to the latest data. The Jacobi method converges if the system matrix $\boldsymbol{K}$ is strictly diagonally dominant as a sufficient condition (Hackbusch 1991).

$$|K_{ii}| > \sum_{j=1,\, j \neq i}^{n} |K_{ij}| \qquad \text{for all } i \tag{5.23}$$

This does not apply to the considered structural finite element problems. However, convergence can be achieved by additional damping. The Gauss-Seidel converges if the system matrix $\boldsymbol{K}$ is strictly diagonally dominant or if the system matrix $\boldsymbol{K}$ is positive definite. The second condition is true, if the finite element model is properly restrained and stable (Bathe 1996). Besides the use as stand-alone iterative solvers, the damped Jacobi method or the Gauss–Seidel can be applied as smoothers within the multigrid method.

### 5.3.5   Symmetric Gauss-Seidel Method

The symmetric Gauss-Seidel Method bases on two half steps, the classical Gauss-Seidel iteration, labeled as forward sweep (fGS), and additionally a backward sweep (bGS), with the splitting matrices

$$\boldsymbol{S}_{fGS} = \boldsymbol{D} - \boldsymbol{L} \quad \text{and} \quad \boldsymbol{S}_{bGS} = \boldsymbol{D} - \boldsymbol{U} \tag{5.24}$$

The following equations together describe one step of the symmetric Gauss-Seidel method

$$\boldsymbol{u}^{k+\frac{1}{2}} = (\boldsymbol{D} - \boldsymbol{L})^{-1} \left( \boldsymbol{U}\boldsymbol{u}^{k} \quad + \boldsymbol{f} \right) \tag{5.25}$$

$$\boldsymbol{u}^{k+1} = (\boldsymbol{D} - \boldsymbol{U})^{-1} \left( \boldsymbol{L}\boldsymbol{u}^{k+\frac{1}{2}} + \boldsymbol{f} \right) \tag{5.26}$$

By condensation of $\boldsymbol{u}^{k+\frac{1}{2}}$, it is straightforward to derive the effective splitting matrix

$$\boldsymbol{S}_{sGS} = (\boldsymbol{D} - \boldsymbol{L})\boldsymbol{D}^{-1}(\boldsymbol{D} - \boldsymbol{U}) \tag{5.27}$$

of the symmetric Gauss-Seidel method and its effective iteration matrix

$$\boldsymbol{M}_{sGS} = (\boldsymbol{D} - \boldsymbol{U})^{-1}\boldsymbol{L}(\boldsymbol{D} - \boldsymbol{L})^{-1}\boldsymbol{U} \tag{5.28}$$

Among other things, this matrix form of the iteration matrix is valuable for convergence analysis. However, for implementation issues it is reasonable to consider just the index form of the symmetric Gauss-Seidel method. The forward sweep corresponds to the Gauss-Seidel method of Eq. 5.22 assuming that i counts from 1 to n. Then in the subsequent backward sweep i counts backwards from n to 1. The symmetric Gauss-Seidel method has special properties. Summarily, it is generally not twice as fast convergent as the Gauss-Seidel method which results from analysis of the iteration matrix. On the other hand by a specific implementation with buffering of certain data, one iteration step of the symmetric method counts less operations than two of the Gauss-Seidel method. Nevertheless with respect to advanced solver methods, these details are rather marginal and will not be considered any further in this work. But as an essential advantage of the symmetric version, it is a well suited preconditioner.

### 5.3.6   Relaxation Methods

Relaxation methods are stationary iterative methods. Thus, they can also be presented in the form of Eq. 5.8. For each of the previously introduced methods, there also exists a corresponding relaxation method.

In comparison to the preceding methods, the relaxation methods propose to scale each increment by a constant relaxation factor $\omega$. The general form of the relaxation methods is given by the following short algorithmic expression

$$u_i^{k+1} := (1 - \omega)\, u_i^k + \omega \breve{u}_i^{k+1} \tag{5.29}$$

where for each individual index i, the temporary variable $\breve{u}_i^{k+1}$ is computed as $u_i^{k+1}$ of the Jacobi method in case of the simultaneous over-relaxation method (JOR method) or as $u_i^{k+1}$ of the Gauss–Seidel method in case of the successive over-relaxation

method (SOR method). Then, if $\omega = 1$ this relaxation scheme is identical to the Jacobi and the Gauss–Seidel method, respectively.

The optimum relaxation factor can theoretically be derived from the spectral radius (largest absolute eigenvalue) of the iteration matrix. But as this is expensive, several methods on the practical determination of $\omega$ are proposed in (Hackbusch 1991; Young 1991). Usually in finite element analysis the optimum relaxation for the SOR method is between 1.3 and 1.9 (Bathe 1996). For a finite element model of a heterogeneous solid (Häfner and Könke 2004), the convergence of the JOR method was achieved by a heuristic damping factor of $\omega = 0.8$.

### 5.3.7 Conjugate Gradient Method

The conjugate gradient method has been developed by Hestenes and Stiefel (1952). In contrast to the method described in 5.3.1, the conjugate gradient method is instationary. It is presumed that the matrix $\boldsymbol{K} \in \mathbb{R}^{n \times n}$ and the vector $\boldsymbol{f} \in \mathbb{R}^n$ are real and that the matrix $\boldsymbol{K}$ is symmetric ($\boldsymbol{K} = \boldsymbol{K}^{\mathrm{T}}$) and positive definite

$$\boldsymbol{u}^{\mathrm{T}} \boldsymbol{K} \boldsymbol{u} > 0 \qquad \text{for all } \boldsymbol{u} \neq \boldsymbol{0} \tag{5.30}$$

Then, the minimization problem of the quadratic form $F(x) = \min$

$$F(\boldsymbol{u}) = \frac{1}{2} \boldsymbol{u}^{\mathrm{T}} \boldsymbol{K} \boldsymbol{u} - \boldsymbol{f}^{\mathrm{T}} \boldsymbol{u} \tag{5.31}$$

is equivalent to setting its derivative

$$\operatorname{grad} F(\boldsymbol{u}) = \boldsymbol{K} \boldsymbol{u} - \boldsymbol{f} \tag{5.32}$$

equal to the zero vector

$$\operatorname{grad} F(\boldsymbol{u}) = \boldsymbol{0} \tag{5.33}$$

The conjugate gradient method is an iterative minimizer of the provided quadratic form and thus an iterative solver method for the linear equation system $\boldsymbol{K} \boldsymbol{u} = \boldsymbol{f}$. As an important characteristic of the corresponding algorithm, the quadratic form is always minimized from an approximate vector $\boldsymbol{u}^k$ in the direction of a provided search vector $\boldsymbol{p}^k \neq \boldsymbol{0}$, which can be written as

$$F(\boldsymbol{u}^k + \lambda \boldsymbol{p}^k) = \min \tag{5.34}$$

with both $\boldsymbol{u}^k$ and $\boldsymbol{p}^k$ are constant vectors $\in \mathbb{R}^n$ and a scalar variable $\lambda \in \mathbb{R}$. In detail this leads to the following parabolic function with respect to $\lambda$

$$\left( \frac{1}{2} \boldsymbol{p}^{k\mathrm{T}} \boldsymbol{K} \boldsymbol{p}^k \right) \lambda^2 + \left( \boldsymbol{p}^{k\mathrm{T}} \boldsymbol{K} \boldsymbol{u}^k - \boldsymbol{p}^{k\mathrm{T}} \boldsymbol{f} \right) \lambda + \left( \frac{1}{2} \boldsymbol{u}^{k\mathrm{T}} \boldsymbol{K} \boldsymbol{u}^k - \boldsymbol{u}^{k\mathrm{T}} \boldsymbol{f} \right) = \min \tag{5.35}$$

This yields that the quadratic form is minimized for

$$\lambda = \frac{\boldsymbol{p}^{k\mathrm{T}} \left( \boldsymbol{f} - \boldsymbol{K} \boldsymbol{u}^k \right)}{\boldsymbol{p}^{k\mathrm{T}} \boldsymbol{K} \boldsymbol{p}^k} \tag{5.36}$$

The ideal search direction $\boldsymbol{p}^k$ would be the error $\boldsymbol{e}^k$, but this would presume the knowledge of the exact solution $\boldsymbol{u}$. Therefore, the negative gradient of the quadratic form at $\boldsymbol{u}^k$ represents the best intuitive search direction from the local view of $\boldsymbol{u}^k$. Then, with Eqs. 5.32, 5.3 and 5.6, the search direction corresponds to the residuum $\boldsymbol{r}^k$

$$- \operatorname{grad} F(u^k) = \boldsymbol{f} - \boldsymbol{K}\boldsymbol{u}^k = \boldsymbol{r}^k \tag{5.37}$$

With $\boldsymbol{p}^k = \boldsymbol{r}^k$ in Eq. 5.36, the following equations can be defined

$$\lambda_k = \frac{\boldsymbol{r}^{k\mathrm{T}}\boldsymbol{r}^k}{\boldsymbol{r}^{k\mathrm{T}}\boldsymbol{K}\boldsymbol{r}^k} \tag{5.38}$$

$$\boldsymbol{u}^{k+1} = \boldsymbol{u}^k + \lambda_k \boldsymbol{r}^k \tag{5.39}$$

which describe one step of an iterative method which is called the Method of Steepest Descent due to the property that for any iteration step $k$ the search direction $\boldsymbol{p}^k$ is defined by $\left(-\operatorname{grad} F(\boldsymbol{u}^k)\right)$.

The Method of the Steepest Descent is a relevant step towards the Conjugate Gradient Method, but it turns out that the choice of the search directions $\boldsymbol{p}^k$ is not optimal. As $\boldsymbol{u}^{k+1}$ is optimized with respect to the previous search direction $\boldsymbol{p}^k = \boldsymbol{r}^k$, it is clear that successive search directions are orthogonal or in symbolic form $\left(-\operatorname{grad} F(\boldsymbol{u}^{k+1}) \perp \boldsymbol{p}^k\right)$. However, although it can be shown that $\boldsymbol{r}^k \perp \boldsymbol{r}^{k+1}$ and $\boldsymbol{r}^{k+1} \perp \boldsymbol{r}^{k+2}$, it is generally not true that $\boldsymbol{r}^k \perp \boldsymbol{r}^{k+2}$. Therewith $\boldsymbol{u}^{k+2}$ has lost its optimum with respect to the previously optimized direction $\boldsymbol{r}^k$.

If $u^{k+1}$ is *optimal with respect to* $p^k \neq \boldsymbol{0}$, then this property is passed to $u^{k+2}$, if and only if

$$\boldsymbol{K}\, p^{k+1} \perp p^k \tag{5.40}$$

and the vectors $p^{k+1}$ and $p^k$ are called *conjugate*. In the conjugate gradient method the search directions are pairwise conjugate. As each new direction is derived from the actual remaining residual and conjugate to the prior search direction, it is also conjugate to all previous search directions. Thus a system of conjugate search directions is obtained or equivalent a system of orthogonal residuals. This property can be proofed by induction. With the initial values

$$\boldsymbol{r}^0 = \boldsymbol{f} - \boldsymbol{K}\boldsymbol{u}^0 \; ; \quad \boldsymbol{p}^0 = \boldsymbol{r}^0 \tag{5.41}$$

the following equations describe the algorithm of the conjugate gradient method

$$\lambda_k = \frac{\boldsymbol{r}^{k\mathrm{T}}\boldsymbol{p}^k}{\boldsymbol{p}^{k\mathrm{T}}\boldsymbol{K}\boldsymbol{p}^k} \tag{5.42}$$

$$\boldsymbol{u}^{k+1} = \boldsymbol{u}^k + \lambda_k \boldsymbol{p}^k \tag{5.43}$$

$$\boldsymbol{r}^{k+1} = \boldsymbol{r}^k - \lambda_k \boldsymbol{K}\boldsymbol{p}^k \tag{5.44}$$

$$\boldsymbol{p}^{k+1} = \boldsymbol{r}^{k+1} - \frac{\boldsymbol{r}^{k+1\,\mathrm{T}}\boldsymbol{K}\boldsymbol{p}^k}{\boldsymbol{p}^{k\mathrm{T}}\boldsymbol{K}\boldsymbol{p}^k}\boldsymbol{p}^k \tag{5.45}$$

Eq. 5.42 corresponds to Eq. 5.36. Eq. 5.44 is equivalent to $\boldsymbol{r}^{k+1} = \boldsymbol{f} - \boldsymbol{K}\boldsymbol{u}^{k+1}$. As documented in e.g. (Hackbusch 1991) and with regard to an efficient implementation, it is possible to replace Eq. 5.42 by

$$\lambda = \frac{\boldsymbol{r}^{k\mathrm{T}}\boldsymbol{r}^k}{\boldsymbol{p}^{k\mathrm{T}}\boldsymbol{K}\boldsymbol{p}^k} \tag{5.46}$$

and Eq. 5.45 by

$$\boldsymbol{p}^{k+1} = \boldsymbol{r}^{k+1} + \frac{\boldsymbol{r}^{k+1\mathrm{T}}\boldsymbol{r}^{k+1}}{\boldsymbol{r}^{k\mathrm{T}}\boldsymbol{r}^{k}}\boldsymbol{p}^{k} \tag{5.47}$$

By exact arithmetic the conjugate gradient method will reach the exact solution of an $n$-dimensional problem after $n$ steps. In theory this method can be regarded as a direct solver. However, due to numerical round-off errors the orthogonality is lost and such an ideal result is not achieved. In practice, with respect to a reasonable error tolerance the conjugate gradient method can generally be terminated after considerably less than $n$ steps. This supports the view of the conjugate gradient method as an iterative method, while an iterative method should not converge to the exact solution (even or especially in theory) after n steps. Thus the conjugate gradient method is labeled as semi-iterative method.

## 5.4   Multigrid Method

### 5.4.1   Basic Ideas of the Multigrid Method

The term multigrid method describes an iterative solver strategy rather than one certain algorithm. It is transparent to the FE practitioner's intuition that somehow a coarse mesh solution of a physical problem is a relative good approximation for the same problem on a fine mesh. Therefore certain operators need to be defined to transfer the *problem* from the fine to the coarse mesh and to transfer the *solution* in reverse direction. While it is clear, that a coarse mesh solution requires essentially less computational effort than the fine mesh solution. Then, a coarse mesh solution might provide a good start vector for the iterative process on the fine mesh. In a hierarchy of meshes one might adaptively step from the coarsest mesh to the finest mesh and start each iterative process on a certain mesh by an (approximate) solution of the previous coarser mesh. However, it is important to note that this scheme does not yet really touch the potential of the multigrid method. Assuming that for each mesh one of the introduced classical iterative solver methods is applied, the convergence of the iterative process becomes penally slow on the finest mesh. Then again, the current disequilibrium on the finest mesh, namely the current residual, can be regarded as a new physical problem and the same adaptive procedure through all meshes provides a fast approximation and accelerates the solution process on the fine mesh. This kind of the algorithm is called coarse grid correction. Again, this example rather sketches the basic idea. The sophisticated algorithm of the multigrid method applies certain schemes of *problem* and *solution* transfers in e.g. so called V- or W-cycles, while on the individual meshes the solution is improved by one or a few iteration steps of the classical iterative solver methods. These methods are referred to as smoothers, apparently as local disequilibrium is quickly improved or smoothed, while the global disequilibrium reduces very slowly when applied on a fine mesh. The multigrid method can be treated as stationary iterative solver method, as e.g. illustrated in (Wesseling 1992). For further introduction to the theory of multigrid methods it is referred to (Hackbusch 1985; Briggs 1991; Bramble 1993; Wesseling 1992; Joppich 1996).

## 5.4.2    Algorithms of the Multigrid Method

The multigrid method is applied to solve a linear equation system. Here, it is assumed that this equation system corresponds to a finite element problem on a uniform orthogonal mesh. This mesh, which defines the problem, is referred to as the finest mesh. It is assumed, that there exists a hierarchy of $m+1$ meshes $i = 0 \ldots m$, where $m$ denotes the finest mesh. The problem is defined as

$$\boldsymbol{K}_m \, \boldsymbol{u}_m = \boldsymbol{f}_m \tag{5.48}$$

The index $c$ refers to any coarser mesh $0 \le c < m$. The items (a) to (g) outline the algorithm of one coarse grid correction:

(a) Pre-Smoothing: The actual vector is $\boldsymbol{u}_m^k$. One or a few classical iteration steps are applied.

(b) Evaluation of residual forces on the finest grid

$$\boldsymbol{r}_m^k = \boldsymbol{f} - \boldsymbol{K}_m \boldsymbol{u}_m^k \tag{5.49}$$

(c) Restriction: Transfer of residual forces from fine grid $m$ to coarse grid $c$ by a corresponding matrix $\boldsymbol{P}_m^c$. In practice, the matrix-vector product corresponds to an algorithm.

$$\boldsymbol{r}_c := \boldsymbol{P}_m^c \, \boldsymbol{r}_m^k \tag{5.50}$$

(d) Correction: The actual coarse grid problem is then

$$\boldsymbol{K}_c \, \boldsymbol{u}_c = \boldsymbol{r}_c \tag{5.51}$$

Starting by an initial vector $\boldsymbol{u}_c^0 = \boldsymbol{0}$, one or a few iteration steps $k^*$ of a classical iterative solver method yield an improved approximation $\boldsymbol{u}_c^{k^*}$ which is also a potential correction of the problem on mesh $m$.

(e) Prolongation: Interpolation of the correction $\boldsymbol{u}_c^{k^*}$ of grid $c$ onto the fine mesh $m$ by a corresponding matrix $\boldsymbol{P}_c^m$. Analogous to step (b) an algorithmic implementation of this operation is usual.

$$\Delta \boldsymbol{u}_m := \boldsymbol{P}_c^m \boldsymbol{u}_c^{k^*} \tag{5.52}$$

(f) The displacement increment on mesh $m$ is added to the current displacement vector on mesh $m$ which leads to a temporary variable $\hat{\boldsymbol{u}}$.

$$\hat{\boldsymbol{u}}_m = \boldsymbol{u}_m^k + \Delta \boldsymbol{u}_m \tag{5.53}$$

(g) Post-Smoothing: Only after one or a few classical iteration steps on $\hat{\boldsymbol{u}}_m$ the correction is complete and generates the next approximation $\boldsymbol{u}_m^{k+1}$.
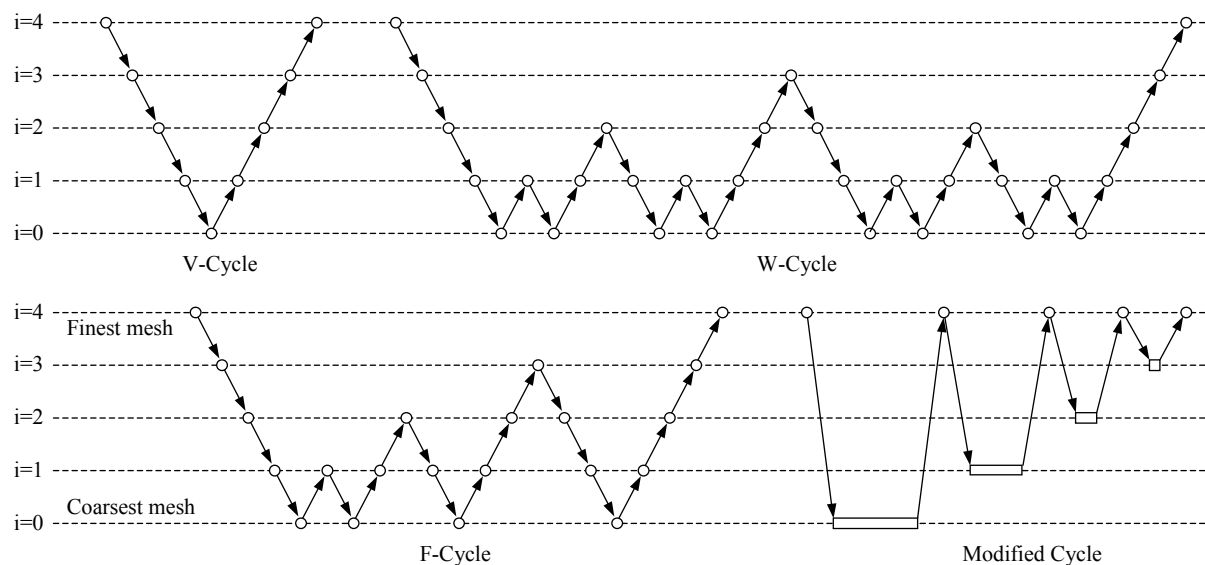
Figure 5.1: Various multigrid cycles with the following steps: prolongation ($\nearrow$), restriction ($\searrow$), one or a few smoothing iterations ($\circ$) and a large number of smoothing iterations according to length of box ($\square$).

Equation 5.51 states a problem similar to Equation 5.48. Therefore the algorithm can be restarted for the problem of Eq. 5.51. For $m = 4$ such a recursive procedure is illustrated in Fig. 5.1 by the V-cycle. Generally it is proposed to solve the problem exactly by a direct solver on the coarsest mesh $i = 0$. In analogy to the shape of the letter V, also the possibility of a W-cycle is included in Fig. 5.1 (Wesseling 1992). Moreover, a F-cycle is illustrated. By the defined operations of restriction, prolongation and smoothing, it is straightforward to construct any of these or also other cycles. Some further details are provided in the benchmark of different cycles (Section 5.11.2).

In the present approach also a modified cycle is implemented. It is illustrated on the right of Fig. 5.1. It requires mesh transfer operators between the finest and any coarser mesh. It is designed to balance the computational effort on the different meshes. The proposed number of iteration steps $s_i$ on mesh $i$ is

$$s_i = c(m - i)^2 \tag{5.54}$$

where $c$ is a heuristic scalar factor. The observed convergence in the examples of (Häfner, Eckardt, Luther and Könke 2006) was good for $c = 1$ and best for $c = 3 \ldots 5$.

# 5.5 Multigrid Preconditioned Conjugate Gradient Method

The Sections 5.3 and 5.4 introduce to the conjugate gradient method and classical iterative solver methods as a basis of the multigrid method. But before an efficient combination of these methods, in terms of the multigrid preconditioned conjugate gradient method, is presented, this topic is motivated with respect to the present engineering application.

The multigrid method is demonstrated as a very effective, iterative solver method for the mechanical analysis of heterogeneous material samples in (Häfner, Eckardt, Luther

and Könke 2006). However, an increase of the ratio of Young's moduli between inclusion and matrix material leads to a significantly slower solution process. The reason can be assigned to the worse conditioning of the problem as well as to the worse material representation on coarse grids. For a similar problem, the Poisson's equation with large coefficient jumps, it was shown in (Tatebe 1993) that the multigrid preconditioned conjugate gradient method shows an essentially superior convergence rate over the multigrid method. In fact, the considered conjugate gradient acceleration can principally be applied to any iterative method (Wesseling 1992). Such an acceleration is not required or even disadvantageous, if the algorithm of the multigrid method is well designed and appropriate for the considered problem. Otherwise, one can try to identify and reduce the essential defect by e.g. additional local smoothing (Wesseling 1992) or advanced algebraic transfer operators (Bayreuther 2004). A potential improvement, which is less dependent of the considered problem, is given by applying the multigrid method as a preconditioner of the conjugate gradient method. An efficient combined preconditioning by the multigrid method and an adaption to shell elements is proposed in (Gee 2004). In the present context multigrid preconditioning will be examined with respect to the aforementioned analysis of heterogeneous materials, whereas all global operations are formulated by effective, element-based procedures (Sections 5.7 to 5.10), such that the storage of a global stiffness matrix is superseded. This leads to a substantially reduced memory demand which is particularly relevant for achieving a high-resolution analysis on the material level.

A linear equation system $\boldsymbol{K}\boldsymbol{u} = \boldsymbol{f}$ can be preconditioned by a matrix $\boldsymbol{H}^{-1}$ as follows.

$$\boldsymbol{H}^{-1}\boldsymbol{K}\boldsymbol{u} = \boldsymbol{H}^{-1}\boldsymbol{f} \tag{5.55}$$

The matrix $\boldsymbol{H}^{-1}$ should be symmetric and positive definite (Tatebe 1993). The conditions of the multigrid preconditioner to match these properties are examined in (Tatebe 1993). According to (Wesseling 1992) the multigrid method will potentially provide a valid preconditioner if the smoother is symmetric[1]. For a derivation of the preconditioned conjugate gradient method a matrix $\boldsymbol{E}$ is defined which satisfies $\boldsymbol{H}^{-1} = \boldsymbol{E}^{\mathrm{T}}\boldsymbol{E}$ as exemplified in (Wesseling 1992). However, a final back substitution leads to an algorithm which only includes $\boldsymbol{H}^{-1}$.

The convergence is improved by Eq. 5.55 if the condition number of the preconditioned matrix $(\boldsymbol{H}^{-1}\boldsymbol{K})$ is lower than that of the original matrix $\boldsymbol{K}$, which can be determined from the analysis of eigenvalues (Hackbusch 1991). If the preconditioning matrix would be $\boldsymbol{H}^{-1} = \boldsymbol{K}^{-1}$ then after one iteration step the exact solution $\boldsymbol{u}$ is found. In this sense, an ideal matrix $\boldsymbol{H}^{-1}$ is a good, but reasonably efficient approximation of $\boldsymbol{K}^{-1}$. With respect to the initial search direction, the vector $\boldsymbol{p}^0 = \boldsymbol{H}^{-1}\boldsymbol{r}^0$ would correspond to the error $-\boldsymbol{e}^0$ (Eq. 5.7), if $\boldsymbol{H}^{-1} = \boldsymbol{K}^{-1}$ (Section 5.3.7). An adequate matrix $\boldsymbol{H}^{-1}$ leads to an improved initial search direction $\boldsymbol{p}^0$. Therefore the preconditioned conjugate gradient method applies the following start conditions.

$$\boldsymbol{r}^0 = \boldsymbol{f} - \boldsymbol{K}\boldsymbol{u}^0 \; ; \quad \tilde{\boldsymbol{r}}^0 = \boldsymbol{p}^0 = \boldsymbol{H}^{-1}\boldsymbol{r}^0 \tag{5.56}$$

---

[1]In the following benchmark of the multigrid preconditioned conjugate gradient method (Section 5.11) only the plain Gauss-Seidel method (Section 5.3.3) has been applied instead of the symmetric Gauss-Seidel method (Section 5.3.5). This implementation of the algorithm showed stable convergence in our examples. For comparison also the symmetric Gauss-Seidel has exemplary been tested, but in the tested examples a relevant difference was not recognized.

The following equations of the preconditioned conjugate gradient method are adopted from (Tatebe 1993) in the notation of the conjugate gradient method in Section 5.3.7.

$$\lambda_k = \frac{\tilde{\boldsymbol{r}}^{k\mathrm{T}}\boldsymbol{r}^k}{\boldsymbol{p}^{k\mathrm{T}}\boldsymbol{K}\boldsymbol{p}^k} \tag{5.57}$$

$$\boldsymbol{u}^{k+1} = \boldsymbol{u}^k + \lambda_k \boldsymbol{p}^k \tag{5.58}$$

$$\boldsymbol{r}^{k+1} = \boldsymbol{r}^k - \lambda_k \boldsymbol{K}\boldsymbol{p}^k \tag{5.59}$$

$$\tilde{\boldsymbol{r}}^{k+1} = \boldsymbol{H}^{-1}\boldsymbol{r}^{k+1} \tag{5.60}$$

$$\boldsymbol{p}^{k+1} = \tilde{\boldsymbol{r}}^{k+1} + \frac{\tilde{\boldsymbol{r}}^{k+1\mathrm{T}}\boldsymbol{r}^{k+1}}{\tilde{\boldsymbol{r}}^{k\mathrm{T}}\boldsymbol{r}^k}\boldsymbol{p}^k \tag{5.61}$$

In each iteration step preconditioning only takes place in Eq. 5.60 and generates a new vector $\tilde{\boldsymbol{r}}^{k+1}$. For the present multigrid preconditioning the matrix $\boldsymbol{H}^{-1}$ is not explicitly build, but the operation defined in Eq. 5.60 is replaced by a multigrid cycle for the residual $\boldsymbol{r}^{k+1}$ and its solution is assigned to $\tilde{\boldsymbol{r}}^{k+1}$. Apart from this final transfer, it is noted that the multigrid cycle for Eq. 5.60 needs to be performed on an own, individual set of variables which is independent of the variables in Eqs. 5.57 to 5.61. The preconditioned version of the method preserves a system of conjugate directions (Section 5.3.7), while each increment is optimized for each improved search direction based on the multigrid method. Thus, with respect to the present application, it follows that this optimization leads to considerably improved increments, if the stiffness of the coarse meshes is generally overestimated with further reference to Section 5.10.1.

## 5.6 Error Measures

Generally it is assumed that the exact error $\boldsymbol{e}$ is not known, such that an error measure is constructed in terms of the residual $\boldsymbol{r}$. In the following error measures the set $A$ defines the sequence of all degrees of freedom with a prescribed force (also if equal to zero) and $B$ all those with a prescribed displacement. The Euclidean norm of residual forces (in $A$) is a usual measure

$$\epsilon_{\mathrm{a}}^k = \left[\sum_{i\in A}(r_i^k)^2\right]^{\frac{1}{2}} \tag{5.62}$$

It is more objective to use the relative measure

$$\epsilon_{\mathrm{r}}^k = \frac{\left[\sum_{i\in A}(r_i^k)^2\right]^{\frac{1}{2}}}{\left[\sum_{i\in A}\left(f_i\right)^2 + \sum_{j\in B}\left(f_j^k\right)^2\right]^{\frac{1}{2}}} \tag{5.63}$$

similar to (Parsons 1997). It is noted that in (Parsons 1997) part of the set $B$, of degrees of freedom with prescribed displacements, is probably not included. In (Häfner, Eckardt, Luther and Könke 2006) the following measure is proposed

$$\epsilon_{\mathrm{E}}^k = \frac{\sum\limits_{i \in A} |r_i^k u_i^k|}{\sum\limits_{i \in A} f_i u_i^k + \sum\limits_{j \in B} f_j^k u_j} \tag{5.64}$$

This measure can be interpreted in terms of relative error in energy. A practical comparison of these measures is performed in the benchmark of Section 5.11.2. Generally the considered algebraic error in solving the linear equation system shall be considerably lower than other error sources as e.g. the discretization error of finite elements. With respect to an overall error efficiency, errors from various sources would be comparable by a measure in terms of error in energy (which is discussed in the context of B-spline finite elements in Section 4.6.7).

## 5.7 Elaborate Properties of Solid Finite Elements

### 5.7.1 Scaling of Solid Finite Elements

A finite element is denoted isoparametric if the displacements $\boldsymbol{U}$ within the finite element are evaluated by the same interpolation functions, assembled in $\boldsymbol{N}(\boldsymbol{X})$, as the element coordinates $\boldsymbol{X}$

$$\boldsymbol{X} = \boldsymbol{N}(\boldsymbol{X})\boldsymbol{x} \tag{5.65}$$
$$\boldsymbol{U} = \boldsymbol{N}(\boldsymbol{X})\boldsymbol{u} \tag{5.66}$$

where it is implied that the nodal coordinates $\boldsymbol{x}$ are arranged in the same order as the coordinates of nodal displacements $\boldsymbol{u}$. With regard to the multigrid method hierarchical finite element meshes will be defined with isoparametric finite elements being similar in shape but various in size. The matrices of these similar finite elements at various scale follow a certain relationship which will subsequently be evaluated.

It is assumed that the finite element geometry of an initial size is given in a coordinate system $\boldsymbol{Z}$. This finite element will be mapped to a coordinate system $\boldsymbol{X}$. The corresponding geometry and interpolation is then given by

$$\boldsymbol{X} = \boldsymbol{N}(\boldsymbol{Z})\boldsymbol{x} \tag{5.67}$$
$$\boldsymbol{U} = \boldsymbol{N}(\boldsymbol{Z})\boldsymbol{u} \tag{5.68}$$

The procedure follows (Bathe 1996; Zienkiewicz and Taylor 1997). Therefore the following equality of partial derivatives is introduced

$$\frac{\partial}{\partial \boldsymbol{Z}} = \frac{\partial \boldsymbol{X}}{\partial \boldsymbol{Z}} \frac{\partial}{\partial \boldsymbol{X}} \ , \qquad \frac{\partial}{\partial Z_i} = \frac{\partial X_j}{\partial Z_i} \frac{\partial}{\partial X_j} \tag{5.69}$$

with the Jacobian matrix $\boldsymbol{J}$ defined as

$$\boldsymbol{J} = \frac{\partial \boldsymbol{X}}{\partial \boldsymbol{Z}} \ , \qquad J_{ij} = \frac{\partial X_j}{\partial Z_i} \tag{5.70}$$

The Jacobian matrix can be calculated by establishing the partial derivatives of $\boldsymbol{X}$ with respect to $\boldsymbol{Z}$ in terms of $\boldsymbol{N}(\boldsymbol{Z})\boldsymbol{x}$ according to Eq. 5.67. For regular mappings the inverse of the Jacobian matrix can be created which provides the inverse relationship

$$\boldsymbol{J}^{-1} = \frac{\partial \boldsymbol{Z}}{\partial \boldsymbol{X}} \tag{5.71}$$

For the special case that the element is scaled by a constant factor $c$, expressed by $\boldsymbol{x} = c\boldsymbol{z}$, it follows that

$$J_{ij} = \delta_{ij} c \tag{5.72}$$

which directly leads to

$$\frac{\partial}{\partial Z_i} = c \frac{\partial}{\partial X_i} \qquad \text{and} \qquad \frac{\partial}{\partial X_i} = \frac{1}{c} \frac{\partial}{\partial Z_i} \tag{5.73}$$

From the kinematics it follows that the strain-displacement matrix $\boldsymbol{B}(\boldsymbol{X})$ exactly includes only terms of first-order partial derivatives with respect to $X_i$. Then, with Eq. 5.73 the following relationship to $\boldsymbol{B}(\boldsymbol{Z})$ holds

$$\boldsymbol{B}(\boldsymbol{X}) = \frac{1}{c} \boldsymbol{B}(\boldsymbol{Z}) \tag{5.74}$$

The integral over the domain of the mapped geometry $\Omega_X(\boldsymbol{X})$ can be replaced by an integral over the domain of the initial geometry $\Omega_Z(\boldsymbol{Z})$

$$d\Omega_X = \det \boldsymbol{J} d\Omega_Z \tag{5.75}$$

where $\det \boldsymbol{J}$ is the determinant of the Jacobi matrix. According to Eq. 5.72 and the dimension $D$ of the domains, $\Omega_X$ and $\Omega_Z$, the determinant of the Jacobi matrix is

$$\det \boldsymbol{J} = c^D \tag{5.76}$$

with D=1, 2 or 3. Therewith the element stiffness matrix of the finite element scaled to $\boldsymbol{X}$ by the constant factor $c$ results as

$$\boldsymbol{K}_X = \boldsymbol{C}_{T,D} \int_{\Omega_X} \boldsymbol{B}(\boldsymbol{X})^{\mathrm{T}} \boldsymbol{C} \boldsymbol{B}(\boldsymbol{X}) d\Omega_X \tag{5.77}$$

where $C_{T,D}$ is a constant term. For three-dimensional elements the constant term is $C_{T,D=3} = 1$. For two-dimensional elements the thickness $t$ is constant and therefore $C_{T,D=2} = t$. Analog, for one-dimensional elements the area $A$ is not included in the integral which leads to $C_{T,D=1} = A$. With Eqs. 5.74 to 5.76 the stiffness matrix of Eq. 5.77 is established in terms of $\boldsymbol{Z}$

$$\boldsymbol{K}_X = c^{D-2} \left( \boldsymbol{C}_{T,D} \int_{\Omega_X} \boldsymbol{B}(\boldsymbol{Z})^{\mathrm{T}} \boldsymbol{C} \boldsymbol{B}(\boldsymbol{Z}) d\Omega_Z \right) \tag{5.78}$$

This means that the stiffness matrix of the scaled element $\boldsymbol{K}_X$ is $(c^{D-2})$-times the stiffness matrix of the initial element $\boldsymbol{K}_Z$

$$\boldsymbol{K}_X = c^{D-2} \boldsymbol{K}_Z \tag{5.79}$$

Herewith, this characteristic is generally shown for solid finite elements of any dimension, independent of number of nodes per element and independent of the initial element geometry. For two-dimensional elements ($D = 2$) this means that the stiffness matrix of an element does not change, if the element is scaled by a factor $c$. Otherwise, ($D \neq 2$), Eq. 5.79 establishes a simple relationship to create stiffness matrices for similar finite elements of different size based on an initial stiffness matrix.

### 5.7.2  Variation of Elastic Material Properties

For linear elastic materials the Young's modulus $E$ can be factored out of the material tensor $\mathbb{C}(E, \nu)$

$$\mathbb{C}(E, \nu) = E\mathbb{C}(1, \nu) \tag{5.80}$$

in contrast to Poisson's ratio $\nu$. In straight equivalence this property is also true for the material matrix $\boldsymbol{C}$ of the finite element method. Under the condition that the Young's modulus $E^e$ is constant within the domain of the finite element $e$, it can as well be factored out of the element stiffness matrix

$$\boldsymbol{K}^e(E^e, \nu^e) = E^e \boldsymbol{K}^e(1, \nu^e) \tag{5.81}$$

For a regular, uniform grid of finite elements which only vary in Young's modulus $E^e$, this characteristic enables a fast evaluation of element stiffness matrices based on one initial matrix $\boldsymbol{K}^e(1, \nu^e)$. The equality of Eq. 5.81 can be transfered to linear algebraic operations, such as the matrix–vector product of $\boldsymbol{K}^e(E^e, \nu^e)$ and an arbitrary vector $\boldsymbol{v}^e$

$$\left(E^e \boldsymbol{K}^e\left(1, \nu^e\right)\right) \boldsymbol{v}^e = E^e\left(\boldsymbol{K}^e\left(1, \nu^e\right) \boldsymbol{v}^e\right) \tag{5.82}$$

where the term of the right hand side counts less operations. Thus, it is neither required to explicitly build nor to store the stiffness matrices for finite elements with various Young's modulus to perform such operations on the element level.

The procedure is different for finite elements with various Poisson's ratio. It is possible to split the element stiffness matrix into parts, where each part is of equal order with respect to Poisson's ratio, such that it is possible to assemble element stiffness matrices of various Poisson's ratio efficiently.

The current implementation only includes operations according to Eq. 5.82. The theoretical range of Poisson's ratio is limited to $\nu = [0.00; 0.50]$. For phases in concrete this range usually reduces to $\nu = [0.15; 0.25]$. It would be possible to cover the occurring range by a predefined set of stiffness matrices at equidistant Poisson's ratios, e.g. fifty-one stiffness matrices would cover the full range by an accuracy of $\nu = \pm 0.005$. For a very high number of different Poisson's ratio in the elements, this can be reasonable, as the usual variation of Poisson's ratio is less significant for the mechanical behavior than the usual variation of Young's modulus. Furthermore, it is quite seldom that more than two effective digits of the Poisson's ratio are provided anyway. Otherwise, ideal for a low number of different Poisson's ratios, as in the implementation, a direct representation of initial stiffness matrices for all occurring Poisson's ratios is useful.

In fact, with the identities of Eq. 5.79 and 5.81 for finite elements of various Young's modulus and various element size (but similar shape and equal Poisson's ratio), only one initial finite element stiffness matrix is required. On the one hand this theoretical aspect is practical for implementation. Moreover, with respect to various Poisson's ratios and various element types, as in the B-spline finite element method (Chapter 4), the number of initial element stiffness matrices to be built can drastically be reduced. Especially for B-spline finite elements of higher order, the corresponding gain in generation effort and memory requirement is relevant.

# 5.8 Definition of Global Finite Element Problem on Orthogonal Grid

The priorly stated principle of virtual displacements leads to the finite element formulation which is applicable to problems of structural mechanics in general. Clearly, general finite element programs include the possibility to compute finite element problems on orthogonal grids. Due to their flexibility these programs usually include a element table to store the node numbers of each element and a node table to store the coordinates of each node. Moreover, the effective finite element problem will be stored in a global stiffness matrix. The solver method will be of a general kind for sparse matrices. For all post-processing during or after computation the various tables need to be recalled. Thereby all element formulations will be based on a general description which is flexible in geometry.

Subsequently a special formulation is introduced for two- and three-dimensional finite elements on orthogonal grids with focus on high computational performance with low memory demand in respect to this particular problem. It will especially be applicable to the mechanical analysis of heterogeneous solids on the mesoscale, where a macroscopic simple domain of a corresponding specimen is sufficient.

Figure 5.2 shows a two-dimensional mesh of $n_{ex} \times n_{ey}$ elements and $n_{nx} \times n_{ny}$ nodes where

$$n_{nx} = n_{ex} + 1 \tag{5.83}$$
$$n_{ny} = n_{ey} + 1 \tag{5.84}$$

The variables

$$i_e = 0 \ldots (n_{ex} - 1) \tag{5.85}$$
$$j_e = 0 \ldots (n_{ey} - 1) \tag{5.86}$$

refer to the elements and

$$i_n = 0 \ldots (n_{nx} - 1) \tag{5.87}$$
$$j_n = 0 \ldots (n_{ny} - 1) \tag{5.88}$$

refer to the nodes. The coordinates $(x,y)$ of a node located at $(i_n, j_n)$ is defined as

$$x = i_n \, l_a \tag{5.89}$$
$$y = j_n \, l_b \tag{5.90}$$

where $l_a$ and $l_b$ mean the element size in the corresponding direction. It follows that the total dimensions $l_x$ and $l_y$ of the mesh are

$$l_x = n_{ex} \, l_a \tag{5.91}$$
$$l_y = n_{ey} \, l_b \tag{5.92}$$

The numbering of elements $p_e$ and nodes $p_n$ is defined according to

$$p_e = i_e + j_e \, n_{ex} \tag{5.93}$$
$$p_n = i_n + j_n \, n_{nx} \tag{5.94}$$

so that $p_e \in [0\,;\,(n_{exy} - 1)]$ with $n_{exy} = n_{ex} n_{ey}$ and $p_n \in [0\,;\,(n_{nxy} - 1)]$ with $n_{nxy} = n_{nx} n_{ny}$. The finite element problem can be defined on vectors of corresponding dimensions. Such essential vectors are the displacements $\boldsymbol{u}_x$ and $\boldsymbol{u}_y$, the type of boundary condition[2]

---

[2]Type of boundary condition is e.g. "0" for prescribed force or "1" for prescribed displacement.
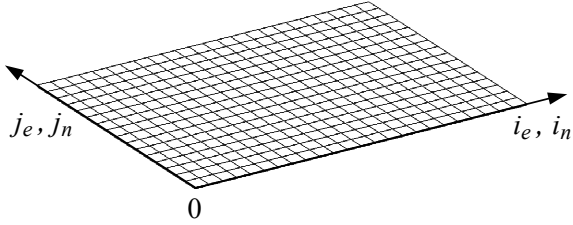
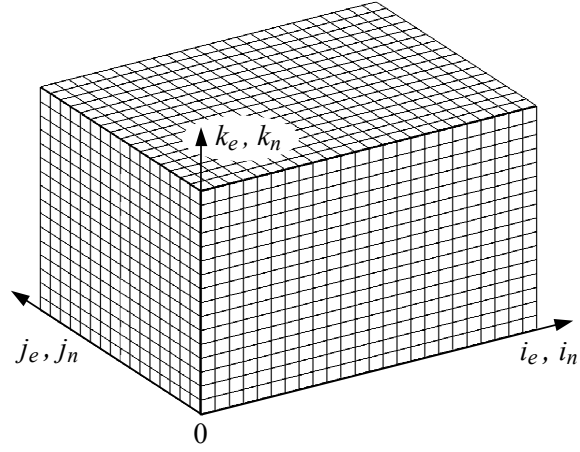Figure 5.2: Two-dimensional, uniform, orthogonal, mesh



Figure 5.3: Three-dimensional, uniform, orthogonal, mesh

$\boldsymbol{b}_{Tx}$ and $\boldsymbol{b}_{Ty}$ and values of boundary condition $\boldsymbol{b}_{Vx}$ and $\boldsymbol{b}_{Vy}$. For each element an individual Young's modulus can be defined and therefore a corresponding vector $\boldsymbol{v}_E$ is allocated. By an integer vector $\boldsymbol{v}_I$ each element can link to a specified material. The material definition includes the Poisson's ratio for linear analysis and may include several other variables such as the stress limit for nonlinear analysis. Therewith the basic finite element definitions are outlined. Iterative solver methods additionally require some vectors such as displacement increments and other swap memory. Furthermore for graphical processing some additional, primarily static memory is appropriate. For the linear elastic analysis, a summary of the overall memory demand is provided in (Häfner, Eckardt, Luther and Könke 2006) and in Section 5.11.1.

The extension to a three-dimensional mesh as shown in Fig. 5.3 is perfectly straightforward. For the three-dimensional mesh of $n_{ex} \times n_{ey} \times n_{ez}$ elements and $n_{nx} \times n_{ny} \times n_{nz}$ nodes only the following definitions need to be added.

$$
\begin{aligned}
n_{nz} &= n_{ez} + 1 & \text{analog to Eqs. 5.83, 5.84} && (5.95) \\
k_e &= 0 \ldots (n_{ez} - 1) & \text{analog to Eqs. 5.85, 5.86} && (5.96) \\
k_n &= 0 \ldots (n_{nz} - 1) & \text{analog to Eqs. 5.87, 5.88} && (5.97) \\
z &= k_n \, l_c & \text{analog to Eqs. 5.89, 5.90} && (5.98) \\
l_z &= n_{ez} \, l_c & \text{analog to Eqs. 5.91, 5.92} && (5.99)
\end{aligned}
$$

Equivalently, the element numbering $p_e$ and node numbering $p_n$ is extended.

$$
\begin{aligned}
p_e &= i_e + j_e \, n_{ex} + k_e \, n_{exy} & \text{analog to Eq. 5.93} && (5.100) \\
p_n &= i_n + j_n \, n_{nx} + k_n \, n_{nxy} & \text{analog to Eq. 5.94} && (5.101)
\end{aligned}
$$

Also the number of vectors needs to be extended, as e.g. by $\boldsymbol{u}_z$, $\boldsymbol{b}_{Tz}$, $\boldsymbol{b}_{Vz}$ and so on. With respect to various operations of the proposed implementation, it is most appropriate to store these vectors of concurrent meaning, but various orientation ($x$, $y$ or $z$), in one continuous data field. For the displacements this means a continuous vector field[3] $\boldsymbol{u}$ of $(\boldsymbol{u}_x, \boldsymbol{u}_y, \boldsymbol{u}_z)$ so that global vector operations with $\boldsymbol{u}$ are simply defined, while the subvectors remain directly accessible.

---

[3]Without consideration of boundary conditions.

# 5.9 Element-based Global Operations

A two-dimensional and three-dimensional uniform, orthogonal grid of finite elements is considered. Due to the prior definitions, for both cases, iterative solver methods can be applied without storage of the global stiffness matrix. Therefore some global operations will be prepared based on operations of a local finite element topology.

## 5.9.1 Global Matrix-Vector Product

For the global matrix-vector product $\boldsymbol{K}\boldsymbol{v}$, of global stiffness matrix $\boldsymbol{K}$ and arbitrary global vector $\boldsymbol{v}$, Eq. 4.10 is recalled. It follows that this global matrix-vector product can be formulated as a sum of matrix-vector products on the element level

$$\boldsymbol{K}\boldsymbol{v} = \sum_e \left(\bar{\boldsymbol{K}}^e \boldsymbol{v}\right) = \sum_e \left(\bar{\boldsymbol{K}}^e \bar{\boldsymbol{v}}^e\right) \tag{5.102}$$

with element stiffness matrix $\bar{\boldsymbol{K}}^e$ and corresponding displacements $\bar{\boldsymbol{v}}^e$ of element $e$ where the bar over the symbols highlights the assignment to global degrees of freedom. However, it is more practical to perform these operations on the element level within local degrees of freedom, also found in (Parsons 1997). For the element $e$ the appropriate components of $\boldsymbol{v}$ are gathered in $\boldsymbol{v}^e$. The local operation $\boldsymbol{K}^e \boldsymbol{v}^e$ is performed and the result is added to the corresponding components of the global result vector. This procedure is performed for all elements, in analogy to Eq. 5.102 (r.h.s.).

## 5.9.2 Operations on Finite Elements Stencils

As one basic idea of the finite element method a body will be divided into parts such that each displacement interpolation function has only small support in the domain of the body. Each displacement interpolation function, or shape function, is assigned to a degree of freedom at a specific node. Therefore, the direct interaction radius of this node is limited. Considering a specific node, a direct stiffness relationship will only be defined to nodes which are attached to the same elements[4].

As a result, an adequate global numbering implied, the global stiffness matrix will be sparse. Among other things, this is an advantageous characteristic for direct solver methods. Special data structures have been developed to store sparse matrices. The following operation is considered

$$f_i = \sum_j K_{ij} u_j \tag{5.103}$$

where $i$ and $j$ refer to the global degrees of freedom. For large matrices $\boldsymbol{K}$ only a small fraction of entries $K_{ij}$ will not be zero. With data structures of sparse matrices all, or most, zero entries are not even processed at all to evaluate the product of Eq. 5.103. The same effect is achieved by only including nodal degrees of freedom which refer to the same

---

[4]This is generally true, but with B-spline finite elements (Chapter 4) the support of the shape functions will increase and cover several elements dependent on the order of the B-splines.

elements as the degree of freedom $i$, which motivates a local node-by-node iterative solver method without storage of a global stiffness matrix.

Such a local scheme will especially be efficient if it is recurrent. Then, it is labeled as finite element stencil. This principle will be exemplified for uniform orthogonal grids of two-dimensional four-node finite elements and three-dimensional eight-node finite elements. However, it is noted that the fundamental idea is more general, as previously introduced, and may be transfered to finite elements of other shape (e.g. triangular) or of other polynomial order, while it can also be regarded as sparse data structure technique.

On a uniform, orthogonal grid of finite elements, for any inner node the topology to its neighboring nodes is identical. The finite element stencil is similar to the finite difference stencil while the first is based on the principle of virtual displacements and the latter refers to a direct discretization of the differential equation (Hackbusch 1985).

### 5.9.3 Stencil for Grid of Two-Dimensional Four-Node Elements

For a uniform orthogonal grid of finite elements, the degrees of freedom (dof) of any interior node can locally and temporarily assigned as (9,10) which refers to the horizontal and vertical component, respectively (Fig. 5.5).
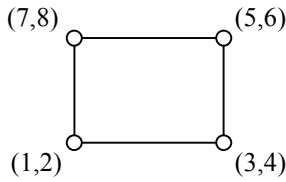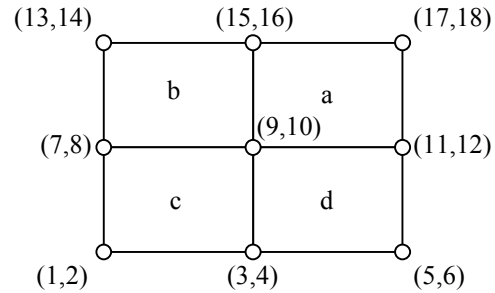


Figure 5.4: Dof of one element



Figure 5.5: Dof of $2 \times 2$ element patch

The element stiffness matrix with Young's modulus $E = 1$ is denoted as basic element stiffness matrix $\bar{\boldsymbol{K}}(\mu) = \boldsymbol{K}_{\mathrm{e}}(1, \mu)$. Then, the stiffness of the center node can be assembled as follows

$$\hat{K}_{9,9} = E^a \bar{K}(\mu^a)_{1,1} + E^b \bar{K}(\mu^b)_{3,3} + E^c \bar{K}(\mu^c)_{5,5} + E^d \bar{K}(\mu^d)_{7,7} \tag{5.104}$$

$$\hat{K}_{9,10} = E^a \bar{K}(\mu^a)_{1,2} + E^b \bar{K}(\mu^b)_{3,4} + E^c \bar{K}(\mu^c)_{5,6} + E^d \bar{K}(\mu^d)_{7,8} \tag{5.105}$$

$$\hat{K}_{10,10} = E^a \bar{K}(\mu^a)_{2,2} + E^b \bar{K}(\mu^b)_{4,4} + E^c \bar{K}(\mu^c)_{6,6} + E^d \bar{K}(\mu^d)_{8,8} \tag{5.106}$$

The superscript a to d refers to the system of one element according to Fig. 5.4. The hat-symbol denotes the reference to the $2 \times 2$ element patch of Fig. 5.5. The corresponding residual forces $\hat{r}_9$ and $\hat{r}_{10}$ are calculated by

$$\hat{r}_9 = \hat{f}_9 - \sum_{i=1}^{8} \left( E^a \bar{K}(\mu^a)_{1,i} u_i^a + E^b \bar{K}(\mu^b)_{3,i} u_i^b + E^c \bar{K}(\mu^c)_{5,i} u_i^c + E^d \bar{K}(\mu^d)_{7,i} u_i^d \right) \tag{5.107}$$

$$\hat{r}_{10} = \hat{f}_{10} - \sum_{i=1}^{8} \left( E^a \bar{K}(\mu^a)_{2,i} u_i^a + E^b \bar{K}(\mu^b)_{4,i} u_i^b + E^c \bar{K}(\mu^c)_{6,i} u_i^c + E^d \bar{K}(\mu^d)_{8,i} u_i^d \right) \tag{5.108}$$

for any interior node, or after correct assignment of $u^{a..d}$ to $\hat{u}$ and corresponding assembly of $\hat{K}_{9,i}$ and $\hat{K}_{10,i}$ from Eqs. (5.107) and (5.108) by

$$\hat{r}_9 = \hat{f}_9 - \sum_{i=1}^{18} \hat{K}_{9,i}\hat{u}_i \tag{5.109}$$

$$\hat{r}_{10} = \hat{f}_{10} - \sum_{i=1}^{18} \hat{K}_{10,i}\hat{u}_i \tag{5.110}$$

Boundary nodes can be included by omitting the terms of inexistent neighboring elements. Local equilibrium at this node with respect to the degree of freedom $i$ only, is achieved by adding the increment $\Delta\hat{u}_i$ to $\hat{u}_i$.

$$\Delta\hat{u}_i = \frac{\hat{r}_i}{\hat{K}_{ii}} \tag{5.111}$$

Such an increment can either refer to Eq. 5.17 of the Jacobi method or to Eq. 5.22 of the Gauss-Seidel method (Section 5.3, especially 5.3.4). Local equilibrium for both degrees of freedom $\hat{u}_9$ and $\hat{u}_{10}$ is established by the local increment vector

$$\begin{bmatrix} \Delta\hat{u}_9 \\ \Delta\hat{u}_{10} \end{bmatrix} = \begin{bmatrix} \hat{K}_{9,9} & \hat{K}_{9,10} \\ \hat{K}_{10,9} & \hat{K}_{10,10} \end{bmatrix}^{-1} \begin{bmatrix} \hat{r}_9 \\ \hat{r}_{10} \end{bmatrix} \tag{5.112}$$

For four rectangular finite elements of same Poisson's ratio and same shape several prior equations can be shortened as due to the equalities

$$\bar{K}(\mu)_{1,1} = \bar{K}(\mu)_{3,3} = \bar{K}(\mu)_{5,5} = \bar{K}(\mu)_{7,7} \tag{5.113}$$

$$\bar{K}(\mu)_{1,2} = -\bar{K}(\mu)_{3,4} = \bar{K}(\mu)_{5,6} = -\bar{K}(\mu)_{7,8} \tag{5.114}$$

$$\bar{K}(\mu)_{2,2} = \bar{K}(\mu)_{4,4} = \bar{K}(\mu)_{6,6} = \bar{K}(\mu)_{8,8} \tag{5.115}$$

e.g. the Eqs. 5.104 to 5.106 can be simplified to

$$\hat{K}(\mu)_{9,9} = (E^a + E^b + E^c + E^d)\bar{K}(\mu)_{1,1} \tag{5.116}$$

$$\hat{K}(\mu)_{9,10} = (E^a - E^b + E^c - E^d)\bar{K}(\mu)_{1,2} \tag{5.117}$$

$$\hat{K}(\mu)_{10,10} = (E^a + E^b + E^c + E^d)\bar{K}(\mu)_{2,2} \tag{5.118}$$

### 5.9.4 Stencil for Grid of Three-Dimensional Eight-Node Elements

The extension of the stencil from the two-dimensional to the three-dimensional problem is straightforward. Nevertheless, the number of degrees of freedoms essentially increases. The notation is analog. The superscript a to h refers to the system of one brick element according to Fig. 5.6. The hat-symbol denotes the reference to the eight brick elements of Fig. 5.7. In this figure only the degrees of freedom $(1, 2, 3)$ which are assigned to the highlighted node will subsequently be relevant. The stiffness of this node is assembled by

$$\hat{K}_{1,1} = E^a\bar{K}(\mu^a)_{1,1} + E^b\bar{K}(\mu^b)_{4,4} + \ldots + E^h\bar{K}(\mu^h)_{22,22} \tag{5.119}$$

$$\hat{K}_{2,2} = E^a\bar{K}(\mu^a)_{2,2} + E^b\bar{K}(\mu^b)_{5,5} + \ldots + E^h\bar{K}(\mu^h)_{23,23} \tag{5.120}$$

$$\hat{K}_{3,3} = E^a\bar{K}(\mu^a)_{3,3} + E^b\bar{K}(\mu^b)_{6,6} + \ldots + E^h\bar{K}(\mu^h)_{24,24} \tag{5.121}$$
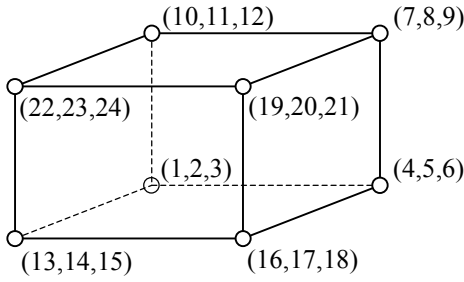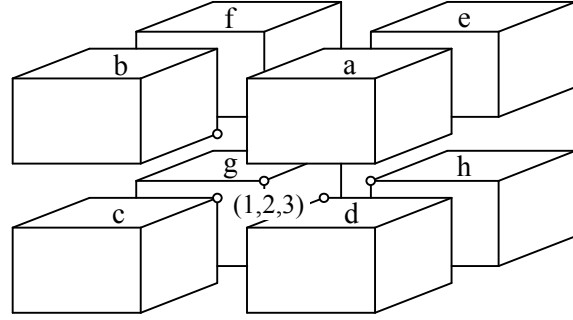
Figure 5.6: Dof of one brick element



Figure 5.7: $2 \times 2 \times 2$ brick elements

and the residual forces are

$$\hat{r}_1 = \hat{f}_1 - \sum_{i=1}^{24} \left( E^a \bar{K}(\mu^a)_{1,i} u_i^a + E^b \bar{K}(\mu^b)_{4,i} u_i^b + \ldots + E^h \bar{K}(\mu^h)_{22,i} u_i^h \right) \tag{5.122}$$

$$\hat{r}_2 = \hat{f}_2 - \sum_{i=1}^{24} \left( E^a \bar{K}(\mu^a)_{2,i} u_i^a + E^b \bar{K}(\mu^b)_{5,i} u_i^b + \ldots + E^h \bar{K}(\mu^h)_{23,i} u_i^h \right) \tag{5.123}$$

$$\hat{r}_3 = \hat{f}_3 - \sum_{i=1}^{24} \left( E^a \bar{K}(\mu^a)_{3,i} u_i^a + E^b \bar{K}(\mu^b)_{6,i} u_i^b + \ldots + E^h \bar{K}(\mu^h)_{24,i} u_i^h \right) \tag{5.124}$$

or in a generic form where $\alpha = 1 \ldots 8$ means $a \ldots h$ in the index.

$$\hat{r}_j = \hat{f}_j - \sum_{\alpha=1}^{8} E^\alpha \sum_{i=1}^{24} \bar{K}(\mu^\alpha)_{[3(\alpha-1)+j],i} u_i^\alpha \tag{5.125}$$

Analog to Eq. 5.111 the increment according to the stationary iterative method can be computed for the three-dimensional case.

### 5.9.5 Local Schemes of Advanced Finite Elements for Heterogeneous Material

In the prior sections constant material properties are assigned to each element. This leads to plain pixel or voxel discretization. This method is applicable to obtain reasonable overall properties of a heterogeneous material sample, but due to the grid discretization there will be errors in the stress solution along material interfaces.

It is possible to improve the accuracy of the geometrical discretization by advanced finite elements while maintaining a uniform orthogonal mesh. One option are multiphase B-spline finite elements as presented in Chapter 4. This discretization type is illustrated in Fig. 5.8 (left). The large black dots indicate integration points to each of which individual material properties can be assigned. Thus a smooth transition of material properties is possible within a finite element. As all finite elements are based on the same topology, similar local schemes as described in Section 5.9.1 to 5.9.4 can be created and the storage of a global stiffness matrix is not required.

The same is principally possible for other advanced finite elements with additional shape functions which are declared as internal degrees of freedom (finite elements with em-
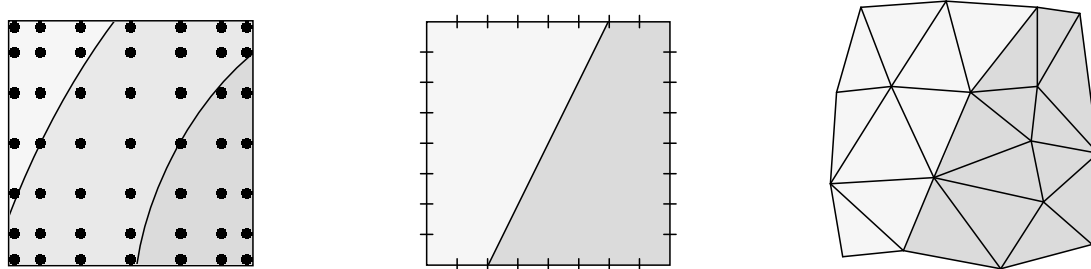
Figure 5.8: Discretization of heterogeneous material by a multiphase finite element (left), a finite element enriched by additional shape functions (center) and an aligned triangular mesh (right).

bedded discontinuities) or as global degrees of freedom (extended finite elements). As a condition the material interfaces is not completely variable but assigned to a finite pre-defined number of possibilities. In Fig. 5.8 (center) from corner to corner of one edge there are nine different settings, marked by a short line. According to this pattern there are $(23 \cdot 7 + 15)4/2 = 352$ different possible material interfaces which can be assigned to the element. The stiffness matrices need to be stored decoupled for the different material phases in the element. Then, it is possible to include such finite elements into a local scheme of a uniform grid, based on a comparatively low number of predefined element stiffness matrices. And the storage of a global stiffness matrix would not be required.

### 5.9.6   Local Schemes of Irregular Triangular Mesh

This section shall only briefly highlight that also for a irregular mesh of triangular finite elements (Fig. 5.8 (right)), required parts of a global stiffness matrix can efficiently be assembled based on a comparatively low number of element stiffness matrices. As the element stiffness matrix is invariant with respect to linear scaling of the finite element (Section 5.7.1), only the angles $\alpha$ and $\beta$ are required to determine the relevant shape of the finite element (Fig. 5.9). With the definition that $\alpha \leq \beta \leq \gamma$ it follows that there are the following bounds on $\alpha$ and $\beta$

$$0° < \alpha \leq 60° \tag{5.126}$$
$$\alpha \leq \beta < 90° \tag{5.127}$$

Hence, for an allowed tolerance of $\pm 0.5°$ there are *only* about 3600 different elements stiffness matrices required. Especially for very large models with $\geq 10^6$ degrees of freedom such an element library represents an effective alternative to storing a global stiffness matrix. Global operations on these elements can be performed as illustrated in Fig. 5.9. The global degrees of freedom $\boldsymbol{u}^e$ are transformed into local degrees of freedom $\bar{\boldsymbol{u}}^e$. These can be multiplied by the basic stiffness matrix $\bar{\boldsymbol{K}}^e(\alpha, \beta)$ to obtain the effective force vector $\bar{\boldsymbol{f}}^e$. A multiplication with the Young's modulus of this element is also required. Then the force vector can be transformed back into the global coordinate system $\boldsymbol{f}^e$. In addition for each element only a transformation angle and a triangle shape type (with respect to $\alpha$ and $\beta$) needs to be stored. It is further noted, that this principle is not limited to the three-node triangular finite elements as long as a definition is unique (e.g. nodes on center of element edge). It is only a matter of model size when it becomes more efficient to use a predefined library of finite elements. This supports the basic idea of the present approach to reduce the memory demand to a minimum.
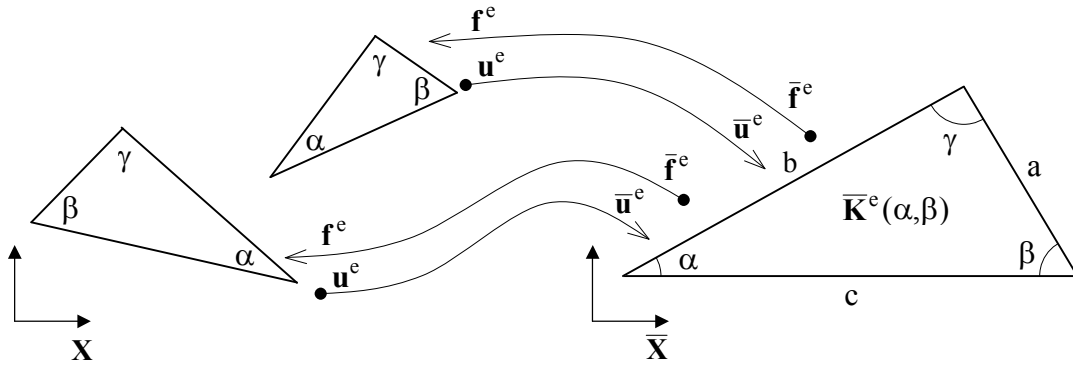
Figure 5.9: Scheme of establishing a product of element stiffness matrix and displacement vector in a global coordinate system $X$ based on a triangular element with angles $\alpha$ and $\beta$ in a local coordinate system $\bar{X}$.

## 5.10 Transfer Operators

### 5.10.1 Fine-to-Coarse Mesh Transformation of Young's Modulus

A finite element mesh of a heterogeneous material sample is considered. Here, one individual Young's modulus is assigned to each element of a uniform orthogonal grid. As an example in Fig. 5.10 the relevant finite element mesh is at level 7. All coarser grids of finite elements shall represent a good approximation of the heterogeneous material distribution which is defined on the finest mesh. Therefore it is possible to define adequate algebraic operators as discussed in (Bayreuther 2004). However, in this approach only the geometric multigrid method is considered such that the local scheme of finite elements can be applied on each mesh without additional memory demand for storing matrices of
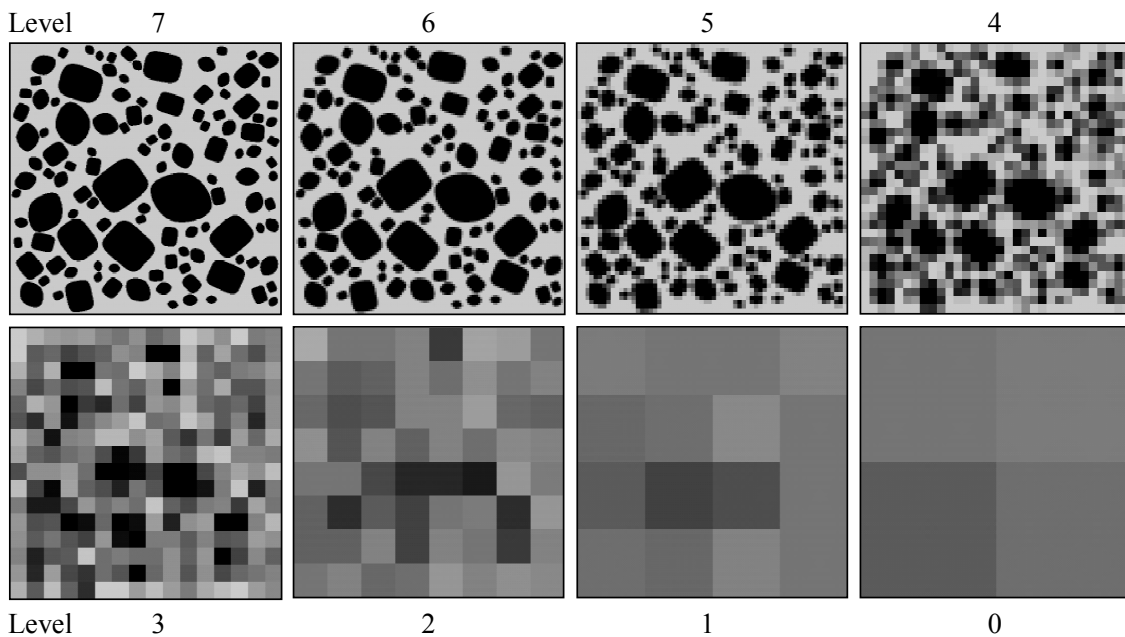


Figure 5.10: Definition of Young's modulus on finest mesh (Level 7) and corresponding coarse grid approximations of Young's modulus (Level 6 to 0)

operators or stiffness matrices of coarse grids. A doubling of mesh size means that four finite elements of the original mesh are represented by one element on the next coarser mesh. This corresponds to a kind of homogenization. An adequate effective Young's modulus of this element is in between the Reuss bound and the Voigt bound (Section 3.3.4). But as the original patch of elements might have different effective stiffnesses with respect to different directions, according to the prior definitions, such an anisotropic property can not be assigned to one coarse finite element. In this approach just the Voigt bound is applied which corresponds to the arithmetic mean of the various original Young's moduli. Therefore the coarser meshes will effectively be too stiff, which will result in slower but stable convergence. For larger ratios of Young's modulus in the heterogeneous material this defective overestimation of stiffness will become more severe (which explains the remedy by the multigrid preconditioned conjugate gradient method in connection with the last paragraph of Section 5.5). For the Reuss bound the iteration process can become instable. The Hashin-Shtrikman bound (Section 3.3.4) would be an appropriate alternative to define effective Young's moduli on coarser meshes based on the finest mesh. This option would establish an approximation which is closest to the original problem. But for some problems this choice might not be convergent[5]. For the sake of solving stability, the Voigt bound is applied. A corresponding example is shown in Fig. 5.10.

## 5.10.2 Restriction: Fine-to-Coarse Mesh Transformation of Forces

The starting point is any arbitrary vector of forces on a fine mesh. A best possible, equivalent representation of such forces on a coarse mesh is intended. There are several different restriction operators defined in connection with the multigrid method (Wesseling 1992). The applied restriction operator corresponds to the fundamental finite element definition with respect to the mechanical problem.

$$\boldsymbol{f}^e = \sum_i \left( \boldsymbol{N}^e_{\text{at } \boldsymbol{X}_i} \right)^{\text{T}} \boldsymbol{F}_i \tag{5.128}$$

The vector $\boldsymbol{F}_i$ denotes a point load[6] at position $\boldsymbol{X}_i$ within the element $e$. This load is assigned to the force vector $\boldsymbol{f}^e$ of element $e$ by the evaluation of the element shape function $\boldsymbol{N}^e$ at coordinate $\boldsymbol{X}_i$. In Fig. 5.11 a force $\boldsymbol{F}_i$ (×-symbol), e.g. from a finer mesh, is assigned to the nodal force vector of the lower left node $\boldsymbol{f}_1$ (gray node) of a bilinear finite element. This yields

$$\boldsymbol{f}_{1,i} = \left( 1 - \frac{s_{x,i}}{h_x} \right) \left( 1 - \frac{s_{y,i}}{h_y} \right) \boldsymbol{F}_i \tag{5.129}$$

With respect to an implementation it can further be utilized that in the considered example the relevant values of the fractions $\frac{s_{x,i}}{h_x}$ and $\frac{s_{y,i}}{h_y}$ are limited to $\frac{s}{h} \in \left[ 0; \frac{1}{4}; \frac{1}{2}; \frac{3}{4} \right]$. A corresponding predefined template minimizes the computational effort in contrast to the formal symbolic definition of Eq. 5.128. An extension to three dimensions is straightforward.

---

[5] Any underestimation of coarse grid stiffness can lead to a relevant overestimation of displacement increments from coarse grid correction and thus to oscillating behavior.

[6] In the present context, for the computation of an equivalent coarse mesh residual, the problem of a singularity does not apply.
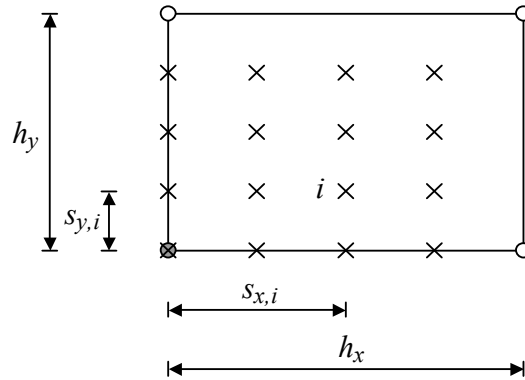
Figure 5.11: A rectangular four-node finite element of size $h_x \times h_y$ and some selected point loads located at $(s_{x,i}, s_{y,i})$, which may result from the nodal disequilibrium of a finer mesh, relevant with respect to the gray node of the element (lower left corner).

### 5.10.3  Prolongation: Coarse-to-Fine Mesh Interpolation of Displacements

The relationship to determine the displacement $\boldsymbol{U}$ at coordinate $\boldsymbol{X}_i$ within an element $e$ with nodal displacements $u^e$ is defined by the interpolation or shape function $\boldsymbol{N}^e$.

$$\boldsymbol{U}_{\text{at } \boldsymbol{X}_i} = \boldsymbol{N}^e_{\text{at } \boldsymbol{X}_i} \, \boldsymbol{u}^e \tag{5.130}$$

For usual finite elements the displacement at a coordinate of a node corresponds to the nodal value of the degree of freedom. Therefore the basic Eq. 5.130 is sufficient to construct any coarse-to-fine mesh interpolation operator. Again, specific templates can reduce the computational effort.

### 5.10.4  Transfer Operators for B-Spline Finite Elements

A multigrid method for web-splines[7] is presented in (Höllig, Reif and Wipper 2002). As an alternative method the convergence of B-spline finite elements could be accelerated by coarse grid corrections from the present, existing multigrid method for bilinear finite elements. This only requires transfer operations between a mesh of classical, bilinear finite elements (B-splines of order $k = 1$) and a mesh of B-Spline finite elements of order $k = 2$ with an identical number of elements. The B-spline finite element problem is only transfered to the bilinear finite elements and then the present multigrid method with bilinear finite elements can be applied. After each cycle the displacement increment is transfered to the B-spline mesh again. After that smoothing is performed on the finest mesh of B-spline finite elements. It is assumed that the transfer operators need to be reasonably adequate, but not exact, as each coarse grid correction step is always an approximation only.

The restriction operator is not discussed in detail. From the residual forces of a B-spline finite element one could retrieve corresponding body loads $\boldsymbol{p}^e_b$ or surface loads $\boldsymbol{p}^e_s$, which

---

[7]Web-splines means weighted extended B-splines. Web-splines are introduced to model a curved domain which is not aligned to a grid. Such an extension of B-splines along the boundary of the domain assures that each finite element shape function has sufficient support for a stable numerical analysis. In the interior of the domain the web-splines principally correspond to B-splines (Chapter 4).
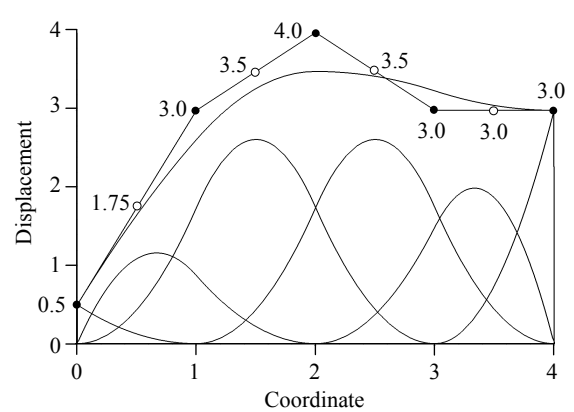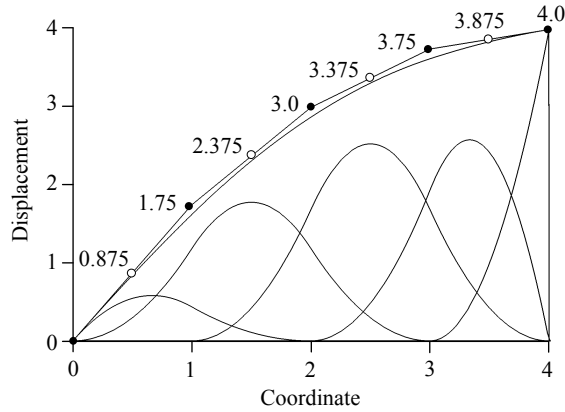
Figure 5.12: A piecewise, linear function (●) is approximated by quadratic B-splines. The values at (○) denote the coefficients which are assigned to the individual B-spline functions.

Figure 5.13: Another example, analog to Fig. 5.12.

can be compiled into a corresponding element force vector $\boldsymbol{f}^e$ by Eq. 4.8. The prolongation operator is more involving. A $C^0$-continuous displacement solution of linear finite elements can not exactly be mapped onto a B-spline finite element space which is $C^1$-continuous by definition. An exact interpolation of B-splines through all nodal values would require to build and solve an equation system. This would be very costly. Alternatively an intuitive operator is introduced and exemplified for one-dimensional examples.

For the transfer of a linear displacement field this operator is exact. This will be clear with respect to the following example and in connection with the first example of bar elements (Fig. 4.5). Figure 5.12 shows four piecewise linear functions with nodal values (●) on $U = -\frac{1}{4}x^2 + 2x$. The coefficients, or degrees of freedom, of B-spline shape functions are the mean values (○) of neighboring nodal values. At the boundary the nodal values correspond to the B-spline coefficients. Figure 5.12 shows an adequate approximation of the piecewise linear function by B-splines of order $k = 2$. Another example is shown in Fig. 5.13. Here, the transformation appears less accurate. However, as a global approximation it is reasonable and appropriate to the purpose of coarse grid correction.

The two-dimensional counterpart is illustrated in Fig. 5.14. The B-spline coefficients correspond to an evaluation of the bilinear solution at coordinates marked by a circle (○).
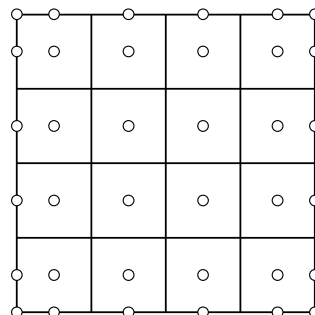


Figure 5.14: Coordinates for evaluation of coefficients which are assigned to bivariate B-spline functions; the two-dimensional analogy to Figs. 5.12 and 5.13.

# 5.11   Benchmark

The present benchmark evaluates the characteristics of the proposed multigrid methods in the mechanical analysis of heterogeneous solids. In this benchmark classical finite elements of linear order were applied. Sections 5.11.1 to 5.11.3 refer to various aspects of the multigrid method in its application to two-dimensional models. Some corresponding results from three-dimensional models are presented in Section 5.11.4.

## 5.11.1   Memory Demand

For the orthogonal grids of $n_{nx} \times n_{ny}$ nodes all data is stored in vectors of length $(n_{nx}n_{ny})$. In total thirteen vectors of 64-bit precision (double) are allocated for: Young's modulus, Poisson's ratio, displacements (x,y), displacement increments (x,y), residual forces (x,y), swap memory (2), values of boundary conditions (x,y) and values of post-processing. Additionally three vectors of 32-bit precision (integer) are allocated for: material type and type of boundary condition (x,y). In total this leads to 116 bytes per node. A problem of $2048 \times 2048$ elements includes 8.4 million degrees of freedom. For this mesh the multigrid method can be applied based on a hierarchy of eleven meshes (with 1024, 512 . . . 2 elements along the side). Altogether these meshes include 5600603 nodes. For the provided 116 bytes per node this yields 620 MB. In the corresponding computation the operating system shows a memory usage of 623 MB. It is true that some memory could be shared and the precision be reduced where it is not needed. Nevertheless, as only essential vectors are stored, it is clear that the memory usage is close to a possible minimum for the proposed method and in general low for such a large finite element problem.

## 5.11.2   Computation Times and Convergence

First, a previous benchmark of the multigrid method from (Häfner, Eckardt, Luther and Könke 2006) is presented by Fig. 5.15. It is included to show the relevant effects which motivated for further developments. The study is based on a two-dimensional model of concrete. The applied load cases, Ex. 1 and Ex. 2, are illustrated in Fig. 5.15. Both load cases have been tested for different ratios $R$ of Young's modulus between aggregates and matrix ($R$=2/1, $R$=4/1 and $R$=8/1). The allowed error tolerance was $\epsilon_{\mathrm{E}} = 1.0 \cdot 10^{-6}$ (Eq. 5.64). The tests were computed on a single processor with clock frequency 2.8 GHz (also the following examples). In this benchmark the computation time increases approximately by the order of $N^{1.1}$ for $N$ degrees of freedom. This is almost linear and therefore close to the theoretical optimum (Parsons 1997). However, following examples show that the order can still be decreased. Figure 5.15 illustrates another important effect. The solution time of the multigrid method increases with increasing ratio of Young's modulus $R$. One relevant effect results from the decreasing quality of the interpolated material distribution on the coarse meshes. However, also the problem on the fine mesh can be considered as worse conditioned. This topic is in the focus of Section 5.11.3.

The benchmark of Fig. 5.15 was only based on the modified multigrid cycle (Fig. 5.1), as documented in (Häfner, Eckardt, Luther and Könke 2006). After that the implementation has been prepared such that other multigrid cycles can be performed. The algorithm can
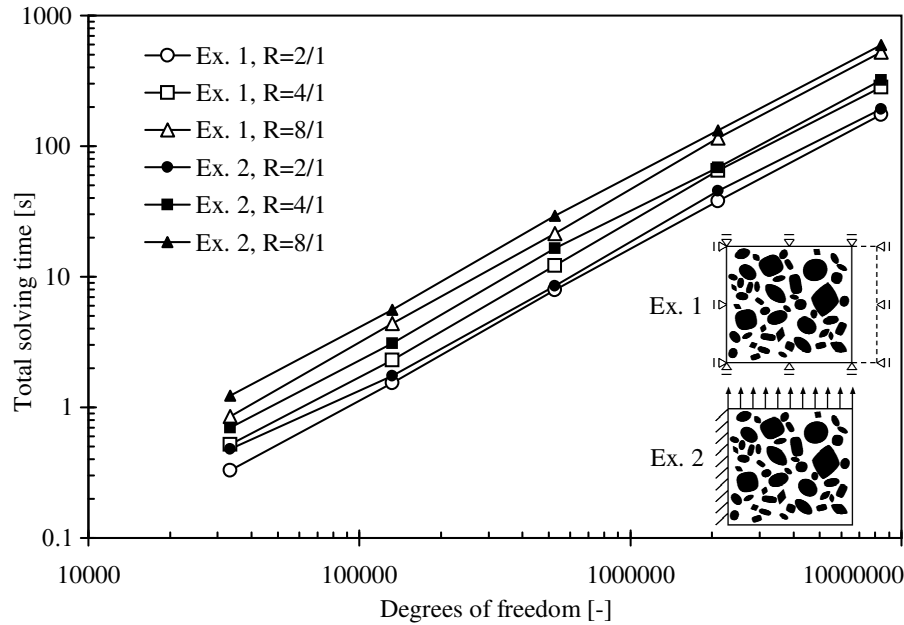
Figure 5.15: Computation times of multigrid method according to modified cycle

follow any list of numbers which describe a valid multigrid cycle. The algorithm detects whether the next number means restriction or prolongation. The end of the list (cycle) is marked by {-1}. For example the F-cycle for the levels $0 \ldots 4$ of Fig. 5.1 is described by the list

$$\text{F-cycle: } \{4, 3, 2, 1, 0, 1, 0, 1, 2, 1, 0, 1, 2, 3, 2, 1, 0, 1, 2, 3, 4, -1\}$$

An additional list of equal length describes the number of smoothing steps on each level. Thus, also the modified cycle can simply be included into this scheme. For testing a new cycle it is only required to write an algorithm which creates the corresponding list. Otherwise, it is also simply possible to create or edit a cycle in usual text file format and load it into the program. However, for large cycles an algorithm is preferable. For example the list from the W-cycle for the levels $0 \ldots 7$ is graphed in Fig. 5.16.

For various cycles a new benchmark has been performed. A typical model of the study is illustrated in Fig. 5.17. It is a two-dimensional model of concrete. The side length of the square is 100 mm. The aggregates sizes range in the interval 4 mm to 32 mm. They are graded according to the Fuller curve. The volume of aggregates is about 50 %. The ratio of Young's modulus between aggregates and matrix is $R=2/1$. The load case corresponds to the mixed boundary conditions of Fig. 3.4. An example of a stress solution is shown
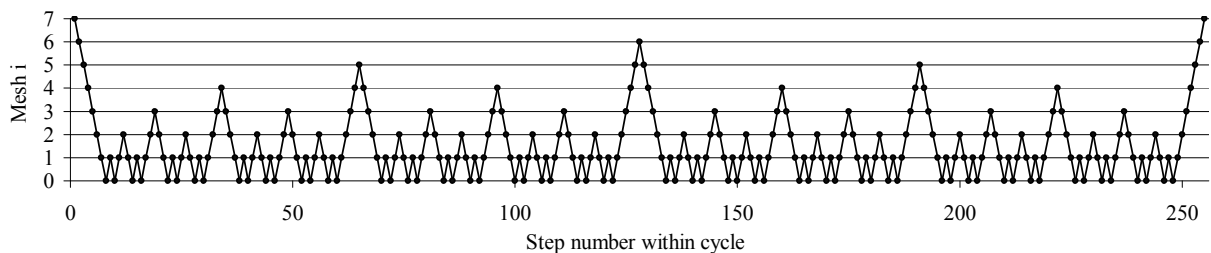


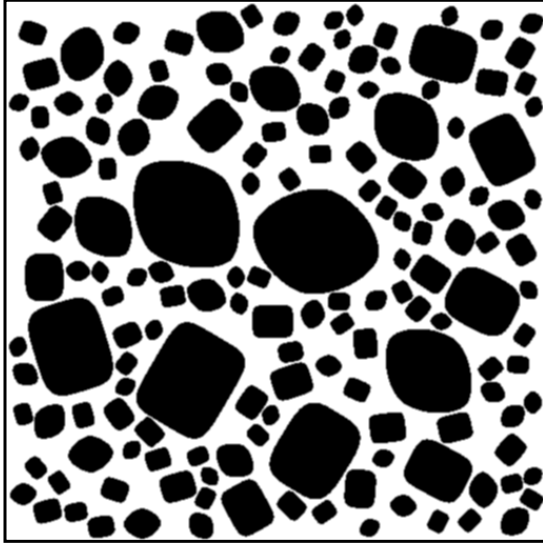Figure 5.16: W-cycle for the levels $0 \ldots 7$

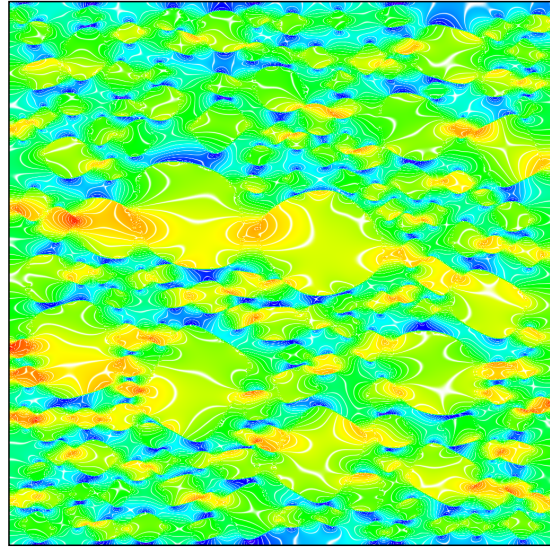Figure 5.17: Typical concrete sample of present study



Figure 5.18: Normal stress in horizontal direction from model of Fig. 5.17

in Fig. 5.18. The results of the benchmark are summarized in Fig. 5.19. The error tolerance was $\epsilon_E = 1.0 \cdot 10^{-6}$ (Eq. 5.64). For all model sizes the solution times of V-, F- and W-cycle are almost identical. Smoothing is performed by the Gauss-Seidel method. The number of smoothing loops in each cycle step was set to 1. The solution times of the modified cycle are about three times larger. It is observed that the number of cycles for achieving the solutions principally remains constant for different model sizes. In the present example the number of cycles was 14 for the V-cycle, 11 for the F- and W-cycle, and 9 for the modified cycle, except from two cases where the number of cycles differed by 1. It is clear that a certain cycle may just step above or below the defined error tolerance, which decides over the number of cycles. It is most interesting to analyze the order to which the computational effort increases with increasing model size. If the model size increases by
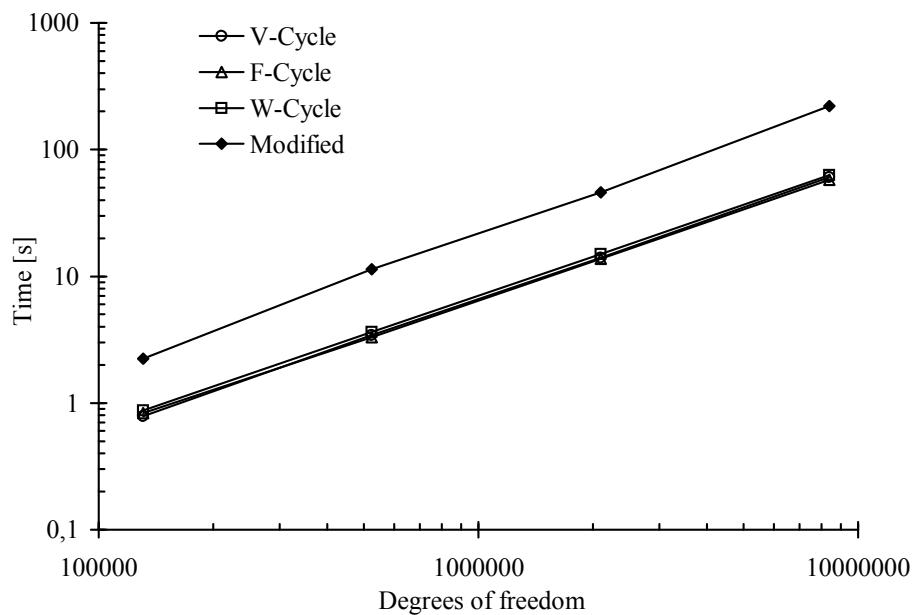


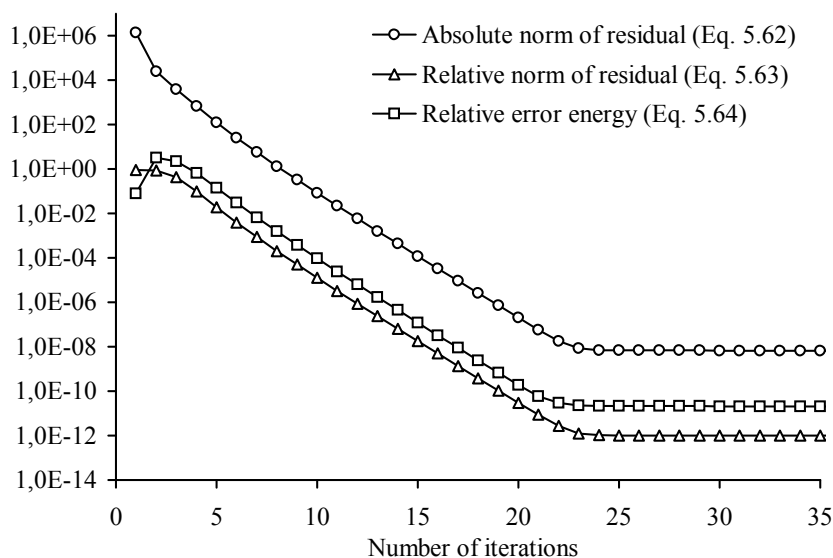Figure 5.19: Computation times of multigrid method for various cycles

Figure 5.20: Convergence of multigrid method

the factor $a$ and the computational effort increases by the factor $b$, then with $a^x = b$ the variable $x$ denotes the described order. It is evaluated by $x = \log_a(b)$ which is equal to $x = \log_{10}(b)/\log_{10}(a)$. For the V-cycle the computation time was 3.44 seconds for $512^2$ elements and 60.44 seconds for $2048^2$ elements. It follows that $a = 17.59$, $b = 16$ and $x = 1.034$. Also for the F- and W-cycle an order of about 1.03 is observed (Fig. 5.19). The present example confirms the order 1.1 for the modified cycle from (Häfner, Eckardt, Luther and Könke 2006). It can be summarized that the effort of the multigrid method only increases (almost) linear with problem size in the present mechanical analysis of heterogeneous solids. Especially with respect to very large models, this represents an important characteristic.

Besides, the convergence behavior is analyzed with respect to the three error measures from Eqs. 5.62, 5.63 and 5.64. Figure 5.20 illustrates the convergence of the V-cycle from the present example. As introduced before, the relevant error tolerance of the present example $\epsilon_E = 1.0 \cdot 10^{-6}$ (Eq.5.64) is achieved after the 14th V-cycle. It is noted that the relative error measures (Eqs. 5.63 and 5.64) are invariant to scaling of applied forces and prescribed displacements. Therefore these measures are proposed. The relative error measure in terms of energy (Eq. 5.64) is especially descriptive for engineers. If the error is not extremely localized, then a relative error of energy from the solution of $\epsilon_E = 1.0 \cdot 10^{-4}$ is sufficient for many practical purposes. Often the discretization error of finite elements is larger. In general the multigrid method tends to distribute the remaining solution error over the domain. A solution with an error below $\epsilon_E < 1.0 \cdot 10^{-6}$ can be considered as very accurate. Even far below this error level (after the 14th cycle), the graphs of Fig. 5.20 indicate stable convergence. The convergence is only limited by the computational precision (double format with 15 digits) which leads to a sudden horizontal trend in the diagram.

For further analysis of the implemented multigrid method, it is quite interesting, how the computational effort is distributed between the different routines. Figure 5.21 shows the distribution for the V-cycle with one pre- and post-smoothing step on each level. However, the illustrated distribution only refers to the present implementation. As expected the smoothing process and the computation of residual forces for restriction are most
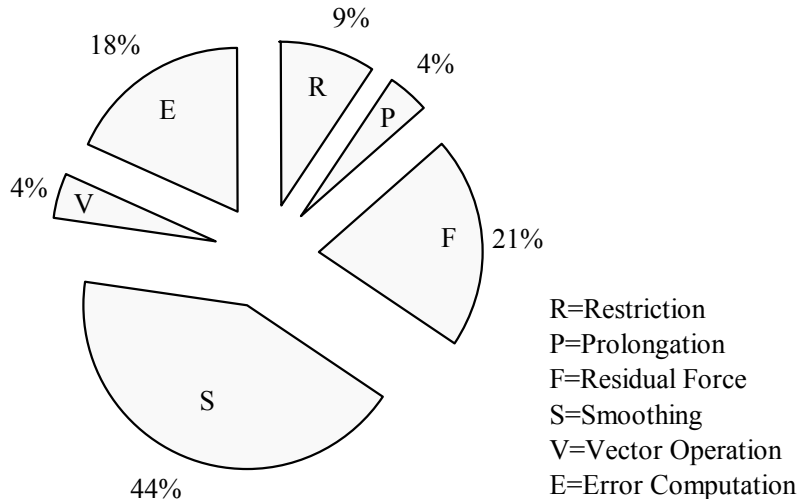
Figure 5.21: Distribution of computational effort between different routines of V-cycle

expensive. As in one V-cycle the residual forces are computed once on each level and smoothing is performed twice, the relationship of 21% to 44% is reasonable. Restriction and prolongation are efficient for orthogonal grids. Vector operation denotes processes like setting vectors to zero or adding an increment. It is noted that, except for Fig. 5.15, the computation times from evaluating the solution error after each cycle is not included in the present studies. It is convenient that the results do not depend on type and frequency of observed error. Work load distributions such that in Fig. 5.21 indicate which routines are relevant for improving efficiency.

### 5.11.3   Computation Times for Large Ratios of Young's Modulus

The results of the first benchmark of Fig. 5.15 indicate that the computation times of the multigrid method essentially increase with increasing ratio of Young's modulus between the phases. As prepared in Section 5.5 the present work proposes a remedy by the multigrid preconditioned conjugate gradient method. The multigrid method and the preconditioned version are compared for ratios of up to $R = 200/1$ in Fig. 5.22. For further reference results from the conjugate gradient method are included. The three diagrams refer to the different model sizes of about 32000, 131000 and 524000 degrees of freedom.  As expected, only for small models the efficiency of the conjugate gradient method is comparable to that of the both multigrid methods. For the low ratio $R = 2/1$ the multigrid method is a few percent more efficient than the multigrid preconditioned conjugate gradient method. For all model sizes the multigrid preconditioned conjugate gradient method is significantly less sensitive to an increasing ratio $R$ and considerably more efficient than the multigrid method. This marks an important improvement with respect to (Häfner, Eckardt, Luther and Könke 2006). Moreover, it is observed (without illustration), that the preconditioned version is more efficient for boundary conditions of the type SUBC (Fig. 3.1). The results of Fig. 5.22 are all based on the modified cycle. Figure 5.23 compares the two variants with different cycles for a ratio of Young's modulus $R = 200/1$. The results of the modified cycle are not quite the same in Fig. 5.22 and Fig. 5.23. This may be due to different analysis and model parameters. However, the results within one diagram are consistent. In the present examples the multigrid method is generally most efficient with one smoothing step on
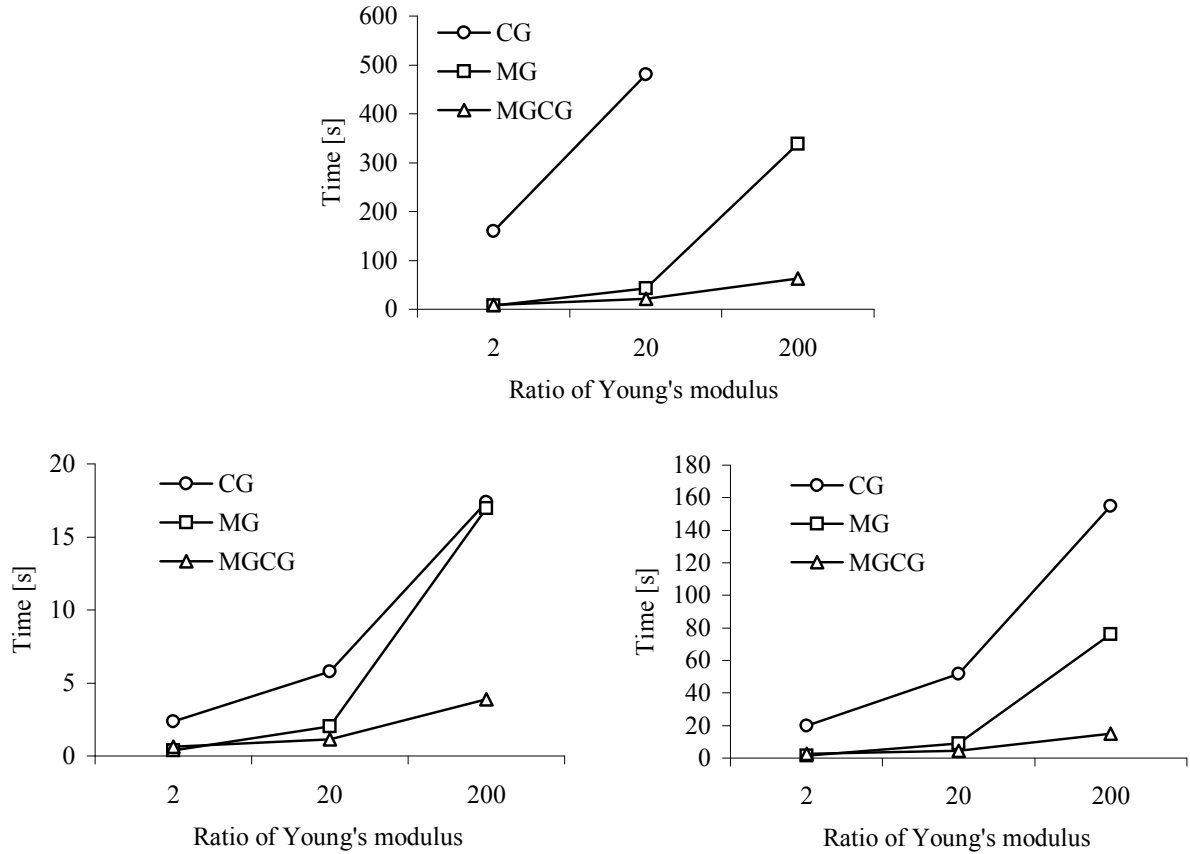
Figure 5.22: Computation times of conjugate gradient method (CG), multigrid method (MG) and multigrid preconditioned conjugate gradient method (MGCG) in the analysis of two-dimensional concrete models. Inclusion volume is 40%. The ratio of Young's modulus is set to $R = 2/1$, $R = 20/1$ and $R = 200/1$. The model size is: 32000 (left), 131000 (right) and 524000 (top) degrees of freedom.
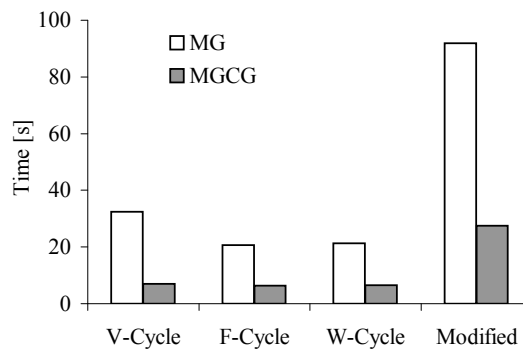


Figure 5.23: Comparison between multigrid method (white bars) and multigrid preconditioned conjugate gradient method (gray bars) for a ratio of Young's modulus $R = 200/1$ with respect to different cycles. Model size: 131000 degrees of freedom.

each level. However, for the preconditioned version two smoothing steps were performed on each level for best efficiency. The considered large ratios of Young's modulus $R$ occur in certain heterogeneous materials or in damage analysis.
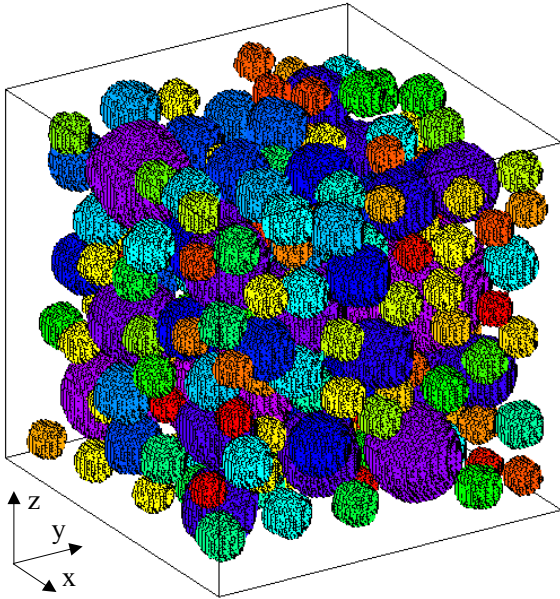
Figure 5.24: Three-dimensional concrete model with 212 inclusions based on $128^3$ voxels
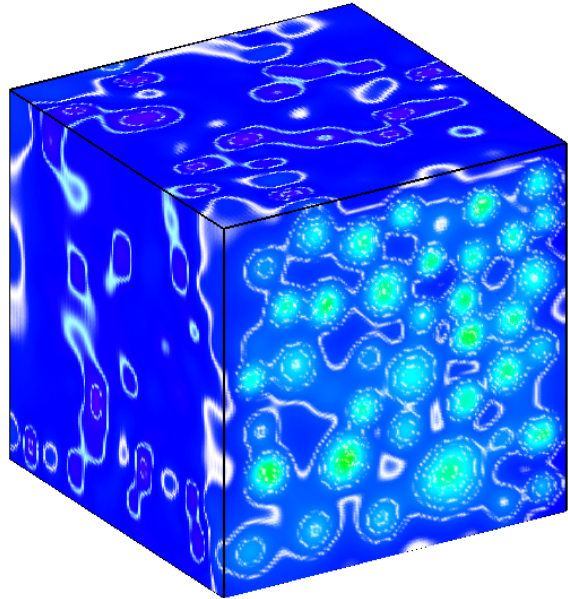


Figure 5.25: Normal stress $\sigma_{xx}$ for deformation in x-direction (MBC) of model shown in Fig. 5.24

### 5.11.4   Computation Times of Three-Dimensional Models

Three-dimensional modeling is straightforward by grid-based procedures. Section 5.8 introduces to the global numbering scheme for three-dimensional models. The local formulation for three-dimensional finite elements is prepared in Section 5.9.4. First results from the latest implementation of the multigrid method for three-dimensional models in Mulgrido are presented. Figure 5.24 shows a geometrical model of concrete similar to those applied in the present study. Figure 5.25 illustrates the stress solution $\sigma_{xx}$ for a deformation in x-direction according to mixed boundary conditions (MBC). The computation times from three-dimensional models are presented in Fig. 5.26 with reference to results of Fig. 5.19 from two-dimensional models. The ratio of Young's modulus between
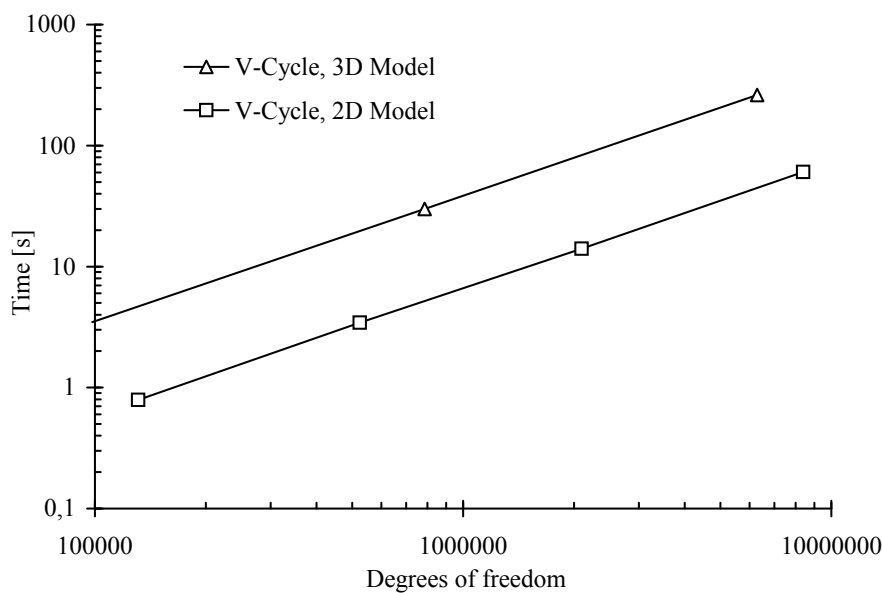


Figure 5.26: Computation times of multigrid method for three-dimensional models with reference to two-dimensional models from Fig. 5.19. (Note: hidden triangle of graph is located at {98304; 3.48})
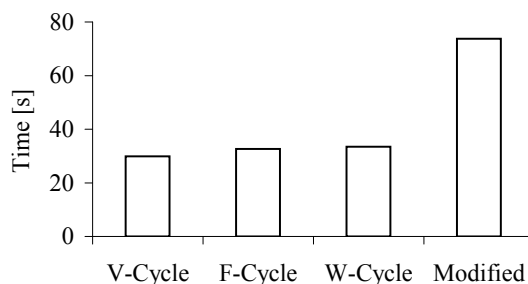
Figure 5.27: Comparison of computation times from the multigrid method in application to three-dimensional models with respect to the different cycles for a ratio of Young's modulus R=2/1. Model size: 262000 degrees of freedom.

the phases was $R=2/1$. Only about 100 inclusions have been modeled such that these are well presented by the smaller models. The same error tolerance as for the two-dimensional models $\epsilon_{\mathrm{E}} = 1.0 \cdot 10^{-6}$ (Eq. 5.64) has been applied. For the three-dimensional model only 12 V-cycles were required to reach the defined error tolerance in contrast to 14 V-cycles for the two-dimensional model (Section 5.11.2). Similar to Fig. 5.21 the largest computational effort was spent on smoothing operations and computing residual forces. From the local formulations of Sections 5.9.3 and 5.9.4 follows that there are essentially more arithmetic operations necessary to compute the residual force of one degree of freedom for the three-dimensional model than for the two-dimensional model. This explains that in spite of less required multigrid cycles the computation of the three-dimensional model is more expensive. Moreover, several loops are required for each node in three-dimensional models to collect the residual forces from the neighboring elements. In the implementation of two-dimensional models the computation of a residual force can be written into one equation. Thus, there is still some potential to increase the efficiency of the implementation for three-dimensional models. Nevertheless, the present absolute computation times of the multigrid method for three-dimensional models are competitive. It is most relevant how the computational effort scales with increasing model size. For the model with $32^3$ elements the computation time was 3.48 seconds and for that with $128^3$ elements 262.12 seconds (V-cycle). Recalling the formulation $a^x = b$ of page 110, it follows that $a = 64$, $b = 75.3$ and thus $x = 1.039$. This is an excellent result. For both the F- and W-cycle even an order of $x = 1.022$ was determined. For the modified cycle it was $x = 1.09$. This confirms the results from two-dimensional models. Also for three-dimensional models the computational effort from the multigrid method (almost) increases linear with increasing model size in the present implementation. The computational effort from the different cycles is compared in Fig. 5.27.

## 5.12   Conclusions

The present work introduces to stationary iterative solver methods in the matrix form and prepares for the later applied index form. For the conjugate gradient method, the multigrid method and multigrid preconditioning of the conjugate gradient method, some relevant fundamentals for an implementation of these methods are provided. The complexity of the general problem is reduced by utilizing certain properties of solid finite elements and defining a clear global numbering system. Based on the discussed index

form, element-based global operations lead to a compact and efficient formulation of the heterogeneous finite element problem on orthogonal grids in two and three dimensions. Moreover, similar local schemes are outlined for advanced finite elements of an orthogonal mesh or triangular elements of an irregular mesh. The transfer operators of the multigrid method are adequately derived by the fundamental equations of solid finite elements. Besides, also the transfer of the heterogeneous material to coarser grids is discussed. With regard to B-spline finite elements, an intuitive transfer operator is exemplified for the one-dimensional problem. Transparent access to the memory demand of two-dimensional finite element models is provided. A modified multigrid cycle with balanced computational effort between all grids is successfully applied. Based on a list of levels any valid multigrid cycle can be performed. A benchmark of the V-, W- and F-cycle indicates that the computation times only increase by the order 1.03 with respect to increasing model size. The same order is achieved for three-dimensional models. This is very close to the optimal result of linear order (1.00). Objective error norms are introduced in terms of relative norm of residual and relative error energy. The convergence of the multigrid method is uniform and stable until the limit of computational precision is reached. As a major conclusion of the present chapter, the multigrid preconditioned conjugate gradient method is essentially more efficient for large ratios of Young's modulus in the material than the multigrid method. This is significant for damage analysis (Chapter 6).

**Chapter 6**

# Numerical Model: Aspects of Damage Simulation

## 6.1  Introduction

In the previous chapters grid-based methods are prepared for the linear elastic analysis of heterogeneous solids. The present chapter discusses an extension to damage simulation for bilinear finite elements. The direct stress solution of standard bilinear finite elements is severely defective, especially along material interfaces. Various nonlocal formulations are applied to improve the stress solution. Such a corrective data processing can either refer to input data in terms of Young's modulus or to the obtained finite element stress solution, as well as to a combination of both. A damage-controlled sequentially linear analysis is applied in connection with an isotropic damage law. By a high resolution of the heterogeneous solid, local isotropic damage on the material subscale allows to simulate complex evolution of damage regions. Therefore certain anisotropic effects can be simulated. Then a complex constitutive law on the macroscale is replaced by a simpler constitutive law on the mesoscale. Thus, a close relationship between subscale geometry and material behavior is achieved. Based on an effectively global secant stiffness the analysis is numerically stable. The iteration step size is controlled for an adequate simulation of the damage path. This requires many steps, but in the iterative solution process each new step starts with the solution of the prior step. The present chapter discusses some relevant numerical aspects of the proposed grid-based concept for a stable damage simulation of heterogeneous solids.

## 6.2  Notes on Grid-Based Data Structure

In arbitrary finite element meshes a node table with nodal coordinates and an element table which stores element type and corresponding interconnected nodes is required. Based on a predefined mesh topology (Section 5.8), the computational effort and memory demand of the grid-based finite element problem is considerably low. For the linear problem the memory demand is summarized in Section 5.11.1. Figure 6.1 (a) shows the material type. A usual pixel image can be read into the finite element program and each different color will be interpreted as an individual material type. One constitutive law and one Poisson's ratio can be assigned to each material type. The material type identifies the different materials within the heterogeneous solid and generally its number is countable. In Fig. 6.1 (a) three different material types are defined for inclusions, matrix mater-
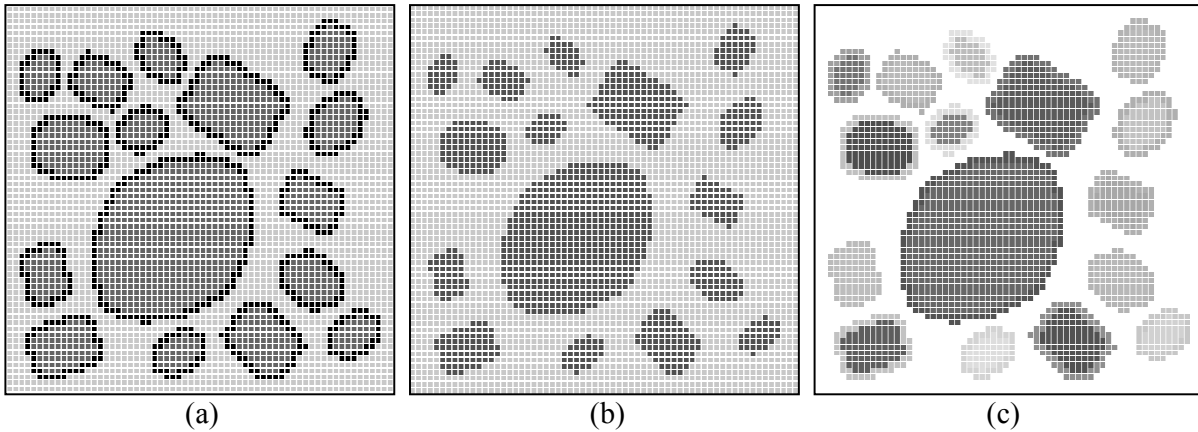
Figure 6.1: Small heterogeneous material sample of $64 \times 64$ finite elements in terms of (a) material type, (b) Young's modulus and (c) individual phases.

ial and interfacial transition zones. Figure 6.1 (b) shows the defined Young's modulus which is principally decoupled from the material type. It is possible to assign one specific Young's modulus to all elements of one material type. But the Young's modulus can also be modified in any way, e.g. for modeling some randomness. In Fig. 6.1 (c) each color indicates an area of neighboring finite elements of the same material type. The data of Fig. 6.1 (c) is generated automatically from Fig. 6.1 (a). It is used within the nonlocal approach where it is useful to average stress values only within a considered inclusion and neglect values of the matrix material or neighboring inclusions. Additional data layers are required in damage simulation, such as e.g. damage parameter and equivalent strain. Grid-based processing is quite efficient for application of a nonlocal formulation, because distances and directions between nodes or elements can effectively be determined.

## 6.3   Nonlocal Formulations

### 6.3.1   Nonlocal Formulation for Recovery of Strains/Stresses

The motivation of a nonlocal formulation for damage simulation is given by the items (a.1) to (a.3) in Section 3.4.3. Independent of a damage material law, nonlocal formulations can be applied to improve the strains and stresses of a linear elastic finite element solution. Within this context the meaning of nonlocal formulations is extended to averaging techniques in general. It is highlighted that the finite element analysis is still based on a local formulation. Averaging is only applied to reduce local errors in the strain/stress solution. There are the following characteristics of emerging errors in finite elements:

b.1 In displacement-based finite elements the classical discretization error is related to limited approximation quality of shape functions due to limited order or limited resolution of finite elements.

b.2 The orientation of the finite element influences the error distribution. A systematic element orientation supports a systematic error with respect to a certain direction, especially in terms of strains and stresses.
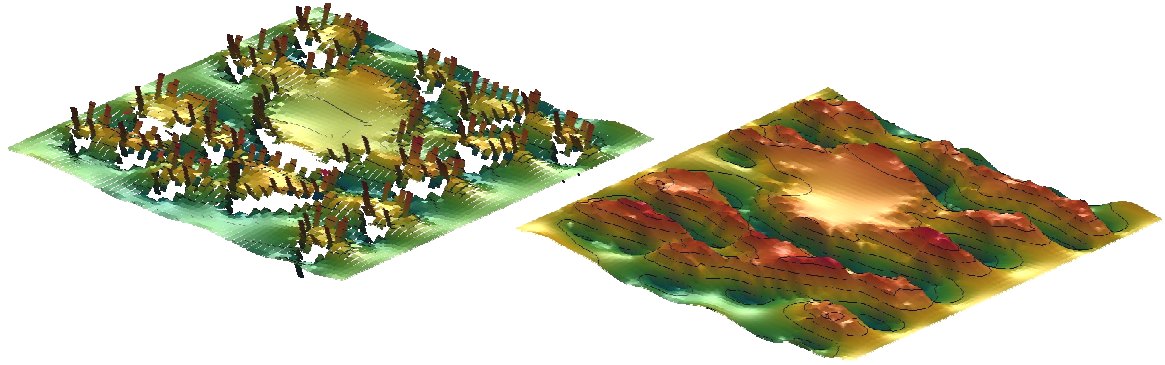
Figure 6.2: Stress solution $\sigma_{xx}$ before (on the left) and after nodal interpolation of element stress at nodes (on the right) for uniaxial load of material sample (Fig. 6.1) in $x$-direction.

  b.3 In common grid-based finite element models smooth surfaces of material phases are transformed into an angular discretization which leads to severe defects in the stress and strain solution independent of element order or resolution.

As in the present approach a nonlocal formulation of damage modeling is applied anyway, nonlocal averaging of the linear elastic solution does not increase the fuzziness, but may significantly improve the defects according to (b.1) to (b.3). Especially, the error of stresses according to (b.3), the grid-based discretization, can effectively[1] be corrected. There are various nonlocal formulations to improve the strain or stress solution of finite elements:

  c.1 The use of a weighting function (Section 3.4.4),

  c.2 averaging of element values at nodes and

  c.3 special techniques such as patch recovery based on selected superconvergent points.

Nonlocal averaging according to (c.1) is automatically included in the subsequent nonlocal damage formulation. However, it is reasonable to reduce the error mainly induced by grid-based discretization in advance. Figure 6.2 shows the effect on nodal averaging of the stress solution $\sigma_{xx}$. Similar good results are achieved for $\sigma_{yy}$ and $\sigma_{xy}$ (without illustration). The corrected stress solution is continuous and also the gradients as well as the isolines of stresses are recovered. Figure 6.3 shows the isolines of the stress solution according to Fig. 6.2 (left); and Fig. 6.4 that of Fig. 6.2 (right). In Fig. 6.3 it is obvious that almost all isolines are aligned horizontally. Although the nonlocal formulation of the damage will smooth the defect, it is assumed that an improved stress according to Fig. 6.4 will further reduce the mesh directional bias (the present implementation does not include this correction.).

As a further and rather unusual treatment of the problem an averaged material representation is introduced. Therewith the original problem is replaced by a substitute problem

---

[1]Corrective post-processing only improves the solution of bilinear finite elements in terms of stresses, but not in terms of energy. A significant remedy of defective stresses along material interfaces is achieved by multiphase B-spline finite elements (Section 4.6). However, the present implementation of this method in Mulgrido does not include damage simulation. It is proposed to apply multiphase B-spline finite elements in future damage simulation.
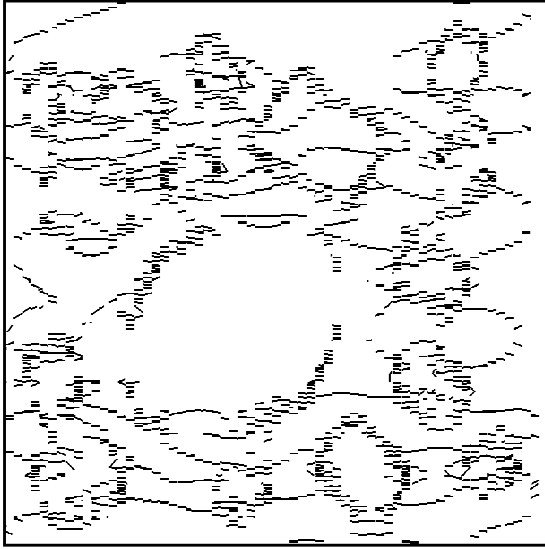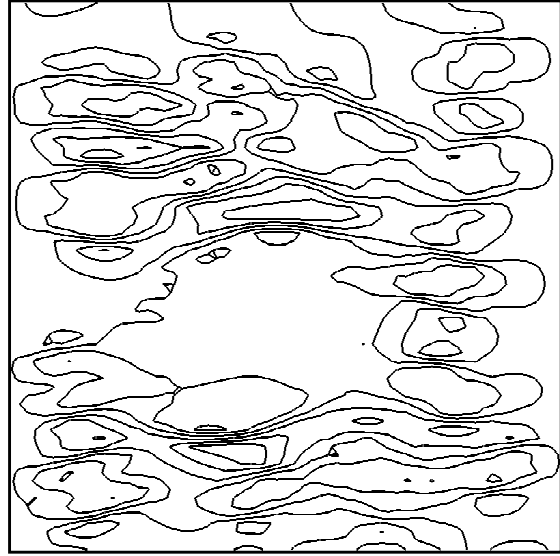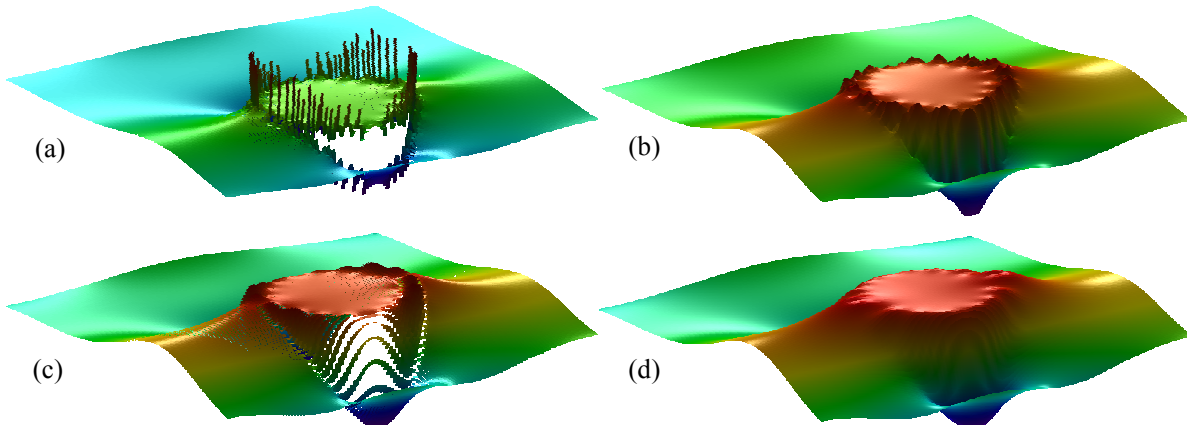
Figure 6.3: Isolines of stress $\sigma_{xx}$ in Fig. 6.2, left.



Figure 6.4: Isolines of stress $\sigma_{xx}$ in Fig. 6.2, right.



Figure 6.5: Normal stress in direction of uniaxial tension of circular inclusion on uniform grid of bilinear finite elements: (a) direct element solution, (b) stress interpolated at nodes, (c) stress of model with nonlocal Young's modulus, (d) a combination of (b) and (c).

similar as described in Section 4.6.1. The substitute problem is only introduced to improve the stress solution in grid-based modeling and shall principally correspond to the same problem. It is noted that an averaged material representation is achieved by nonlocal averaging of Young's modulus, but in contrast to Section 4.6.2, here only one Young's modulus is assigned to one bilinear finite element. The effect of this averaging in the material model on bilinear finite elements is shown in Fig. 6.5. From there it is concluded that good recovery of stress values is achieved by nodal averaging. An additional slight smoothing of Young's modulus might further improve the result, but, clearly, this option needs to be treated carefully. It is included as an alternative option which can be useful within the present or similar context.

## 6.3.2    Nonlocal Formulation of Damage Law

For the nonlocal formulation of the considered damage law (Section 3.4.2), the local equivalent strain $\widetilde{\epsilon}$ of Eq. 3.46 is replaced by its nonlocal counterpart. In the finite element model the integral of Eq. 3.52 is replaced by a sum on discrete points according to

$$\bar{f}(\boldsymbol{x}) = \frac{\displaystyle\sum_{i \in A(\boldsymbol{x})} \alpha_0(\boldsymbol{x} - \boldsymbol{\xi}_i) f(\boldsymbol{\xi}_i)}{\displaystyle\sum_{i \in A(\boldsymbol{x})} \alpha_0(\boldsymbol{x} - \boldsymbol{\xi}_i)} \tag{6.1}$$

The sequence $A(\boldsymbol{x})$ only includes source points $\boldsymbol{\xi}_i$ which are within the same individual phase (Fig. 6.1 (c)) as effect point $\boldsymbol{x}$ to avoid averaging over different materials. It follows that the denominator in Eq. 6.1 can be different for different $\boldsymbol{x}$. In the present implementation the coordinates of source points refer to the center of elements[2]. It is reasonable to restrict element size $h$ in relation to the interaction radius $R$ of the weighting function by $h \leq \frac{R}{3}$ (Jirásek 1999).

On the defined uniform, orthogonal grid the weighting function can be applied as a predefined discrete stencil, which can arbitrarily be trimmed along phase or model boundaries. Therefore nonlocal formulations on uniform grids are quite effective. Furthermore as the local equivalent strain only includes the positive parts of stresses, it appears more accurate to apply nonlocal averaging already to the stresses in Eq. 3.47. From this it follows that there are several possible variations of the method which need to be considered for achieving an optimal result.

## 6.3.3    Nonlocal Formulation in Adaption to Heterogeneous Material

Besides stabilizing the numerical mechanical analysis, the nonlocal formulation also reflects the observed development of damage in material. Specific crack band width or size of damage region occurs in different materials. It depends on a specific internal length of each material. For heterogeneous materials it essentially results from the microstructure. Then, the type and size of weighting function not only determines the smoothing radius of post-values as shown in Fig. 6.6, but will also define the size, as well as the curvature, of the developing damage region. In this regard, various weighting functions, such as the Gauss distribution function and the bell-shaped function (Section 3.4.4), show perceivable differences (Jirásek 1999).

To track the physical phenomenon, concrete material is selected. It is a comprehensible explanation that material points in the closest neighborhood around an inclusion in a generally weaker matrix will not be damaged independently of each other. In this perception the aggregate will "distribute" the damage. From a combined experimental and numerical approach, it is adopted in (Ferrara and di Prisco 2002) that the material characteristic length is roughly equal to the maximum aggregate size. In a numerical study

---

[2]The stresses at the center of bilinear rectangular finite elements are denoted superconvergent. However, in combination with nodal averaging of Section 6.3.1, a more accurate numerical integral based on nodal values would be useful to reduce the mesh dependency as best as possible.
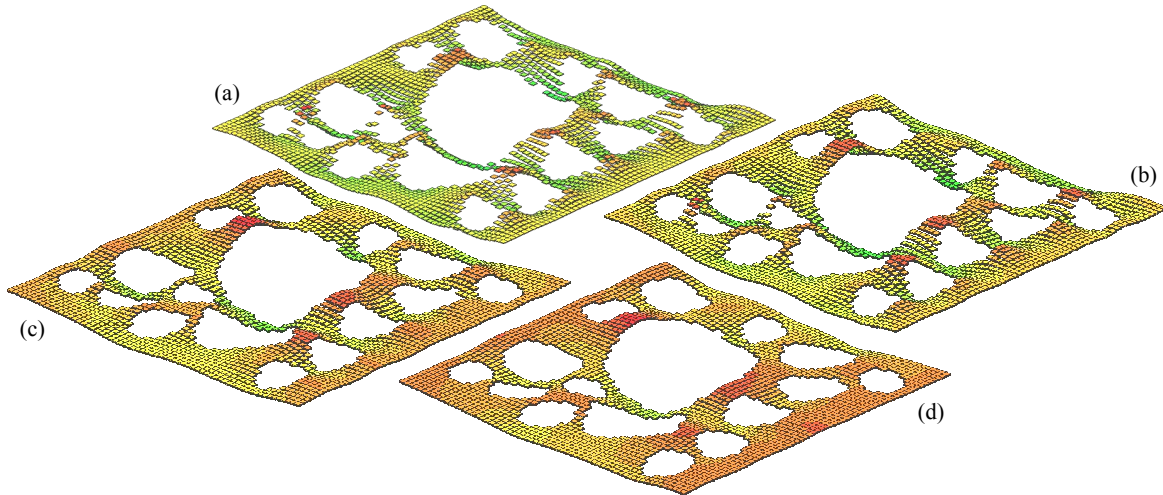
Figure 6.6: Nonlocal equivalent strain in center of elements according to bell-shaped function with (a) R=1, (b) R=5, (c) R=10 and (d) R=15 of specimen in Fig. 6.1 with side length 100.

in (Feist 2004) the interaction radius is set to the triple of the maximum aggregate size which also confirms the principle idea. With respect to damage modeling on the mesoscale, the relevant size may be related to the largest aggregate size which is not explicitly modeled, as included aggregates will interact intuitively.

### 6.3.4   Nonlocal Formulation for Grid-Based Modeling of Material Interfaces

The present approach discusses the possibility of a purely grid-based approach for ideal data structures, optimal embedding into the multigrid method and extension to three-dimensional modeling. In this context a possibly novel idea for modeling material interfaces on a grid shall only be mentioned.

Besides the stress values also the stress directions can be recovered. By a proper definition of a multiphase material also the orientation of a (one-pixel thick) interface can be approximated by a nonlocal formulation, as indicated in Fig. 6.7. With both strain and interface directions being approximated, a special interface solution can be applied, e.g. isotropic softening of interface elements is defined only for positive normal stress perpendicular to the orientation of the interface. A corresponding method requires some kind
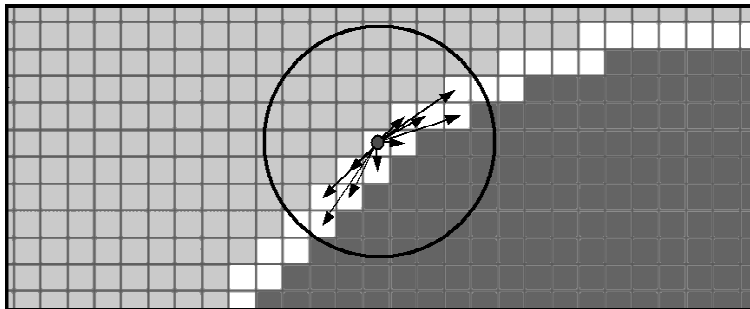


Figure 6.7: Interpolation of directions to approximate the interface orientation based on plain grid discretization

of regularization with respect to element size, another weighting function for directions, as well as several additional considerations. It is highlighted that this concept presumes a very high resolution of the material, which represents a basic principle of the present approach of grid-based modeling.

# 6.4 Damage-Controlled Sequentially Linear Analysis

Damage processes describe a nonlinear behavior. There are various iteration procedures to solve the corresponding nonlinear problem. Load-controlled methods will fail to converge after an ultimate load is reached and a global softening behavior can not be simulated. A displacement-controlled analysis enables to step beyond an ultimate loading. However, a snap-back can not be detected by displacement-control. Snap-back behavior describes the phenomenon that for equilibrium on the nonlinear path, both, the load as well as the displacement will be reduced. Such a behavior can refer to an actual brittle behavior of a material or structure. But it will also occur due to an unrealistic linear softening branch in the material model or unregularized strain localization in the numerical model (Jirásek 1999). The arc-length method is an advanced iteration procedure which potentially covers post-peak behavior as well as snap-back. For example, recently the arc-length method has been demonstrated for simulating of such damage processes in concrete by Most (2005).

The present article follows a sequentially linear approach similar to (Rots and Invernizzi 2003). This method mitigates the problem to achieve a stable numerical iteration procedure. In fact, each iteration step is performed by linear analysis based on the secant stiffness matrix. The sequentially linear approach covers post-peak behavior, snap-back and is any case stable, at least from a numerical point of view. The algorithm is outlined by the following steps:

(1) Perform a linear elastic analysis with unit load.

(2) Determine a critical load factor for a small increase of damage, e.g. such that exactly one element of the model will pass the peak point in the stress-strain diagram.

(3) Scale displacement solution according to critical load factor and record actual status of load and displacement.

(4) Update damage variables according to this scaled displacement solution.

(5) Build a new secant stiffness matrix. For the scalar damage law only a modified field of Young's modulus is stored (Eq. 3.51). Continue with item (1).

The linear elastic analysis in each new iteration is based on the modified field of Young's modulus (Eq. 3.51). However, the initial field of Young's modulus is still required to update the damage variables. This iteration scheme is declared as damage-controlled. In each step a small additional, controlled damage occurs.

From the documented algorithm it follows that in each iteration step the actual load limit is a little bit overestimated, as it is already used to initiate a small damage increment for the next iteration step. However, it is also possible to achieve exact equilibrium. Then,

for the actual damage situation the linear secant solution is scaled by a load factor just that in no element additional damage will occur. Then this describes the maximum load for which the current damage state is still exactly valid.

There are various possible measures to control the damage process. In (Rots and Invernizzi 2003) the linear secant solution is scaled such that the stress in the most critical element corresponds to the ultimate stress. A possible criterion to induce additional damage is that the maximum strain which was detected in any of the finite elements in the last load step, will be increased by a predefined factor just above 1. It is possible to apply local or nonlocal measures of strains or stresses. Moreover, the damage could directly be controlled based on the damage variables $\omega$ (Eq. 3.48) of the finite elements. Nevertheless, any of these measures can be reduced to an over-estimation of the actual valid load factor on the actual secant stiffness to continue the damage process. If the damage increments of any measure will be small enough, then there will be no (relevant) difference in the damage path. An ideal damage increment is small enough such that the damage simulation is accurate, but at the same time possibly large for achieving best efficiency. In the present approach the increment corresponds to one additional damaged element (while the stiffness of all previously damaged elements is also updated). This represents a relative small increment. However, the computational effort of each step according to the multigrid method (Section 5.4) is minimal in comparison to other solver methods. The solution of the last step can be applied as the start vector of the actual step. In general a decrease of the damage step size results in a decrease of iteration time per step. The reduction of effective computation time by starting each load step from the previous converged solution, instead of the zero vector, is analyzed in Section 6.5.3. Generally the simulation of damage processes on the material level requires several steps to detect the correct damage path, if it is sensitive to multiple bifurcation. The evolution of damage around numerous inclusions with simultaneous loading and unloading of different regions can not accurately be approximated in a few steps. In the following Section 6.5 the proposed method of damage simulation is analyzed with respect to some relevant numerical aspects.

## 6.5 Numerical Examples

### 6.5.1 Effects of Mesh Orientation and Mesh Size

The first example is dedicated to analyze mesh directional bias of the damage development on an orthogonal grid. The applied isotropic damage law for tension (Section 3.4.2) operates on nonlocal equivalent strains. Nonlocal equivalent strains are computed by a weighting function according to Eq. 6.1 which represents the numerical counterpart of Eq. 3.54. The (local) equivalent strains (Eq. 3.45) are derived from principal stresses (Eq. 3.47) which are based on the stress solution of finite elements. However, the direct stress solution of finite elements shows certain defects which have been summarized by the items (b.1) to (b.3) in Section 6.3.1. These are the classical discretization error (b.1), a systematic error from orientation of finite elements (b.2) and local defects along material interfaces due to grid discretization (b.3). While the nonlocal formulation is also motivated by other important reasons (Section 3.4.3), nonlocal weighting also essentially
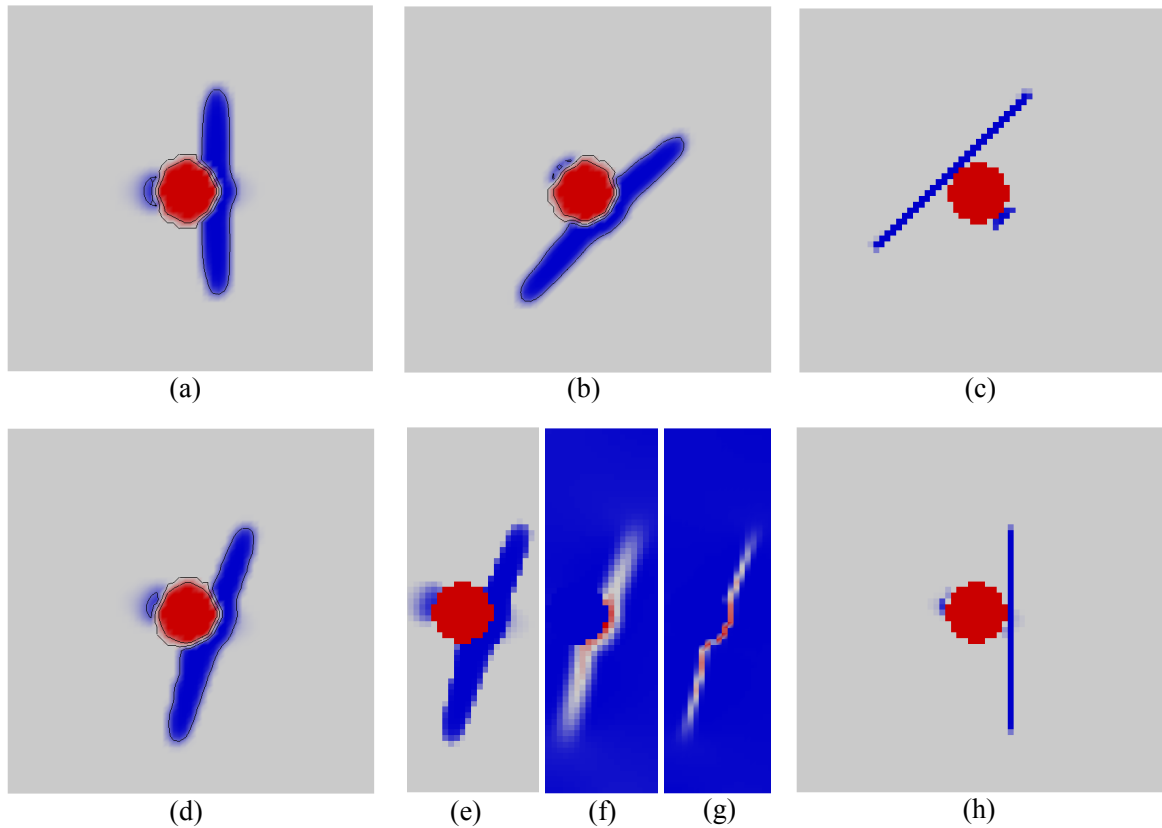
Figure 6.8: All images except (f) and (g) show the degraded Young's modulus (blue) according to damage. (a) horizontal tension, (b) diagonal tension, (c) as (b) but without nonlocal weighting, (d) direction of applied tension between (a) and (b) with slight deviation of damage orientation, (e) same as (d) but graphical output is not interpolated, (f) nonlocal equivalent strains according to (e), (g) equivalent strains, (h) same loading as (d) but severe deviation from angle without nonlocal formulation.

compensates local defects of the stress solution according to the items (b.1), (b.2) and (b.3). Especially defects according to (b.3), which only occur due to the orthogonal grid are automatically reduced. The improvement of the stress solution can directly be visualized by isometric stress plots (similar to Figs. 6.3 and 6.4). However, there remains the question if the nonlocal correction also effectively corrects mesh directional bias of the damage progress. In other words the focus of the following example is mainly on the effect of item b2.

The present example is a plane stress problem of a circular inclusion (16 mm diameter) in a quadratic plate (100 mm side length). The model is discretized by $64 \times 64$ classical bilinear finite elements. The Young's modulus of the inclusion is $200000 \, \text{N/mm}^2$ and that of the matrix is $100000 \, \text{N/mm}^2$ . The nonlocal radius of the bell-shaped function (Eq. 3.55) is 5 mm. The limit elastic strain is $\epsilon_0 = 1.0 \cdot 10^{-4}$ and ductility is determined by $\epsilon_f = 1.7 \cdot 10^{-4}$ (Eq. 3.48). Uniaxial tension tests in various directions are performed: in horizontal direction ($0°$), in diagonal direction ($-45°$) and in the direction in between ($-22.5°$). Displacement boundary conditions are applied to avoid rigid body motion only. Rigid support is on lower left corner and horizontally sliding support on lower right corner of square, such as in Fig. 3.1.

The results are illustrated in Fig. 6.8. From Fig. 6.8 (d) follows that to a large extent mesh directional bias has been reduced by the nonlocal formulation in comparison to the
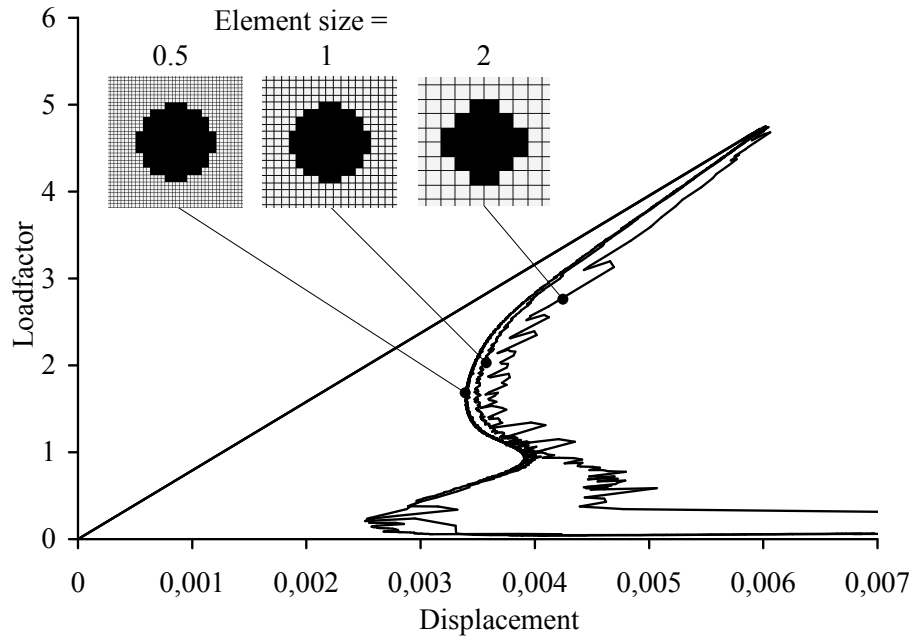
Figure 6.9: Load-displacement curves for uniform, orthogonal meshes with different element sizes

local formulation of Fig. 6.8 (h). However, in Fig. 6.8 (d) the damage region does not exactly develop perpendicular to the applied direction of uniaxial tension (about $-19°$ instead of $-22.5°$). This can result from the large expansion of the damage region while the specimen is asymmetric to the corresponding direction of applied uniaxial tension. It is useful to repeat the example with a larger specimen size. If the deviation persists, then an improvement might be achieved by previous averaging of stresses at nodes (Section 6.3.1). Undoubtfully, the application of higher-order elements as introduced in Chapter 4 represents a more promising option. Nevertheless, the present example still indicates only relative small mesh directional bias. Especially, the local equivalent strain of Fig. 6.8 (g) shows the inclined damage orientation across the elements.

The next example considers the dependence from the size of finite elements on the simulated damage behavior. The examined effect can mainly be associated to the discussed item b1. And if the interaction radius only covers one or a few elements, then there is only a small correction to expect from the nonlocal formulation. Thus, the major question arises: how many elements need to be within the interaction radius for a proper simulation of damage? The square model from the previous example is scaled to the size $64\,\text{mm} \times 64\,\text{mm}$. The nonlocal radius of the bell-shaped function (Eq. 3.55) is set to 7.5 mm. All other parameters remain. Uniaxial tension in horizontal direction is applied. The load factor 1 corresponds to an edge load of $2\,\text{N/mm}^2$. The response from the damage behavior is tracked by the load-displacement relationship with respect to the center coordinate of the right edge of the square. The test is performed for three different sizes of square finite elements: 0.5 mm, 1 mm and 2 mm side length. The result is illustrated in Fig. 6.9. There is hardly any difference between the graphs for the elements of size 0.5 mm and 1 mm until almost complete softening. Thus, the example shows no (relevant) dependence from mesh size for these finer discretizations. The graph from element size 2 mm is still quite close to the other graphs until a certain significant point where the specimen is already heavily damaged. This significant point is part of the subsequent study. The

present example shows that according to the nonlocal formulation a dependence on the mesh size can effectively be avoided. The ratio of the interaction radius to element size of the coarsest mesh was 7.5 mm / 2 mm = 3.75. The ratio of 3.75 appears still acceptable. This result is in accordance to the guide value 3 of Jirásek (1999).

From the presented examples follows that mesh directional bias and dependence from mesh size can be avoided to the largest extent by the nonlocal formulation. Moreover, it is supposed that even defects from the inaccurate geometrical representation of interfaces (b.3) can be reduced, similar as for (b.1) and (b.2). In combination with the correct parameter settings, grid-based damage simulation can be quite accurate. This statement represents the major conclusion from the present subsection. Undoubtfully, the result also depends on the accuracy of the material law and on corresponding material parameters. For example, certain problems require to include a damage formulation for compression. Nevertheless, the present examples also highlight that a complex, anisotropic damage behavior on the macroscale can be simulated by a simpler damage formulation on the mesoscale. This valuable option represents one major item from the motivation and objectives of the general research on direct modeling of heterogeneous solids. Due to the uniform grid, damage can equally grow or initiate somewhere in the model without the need of remeshing. But in general this advantage is computationally expensive. The efficiency of the proposed multigrid methods for damage simulation is in the focus of Section 6.5.3.

## 6.5.2   Study of Damage Progress

The graphs of Fig. 6.9 show a snap-back. After reaching the peak load, both load and displacement become smaller. This means that the applied parameter settings lead to an effectively quite brittle material behavior. If the nonlocal radius $R$ is increased then more energy is absorbed by the damage process (in a one-dimensional example, the absorbed energy corresponds to the enclosed area of the load-displacement curve). Also the peak load slightly increases. This effect is shown in Fig. 6.10. The graph of interaction radius 7.5 mm corresponds to that of element size 1 mm of Fig. 6.9. The model and all parameter settings also correspond. Five states states of this graph A...E have been selected. The corresponding damage process zone and the normal stress $\sigma_{xx}$ are illustrated in Fig. 6.11. In the very first iterations damage develops symmetrically on the left and on the right side of the inclusion. State A shows that the further damage progress decides for the right side. It is noted that the width of the inclusion is 11 elements and the total width of the model is 64 elements. Thus, the inclusion can not be quite in the center. It is effectively half an element left and half an element below of the model center. It is clear that the stress $\sigma_{xx}$ is low within the damaged region but large above and below it. The damage region almost increases symmetrically to a horizontal axis until state C. Then the damage growth decides for the lower part, while the upper damage process zone does hardly increase anymore. In state D the damage zone is close to the lower edge. The edge is broken in state E. However, state E represents quite a special snap-shot, because the width of the lower damage zone is not yet fully developed and some normal stress is still transfered. In the next few iterations this changes and the damage on the lower part completely develops. The corresponding deformation states B...E are shown in Fig. 6.12. The present study provides some information about the special curvature of the graphs
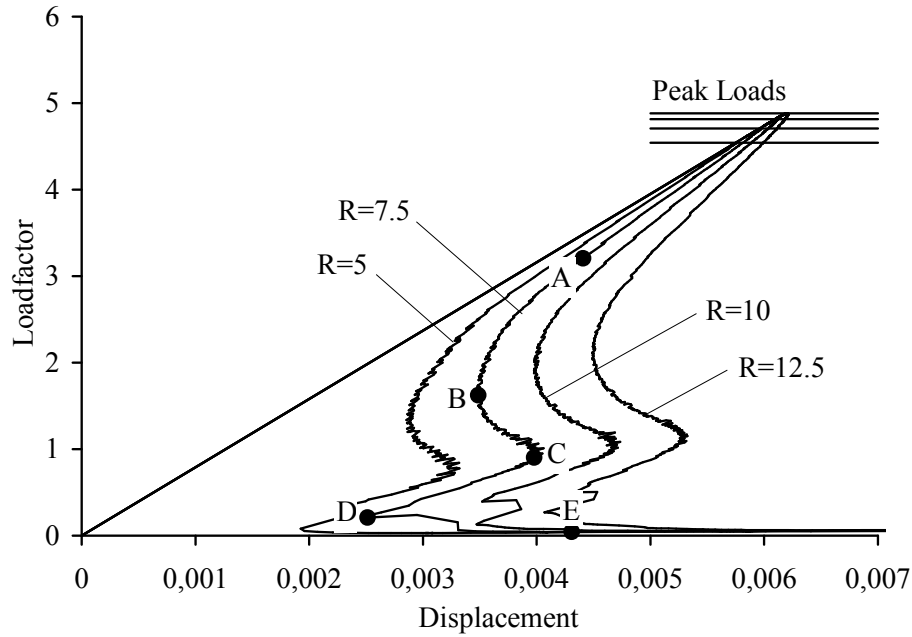
Figure 6.10: Load-displacement curves for different interaction radii of the weighting function
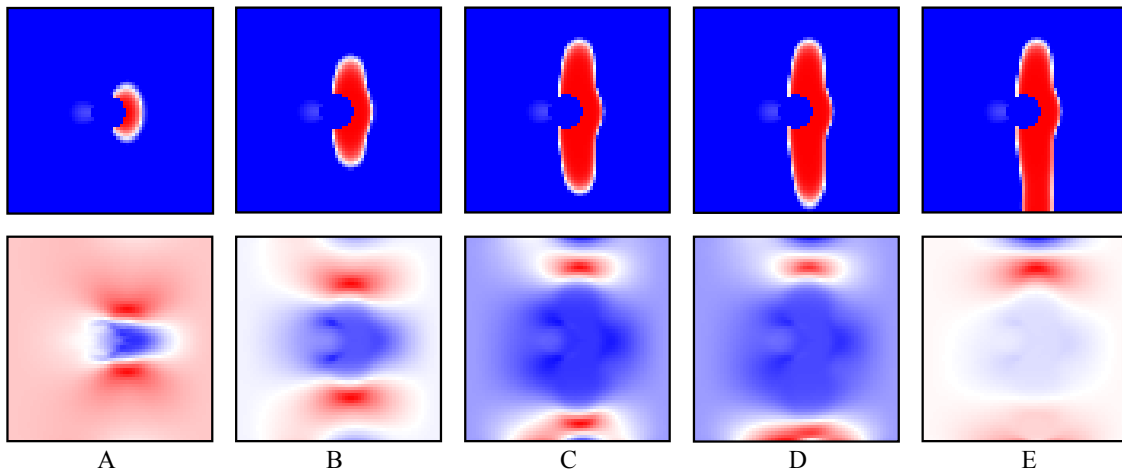


Figure 6.11: Damage process zone (in red), images on the top, and normal stress $\sigma_{xx}$ below (red marks high stress and blue low stress) according to the five, marked states A to E of Fig. 6.10

in Figs. 6.9 and 6.10. Now, it can also be understood what it means that the graph of element size 2 mm in Fig. 6.9 is different after state D. In fact, in the coarser mesh, even after state D, the damage develops symmetrically. The reason results from the simple fact that on the coarse mesh the inclusion with the selected width of six elements has exactly been put in the center of the model. Thus, the final deviation of the 2 mm graph in Fig. 6.9 from the other graphs may mainly result from this apparently, minor and ignored difference. In fact, if the inclusion of the width 11 is put half an element above the center, then the damage breaks through the upper edge. Then, state E is horizontally mirrored. This is clear due to symmetry, but has also been tested to exclude other effects. This observation indicates that apparently minor changes of the microstructure can lead into essentially different damage processes and observed damage behavior on the macroscale. It is proposed to perform many small steps such that each damage state, which decides over the following damage growth, can accurately be detected. If the problem is sensitive
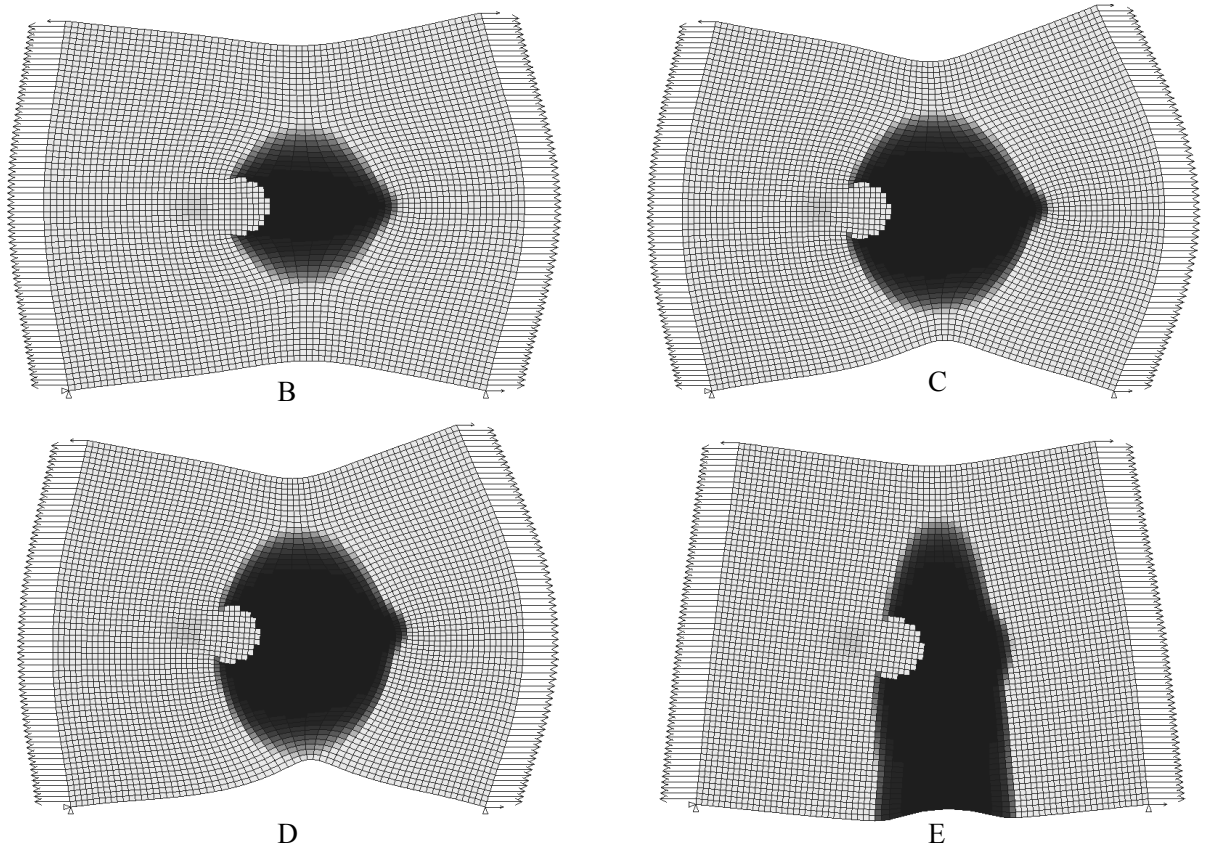
Figure 6.12: Magnified deformation according to states B . . . E of Fig. 6.10

to the microstructural arrangement in this way, then it is proposed to perform a statistical analysis based on many simulations. For the linear elastic behavior in terms of effective properties this is exemplified in Chapter 7.

Some additional results are presented. Figure 6.13 shows various load-displacement curves with respect to a modification of the parameter $\epsilon_f$ (Eq. 3.48). All other parameters are equal to the model of Fig. 6.9 with element size of 1 mm. The graphs show that with increasing ductility the peak load and the absorbed energy increases, but the typical shape of the curves principally remains. In (Häfner, Eckardt, Luther and Könke 2006) results from geometrical modeling and linear elastic analysis are presented. Two corresponding images are shown on the left of Fig. 6.14. It was predicted that cracks will initiate at zones where very large stresses occur (black zones in center image of Fig. 6.14). For further interest damage simulation has been performed on this geometry. In fact, damage initiates on the left side of the large inclusion (which is located in the upper right half). The developed damage distribution after several iterations is illustrated in the right image of Fig. 6.14 in terms of equivalent strains (large equivalent strains are black). While the damaged region is larger, the equivalent strains are only large in a very localized region (similar to image (g) of Fig. 6.8) which appears like a discrete crack. This result exemplifies the proposed analysis for a model with several inclusions.
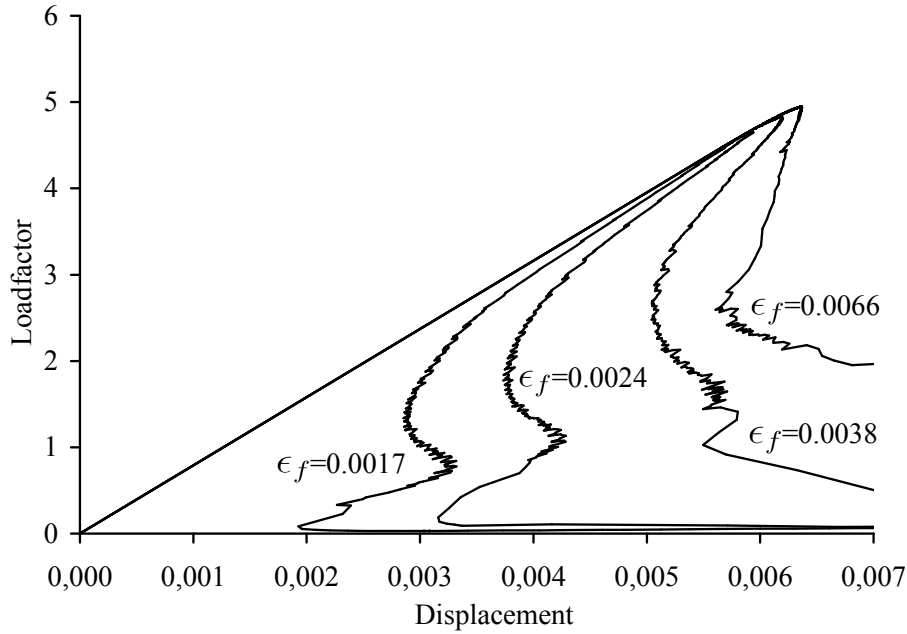
Figure 6.13: Load-displacement curves for different ductility in terms of parameter $\epsilon_f$
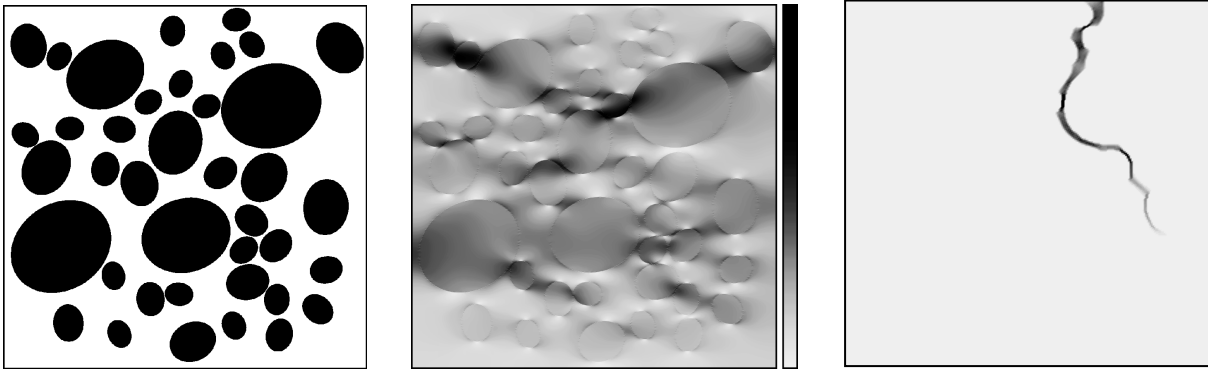


Figure 6.14: Geometrical model of inclusions in a matrix (left). Mises stress from linear elastic analysis (center). Local equivalent strain from damage simulation according to uniaxial tension in horizontal direction (right).

## 6.5.3 Computational Effort

Numerical efficiency is a key aspect of the present grid-based approach. The multigrid method has been applied as fast iterative solver method for the linear elastic analysis of heterogeneous solids in Chapter 5. The major characteristics are low memory demand, low computation times and the computational effort only increases linear with increasing size of the problem. It is favorable, that the efficiency is also possibly high for the proposed damage simulation. Therefore the damage simulation is performed according to a damage-controlled sequentially linear analysis as introduced in Section 6.4. Then each load step corresponds to a linear elastic analysis with a new distribution of Young's modulus $\hat{E}$ (Eq. 3.51) in the model. The modified Young's modulus $\hat{E}$ represents the current damage state and can be interpreted as secant stiffness. It follows that there is no modification of the multigrid method required for damage simulation, except that the applied Young's modulus is $\hat{E}$ instead of the initial Young's modulus $E$ (Eq. 3.51) of the undamaged model.
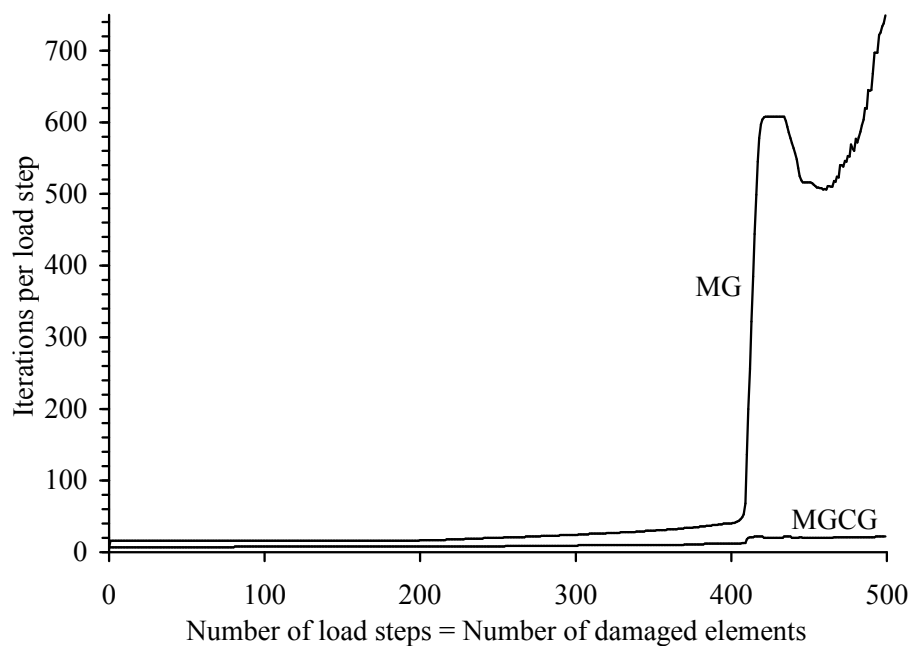
Figure 6.15: Comparison of the number of iterations per load step between the multigrid method (MG) and the multigrid preconditioned conjugate gradient method (MGCG)

As according to the damage law (Section 3.4.2) in each element the secant stiffness $\hat{E}$ is always positive, the global stiffness matrix (which is neither created nor stored) remains positive definite and the finite element element problem numerically stable (for confidence it is possible to define a lower limit of $\hat{E}$ such as $1.0 \cdot 10^{-12}$ which is far below $E$, but not zero). Thus it is possible to run a stable simulation up to complete damage. In the present concept it is proposed that in each load step one finite element enters the damage state. This is done for precisely controlling the damage evolution and achieving an accurate solution. It would also be possible that in each load step two or more elements enter the damage state. In the present approach the number of load steps and number of damaged finite elements are equal.

The present example corresponds to that of Fig. 6.9 with element size 1 mm, but with interaction radius 5 mm. The multigrid method and the multigrid preconditioned conjugate gradient method are applied. For both cases, the W-cycle with three smoothing steps on each level is performed. And in both cases each load step starts from the zero vector. The error tolerance for each load step was $\epsilon_r = 1.0 \cdot 10^{-6}$ (Eq. 5.63). The number of cycles per load step is compared in Fig. 6.15. From the beginning the preconditioned version requires less cycles. But it also needs to be considered that the cycle of the preconditioned version requires more operations. A critical point is reached at about 410 load steps. In the present example this load step corresponds to the situation when the damage reaches the edge (similar to state E of Fig. 6.12). In both methods the number of cycles increases here. However, the number of cycles from the plain multigrid method increases essentially more. The advantage of the preconditioned version is significant. It follows that for damage simulation the preconditioned version should be applied. One reason lies in the large ratios of Young's moduli which occur within the model due to damage (Section 5.11.3). The sudden increase of cycles at about load step 410 can be explained by the change from a uniaxial tension problem into a bending problem (compare state D and E of Fig. 6.12).
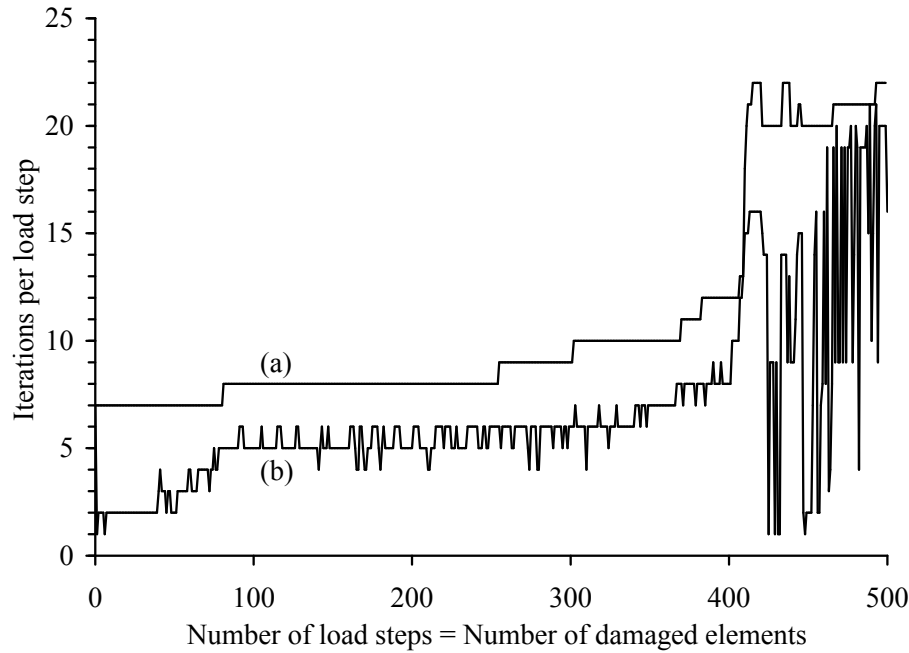
Figure 6.16: Number of iterations per load step of the multigrid preconditioned conjugate gradient method, when (a) each load step starts from the zero vector or (b) each load step starts from the solution vector of the last load step.

Only the multigrid preconditioned conjugate gradient method is considered in the following. In the previous example the iteration of each load step started from the zero vector. It is examined how the number of iterations changes if each load step starts from the solution of the last load step. For the same parameters as in the foregoing example the result is shown in Fig. 6.16. Graph (b) indicates a relevant reduction compared to graph (a). In the first 100 load steps the number of iterations reduces from 719 to 321 which means only 45% of the previous effort. After all 500 load steps the ratio is 5398 to 3311 which still yields a reduction to 61%. In this case the error tolerance for each load step was $\epsilon_r = 1.0 \cdot 10^{-6}$ (Eq. 5.63). For a error tolerance of $\epsilon_r = 1.0 \cdot 10^{-8}$ the two corresponding values are 52% for 100 load steps and 68% for 500 load steps. Thus, the larger the error tolerance, the larger is the gain from the previous solution. Altogether roughly half of the computational effort represents a relevant saving. But as in each load step there is only one additional damaged element, while clearly all other damaged elements are also updated, it could have been expected that the previous solution provides an even better start vector for the next load step. It follows that the gain from the previous solution should be larger for a smaller element size. Therefore the test is repeated for a mesh with element size 0.5 mm instead of 1 mm (the meshes are shown in Fig. 6.9). There the effort reduces to 37% for 400 load steps and to 53% for 2000 load steps (without illustration) based on an error tolerance of $\epsilon_r = 1.0 \cdot 10^{-6}$. Thus, the gain from the previous solution is larger for a smaller element size, but the improvement is not quite essential. On the other hand, for half the mesh size the same damage region corresponds to four times the number of damaged elements (or load steps).

According to a very rough estimation, for increasing model size there is a linear increase of computational effort per load step and a linear increase of number of load steps. Thus, in total the computational effort of damage simulation increases about by quadratic order with respect to model size. A corresponding test has been performed. A computer

with 1.1 GHz processor was used. For element size 1 mm ($64 \times 64$ finite elements, 8447 degrees of freedom) the computation time for 500 load steps was 82.22 seconds. For element size 0.5 mm ($128 \times 128$ finite elements, 33279 degrees of freedom) the computation time for 2000 load steps was 1214.22 seconds. Recalling the formulation $a^x = b$ (page 110), this yields $a = 33279/8447 = 3.94$, $b = 1214.22/82.22 = 14.77$ and thus an order of $x = 1.96$. The present example confirms the supposed quadratic order. This principally also means that the order could roughly be linear, if the load step (damage increment) increases linear with model size. However, this has not been tested. Here this study ends. For future application it is indicated to rethink the required error tolerance, the size of the load steps and to consider further options to improve the start vector of the next load step. In any case, a significant reduction of computational effort has been achieved by the preconditioned version in comparison to the plain multigrid method (Fig. 6.15).

## 6.6   Conclusions

Nonlocal damage modeling on orthogonal grids is exemplified by an isotropic material law with exponential softening for tension. A damage-controlled procedure of linear steps is performed, which means that from one step to another only a certain increment of damage occurs. Defects of stresses from the grid-based solution of bilinear finite elements can significantly be improved by nonlocal post-processing. The uniform grid supports an effective implementation of nonlocal averaging by a predefined discrete representation of the weighting function. Within a reasonable parameter space, only low sensitivity to mesh orientation and mesh size is observed in the present examples. From this follows that grid-based procedures can be prepared for an accurate simulation of damage. Certain damage-induced anisotropic mechanical behavior on the macroscale can be simulated by an isotropic damage formulation on the mesoscale. According to the uniform grid the damage can both equally grow and initiate somewhere within the domain without the need of remeshing. This advantage over an irregular also means an increased model size. However, the applied multigrid method (Chapter 5) is developed for best efficiency in linear grid-based mechanical analysis of very large models. For damaged models a relevant remedy is achieved by the multigrid preconditioned conjugate method. An investigated example shows that minimal changes of the microstructure can initiate different damage mechanisms up to different macroscopic failure. If the mechanical response of a heterogeneous solid is sensitive in such a way, then it is recommended to perform a statistical analysis based on different possible geometrical arrangements of the microstructure. However, the present work only includes a corresponding statistical study for the effective linear elastic mechanical behavior (Chapter 7). The present chapter documents the first successful steps to extend the proposed grid-based approach to damage simulation of heterogeneous solids and thus prepares for future developments.

# Chapter 7

# Study on Effective Mechanical Behavior

## 7.1 Apparent Properties of Various Specimen Sizes

Homogenization is exemplified for two-dimensional models of heterogeneous solids according to Section 3.3. The constitutive relationship for homogenization with respect to homogeneous boundary conditions is defined as

$$
\begin{bmatrix} \langle \sigma_{11} \rangle \\ \langle \sigma_{22} \rangle \\ \langle \sigma_{12} \rangle \end{bmatrix} = \begin{bmatrix} C_{11}^{\text{app}} & C_{12}^{\text{app}} & C_{13}^{\text{app}} \\ C_{21}^{\text{app}} & C_{22}^{\text{app}} & C_{23}^{\text{app}} \\ C_{31}^{\text{app}} & C_{32}^{\text{app}} & C_{33}^{\text{app}} \end{bmatrix} \begin{bmatrix} \langle \epsilon_{11} \rangle \\ \langle \epsilon_{22} \rangle \\ 2\langle \epsilon_{12} \rangle \end{bmatrix} \tag{7.1}
$$

for the two-dimensional problem (analog to Eq. 3.11). The considered square model of side length 100 contains ten circular inclusions of diameter 20. The Young's modulus of the inclusions is $E_{\text{incl.}} = 400000$ and that of the matrix is $E_{\text{matrix}} = 100000$. The Poisson's ratio of both phases is $\nu_{\text{incl.}} = \nu_{\text{matrix.}} = 0.2$. Table 7.1 shows the obtained results for homogeneous displacement boundary conditions and Table 7.2 those for homogeneous traction boundary conditions. Also in the numerical model it is satisfied to a high precision that $C_{ij} = C_{ji}$ for $i \neq j$. A magnification of the corresponding deformation states is illustrated in Figs. 7.1 and 7.2.

| Load case | $\langle \epsilon_{11} \rangle$ | $\langle \epsilon_{22} \rangle$ | $2\langle \epsilon_{12} \rangle$ | $\langle \sigma_{11} \rangle$ | $\langle \sigma_{22} \rangle$ | $\langle \sigma_{12} \rangle$ |
|---|---|---|---|---|---|---|
| $\epsilon_{11}^0 = 0.01$ | 0.01 | $\approx 0$ | $\approx 0$ | 1486.8385 | 306.34816 | 0.03024534 |
| $\epsilon_{22}^0 = 0.01$ | $\approx 0$ | 0.01 | $\approx 0$ | 306.34816 | 1506. 8239 | -0.01221561 |
| $2\epsilon_{12}^0 = 0.01$ | $\approx 0$ | $\approx 0$ | 0.01 | 0.03024534 | -0.01221561 | 592.30535 |

Table 7.1: Numerical results of average strains $\langle \boldsymbol{\epsilon} \rangle$ and stresses $\langle \boldsymbol{\sigma} \rangle$ over the domain $\Omega$ for homogeneous displacement boundary conditions. In this table $(\cdot) \approx 0$ means $|\cdot| < 10^{-18}$

| Load case | $\langle \epsilon_{11} \rangle$ | $\langle \epsilon_{22} \rangle$ | $2\langle \epsilon_{12} \rangle$ | $\langle \sigma_{11} \rangle$ | $\langle \sigma_{22} \rangle$ | $\langle \sigma_{12} \rangle$ |
|---|---|---|---|---|---|---|
| $\sigma_{11}^0 = 1.00$ | $7.17827 \cdot 10^{-6}$ | $-1.53176 \cdot 10^{-6}$ | $-4.23663 \cdot 10^{-9}$ | 1.00 | $\approx 0$ | $\approx 0$ |
| $\sigma_{22}^0 = 1.00$ | $-1.53176 \cdot 10^{-6}$ | $7.18477 \cdot 10^{-6}$ | $2.67115 \cdot 10^{-8}$ | $\approx 0$ | 1.00 | $\approx 0$ |
| $\sigma_{12}^0 = 1.00$ | $-4.23663 \cdot 10^{-9}$ | $2.67115 \cdot 10^{-8}$ | $1.73984 \cdot 10^{-5}$ | $\approx 0$ | $\approx 0$ | 1.00 |

Table 7.2: Numerical results of average strains $\langle \boldsymbol{\epsilon} \rangle$ and stresses $\langle \boldsymbol{\sigma} \rangle$ over the domain $\Omega$ for homogeneous traction boundary conditions. In this table $(\cdot) \approx 0$ means $|\cdot| < 10^{-11}$
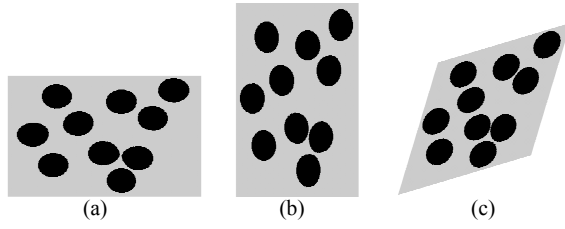
Figure 7.1: Deformed specimen for homogeneous displacement boundary conditions
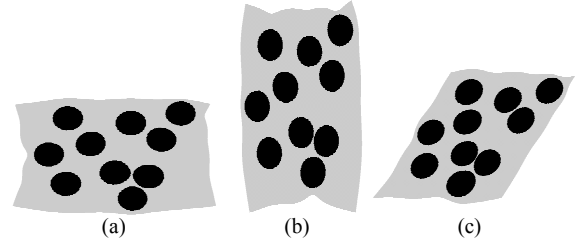


Figure 7.2: Deformed specimen for homogeneous traction boundary conditions

The apparent properties $\boldsymbol{C}_\epsilon^{\text{app}}$ according to homogeneous displacement boundary conditions result from Table 7.1 as

$$\boldsymbol{C}_\epsilon^{\text{app}} = \begin{bmatrix} 148683.85 & 30634.816 & 3.0245336 \\ & 150682.39 & -1.2215607 \\ \text{sym.} & & 59230.535 \end{bmatrix} \tag{7.2}$$

All three load cases of Table 7.2 are required to solve for any entry of $\boldsymbol{C}_\sigma^{\text{app}}$ from the homogeneous traction boundary conditions which yields

$$\boldsymbol{C}_\sigma^{\text{app}} = \begin{bmatrix} 145949.07 & 31115.778 & -12.231000 \\ & 145817.86 & -216.29494 \\ \text{sym.} & & 57476.77 \end{bmatrix} \tag{7.3}$$

The eigenvalues $\lambda$ of $(\boldsymbol{C}_\epsilon^{\text{app}} - \boldsymbol{C}_\sigma^{\text{app}})$ are evaluated according to the fundamental equation

$$\det(\boldsymbol{C}_\epsilon^{\text{app}} - \boldsymbol{C}_\sigma^{\text{app}}) - \lambda \boldsymbol{I} = 0 \tag{7.4}$$

where $\boldsymbol{I}$ is the identity matrix. For the present case the eigenvalues are

$$\lambda_1 = 4981.3956 , \quad \lambda_2 = 2635.2283 , \quad \lambda_3 = 1736.4511 \tag{7.5}$$

All eigenvalues are positive. Thus, the inequality $(\boldsymbol{C}_\epsilon^{\text{app}} > \boldsymbol{C}_\sigma^{\text{app}})$ which follows from Eq. 3.25 is satisfied for this numerical example. From mixed boundary conditions, as discussed in Section 3.3.3, the apparent Young's modulus $E_m^{\text{app}} = 148034.37$ and apparent Poisson's ratio $\nu_m^{\text{app}} = 0.20570461$ are obtained. The applied plane stress case and the assumption of ideal isotropic material behavior lead to the following apparent material properties $\boldsymbol{C}_{\text{m}}^{\text{app}}$ for mixed boundary conditions.

$$\boldsymbol{C}_{\text{m}}^{\text{app}} = \begin{bmatrix} 148034.37 & 30451.352 & 0 \\ & 148034.37 & 0 \\ \text{sym.} & & 58791.51 \end{bmatrix} \tag{7.6}$$

In this example it follows from the analysis of eigenvalues that also the inequalities of Eq. 3.32 $(\boldsymbol{C}_\epsilon^{\text{app}} > \boldsymbol{C}_{\text{m}}^{\text{app}})$ and $(\boldsymbol{C}_{\text{m}}^{\text{app}} > \boldsymbol{C}_\sigma^{\text{app}})$ hold. However, in further examples this was not always true. This can be explained as the proposed homogenization procedure for these mixed boundary conditions presumes ideal isotropy, which is not exactly valid. Numerical errors might also cause a change of inequalities, but only if the two material matrices are quite close. Nevertheless, it can be concluded, that the proposed homogenization procedure with specific mixed boundary conditions (Section 3.3.3) leads to a reasonable approximation of apparent properties by only one load case.
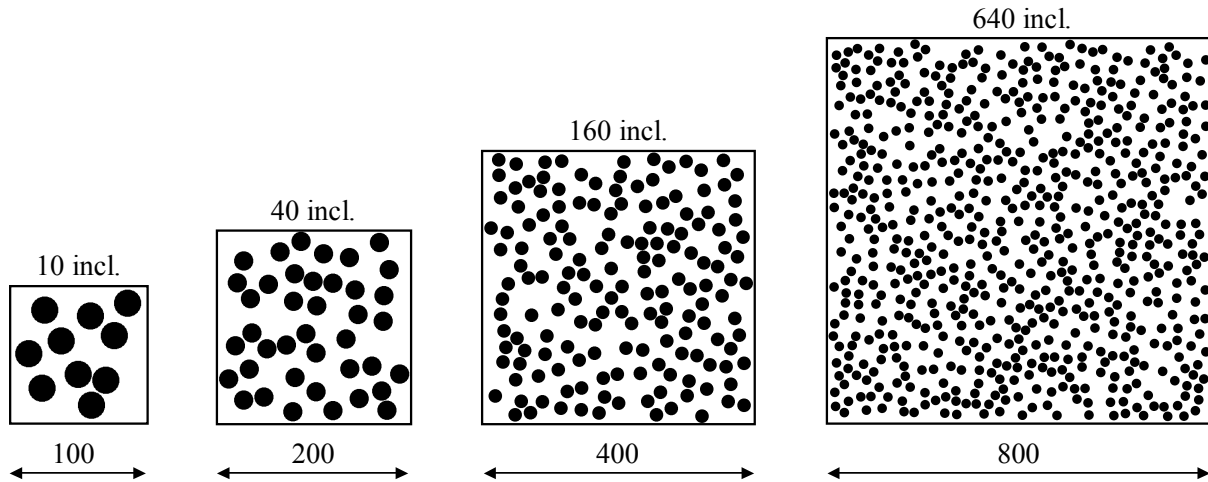
Figure 7.3: Four specimen with different side length: 100, 200, 400 and 800 (not drawn to scale). In all models the area fraction of circles is 31.415%. The diameter of circles is 20. The geometrical arrangement of circles in the different models is random and independent of each other.

For the specimen of side length 100 with ten inclusions it was demonstrated that $\boldsymbol{C}_\epsilon^{\mathrm{app}}$ and $\boldsymbol{C}_\sigma^{\mathrm{app}}$ represent upper and lower bounds of $\boldsymbol{C}_{\mathrm{m}}^{\mathrm{app}}$, respectively. These are also the bounds of the effective properties $\boldsymbol{C}^{\mathrm{eff}}$ as given by Eq. 3.25. With increasing size of specimen the apparent properties will converge to the effective properties. This effect is examined in the following. Figure 7.3 shows four specimen of different size. It includes the undeformed state of the specimen with side length 100 from the previous example (Figs. 7.1 and 7.2). In the same way as exemplified before, for all specimen of Fig. 7.3 the apparent properties have been determined. The result is shown in Fig. 7.4. The graphs KUBC and SUBC represent the average $(C_{11}^{\mathrm{app}} + C_{22}^{\mathrm{app}})/2$, respectively. The result of MBC has been determined according to the average from a load case in x- and y-direction. The averages have been calculated to reduce the effect from possible anisotropy of these specimen. It follows from Eqs. 7.2 and 7.3 that this is a minor correction. Fig. 7.4 illustrates that
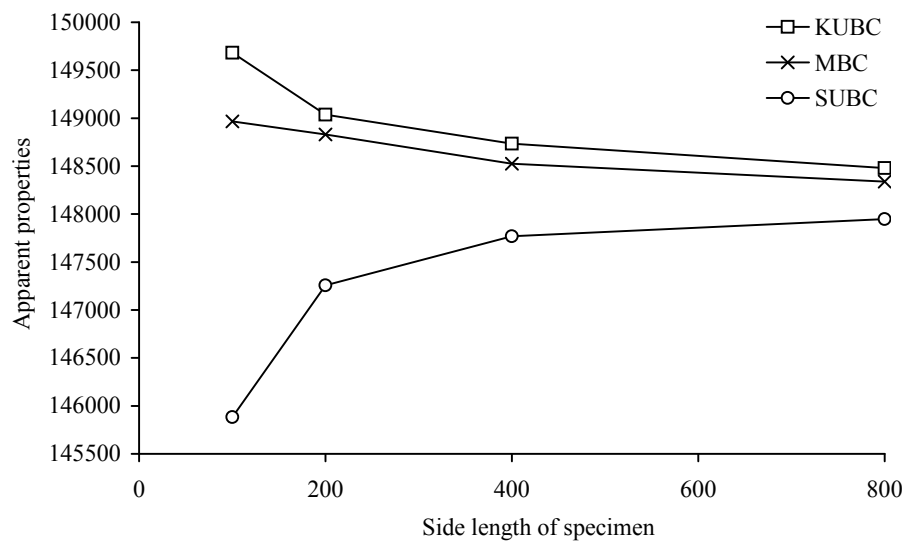


Figure 7.4: Apparent properties of the specimens shown in Fig. 7.3 according to homogeneous displacement boundary conditions (KUBC), homogeneous traction boundary conditions (SUBC) and mixed boundary conditions (MBC). (Abbreviations are defined in Section 3.3.2)

the graphs KUBC and SUBC principally converge with increasing size of specimen, and furthermore that MBC is bounded by KUBC and SUBC. For double side length of the specimen the distance between KUBC and SUBC approximately halves. The exact factors from Fig. 7.4 are 0.47, 0.54 and 0.55 (sorted after increasing size of specimen). It is concluded that the present results are consistent with the provided theory of Section 3.3. With respect to the following study, it is decided that it is sufficient to consider only mixed boundary conditions.

## 7.2   Statistical Study of Random Arrangements

The models from the foregoing section (Fig. 7.4) only represent one possible geometrical arrangement of inclusions. The results may vary with varying geometrical arrangements. This random effect is analyzed in the present section based on numerous different geometrical arrangements. For the evaluation of the results, it is briefly introduced to some fundamental equations of statistics (Bosch 1993).

For a set of $n$ samples $X_i$ with $i = 1 \ldots n$ the mean value $M(X)$ is defined as

$$M(X) = \frac{1}{n} \sum_{i=1}^{n} X_i \tag{7.7}$$

The variance $\mathrm{VAR}(X)$ represents a certain measure of scatter

$$\mathrm{VAR}(X) = \frac{1}{n-1} \sum_{i=1}^{n} (X_i - M(X))^2 \tag{7.8}$$

The standard deviation $S(X)$ is the square root of the variance.

$$S(X) = \sqrt{\mathrm{VAR}(X)} \tag{7.9}$$

The range $R = \max(X) - \min(X)$ represents a further measure of scatter. However, for a comparison of different random sample sets, it is more adequate to compare quantiles. For the present purpose the following definition of an $\alpha$-quantile $Q(X)_\alpha$ is sufficient: $100\,\alpha\,\%$ of the $n$ samples $X_i$ are smaller than $Q(X)_\alpha$.

It is useful to determine confidence intervals on the mean value with respect to number of samples. The following confidence interval is only exact for a normal distribution. Otherwise acceptable approximations can be achieved, if the number of samples $n$ is larger than 30 (Bosch 1993). The probability that the mean value is in the confidence interval

$$\left[ M(X) - z_{1-\alpha} \frac{S(X)}{\sqrt{n}} \,;\; M(X) + z_{1-\alpha} \frac{S(X)}{\sqrt{n}} \right] \tag{7.10}$$

is $1 - 2\alpha$ where $z_{1-\alpha}$ denotes the quantile of the standard normal distribution. Such quantiles are provided by tables in most textbooks of statistics. For example, if the quantile is $z_{0.995} = 2.57583$, then Eq. 7.10 represents the 99% confidence interval.

For arbitrary distribution types the $1 - 2\alpha$ confidence interval for the variance is approximately

$$\left[ S(X)^2 - z_{1-\alpha} \sqrt{\frac{m_4 - (S(X)^2)^2}{n}} \,;\; S(X)^2 + z_{1-\alpha} \sqrt{\frac{m_4 - (S(X)^2)^2}{n}} \right] \tag{7.11}$$

for a large number of samples (Bosch 1993), where the variable $m_4$ is defined as

$$m_4 = \frac{1}{n} \sum_{i=1}^{n} (X_i - M(X))^4 \tag{7.12}$$

The $1 - 2\alpha$ confidence interval of the standard deviation is obtained from the (positive) square roots of the interval bounds in Eq. 7.11.

If for each sample two characteristics $X$ and $Y$ are obtained and examined, it is often of interest, if and how the values of $X$ and $Y$ depend on each other. Such a relationship is quantified by the covariance

$$\text{COV}(X;Y) = \frac{1}{n-1} \sum_{n=1}^{n} (X_i - M(X))(Y_i - M(Y)) \tag{7.13}$$

However, the covariance is not invariant with respect to a change of scale. Therefore it is proposed to apply the correlation coefficient

$$\rho(X;Y) = \frac{\text{COV}(X;Y)}{S(X)\,S(Y)} \tag{7.14}$$

The possible range of the correlation coefficients is $[-1;1]$. If $\rho(X;Y) = 0$ then $X$ and $Y$ are independent of each other. The closer $\rho(X;Y)$ is to -1 or to 1, the stronger $X$ and $Y$ are correlated. For a positive (negative) correlation $\rho(X;Y) > 0$ ($\rho(X;Y) < 0$), $Y$ is expected to be large (small), if $X$ is large.

In the following it is briefly commented on probability density function and histogram. Figure 7.5 shows the probability density function (pdf) of the standard normal distribution. Figure 7.6 presents a histogram based on 100 random samples which have been generated according to the standard normal distribution. Each bar illustrates the absolute frequency of samples within the range of the bar, which is denoted as class. Here the class width is 0.5. The area below any valid probability density function corresponds to 1. The histogram can be scaled such that total area of bars is also equal to 1. Then, the scaled histogram represents an approximation of the probability density function. With increasing number of samples the expected approximation quality of the histogram improves. In the following study such scaled histograms are used and denoted as normalized histogram. For simplicity the bars are replaced by one graph, as for example the dashed graph in Fig. 7.6.
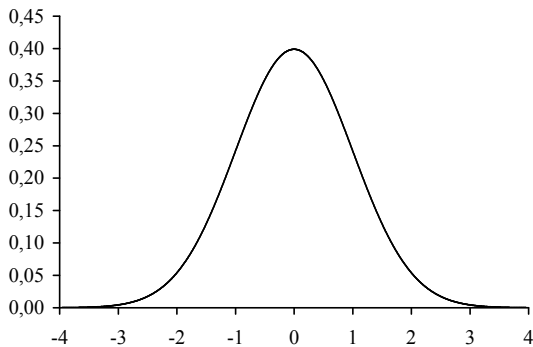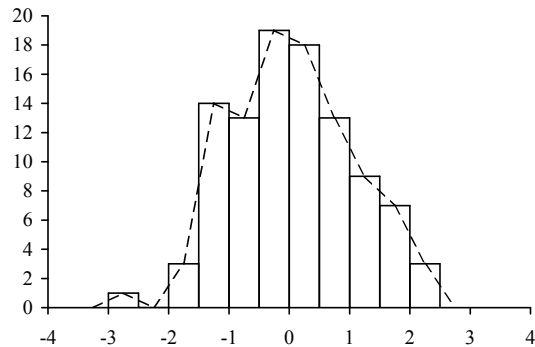


Figure 7.5: Standard normal distribution        Figure 7.6: Histogram based on 100 samples

Figure 3.5 illustrates the applied load case. The result is evaluated in terms of deformation energy. Deformation energy means external work $E_W$, the energy which is required to deform the body to a specific amount. For the present load case, it is $E_W = \frac{1}{2}(R_1 u_{1+})$. If $u_{1+} = 1$, then it follows that $2E_W = R_1$. The dimensions of the square are the width $W$ and the height $H$, with $W = H$. It follows that, $R_1 = \sigma_{11}^b H$ and $\epsilon_{11}^0 = \frac{1}{W}$, and thus $\sigma_{11}^b = R_1 \epsilon_{11}^0$. As for the present load case, it is true that $\epsilon_{12}^0 = 0$ and $\epsilon_{22}^0 = 0$, it follows that $\sigma_{11}^b = C_{11} \epsilon_{11}^0$. Finally, it can be concluded that

$$2E_W = R_1 = C_{11} \qquad \text{if } u_{1+} = 1 \tag{7.15}$$

such that it is possible to interpret the result in the diagrams as twice the deformation energy for $u_{1+} = 1$ (or directly as the deformation energy for $u_{1+} = \frac{1}{2}\sqrt{2}$), as the resulting force $R_1$ for $u_{1+} = 1$ or an approximation of $C_{11}$ according to mixed boundary conditions. This rich interpretation supports the objectivity and meaning of the following results.

The first study examines the influence from random arrangement of inclusions with respect to varying size of specimen. The applied parameters of the study are analog to that of Fig. 7.3, only the arrangement of inclusions is random. For each specimen size, 9000 different geometrical arrangements have been analyzed. The result is shown in Fig. 7.7. With increasing specimen size the mean value of deformation energy decreases by 0.4% from size 100 to 200 and by further 0.2% from size 200 to 400. With increasing specimen size the influence from random arrangement decreases. In fact, for double side length the standard deviation approximately halves. The factors are 0.44 from 100 to 200 and 0.47 from 200 to 400. The 99% confidence interval of the mean value according to Eq. 7.10 is $[149299; 149393]$ for size 100, $[148725; 148767]$ for size 200 and $[148437; 148457]$ for size 400. The 99% confidence interval of the standard deviation is determined by Eq. 7.11 as $[1711; 1779]$ for size 100, $[755; 785]$ for size 200 and $[360; 374]$ for size 400. From the evaluated confidence intervals it follows that the achieved mean values and standard
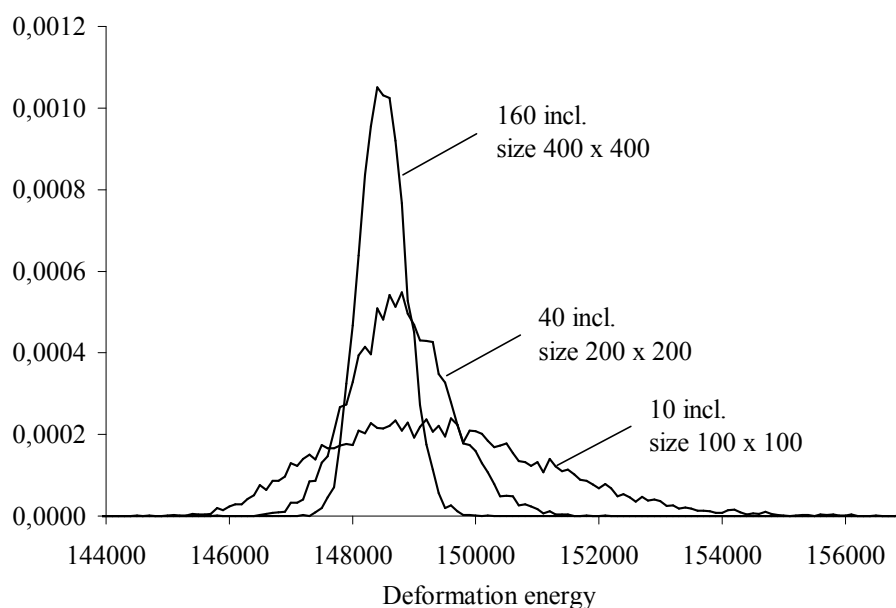


Figure 7.7: Normalized histograms of deformation energy (Eq. 7.15) for various sizes of specimen, each based on 9000 samples (class width 100). From size 100 to 400: mean values are 149346, 148746, 148447 and standard deviations are 1745, 770, 367, respectively.
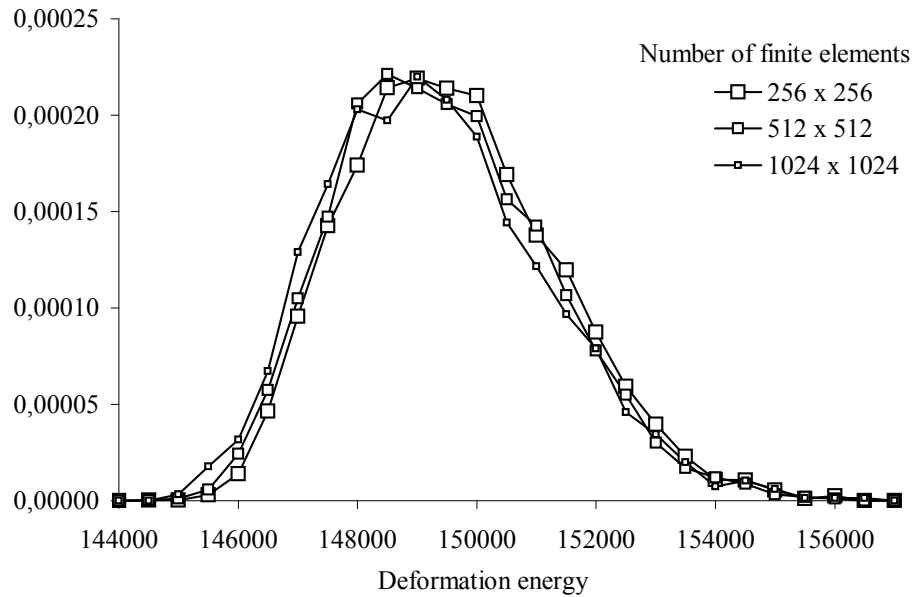
Figure 7.8: Normalized histograms of deformation energy (Eq. 7.15) for various resolution of meshes, each based on 6000 samples (class width 500). From coarse to fine mesh: mean values are 149345, 149186, 149070 and standard deviations are 1753, 1750, 1825, respectively.

deviations are reasonably accurate from a statistical point of view. This means that the number of samples is sufficient.

In the following the numerical error due to finite elements and due to geometrical approximation of the circles is discussed. Only bilinear finite elements have been applied in this study, but the resolution is relatively high. In the foregoing example the small model of the dimensions $100 \times 100$ is discretized by $256 \times 256$ finite elements. For the larger models the element size is kept constant, such that model size 200 is based on $512 \times 512$ and size 400 on $1024 \times 1024$ finite elements.

For a rough estimation on the dimension of the numerical error, the model of side length 100 is analyzed based on two refined meshes. The corresponding histograms are illustrated in Fig. 7.8. The mean values from coarse and finest mesh differ by 0.18%. It can be concluded that the numerical error of the coarse mesh is larger. For further reference, the 99% confidence interval from statistics is only about $\pm 0.04\%$ for each mean value. This highlights that it is principally indicated to apply higher order finite elements in such studies, for example the proposed B-spline finite elements[1]. Nevertheless, the numerical error appears not too significant with respect to the following examples. This also becomes quite obvious from a comparison to subsequent histograms.

A further study is dedicated to analyze the effect from shape of inclusions. Like in the previous examples, in all models the area fraction of inclusions is 31.415%. The number of inclusions also remains equal for the different shapes. The Young's modulus of matrix is 100000 and that of inclusions is 400000. The Poisson's ratio is 0.2 for both phases. Figure 7.9 compares the previous example of circles with ellipsoid inclusions of the aspect ratio 4:1. The corresponding size of specimen is 100. The histogram directly shows that the scatter from ellipses is considerably larger. As an explanation it is supposed that

---

[1]Only the conjugate gradient method has been introduced for B-spline finite elements. Thus, for a larger study bilinear finite elements were applied in connection with the more efficient multigrid method.
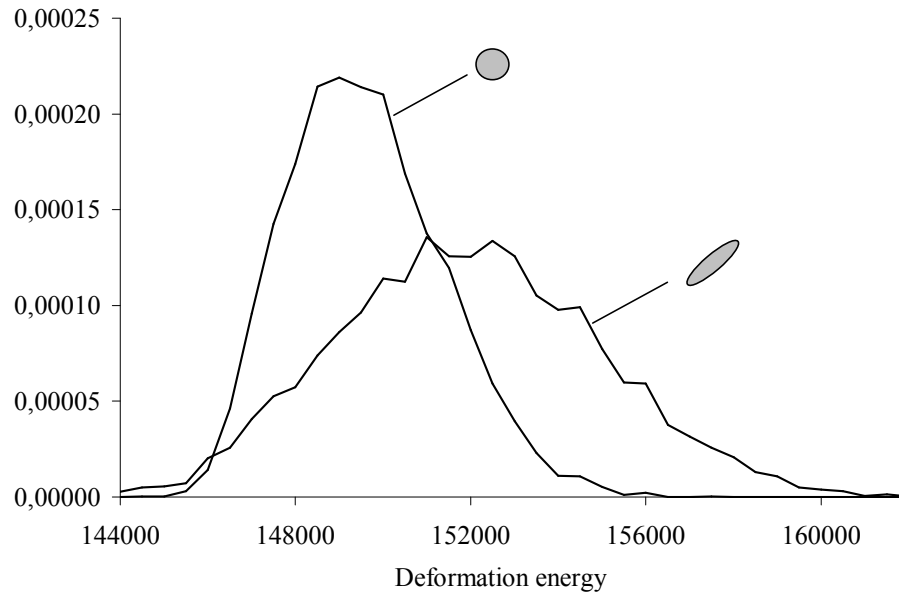
Figure 7.9: Normalized histograms of deformation energy (Eq. 7.15) based on 6000 samples each (class width 500). For circular inclusions and ellipses of aspect ratio 4/1: mean values are 149345 and 151704 and standard deviations are 1754 and 2982, respectively.



Figure 7.10: Normalized histograms of deformation energy (Eq. 7.15) based on 6000 samples each (class width 200). For circular inclusions and ellipses of aspect ratio 4/1: mean values are 148449 and 151249 and standard deviations are 368 and 793, respectively.

especially due to rotation of ellipses a larger variety of geometrical arrangements can develop. With 2982 versus 1754 the standard deviation of deformation energy from ellipses is 1.7-times larger than that from circles. The mean values differ by 1.6%. Figure 7.10 shows the results from an analog study based on 160 inclusions in a square specimen of side length 400. Here, the standard deviation from ellipses is 2.1-times larger than that from circles. The mean values differ by 1.9%. It can be concluded that there is a certain effect from shape of inclusions on the deformation energy, or on the apparent properties according to Eq. 7.15. The stiffness tends to increase if ellipsoid inclusions of

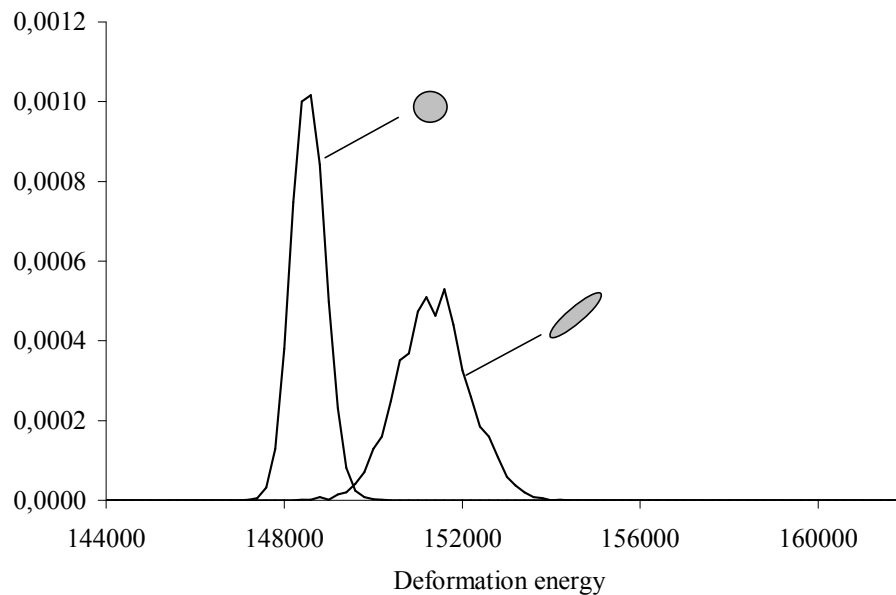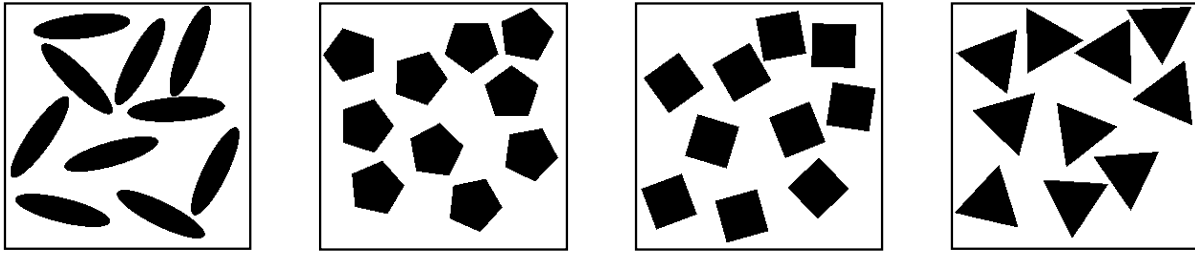Figure 7.11: Various shapes of inclusions. The geometrical arrangement of inclusions is random.
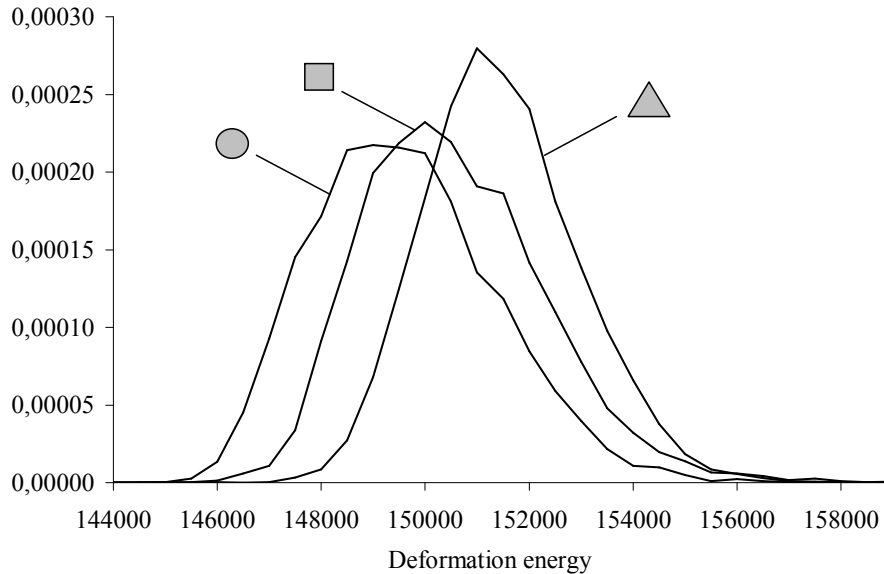


Figure 7.12: Normalized histograms of deformation energy (Eq. 7.15) based on 9000 samples each (class width 500). For circles, squares, triangles: mean values are 149346, 150314, 151210 and standard deviations are 1745, 1764, 1470, respectively (Pentagon 149802; 1630).

aspect ratio 4:1 are applied instead of circular inclusions. This observed stiffening effect is in agreement to Tsukrov and Novak (2004) who propose a numerical procedure of conformal mapping for modeling irregular shapes and moreover present several further results. However, as there is a relevant overlapping range of histograms in Fig. 7.9, the stiffening effect is not necessarily observed for two random samples of size 100.

The results from the foregoing example of ellipses motivates a further study on other inclusion shapes. On the left Fig. 7.11 shows a specimen with a random arrangement of ellipses of aspect ratio 4:1. It further illustrates specimens with pentagons, squares and equilateral triangles. Figure 7.11 displays finite element models in original resolution of $256 \times 256$ pixels. The various inclusions shapes are accurately represented. The polygonal shapes have been generated according to the formula of supershapes (Section 2.2: Eq. 2.3 and Section 2.7: Table 2.2). Figure 7.12 represents the results of the analysis. The histogram from the pentagons has not been included. It would be in between the histogram from circles and that from squares. The ranges of the different examples largely overlap. This highlights that only a few samples might not quite reflect the observed relationship. For squares, and even more for triangles, the frequency of effectively stiffer specimen is larger in comparison to circles. From the basis reference of circles, the mean value from squares is 0.65% larger, and that from triangles 1.25%. It can be concluded, that there is a
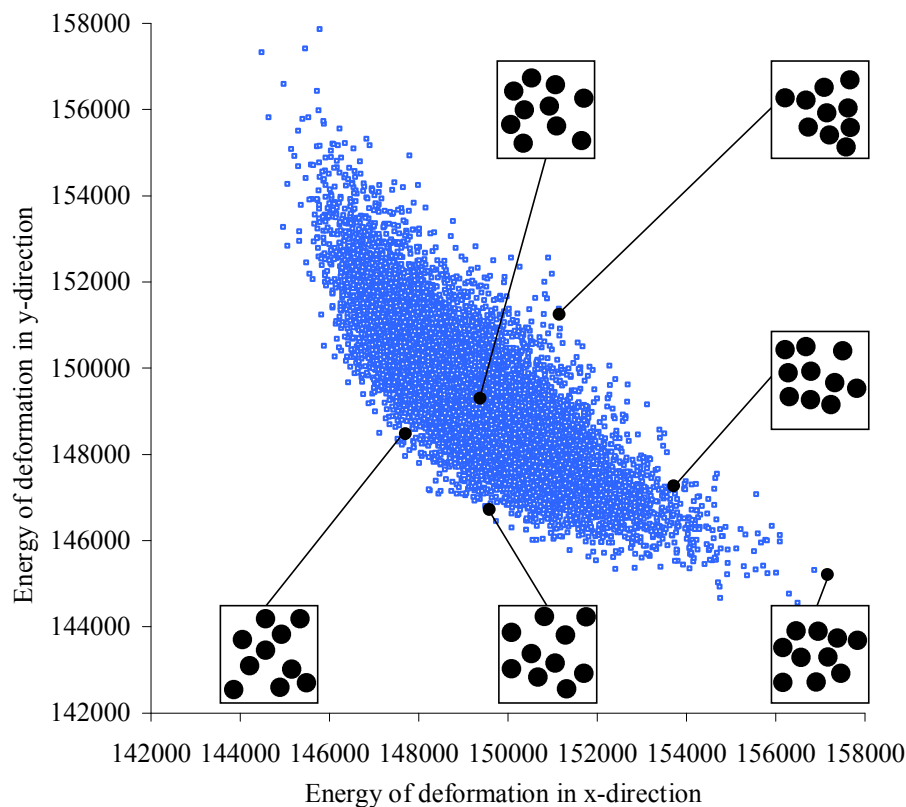
Figure 7.13: Scatter plot of deformation energies (Eq. 7.15) based on a load case in x-direction and a load case in y-direction for each sample (10000 samples). Size of specimen is 100. For x- and y-direction: mean values are 149339 and 149336, standard deviations are 1736.6 and 1735.5. The correlation coefficient is -0.81.

clear effect from shape of inclusions on the apparent properties. On the other hand, it also turns out that this effect is limited to at most a few percent of effective stiffness. For the present small specimen of size 100, the influence from random arrangement of inclusions is larger. The total range in the histogram of circles is about 7.5% with respect to the mean value of deformation energy. In summary, there are random effects in heterogeneous solids which depend on shape of inclusions, arrangement of inclusions and sample size (scale of observation).

The previous studies on deformation energy are based on one load case of mixed boundary conditions which can be characterized as a deformation state in x-direction (horizontal). The present study additionally includes the deformation energy for an equivalent deformation state in y-direction (vertical) for each sample. The major parameters of this example correspond to the previous studies. Circular inclusions are applied. For a square specimen of size 100, Figure 7.13 represents the scatter plot of the deformation energies according to random geometrical arrangements of inclusion. For some samples the corresponding geometry is shown. It is principally observed that the deformation energy with respect to a certain direction increases, if inclusions are aligned parallel to this direction and further-more if the spaces in between are small. An ideal parallel arrangement of phases yields a Young's modulus of 130835 (Reuss) for a deformation perpendicular to phase orientation and 194248 (Voigt) for a deformation parallel to phase orientation. It is clear, that such an ideal parallel arrangement of phases can not be created by circular inclusions. However, the theoretical bounds reflect a strong directional dependency. It is interesting to examine,
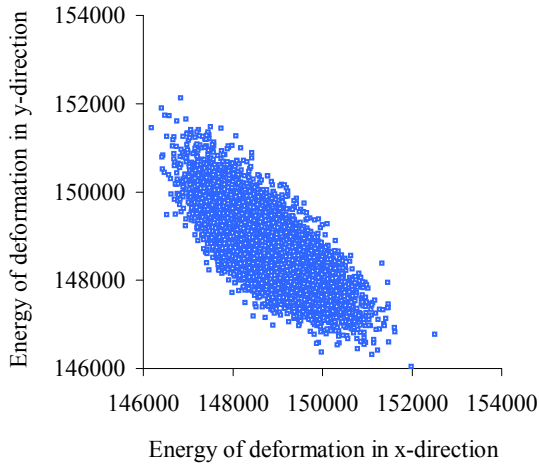
Figure 7.14: Same type of scatter plot as Fig. 7.13, but size of specimen is 200. For x- and y-direction: mean values are 148743 and 148756, standard deviations are 780 and 776. The correlation coefficient is -0.76.
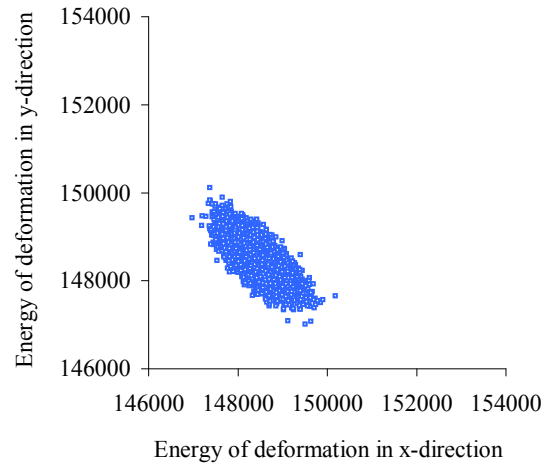
Figure 7.15: Same type of scatter plot as Fig. 7.13, but size of specimen is 400. For x- and y-direction: mean values are 148452 and 148453, standard deviations are 370 and 368. The correlation coefficient is -0.73.

if and in which quantity such a directional dependency is present in the current example of circular inclusions. Equation 7.14 yields a correlation coefficient of $-0.81$ for the samples shown in Fig. 7.13. This indicates that, in models of randomly arranged inclusions, there is a strong correlation of effective stiffness between perpendicular directions. From this very small model of ten inclusion it is not known, if this strong correlation is also present in models of more inclusions. Thus, the study is repeated for a model of size 200 with 40 inclusions and a model of size 400 with 160 inclusions. The scatter plots of these larger models are given in Figs. 7.14 and 7.15. In analogy to Fig. 7.7, the scatter of deformation energy decreases with increasing specimen size. The computation according to Eq. 7.14 leads to a correlation coefficient of -0.76 for model size 200 (Fig. 7.14) and of -0.73 for model size 400 (Fig. 7.15). This means that the strong correlation principally persists for an increasing number of inclusions and does not vanish due to random arrangement of inclusions. For the present models with randomly arranged inclusions, the descriptive interpretation is: if the stiffness with respect to a certain direction is relatively large, then it strongly tends to be relatively low in the perpendicular direction.

A further example studies the effect from voids on the deformation energy, with respect to volume ratio of voids and random arrangement of voids. The result is illustrated in Fig. 7.16. The influence from volume ratio of voids can best be evaluated from the graph of mean value. For each marked volume ratio, 10000 different geometrical arrangements of voids have been analyzed. The observed scatter is included in terms of 0.01 and 0.99 quantiles (the term quantile is introduced on page 137). In the present example with constant diameter of voids, the effect on the absolute value of deformation energy from random arrangement of voids is largest between 10% and 40% volume ratio. The maximal influence from random arrangement corresponds to approximately 5% change of volume ratio. Nevertheless, for a constant volume ratio of 50% the range of deformation energy in between quantiles is relatively large in comparison to mean value, in fact, it is about 20% of mean value. This describes a relevant random effect from geometrical arrangement onto the apparent elastic properties.
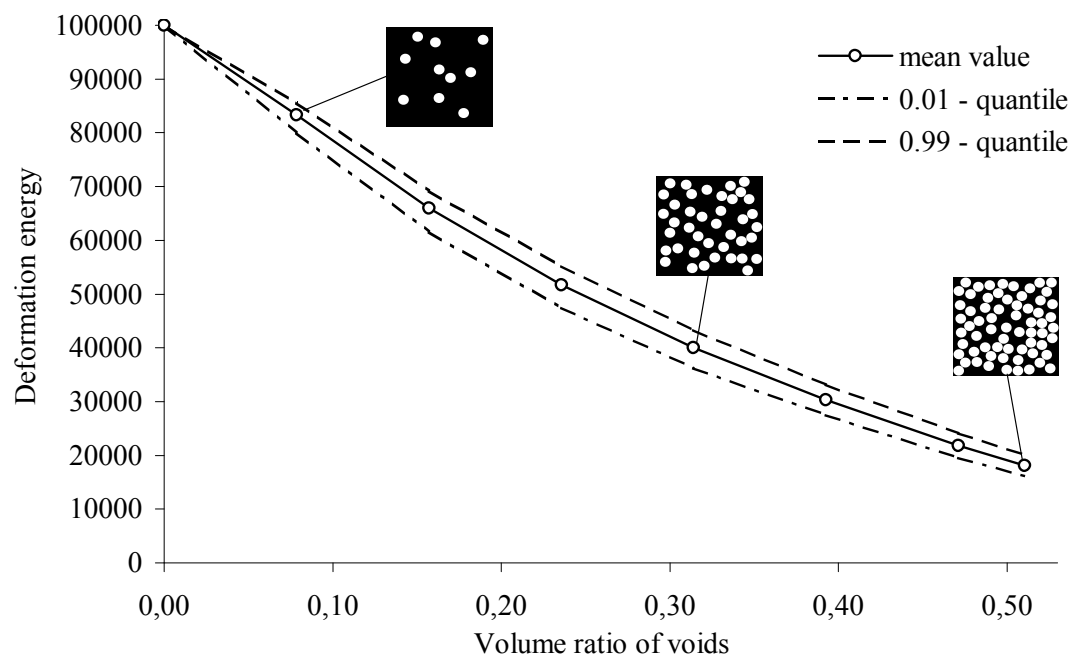
Figure 7.16: Deformation energy (Eq. 7.15) for random geometrical arrangements of voids

The present study highlights that, based on an accurate analysis and on many numerical experiments, quite precise statistical predictions on the effective material behavior can be achieved, which could hardly be established by real experiments. Statistical parameter studies on numerical models represent a relevant option to gain more essential knowledge of random effects in heterogeneous solids. This also includes characteristics of damage behavior or other physical properties such as for example thermal conductivity.

## 7.3    Study of Concrete

Concrete is an important building material. It represents a heterogeneous solid which can be composed in many different ways to meet certain properties. Section 1.1 provides a brief introduction to concrete. Figure 1.1 (e) shows a typical cross section geometry of the real material. Stock, Hannant and Williams (1979) performed experiments on concrete to examine the effect from volume ratio of aggregates onto the effective[2] Young's modulus. The aggregates are stiffer than the matrix such that with increasing volume ratio of aggregates the effective Young's modulus increases. The observed relationship from the experiments represents a valuable reference for a comparison of concrete models with real concrete in terms of linear elastic behavior.

The applied concrete model of the mesoscale consists of two phases: aggregates and cement stone (Section 1.2). The model supposes ideal bond between the phases. In the experiment the mean Young's modulus of the cement stone was determined as 11.6 kN/mm$^2$ and that of the aggregates as 74.5 kN/mm$^2$. The Poisson's ratio is not specified by the experiments

---

[2]From the definitions of Section 3.3.2 follows that from specimen or models of finite size generally only apparent properties can be obtained. Apparent properties can serve as an approximation of effective properties. It is noted that certain bounds are only exactly valid for effective properties. Nevertheless, in many works and in the following the term effective properties is applied instead of apparent properties.
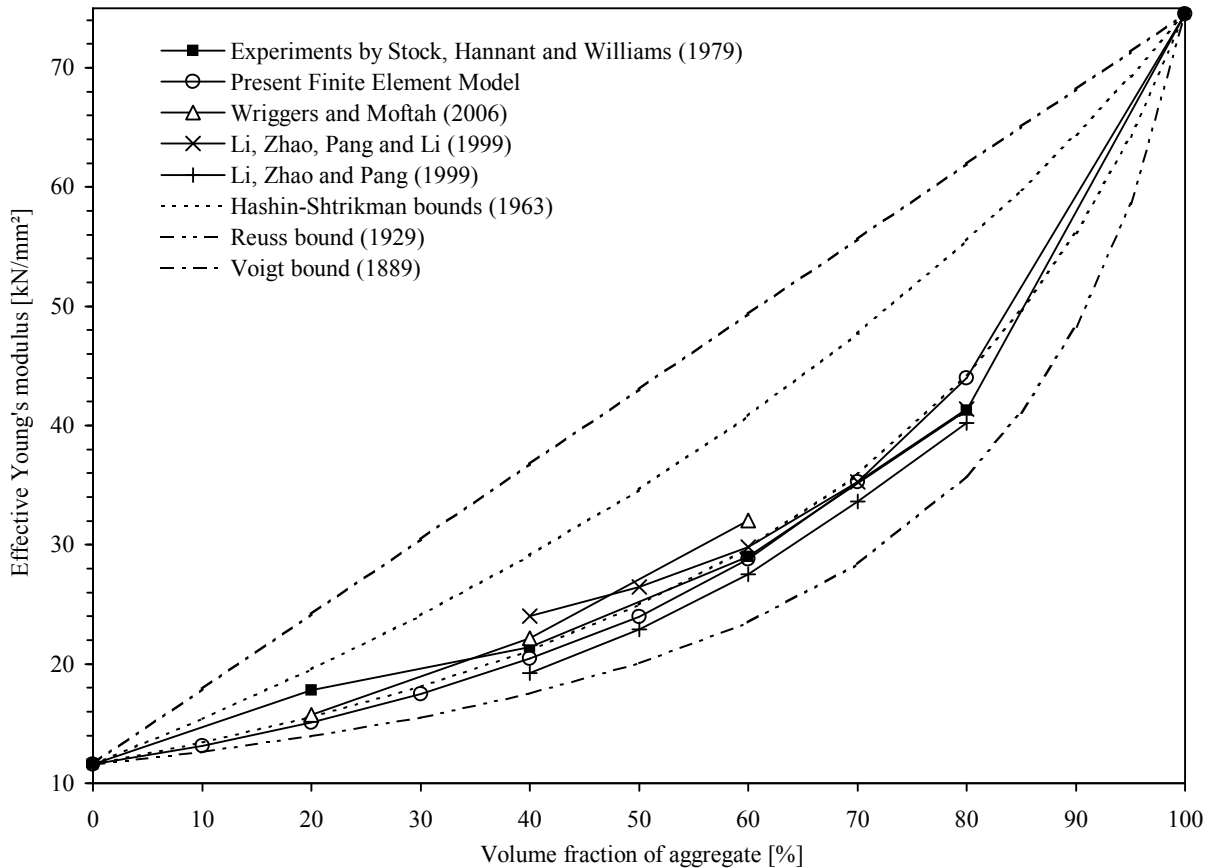
Figure 7.17: A comparison of various models to experiments of Stock, Hannant and Williams (1979)

and was defined as $\nu = 0.2$ for both constituents. In the experiment a grading curve of particle sizes from 0.15 mm to 19 mm was used. For a square, two-dimensional sample of 100 mm side length, the resolution $2048 \times 2048$ finite elements leads to an element size of 0.05 mm. Common bilinear finite elements have been applied in the analysis. Therefore it was decided to use a grading curve which starts from 0.5 mm such that the smallest particles in the model can accurately be represented by the finite elements. The homogenization of Young's modulus was performed based on mixed boundary conditions according to Eq. 3.38.

The results of the present finite element model show principally good agreement with the results of the real experiments (Fig. 7.17). It needs to be considered that there are several possible reasons for deviation, such as natural deviation of material parameters in real specimen or type of testing procedure. For example at a aggregate volume ratio of 80% the determined average Young's modulus from the tension tests was $41.3 \, \text{kN/m}^2$ and that from the compression tests was $39.1 \, \text{kN/m}^2$ (Stock, Hannant and Williams 1979). Additionally, for the tension tests of 80% aggregate volume a standard deviation of $2.85 \, \text{kN/m}^2$ was estimated based on four tests. From four compression tests the corresponding standard deviation was $1.52 \, \text{kN/m}^2$. The observed scatter from the experiments shows that concrete is subjected to a certain range of randomness. Besides, the Poisson's ratios of aggregates and cement stone are not available from the experiments. From the prior arguments clearly follows that an exact match of the numerical model to these experiments would represent a random effect or at least a deviation of $2 - 3 \, \text{kN/m}^2$ still could be considered as perfectly accurate.
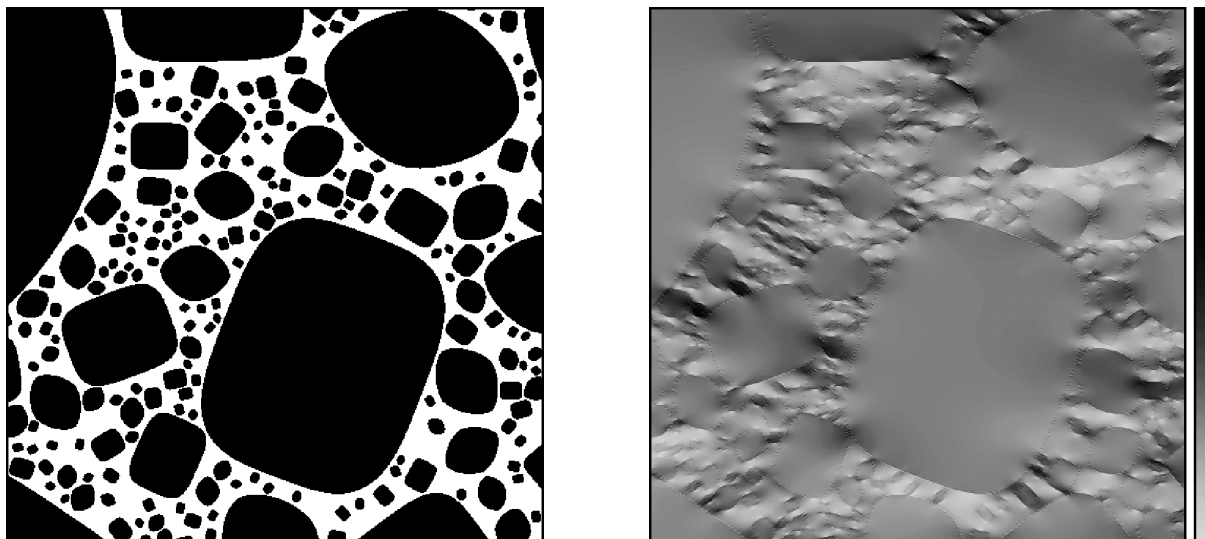
Figure 7.18: Magnified cut-out of inclusion-matrix model of concrete on the left and corresponding Mises stress according to mainly horizontal tension on the right (Häfner, Eckardt, Luther and Könke 2006)

The results from various numerical model are included in Fig. 7.17. In (Li, Zhao, Pang and Li 1999) a four-phase sphere model is presented. It includes an interfacial transition zone which generally represents an improvement with respect to the assumption of rigid bond. But it is noted that the corresponding parameters, such as e.g. thickness and stiffness of interfacial transition zone, were not specified in (Stock, Hannant and Williams 1979). The prediction of a previous model (Li, Zhao and Pang 1999) is also included in Fig. 7.17. The Hashin-Shtrikman bounds are rigorous bounds based on ideal assumptions such as isotropy or infinite sample size of three-dimensional bodies (Section 3.3.4). For further orientation, the bounds from Reuss (1929) and Voigt (1889) illustrate the theoretically possible range of effective Young's modulus with respect to volume ratio of two phases. In addition to the diagram published in (Häfner, Eckardt, Luther and Könke 2006), the recent results of a three-dimensional model from (Wriggers and Moftah 2006) have been included. At 60% volume fraction of aggregates the deviation to the Young's modulus of the compression test is $1.4\,\mathrm{kN/m^2}$ and to that from the tension test is $3.1\,\mathrm{kN/m^2}$. As the standard deviation of the experiments (tension test) at 60% was $1.88\,\mathrm{kN/m^2}$, the deviation of this numerical result is not quite significant. Additionally, with respect to the result of the present model (Häfner, Eckardt, Luther and Könke 2006) at 80% ($44.0\,\mathrm{kN/m^2}$), it could be assumed that finite element models generally behave to stiff for higher volume fractions. But only at 80% the experimental results (page 146) are essentially below the rigorous Hashin-Shtrikman bound ($44.2\,\mathrm{kN/m^2}$). The reason for that is not quite clear. (Besides, it is noted that the experimental results appear unusual at 20% volume ratio.) The present results are also, but only close below the lower Hashin-Shtrikman bound. These strict assumptions do not apply to the two-dimensional finite element model with plane stress condition. For 80% volume ratio of aggregates, the effective Young's modulus has additionally be computed on a larger model of $134 \cdot 10^6$ degrees of freedom and a particle size range of 0.15 mm to 19 mm. This lead to 43.775 kN/m² (Häfner, Eckardt, Luther and Könke 2006). A magnified cut-out from a typical concrete model of the present study is given in Fig. 7.18. In summary, in the present example good agreement of effective Young's modulus was obtained between experiment and two-dimensional model. This is consistent with the statement given in (Guidoum and Navi 1993) that in the estimation of
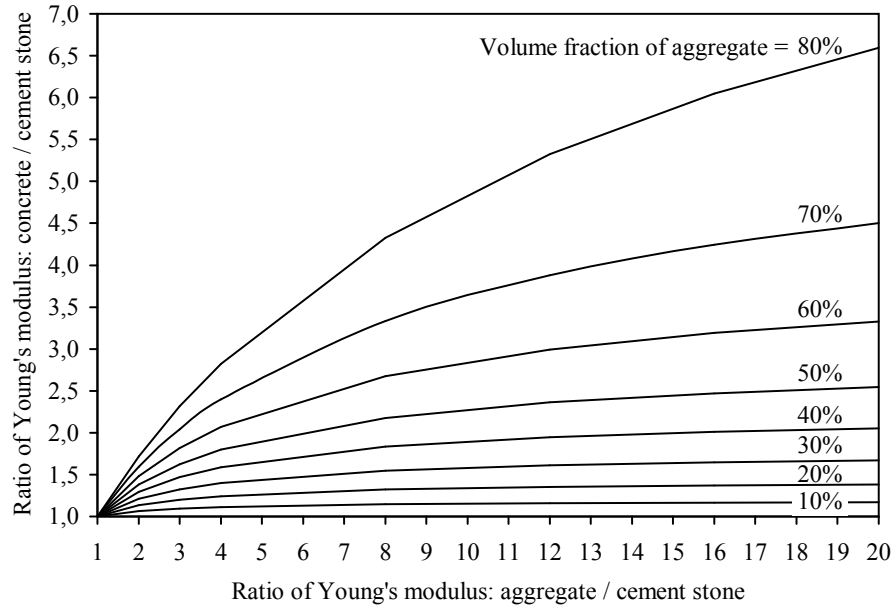
Figure 7.19: Effective Young's modulus of different mixtures

effective Young's modulus of concrete specimen there is no significant difference between two- and three-dimensional models. However, in general three-dimensional models are preferable. The good agreement of the proposed finite element model to the experiment motivated a further parameter study on concrete mixtures (Häfner, Eckardt, Luther and Könke 2006). The tests were performed based on a square model of side length 100 mm with $2048 \times 2048$ finite elements. For aggregates and matrix the Poisson's ratio was set to 0.2. The aggregates of the size range 0.5 mm to 32 mm were graded after the Fuller curve. The results, shown in Fig. 7.19, indicate that the effective Young's modulus of concrete increases overproportionally with increasing aggregate concentration. Furthermore it is observed that, depending on the aggregate volume ratio, there is no significant increase of effective stiffness beyond a certain stiffness of aggregates. However, the present analysis of concrete represents only one of many possible studies which can be performed by the proposed numerical methods in the mechanical analysis of heterogeneous solids.

# Chapter 8

# Conclusions

The present work is dedicated to computational methods in the mechanical analysis of heterogeneous solids. Such simulation methods represent an important counterpart to real experiments. Simulation provides direct access to investigate the mechanical behavior of heterogeneous solids in many ways. Moreover, computation provides systematic procedures for improving materials and even developing new materials.

Based on the provided information of a heterogeneous solid, an analog computational representation is generated. It includes a geometrical model, a mechanical model and a numerical model. An inadequate assumption or an oversimplification within any of these models generally causes an essential discrepancy between simulation and experiment.

The initial questions which motivated the present approach are presented in Section 1.3. All questions (items Q1 to Q5) demand for an improvement of the effective quality with respect to either the geometrical model or the numerical model. More accurate geometrical representations of heterogeneous solids shall be generated. The computation times and especially the memory demand of the numerical model shall be reduced as best possible. This is important to achieve an adequate resolution of heterogeneous specimen. Otherwise, the discretization of complex heterogeneous solids tends to be oversimplified. For further enhancement of the numerical model, improved finite elements shall be developed. Finally, an extension to damage simulation shall be achieved.

The grid-based strategy represents the proposed key to achieve the declared objectives. Grid-based procedures are primely suited to develop efficient and numerically stable algorithms for flexible geometrical modeling. By an element-based formulation on a uniform grid, the storage of a global stiffness matrix is superseded. Therefore the memory demand essentially reduces. The multigrid method is the solver method of choice for very large problems. This results from its characteristic that the computational effort only increases linear with problem size. The multigrid method has effectively been implemented based on a local finite element scheme. For the uniform grid a special formulation of B-spline finite elements is developed where the order of B-splines is variable. Several advantages from the linear analysis can be maintained for the damage simulation.

According to a systematic adaption and combination of grid-based procedures the effort and complexity of several methods have effectively been reduced. Most of the proposed concepts have been implemented into the new, grid-based finite element program Mulgrido. Based on a uniform data management the implementation is straightforward and efficient. Relevant disadvantages, which generally result from grid discretization, have been corrected by modified methods. The resolution of the geometry can be higher than that of the finite element grid by employing the multiphase concept to the local formu-

lation of B-spline finite elements. Moreover, a material transition zone is introduced to correct the defective stress solution along material interfaces. A selective summary of the major contributions and the conclusions from the present approach is provided in the following.

The geometrical model represents the first, intuitive abstraction level of heterogeneous solids (Chapter 2). The developments started with modeling spheres and ellipsoids. In grid-based modeling it is not required to define the topology of surfaces. Instead pointwise information is sufficient. The accuracy of the geometrical model increases with increasing resolution. Three-dimensional modeling is straightforward. The grid-based approach includes arbitrary, irregular inclusion shapes. Short formulas such as superellipses and supershapes are presented. Thus, a large variety of shapes is available which can be controlled by only a few parameters. More accurate geometrical representations of inclusion-matrix materials can be generated by an adaption of the inclusion shape.

An accurate particle-size distribution of aggregates is important for concrete. A grading curve represents a mass distribution function with respect to particle size. A general transformation into a distribution function with respect to particle number is developed. By the inverse distribution function of particle number, adequate sizes of aggregates can be generated in a natural way. It is a short, convenient formulation to obtain correct volume ratios of the different particle sizes. The formulation also permits to approximate the number of aggregates in concrete specimen. Thus, the possible size range of the model can be anticipated. The volumetric formulation is transformed into a size distribution function of a section. It provides a proper basis for two-dimensional modeling of concrete.

Separation checks are performed to assure that inclusions do not overlap. Generally analytical formulations are only available for spheres or ellipsoids. Numerical separation checks are developed for arbitrary shapes of inclusions. For each new inclusion to place within in the domain, a separation from all previous inclusions needs to be assured. Thus, in most methods the effort increases overproportional to total number of inclusions. This negative effect is avoided in the proposed grid-based method. A grid-based image of the inclusion contour is tested for direct placement on the domain grid. In connection with accurate grading of particle sizes, a volume fraction of aggregates over 85 % was achieved by this method in a two-dimensional example. This comes close to the maximum volume fraction of aggregates in real concrete. Besides, also a prototypical, but quite effective compaction algorithm is presented.

Digital image-based modeling plays an important role to record and identify two- or three-dimensional objects or structures. An introduction to the recognition of aggregates in concrete is provided. Methods and results of an implementation are summarized. Various use of digital images is demonstrated. A digital image can already represent the complete geometrical model. It is also possible to add some objects. Or image data can be recognized as inclusion shapes which can be placed into the domain. This only describes some selected options. As the basic characteristic a direct link between the real material and computational model is established in terms of geometry.

With regard to the mechanical model (Chapter 3), the geometry is interpreted as a continuous assembly of multiple, homogeneous phases, labeled by the term multiphase model. The fundamental theory of continuum mechanics for homogeneous bodies is provided. It represents the basis for the finite element formulation. Classical, analytical and modern,

numerical approaches of homogenization are prepared for the final study on the effective mechanical behavior of heterogeneous solids. A convenient, alternative solution for mixed boundary conditions is proposed. An isotropic constitutive law with exponential softening for tension is documented. Some background of a non-local formulation is prepared which will be revisited in the numerical model. Based on a high resolution of the heterogeneous body, the isotropic material law allows for simulating complex damage processes as well as effectively anisotropic behavior. The present mechanical model is capable of being extended to improved material laws. Nevertheless, it provides a clear basis for the following major contributions within the numerical model. The posed mechanical problem is solved numerically by finite elements.

A special formulation of B-spline finite elements is developed (Chapter 4). It starts by a descriptive introduction to one-dimensional B-spline finite elements. It is important to recognize that the present formulation allows to treat B-spline finite elements similar to common finite elements with polynomial shape functions. A formulation of two-dimensional B-spline finite elements is presented which is characterized by the following relevant aspects. It is a local, element-based formulation for uniform orthogonal grids. It follows that all elements (in the inner domain) are similar such that computational effort and memory demand from element stiffness matrices almost vanish. The polynomial order of the B-spline finite elements is variable. Therefore the approximation quality of these finite elements can arbitrarily scaled. Modified B-splines are employed such that the definition of displacement boundary conditions is straightforward. In an example of a homogeneous model, the accuracy of the method follows the analytical prediction: the approximation quality exemplary increases with order of B-splines. For heterogeneous models multiphase B-spline finite elements are developed. Thereby various material phases can be mapped onto a variable number of integration points within the finite element, while the variable order of elements is maintained. This means that the accuracy of geometry within one finite element and the approximation quality of one finite element can both essentially be increased. This represents a significant improvement to standard finite element schemes. However, for the correction of defective stresses along material interfaces, corresponding transition zones are introduced. Several test cases exemplify this novel method up to the B-spline order $k = 8$. An error estimation with respect to various sources and parameters is included. The B-spline finite problem can effectively be solved without storage of a global stiffness matrix by iterative solver methods.

For the proposed multigrid methods (Chapter 5), an introduction to several, associated iterative solver methods is provided. A clear transformation from the matrix form to the relevant index form is performed. Certain characteristics of solid finite elements are analyzed for the efficient application to heterogeneous problems. A uniform, global numbering system is introduced. Element-based operations are prepared for a compact and efficient formulation of the heterogeneous finite element problem in two and three dimensions. A similar approach for advanced finite elements of an orthogonal mesh or triangular elements of an irregular mesh is outlined. Transfer operators of the multigrid method for restriction, prolongation and for the coarse grid representation of the heterogeneous material are discussed. With regard to B-spline finite elements, an intuitive transfer operator is exemplified for the one-dimensional problem. The implementation is prepared such that arbitrary multigrid cycles can be performed. A modified multigrid cycle with balanced computational effort between all grids is successfully applied. The performance of vari-

ous cycles is tested. The multigrid method shows excellent efficiency for well-conditioned problems. However, the multigrid preconditioned conjugate gradient method is essentially more efficient, if large ratios of Young's moduli occur within the domain. This represents an important improvement with regard to (Häfner, Eckardt, Luther and Könke 2006) and is not only significant, but decisive for damage analysis.

Damage simulation is performed (Chapter 6). The focus is on numerical aspects with respect to the proposed grid-based approach. Therefore a basic, isotropic material law is sufficient. For each finite element an individual damage state can be stored. Therefore complex damage distributions can develop. The present implementation only includes damage simulation for bilinear finite elements. An extension to B-spline finite elements represents a valuable option for future projects. Nevertheless, severe defects of stresses from the grid-based solution of bilinear finite elements can significantly be improved by nonlocal post-processing. This can either be based on nodal averaging of stresses or on the application of a weighting function to stresses. These procedures denote a significant improvement of grid-based modeling. Moreover, the uniform grid supports an effective implementation of nonlocal averaging by a predefined discrete representation of the weighting function. Thus, nonlocal averaging is much more efficient than for irregular mesh geometries. It is shown that the dependency on orientation and size of finite elements is essentially reduced by the nonlocal formulation. A damage-controlled procedure of linear steps is performed, which means that from one step to another only a certain increment of damage occurs. According to the linear analysis the problem remains well defined, independent from the degree of damage. The progress of damage can be controlled such that for example only one element in the domain enters the damage state per iteration step. Then, the current solution represents a very good start vector for the next iteration step. The corresponding efficiency is evaluated in some examples. According to the uniform and small steps of damage progress, the active process zone and unloading of certain regions is accurately determined. It is summarized that the efficiency from the linear analysis is maintained, some relevant defects have been corrected and the observed damage behavior is reasonable. Thus, the present grid-based approach has effectively been extended to damage simulation. The proposed damage simulation on orthogonal grids represents a prototypical, but quite promising basis for further developments.

A study on the effective mechanical behavior of heterogeneous solids is presented (Chapter 7). A comprehensible numerical example demonstrates the derivation of apparent properties according to kinematic uniform and static uniform boundary conditions. The relationship from size of specimen to these upper and lower bounds of effective properties is examined. The deformation energy according to certain mixed boundary conditions is equivalent to the linear elastic parameter of the material matrix which couples associated normal strains and normal stresses of same orientation. Therefore, the deformation energy is not only an objective and but also significant measure. The effect from different geometrical arrangements of inclusions is examined while size and volume fraction of inclusions always remain constant. Each test case is based on between 6000 and 10000 different geometrical arrangements. Therefore adequate approximations of the probability density function are achieved. For small specimen with ten circular inclusions a scatter of deformation energy of about 7.5 % is observed. For the double side length of the specimen the observed standard deviation of deformation energy approximately halves. A refinement of the mesh shows that a relevant approximation error from finite elements can be

excluded. A further study considers the influence from inclusion shapes. It is observed that the mean value of deformation energy increases from circles to pentagons, to squares, to equilateral triangles and is maximum for ellipsoids of the ratio 4:1. However, the observed span of mean value is only 1.9%. It can be concluded that there is a clear, but minor effect from inclusion shape on the mean value of effective elastic properties. For small specimen with ten inclusions the standard deviation according to random geometrical arrangement is also about 1%. The volume fraction of inclusions is much more significant. A similar study is performed for varying volume fraction and random arrangement of voids which principally confirms this statement. Moreover, a directional dependency from random arrangement of inclusions is analyzed for small and larger specimen. It is observed that deformation energies from a load case in x-direction and one in y-direction are correlated. Finally a study on the effective mechanical behavior of concrete is presented. In terms of effective Young's modulus good agreement to real experiments is achieved for the full range of aggregate volume fractions from 20 % to 80 %. An additional study shows the influence from volume fraction and ratio of Young's modulus between aggregate and cement stone on the effective Young's modulus. The complete homogenization study of this thesis is based on more than 100000 different geometrical representations. The comprehensive study is effectively performed by the proposed grid-based approach from geometrical modeling to efficient iterative solver methods. Especially the flexible and stable generation of geometries allowed for a study on the effect from shape of inclusions.

The present approach shows certain advantages over other methods. Several disadvantages from classical grid-based modeling have been corrected by improved methods. In particular, the local formulation of multiphase B-spline finite elements in combination with material transition zones represents a promising novel alternative of modeling heterogeneous solids on orthogonal grids, while the storage of a global stiffness matrix is superseded. For increasing model size exemplary linear scaling of computational effort is achieved by the multigrid method. It is demonstrated that the present approach can effectively be extended for modeling nonlinear behavior of heterogeneous solids. Due to uniform orthogonal grids, all methods are straightforward to achieve for three-dimensional analysis of heterogeneous solids. Hence, it is evident that, especially for very large models of the future, the considered grid-based procedures bear significant potential.

# References

Aboudi, J. (1991). *Mechanics of Composite Materials - A Unified Micromechanical Approach.* Amsterdam: Elsevier.

Al-Rousan, T., E. Masad, E. Tutumluer and P. Tongyan (2006). Evaluation of image analysis techniques for quantifying aggregate shape characteristics. *Construction and Building Materials (in press).*

Amieur, M., S. Hazanov and C. Huet (1993). Numerical and experimental study of size and boundary conditions effects on the apparent properties of specimens not having the representative volume. In C. Huet (Ed.), *Micromechanics of Concrete and Cementitious Composites*, pp. 181–202. Universitaires Romandes Lausanne.

Backoff, C. (2003). Bitmap - Bildanalyse zur Identifizierung der Kornstruktur von Beton aus digitalisierten Aufnahmen. Student research project, Institute of Structural Mechanics, Bauhaus-University Weimar.

Barrett, R., M. Berry, T. F. Chan, J. Demmel, J. Donato, J. Dongarra, V. Eijkhout, R. Pozo, C. Romine and H. V. der Vorst (1994). *Templates for the Solution of Linear Systems: Building Blocks for Iterative Methods, 2nd Edition.* Philadelphia: SIAM.

Bathe, K.-J. (1996). *Finite Element Procedures.* New Jersey: Prentice Hall.

Bažant, Z. P. and M. Jirásek (2002). Nonlocal integral formulations of plasticity and damage: survey of progress. *Journal of Engineering Mechanics, ASCE 128*, 1119–1149.

Bažant, Z. P. and J. Planas (1998). *Fracture and Size Effect in Concrete and Other Quasibrittle Materials.* Boca Raton: CRC Press.

Bažant, Z. P., M. R. Tabbara, M. T. Kazemi and G. Pijaudier-Cabot (1990). Random particle model for fracture of aggregate or fiber compsoites. *Journal of Engineering Mechanics, ASCE 116*, 1686–1705.

Bayreuther, C. (2004). *Mehrskalenmodelle in der Festkörpermechanik und Kopplung von Mehrgittermethoden mit Homogenisierungsverfahren.* Ph. D. thesis, University of Stuttgart.

Beddow, J. K. and T. Meloy (1980). *Testing and Characterization of Powders and Fine Particles.* London: Heyden.

Bosch, K. (1993). *Statistik-Taschenbuch.* München: Oldenburg.

Bramble, J. H. (1993). *Multigrid Methods.* Essex: Longman.

Briggs, W. L. (1991). *A Multigrid Tutorial* (3rd ed.). Philadelphia: Lancaster.

Brzezicki, J. M. and J. Kasperkiewicz (1999). Automatic image analysis in evaluation of aggregate shape. *Journal of Computing in Civil Engineering, ASCE 13*, 123–128.

Caliskan, S. (2003). Aggregate/mortar interface: influence of silica fume at the micro- and macro-level. *Cement and Concrete Composites 25*, 557–564.

Carpinteri, A., B. Chiaia and P. Cornetti (2004). The elastic problem for fractal media: basic theory and finite element formulation. *Computers and Structures 82*, 499–508.

D'Addetta, G. A. (2004). *Discrete Models for Cohesive Frictional Materials*. Ph. D. thesis, University of Stuttgart.

D'Addetta, G. A., F. Kun and E. Ramm (2002). On the application of a discrete model to the fracture process of cohesive granular materials. *Granular Matter 4*, 77–90.

D'Addetta, G. A. and E. Ramm (2006). A microstructure-based simulation environment on the basis of an interface enhanced particle model. *Granular Matter 8*, 159–174.

De Boor, C. (1978). *A Practical Guide to Splines*. New York: Springer.

De Borst, R., J. J. C. Remmers, A. Needleman and M.-A. Abellan (2004). Discrete vs smeared crack models for concrete fracture: bridging the gap. *International Journal for Numerical and Analytical Methods in Geomechanics 28*, 583–607.

Desai, S. C. (2001). *Mechanics of Materials and Interfaces*. Boca Raton: CRC Press.

Dickson, L. E. (1914). *Elementary Theory of Equations*. New York: Wiley.

Duschek, A. (1961). *Vorlesungen über höhere Mathematik*. Wien: Springer.

Ebert, M. (2002). *Experimentelle und numerische Untersuchung des dynamischen Verhaltens von Stahlbetontragwerken unter Berücksichtigung stochastischer Eigenschaften*. Ph. D. thesis, Institute of Structural Mechanics, Bauhaus-University Weimar.

Eckardt, S., S. Häfner and C. Könke (2004). Simulation of the fracture behaviour of concrete using continuum damage models at the mesoscale. In P. Neittaanmäki, T. Rossi, K. Majava and O. Pironneau (Eds.), *Proceedings of ECCOMAS 2004, Fourth European Congress on Computational Methods in Applied Sciences and Engineering, 24-28 July 2004*, Jyväskylä, Finland.

Eshelby, J. D. (1957). The determination of the elastic field of an ellipsoidal inclusion, and related problems. *Proceedings of the Royal Society of London. Series A, Mathematical and Physical Sciences 241*, 376–396.

Feist, C. (2004). *A Numerical Model for Cracking of Plain Concrete Based on the Strong Discontinuity Approach*. Ph. D. thesis, University of Innsbruck, Austria.

Ferrara, L. and M. di Prisco (2002). A non-local approach with evolutionary internal length for the analysis of mode I fracture processes in concrete. In *Proceedings of EM 2002, 15th Engineering Mechanics Division Conference of the American Society of Civil Engineers, 2-5 June 2002*, Columbia University, New York.

Garboczi, E. J. (2002). Three-dimensional mathematical analysis of particle shape using X–ray tomography and spherical harmonics: Application to aggregates used in concrete. *Cement and Concrete Research 32*, 1621–1638.

Gardner, M. (1993). Piet Heins Superellipse. In *Mathematischer Karneval*, pp. 245–258. Berlin: Ullstein.

Gee, M. (2004). *Effiziente Lösungsstrategien in der nichtlinearen Schalenmechanik.* Ph. D. thesis, University of Stuttgart.

Gielis, J. (2003). A generic geometric transformation that unifies a wide range of natural and abstract shapes. *American Journal of Botany 90*, 333–338.

Guidoum, A. and P. Navi (1993). Numerical simulation of thermomechanical behaviour of concrete through a 3d granular cohesive model. In C. Huet (Ed.), *Micromechanics of Concrete and Cementitious Composites*, Universitaires Romandes Lausanne, pp. 213–228.

Hackbusch, W. (1985). *Multi–Grid Methods and Applications.* Berlin: Springer.

Hackbusch, W. (1991). *Iterative Lösung großer schwachbesetzter Gleichungssysteme.* Stuttgart: Teubner.

Häfner, S. (2005). Mulgrido - project information of the grid-based finite element program. Available from:  http://www.mulgrido.de  [August 2005].

Häfner, S., S. Eckardt and C. Könke (2003). A geometrical inclusion-matrix model for the finite element analysis of concrete at multiple scales. In K. Gürlebeck, L. Hempel and C. Könke (Eds.), *Proceedings of IKM 2003, 16th International Conference on the Applications of Computer Science and Mathematics in Architecture and Civil Engineering, 10-12 June 2003*, Bauhaus-University Weimar.

Häfner, S., S. Eckardt, T. Luther and C. Könke (2006). Mesoscale modeling of concrete: Geometry and numerics. *Computers and Structures 84*, 450–461.

Häfner, S., M. Kessel and C. Könke (2006). Multiphase B-spline finite elements of variable order in the mechanical analysis of heterogenous solids. In K. Gürlebeck and C. Könke (Eds.), *Proceedings of IKM 2006, 17th International Conference on the Applications of Computer Science and Mathematics in Architecture and Civil Engineering, 12-14 July 2006*, Bauhaus-University Weimar.

Häfner, S. and C. Könke (2004). A multigrid finite element method for the mesoscale analysis of concrete. In P. Neittaanmäki, T. Rossi, K. Majava and O. Pironneau (Eds.), *Proceedings of ECCOMAS 2004, Fourth European Congress on Computational Methods in Applied Sciences and Engineering, 24-28 July 2004*, Jyväskylä, Finland.

Häfner, S. and C. Könke (2006a). Damage simulation of heterogeneous solids by nonlocal formulations on orthogonal grids. In K. Gürlebeck and C. Könke (Eds.), *Proceedings of IKM 2006, 17th International Conference on the Applications of Computer Science and Mathematics in Architecture and Civil Engineering, 12-14 July 2006*, Bauhaus-University Weimar.

Häfner, S. and C. Könke (2006b). Multigrid preconditioned conjugate gradient method in the mechanical analysis of heterogeneous solids. In K. Gürlebeck and C. Könke (Eds.), *Proceedings of IKM 2006, 17th International Conference on the Applications of Computer Science and Mathematics in Architecture and Civil Engineering, 12-14 July 2006*, Bauhaus-University Weimar.

Hashin, Z. and S. Shtrikman (1963). A variational approach to the theory of the elastic behaviour of multiphase materials. *Journal of Mechanics and Physics of Solids 11*, 127–140.

Hazanov, S. (1998). Hill condition and overall properties of composites. *Archive of Applied Mechanics 68*, 385–394.

Hazanov, S. and M. Amieur (1995). On overall properties of elastic heterogeneous bodies smaller than the representative volume. *International Journal of Engineering Science 33*, 1289–1301.

Hertzberg, R. W. (1986). *Deformation and Fracture Mechanics of Engineering Materials.* New York: Wiley.

Hestenes, M. R. and E. L. Stiefel (1952). Methods of conjugate gradients for solving linear systems. *Journal of Research of the National Bureau of Standards, Section B 49*, 409–439.

Hettich, T. and E. Ramm (2006). Interface material failure modeled by the extended finite-element method and level sets. *Computer Methods in Applied Mechanics and Engineering 195*, 4753–4767.

Hill, R. (1963). Elastic properties of reinforced solids: Some theoretical principles. *Journal of Mechanics and Physics of Solids 11*, 357–372.

Höllig, K. (2003). *Finite Element Methods with B-Splines.* Philadelphia: SIAM.

Höllig, K., U. Reif and J. Wipper (2002). Multigrid methods with web-splines. *Numerische Mathematik 91*, 237–256.

Huet, C. (1993). An integrated approach of concrete micromechanics. In C. Huet (Ed.), *Micromechanics of Concrete and Cementitious Composites*, Universitaires Romandes Lausanne, pp. 117–146.

Jamkar, S. S. and C. B. K. Rao (2004). Index of aggregate particle shape and texture of coarse aggregate as parameter for concrete mix proportioning. *Cement and Concrete Research 34*, 2021–2027.

Jirásek, M. (1999). *Numerical modeling of deformation and failure in materials, Lecture notes of short course, 3-7 May 1999.* RWTH Aachen.

Jirásek, M. and B. Patzák (2002). Consistent tangent stiffness for nonlocal damage models. *Computers and Structures 80*, 1279–1293.

Joppich, W. (1996). *Grundlagen der Mehrgittermethode, Lecture notes.* FH Köln.

Kachanov, M., B. Shafiro and I. Tsukrov (2003). *Handbook of Elasticity Solutions.* Dordrecht: Kluwer.

Kessel, M. (2004). B-Spline basierte Scheibenelemente für rechteckige Gebiete. Student research project, Institute of Structural Mechanics, Bauhaus-University Weimar.

Kessel, M. (2005). Implementierung rechteckiger Scheibenelemente mit B-Spline Ansätzen n-ter Ordnung. Diploma thesis, Institute of Structural Mechanics, Bauhaus-University Weimar.

Kim, H. J. and C. C. Swan (2003). Voxel-based meshing and unit-cell analysis of textile composites. *International Journal for Numerical Methods in Engineering 56*, 977–1006.

Kirchner, S. (2001). *Ausscheidungshärtung dünner Al-0,6Si-0,6Ge- Schichten: Studie zur Übertragbarkeit eines Massivmaterial-Legierungskonzeptes.* Ph. D. thesis, Max-Planck Institut für Metallforschung, Stuttgart.

Koensler, W. (1989). *Sand und Kies.* Stuttgart: Ferdinand Enke Verlag.

Kwan, A. K. H., C. F. Mora and H. C. Chan (1999). Particle shape analysis of coarse aggregate using digital image processing. *Cement and Concrete Research 29*, 1403–1410.

Kwan, A. K. H., Z. M. Wang and H. C. Chan (1999). Mesoscopic study of concrete II: Nonlinear finite element analysis. *Computers and Structures 70*, 545–556.

Leite, J. P. B., V. Slowik and H. Mihashi (2004). Computer simulation of fracture processes of concrete using mesolevel models of lattice structures. *Cement and Concrete Research 34*, 1025–1033.

Lemaitre, J. and J.-L. Chaboche (1990). *Mechanics of Solid Materials.* Cambridge: Cambridge University Press.

Leukart, M. (2005). *Kombinierte anisotrope Schädigung und Plastizität bei kohäsiven Reibungsmaterialien.* Ph. D. thesis, University of Stuttgart.

Leukart, M. and E. Ramm (2006). Identification and interpretation of microplane material laws. *Journal of Engineering Mechanics, ASCE 132*, 295–305.

Li, G., Y. Zhao and S. S. Pang (1999). Four-phase sphere modeling of effective bulk modulus of concrete. *Cement and Concrete Research 29*, 839–845.

Li, G., Y. Zhao, S. S. Pang and Y. Li (1999). Effective Young's modulus estimation of concrete. *Cement and Concrete Research 29*, 1455–1462.

Li, J. (2002). *Three Dimensional Shape Modeling: Segmentation, Reconstruction and Registration.* Ph. D. thesis, University of Michigan.

Mazars, J. (1986). A description of micro and macroscale damage of concrete structures. *International Journal of Fracture 25*, 729–737.

Meleshko, V. V. (2003). Selected topics in the history of the two-dimensional biharmonic problem. *Applied Mechanics Reviews 56*, 33–85.

Michaud, V. J. (1993). Liquid-state propcessing. In S. Suresh, A. Mortensen and A. Needleman (Eds.), *Fundamentals of metal-matrix composites*, pp. 3–22. Boston: Butterworth-Heinemann.

Mishnaevsky, L. L. and S. Schmauder (2001). Continuum mesomechanical finite modeling in materials development: a state-of-the-art-review. *Applied Mechanics Reviews 54*, 49–69.

Mora, C. F. and A. K. H. Kwan (2000). Sphericity, shape factor, and convexity measurement of coarse aggregate for concrete using digital image processing. *Cement and Concrete Research 30*, 351–358.

Most, T. (2005). *Stochastic Crack Growth Simulation in Reinforced Concrete Structures by Means of Coupled Finite Element and Meshless Methods.* Ph. D. thesis, Institute of Structural Mechanics, Bauhaus-University Weimar.

Most, T. and S. Eckardt (2-4 June 2004). Application of a hybrid parallelisation technique to accelerate the numerical simulation of nonlinear mechanical problems. In K. Beucke, B. Firmenich, D. Donath, R. Fruchter and K. Roddis (Eds.), *Proceedings of ICCCBE-X, 10th International Conference on Computing in Civil and Building Engineering*, Bauhaus-University Weimar.

Nagai, G., T. Yamada and A. Wada (2000). Three-dimensional nonlinear finite element analysis of the macroscopic compressive failure of concrete materials based on real digital image. In *Proceedings of ICCCBE-VIII, 8th International Conference on Computing in Civil and Building Engineering, 14-17 August 2000*, California, pp. 449–456.

Nemat-Nasser, S. and M. Hori (1999). *Micromechanics: Overall Properties of Heterogeneous Materials* (2nd edition ed.). Amsterdam: Elsevier.

Parsons, I. D. (1997). Parallel adaptive multigrid methods for elasticity, plasticity and eigenvalue problems. In M. Papadrakakis (Ed.), *Parallel Solution Methods in Computational Mechanics*, pp. 143 – 180. New York: Wiley.

Paz, C. N. M., L. F. Martha, J. L. D. Alves, N. F. F. Ebecken, E. M. R. Fairbairn and A. L. G. A. Coutinho (2003). A computational approach of three-dimensional probabilistic discrete cracking in concrete. In N. Bićanić, R. de Borst, H. Mang and G. Meschke (Eds.), *Proceedings of EURO-C 2003, Computational Modelling of Concrete Structures, 17-20 March 2003*, St. Johann im Pongau, Austria.

Pölling, R. (2000). *Eine praxisnahe, schädigungsorientierte Materialbeschreibung von Stahlbeton für Strukturanalysen*. Ph. D. thesis, Ruhr-Universität Bochum.

Prado, E. P. and J. G. M. van Mier (2003). Effect of particle structure on mode I fracture process in concrete. *Engineering Fracture Mechanics 70*, 1793–1807.

Reuss, A. (1929). Berechnung der Fließgrenze von Mischkristallen auf Grund der Plastizitätsbedingung für Einkristalle. *Zeitschrift für angewandte Mathematik und Mechanik 9*, 49–58.

Rots, J. G. and S. Invernizzi (2003). Keynote paper: Regularized saw-tooth softening. In N. Bićanić, R. de Borst, H. Mang and G. Meschke (Eds.), *Proceedings of EURO-C 2003, Computational Modelling of Concrete Structures, 17-20 March 2003*, St. Johann im Pongau, Austria.

Schlangen, E. (1993). *Experimental and Numerical Analysis of Fracture Processes in Concrete*, Volume 38. Heron.

Schlangen, E. and J. G. M. van Mier (1992). Simple lattice model for numerical simulation of fracture of concrete materials und structures. *Materials and Structures 25*, 534–542.

Schrader, K. (2004a). Implementation des MUltifrontal Massively Parallel Solver über ein C-Interface in SLang zur Lösung großer Gleichungssysteme mit schwachbesetzten Matrizen. Student research project, Institute of Structural Mechanics, Bauhaus-University Weimar.

Schrader, K. (2004b). Parallelisierung des Nested-Dissection-Vorkonditionierers METIS für den MPI-basierten MUMPS-Solver in SLang zur Strukturoptimierung schwachbesetzter Matrizen. Student research project, Institute of Structural Mechanics, Bauhaus-University Weimar.

Schwetlick, H. and H. Kretzschmar (1991). *Numerische Verfahren für Naturwissenschaftler und Ingenieure*. Leipzig: Fachbuchverlag Leipzig.

Sejnoha, M., P. Kabele, J. Němeček, J. Zeman and J. Haslinger (2001). Elastic and inelastic analysis of heterogeneous materials, Lecture notes. In *Ph.D. course at CTU Prague, 9-13 April 2001*, Prague, Czech Republic.

Shakhmenko, G. and J. Birsh (1998). Concrete mix design and optimization. In *2nd International PhD Symposium in Civil Engineering*, Budapest.

Shan, Z. and A. M. Gokhale (2004). Digital image analysis and microstructure modeling tools for microstructure sensitive design of materials. *International Journal of Plasticity 20*, 1347–1370.

Sigmund, O. (2002). Design and manufacturing of extremal materials, Lecture notes. In *CISM course in Udine. Computational Micromechanics of Material Science, 23-27 September 2002*, Udine, Italy.

Stark, U., S. Liebezeit and A. Müller (2005). Brechsand - Abfall oder Werkstoff / Crushed sand - waste or valuable product. *Aufbereitungstechnik 46*, 30–42.

Steinkopff, T., M. Sautter and J. Wulf (1995). Mehrphasige Finite Elemente in der Verformungs- und Versagensanalyse grob mehrphasiger Werkstoffe. *Archive of Applied Mechanics 65*, 496–506.

Stock, A. F., D. J. Hannant and R. I. T. Williams (1979). The effect of aggregate concentration upon the strength and modulus of elasticity of concrete. *Magazine of Concrete Research 31*, 225–234.

Sukumar, N., D. J. Chopp, N. Moës and T. Belytschko (2000). Modeling holes and inclusions by level sets in the extended finite-element method. *Computer Methods in Applied Mechanics and Engineering 190*, 6183–6200.

Tatebe, O. (1993). The multigrid preconditioned conjugate gradient method. In *Proceedings of Sixth Copper Mountain Conference on Multigrid Methods, NASA Conference Publication 3224*, pp. 621–634.

Theuer, M. (2003). Entwicklung eines geometrischen Mesomodells von Beton unter Verwendung variabler Kornformen. Diploma thesis, Institute of Structural Mechanics, Bauhaus-University Weimar.

Tsukrov, I. and J. Novak (2004). Effective elastic properties of solids with two-dimensional inclusions of irregular shapes. *International Journal of Solids and Structures 41*, 6905–6924.

Van Dommelen, J. A. W., W. A. M. Brekelmans and F. P. T. Baaijens (2002). Micromechanics of particle-modified semy-crystalline materials. In H. A. Mang, F. G. Rammerstorfer and J. Eberhardsteiner (Eds.), *Proceedings of WCCM V, Fifth World Congress on Computational Mechanics, 7-12 July 2002*, Vienna, Austria.

Van Mier, J. and M. van Vliet (2003). Influence of microstructure of concrete on size/scale effects in tensile fracture. *Engineering Fracture Mechanics 70*, 2281–2306.

Van Mier, J. G. M., M. R. A. van Vliet and T. K. Wang (2002). Fracture mechanisms in particle composites: statistical aspects in lattice type analysis. *Mechanics of Materials 34*, 705–724.

Voigt, W. (1889). Ueber die Beziehung zwischen den beiden Elasticitätsconstanten isotroper Körper. *Annalen der Physik 38*, 573–587.

Walraven, J. C. (1980). *Aggregate Interlock: A Theoretical and Experimental Analysis.* Ph. D. thesis, Delft University of Technology.

Wang, W., J. Wang and M.-S. Kim (2001). An algebraic condition for the separation of two ellipsoids. *Computer Aided Geometric Design 18*, 531–539.

Wang, Z. M., A. K. H. Kwan and H. C. Chan (1999). Mesoscopic study of concrete I: generation of random aggregate structure and finite element mesh. *Computers and Structures 70*, 533–544.

Wesseling, P. (1992). *An Introduction to Multigrid Methods.* Chichester: Wiley.

Wittmann, F. H., H. Sadouki and T. Steiger (1993). Experimental and numerical study of effective properties of composite materials. In C. Huet (Ed.), *Micromechanics of Concrete and Cementitious Composites*, Universitaires Romandes Lausanne, pp. 59–82.

Wriggers, P. and S. O. Moftah (2006). Mesoscale models for concrete: homogenisation and damage behaviour. *Finite Elements in Analysis and Design 42*, 623–636.

Young, D. M. (1991). *Iterative Solution of Large Linear Systems.* New York: Academic Press.

Yue, Z. Q., S. Chen and L. G. Tham (2003). Finite element modeling of geomaterials using digital image processing. *Computers and Geotechnics 30*, 375–397.

Zaitsev, Y. B. and F. H. Wittmann (1981). Simulation of crack propagation and failure of concrete. *Materials and Structures 14*, 357–365.

Zheng, J. (2000). *Mesostructure of Concrete: Stereological Analysis and Some Mechanical Implications.* Ph. D. thesis, Delft University of Technology.

Zienkiewicz, O. C. and R. L. Taylor (1997). *The Finite Element Method, Fourth Edition, Volume 1, Basic Formulation and Linear Problems.* London: McGraw-Hill.

Zohdi, T. I. (2001). Computational optimization of the vortex manufacturing of advanced materials. *Computer Methods in Applied Mechanics and Engineering 190*, 6231–6256.

Zohdi, T. I. and P. Wriggers (2005). *Introduction to Computational Micromechanics.* Berlin: Springer.

# Sources of Images

Figure 1.1 includes images of the following sources:

(a), (b)    F. A. Finger-Institute for Building Materials,
Faculty of Civil-Engineering, Bauhaus-University Weimar

(c)    PhD Thesis of Steffen Kirchner (Kirchner 2001),
Max-Planck-Institute for Metals Research, Stuttgart

(d)    CeramTec AG, Innovative Ceramic Engineering,
URL: http://www.ceramtec.de in menu item "Materials"

(e)    Photo by author Stefan Häfner

(f)    Berkeley Orthopaedic Biomechanics Laboratory,
Department of Mechanical Engineering, University of California, Berkeley
URL: http://biomech2.me.berkeley.edu/tbone/tbone.html

(g), (h)    Institute of Materials and Machine Mechanics,
Slovak Academy of Sciences, Bratislava
URL: http://www.umms.sav.sk in menu item "Research Topics"

(i)    Courtesy of Ole Sigmund
Department of Mechanical Engineering
Technical University of Denmark, Kgs. Lyngby